Next generation superconducting nanowire single-photon detectors

Kleanthis Erotokritou

A thesis submitted for the degree of
Doctor of Philosophy

School of Engineering
University of Glasgow
Scotland

March 2019

Abstract

Single photon detection advanced rapidly in the last decade. The superconducting nanowire single-photon detector (SNSPD) is an emerging technology, which offers low dark count rates, broadband sensitivity from visible to mid-infrared wavelengths and very high quantum efficiency. All these features are appealing for future emerging applications in remote gas sensing, quantum key distribution and quantum information processing.

By enclosing the detector in an optical cavity, tuned to the operating wavelength, the total system detection of the SNSPD is improved. Based on the cavity design, the detector absorption is boosted at the desired experimental wavelength. Devices have been fabricated and tested, in this thesis, with enhanced detection efficiency at near-infrared, infrared and mid-infrared wavelengths. NbTiN detectors fabricated on Ta_2O_5 / SiO_2 distributed Bragg reflectors (DBR) for front-side coupling exhibit a system detection efficiency of $\approx 90\%$ at $\lambda = 940\,\text{nm}$ for the best device measured. SNSPDs were also fabricated in NbTiN on metallic mirrors for back-side coupling for 1550 and 2333 nm experimental wavelengths. The first design exhibited a system detection efficiency of $\approx 84.5\%$, at $\lambda = 1550\,\text{nm}$ for the best device measured. The second exhibited low system detection efficiency since the device suffered from unexpectedly high dark count rate mainly due to blackbody radiation at 2.2 K. However, it was possible to measure the timing jitter of this device at 350 mK indicating a FWHM of 84 ps.

Another technique to improve the total system detection efficiency of the SNSPD, is by fabricating a hairpin-shaped nanowire atop a single mode waveguide. In this design, photons travel through the waveguide and via evanescent coupling are absorbed in the nanowire. These SNSPD devices have been designed to thread along single mode Si ridge waveguides using a hairpin-shaped nanowire structure, which offers enhanced coupling and absorption efficiency via evanescent coupling. These ultra-thin superconducting MoSi detectors are precisely patterned on top of a single mode Si waveguide (600 nm) with alignment error less than 40 nm. Low temperature electrical and nano-optical characterization was carried out using a two-stage pulse tube (PT) coldhead, using an additional ^4He /^3He sorption pump, low vibration characterization of SNSPD devices at 350 mK was carried out. Characterised devices exhibit low dark count rate <5 counts per second and timing jitter of $\approx 83\,\text{ps}$ full width half maximum (FWHM) at wavelength (λ) = 1550 nm and at critical current $\approx 30\,\mu\text{A}$.

"You cannot teach a man anything;
you can only help him find it
within himself"

Galileo Galilei

Table of Contents

List of Figures

List of Tables

Acknowledgements

First and foremost, I would like to thank my supervisor Prof. Robert Hadfield, for having made this PhD possible. I am really grateful for his continuous guidance and supervision throughout the duration of my PhD studies during these four years. I would like to acknowledge the Engineering and Physical Sciences Research Council (EPSRC) for the funding that has supported me throughout my work.

I would like to show my gratitude to my second supervisor Prof. Marc Sorel, for his help with silicon-on-insulator waveguide circuits and for providing access to the InGaAs camera for detector fibre-coupling on many occasions.

I thank my fellow lab mates Gregor Taylor, Konstantinos Tsimvrakides, Umberto Nasti for the stimulating discussions and for all the fun we had in the lab. Many thanks also to the postdoc members of quantum sensors group who were present all over this journey, thanks to Dr. Robert Heath, Dr. Jharna Paul, Dr. Nathan Gemmell and Dr. Dmitry Morozov for their great support and training in the labs. I'd also like to thank Dr. Archan Banerjee for his work in thin film growth, which allowed me to fabricate my own samples.

I am forever indebted to Dr. Chandra Natarajan and Dr. Alessandro Casaburi, without their laboratory expertise I would still be trying to work out why my experiments were not working. Their friendship has enriched my time as a postgraduate student during the long hours in the lab and socially.

Thanks to all the members, of the Optoelectronic Group with whom I have shared the joys and pains of nanofabrication. Thanks, in order of appearance, Charalambos, Antonio, Francesco, Lourdes and Graham.

It has been a real pleasure to be part of the James Watt Nanofabrication Centre (JWNC). Especially, thanks to Dr. Stephen Thoms and Dr. Kevin Docherty for their indispensable support with electron-beam lithography, which has been critical to the main achievements in this thesis. Moreover, special thanks goes to Kelvin Nanotechnology staff,

Dr. Corrie Farmer and Iain Macgilp for their help when needed.

Completing a three-month research internship at the National Institute for Information and Communications Technology (NICT) in Kobe, Japan was a unique life experience that i will always cherish. Special thanks to Dr. Shigehito Miki, Dr. Taro Yamashita and Dr. Hirotaka Terai for looking after me during my visit. I really enjoyed my time in Japan and felt at home all the time.

Through the EPSRC Engineering Photonic Quantum Technologies programme grant I have collaborated with Prof. Mark Thompson and with his group members Dr. Döndü Shahin and Dr. Jorge Barreto whom I had the pleasure to work with.

Last but not the least, I am extremely grateful for the immeasurable support I have received from my family and friends throughout the duration of my studies.

Author's Declaration

I, KLEANTHIS EROTOKRITOU, declare that this thesis titled, ' Next generation superconducting nanowire single-photon detectors' and the work presented in it are my own. I confirm that:

- This work was done wholly or mainly while in candidature for a research degree at this University.
- Where any part of this thesis has previously been submitted for a degree or any other qualification at this University or any other institution, this has been clearly stated.
- Where I have consulted the published work of others, this is always clearly attributed.
- Where I have quoted from the work of others, the source is always given. With the exception of such quotations, this thesis is entirely my own work.
- I have acknowledged all main sources of help.
- Where the thesis is based on work done by myself jointly with others, I have made clear exactly what was done by others and what I have contributed myself.

Signed: _____

Date: _____

Glossary

Acronyms

AFM	Atomic Force Microscopy
ALD	Atomic Layer Deposition
ARC	Anti-Reflection Coating
bit	Binary Digit
BBR	Black-Body Radiation
BPF	Band-Pass Filter
BS	Beam Size
BSS	Beam Step Size
CAD	Computer-Aided Design
CLG	Classical Logic Gate
CO	Carbon Monoxide
CPS	Counts Per Second
CPU	Central Processing Unit
CPW	CoPlanar Waveguide
cQED	Cavity Quantum Electrodynamics
CW	Continuous Wave
DBR	Distributed Bragg Reflectors
DC	Direct Current
DCR	Dark Count Rate
DNA	DeoxyriboNucleic Acid
DSA	Digital Signature Algorithm
e-beam	Electron-Beam
EBL	Electron-Beam Lithography
ECDSA	Elliptic Curve Digital Signature Algorithm
EPSRC	Engineering and Physical Sciences Research Council
FDTD	Finite-Difference-Time-Domain
FF	Filling Factor
FIB	Focused Ion Beam

FWHM	Full-Width at Half-Maximum
GC	Gating Coupler
GM	Gifford-McMahon
HMDS	Hexamethyldisilazane
HOM	Hong-Ou-Mandel
HSQ	Hydrogen Silsequioxane
ICP	Inductive Coupled Plasma
JWNC	James Watt Nanofabrication Centre
KIT	Karlsruhe Institute of Technology
LOQC	Linear Optical Quantum Computing
MDI-QKD	Measurement Device Independent Quantum Key Distribution
MFD	Mode Field Diameter
MIBK	Methyl Isobutyl Ketone
MMI	Multi Mode Interference
MRI	Magnetic Resonance Imaging
MZI	Mach-Zehnder Interferometer
NA	Numerical Aperture
ND	Neutral Density
NI	National Instruments
NICT	National Institute of Information and Communications Technology
NIL	Nanoimprint Lithography
NIR	Near Infrared
NMR	Nuclear Magnetic Resonance
OCT	Optical Coherence Tomography
OD	Optical Density
OFHC	Oxygen-Free High Thermal Conductivity
OPO	Optical Parametric Oscillator
OSA	Optical Spectrum Analyser
PCB	Printed Circuit Board
PIC	Photonic Integrated Circuit
PMMA	PolyMethylMethacrylate
PMT	PhotoMultiplier Tubes
PNR	Photon Number Resolution
PNT	Photon-Multiplier Tubes
PPG	Pulse Pattern Generator
PPLN	Periodically Poled Lithium Niobate
PT	Pulse Tube
QC	Quantum Computers

QD	Quantum Dot
QI	Quantum Information
QIP	Quantum Information Processing
QKD	Quantum Key Distribution
QLC	Quantum Logic Circuit
QLG	Quantum Logic Gates
QSG	Quantum Sensors Group
qubits	Quantum Bits
RF	Radio-Frequency
RFQ	Radio-Frequency Quadruple
RIE	Reactive Ion Etching
RMS	Root-Mean-Square
RO	Reverse Osmosis
RRR	Residual Resistivity Ratio
RSA	Rivest-Shamir-Adleman
RT	Room Temperature
SDE	System Detection Efficiency
SEM	Scanning Electron Microscope
SFWM	Spontaneous Four-Wave Mixing
SIM	Small Instrumentation Module
SMA	SubMiniature version A
SMF	Single-Mode Fibre
SMP	SubMiniature push-on
SNAP	Superconducting Nanowire Avalanche Photodetectors
SNR	Signal to Noise Ratio
SNSPD	Superconducting Nanowire Single Photon Detectors
SOI	Silicon-On-Insulator
SPAD	Single-Photon Avalanche Diode
SPD	Single-Photon Detector
SPDC	Spontaneous Parametric Down Conversion
SPS	Single Photon Sources
SPTS	Surface Technology Systems
SRS	Stanford Research Systems
SS	Spot Size
SSPD	Superconducting Single-Photon Detectors
STJ	Superconducting Tunnel Junction
SWCNT	Semiconducting Single-Wall Carbon Nanotube
TCSPC	Time Correlated Single-Photon Counting

TE	Transverse electric
TEM	Transmission Electron Microscopy
TES	Transition Edge Sensor
TM	Transverse magnetic
TMAH	TetraMethylAmmonium Hydroxide
TPA	Two Photon Absorption
UHV	Ultra-High Vacuum
VNA	Vector Network Analyzer
VASE	Variable Angle Spectroscopic Ellipsometry

Roman Symbols

C	kinetic inductance fitting parameter
c	speed of light
CR	Count Rate
CRmax	Maximum Count-Rate
CRmin	Minimum Count-Rate
E	energy
G	ground-plane
$\hbar$	reduced Planck's constant
I_b	bias current
I_c	critical current
IC	integrated circuit
I/O	input output
J_c	current density
k	extinction coefficient
L	inductance
L_k	kinetic inductance
n	real component of refractive index
n_{eff}	effective refractive index
P	power
R	resistance
$R_\square$	square resistance
R_{20K}	resistance of the thin film at 20 K
R_{300K}	room temperature resistance
R_{input}	number of photons entering the cryostat
R_{output}	number of detected photons
R_{load}	load resistance
R_q	root mean square roughness
R_s	sheet Resistance
R_t	hotspot resistance
S	signal-plane
T	temperature
T_c	critical temperature
t_{rise}	rise time
W	width of grating teeth
Z_0	local impedance

Greek Symbols

Δ_t	timing Jitter
ϵ_r	relative permittivity
η	efficiency
η_{abs}	absorption efficiency
$\eta_{coupling}$	coupling efficiency
$\eta_{registering}$	registering efficiency
η_{SDE}	system detection efficiency
$\theta_{insidence}$	incidence angle
Λ	grating period
λ	wavelength
$\lambda/4$	quarter wavelength
μ	average number of photons per pulse
ρ_{20K}	resistivity at 20 K
τ_d	dead time
τ	thickness

Chapter 1

Introduction

In the past few years, data processing requirements have been increasing exponentially. Along with the need to retrieve information from this vast amount of data, there is also a requirement to solve complex problems with computationally expensive algorithms. Considerable scientific and engineering effort is focused on addressing these issues. The ubiquitous classical computers are incapable of solving these issues because of its binary nature, i.e., the fundamental unit of information a classical computer can represent at any given instant of time is only one of two given states, either **1** or **0**. The binary digits (bits) are determined by an electrical voltage that can be either high (**1**) typically 5 V, or low (**0**) typically 0 V or ground. Input data are processed through logic gates that perform Boolean functions on one or more input states and produce an output state. When multiple logic gates are interconnected, composite circuits can be designed to execute complex operations on multiple variables. With the rapid improvements in modern computer architectures it is possible to perform complicated algorithms simultaneously. However, some of these demanding tasks will require tremendous amounts of time or processing power. Over the past decades, the operation of commercially available computers has depended on the advancements of miniaturized silicon-based transistor technology [3]. Based on Moore's law the number of transistors doubles every two years for every square inch of integrated circuits. This trend is approaching an end as transistor sizes are reaching atomic levels [4].

Quantum information processing (QIP) is a pioneering field promising to offer solutions to current technology limitations. In contrast to commercially available computers, quantum computers (QC) encode data in quantum bits (qubits). Substitution of classical bits with qubits allows a system to exist in multiple states simultaneously (superposition).

There are a wide variety of candidate systems available for encoding quantum bits; these include ion traps, nuclear spin addressed through nuclear magnetic resonance (NMR), cavity quantum electrodynamics (cQED), superconducting qubits and photons. These are being investigated for their potential use in quantum technologies. The work presented in this thesis focusses on the realisation of high-performance single-photon detectors, a

crucial underpinning technology for photonic quantum technologies.

1.1 Motivation of Research

By realising a quantum computation system, we can enable significant improvements in computational efficiency in contrast to classical computers. This can be achieved by processing encoded information into quantum states with the use of non-classical correlations of quantum mechanics (entanglement) and superposition principle [5]. Very fast number factoring (Shor's algorithm) [6] and efficiently searching large amounts of data sets (Grover's algorithm) [7] are two examples of great importance in the financial industry. That will enable new modelling methods of financial data by isolating key global risk factors and as a result better investments are made available.

A distinguished candidate for practical quantum computing is photon detection with linear optics. Knill, Laflamme and Millburn in 2001 demonstrated that linear optical elements combined with single photons and projective measurements are possible to establish an efficient scalable quantum computer [5]. Some of the basic elements required for a linear optical quantum computing (LOQC) include beam splitters, phase shifters, single photon source and single photon detection [8]. The main focus of this Thesis is on the final element: single photon detection.

This task is extremely challenging since single-photons in the telecom-band near-infrared light with wavelength (λ) of 1550 nm have low energy levels (0.799 eV). The most promising candidate for highly sensitive single photon detection are the superconducting nanowire single photon detectors (SNSPD). As of 2013 SNSPDs are the fastest single-photon counting technology available with a demonstrated 93 % system detection efficiency (η_{SDE}) for $\lambda = 1550$ nm single photons [9].

SNSPD devices are most commonly illuminated by coupling to an optical fibre. This technique is inefficient, as even the slightest misalignment in the optical circuit will increase the coupling loss. Therefore, nanowires need to be integrated onto a waveguide circuit to eliminate coupling loss. This would enhance the efficiency of these devices significantly with a small footprint allowing multiple coincidence experiments that are impossible to perform with bulky and lossy detectors. They are the main detectors found in advanced photon counting applications such as, quantum key distribution (QKD), linear optical quantum computing (LOQC), space-to-ground communications and integrated circuit testing [10]. Development of scalable components for a fully-integrated photonic quantum computer remains an active research area. Therefore, SNSPDs research is targeted towards next generation waveguide integrated detectors that are highly efficiency ($\eta \approx 99\,\%$) and have reduced dark count rates ($\approx$ Hz), low timing jitter ≈ 10 ps and fast recovery time ($\approx$ ns). Lately the use of waveguide integrated SNSPDs is receiving

considerable interest due to their unique characteristics and the ability to be part of a single waveguide chip integrating generation, routing and detection of a single quanta of light [11–13].

1.2 Overview of Thesis

This thesis describes the author's work to design, fabricate and characterise components for optical quantum information processing using silicon as the material platform, especially single photon detectors (SPDs). It consists of six chapters. Below each chapter contents are described.

In **Chapter 2** - Background and literature review, an introduction to quantum information processing with emphasis on the components required for the realisation of a linear optical quantum computing system is presented. Afterwards, single photon detectors are introduced, and their performance metrics are presented. That is followed by a more in-depth look at superconducting materials and their properties, focussing on the material systems that are used for building superconducting nanowire single photon detectors (SNSPD). Moreover, Chapter 2 explains the choice of silicon-on-insulator (SOI) as the material platform for quantum photonic circuits in this work.

In **Chapter 3** - Fabrication and experimental methods, the methods used to fabricate devices and the experimental methods for low temperature electrical and nano-optical characterisation of these devices are described.

In **Chapter 4** - Cavity enhanced detectors, the work to enhance the performance of fibre-coupled superconducting single-photon detectors is presented. Firstly, a front side cavity integrated SNSPD device for near-infrared photon-counting applications taking advantage of distributed Bragg reflectors (DBR) as its cavity material is introduced. This type of device is a promising candidate for use in quantum dot photoluminescence studies and optical quantum technology applications. Subsequently followed by two back side cavity integrated SNSPD devices designed for infrared and mid-infrared applications that take advantage of metallic mirrors as their cavity material. These types of devices are promising candidates for use in quantum communication and remote sensing application. Moreover, it describes in detail the fabrication process for each device. Chapter 4 then focuses on electrical and optical measurement results of each type of detector.

In **Chapter 5** - Superconducting detectors integrated with silicon (Si) waveguide circuits, the results of attempts to combine silicon waveguides and photonic circuits with superconducting nanowire single-photon detectors (SNSPDs) to form quantum photonic integrated circuits are highlighted. Moreover, the design, fabrication and characterisation of each individual component is presented in full detail.

Finally, the conclusion of this work is discussed in **Chapter 6** - Conclusions, with

regards the results obtained in the previous chapters and avenues for future developments are suggested.

Chapter 2

Background and literature review

Single-photon detection is one of the critical requirements for photonic quantum computing applications. For the realisation of an efficient optical quantum information processing or communication system, it is important to have sensitive enough single-photon detectors (SPDs). This chapter begins with a brief introduction to quantum information processing with emphasis on the components required for the realisation of a linear optical quantum computing system. Afterwards, single photon detectors are introduced, and their performance metrics are presented. That is followed by a more in-depth look at superconducting materials and their properties, focussing on the ones that are used for fabricating superconducting nanowire single photon detectors (SNSPDs).

2.1 Quantum information processing

This section provides a short introduction to quantum information processing with emphasis on quantum photonic integrated circuits and the individual components required for the realisation of a linear optical quantum computing system.

2.1.1 Introduction to quantum information processing

The field of quantum information (QI) concerns how physical information is accessed, stored, processed and represented in the quantum world [14]. In 'classical computers', the basic unit of information is represented as a binary digit or 'bit'. It can represent only one state, at a time, represented as either **1** or **0**. The state of the bit is determined by the distribution of charge (above or below a threshold) in the electrical circuit [15]. Today's modern information processors are made up of semiconductor integrated circuits. Even though they are made up by millions of components, the fundamental logical blocks of an information processor are basic logic gates performing Boolean operations. A classical logic gate (CLG) is part of an electronic circuit that makes logical decisions and produces

an output signal based on the different combination of digital signals that are at its input [16]. They are considered to be the basics of Boolean logic. When multiple logic gates are interconnected, composite circuits can be designed to execute complex operations on multiple variables. The basic gate used in all integrated digital logic circuits is one of the universal gates known as a NAND gate. A NAND gate is constructed by concatenating a NOT gate to an AND gate. This universal gate can generate all other Boolean logic gate combinations. Equally, an information processor with sufficient memory and adequate amount of NAND gates can effectively compute any solvable functions [17]. Whereas,

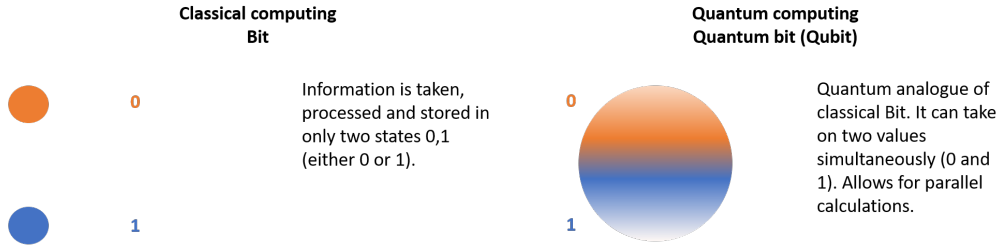

Figure 2.1: Schematic comparing classical and quantum bits.

quantum computers (QC) that are developed in labs right now, work by exploiting the properties of quantum mechanics. Their fundamental advantage over classical computers can be attributed to the following 3 properties:

- **Superposition:** In QC, information is represented with quantum bits or 'qubits' [18]. In contrast to classical bits, qubits can exist in superposition, which means that a qubit can exist in multiple states at once. Therefore, a qubit can exist as a **0** ,**1** or **0** and **1** at the same time [19]. As a result, a QC can execute multiple calculations at once.

- **Entanglement:** Based on quantum mechanics, a single entity can be formed between two or more qubits. These quantum entities can be separated by large distances. If two particles are entangled and if one of them is changed in some way, the other will react in a predictable manner (for example, the exact opposite way).

- **Quantum parallelism:** Due to the QC ability to have a quantum memory register in a superposition state, is possible to execute a large number of operations in parallel in exponentially less time that any classical computer [20].

It follows that in QC, quantum logic gates (QLG) are unitary operators that are applied on a given set of qubits. Similar to CLG, they take bits from one state to another. Unlike most of CLG, QLG are reversible. They are represented as unitary matrices and on each gate the number of input and output qubits must be identical [21].

One of the advantages of realizing a quantum computing system, is that we can achieve very fast number factoring. This was originally proposed by the mathematician Peter Shor

in 1994. Shor's algorithm was formulated to factorise the product of large prime numbers [6]. This algorithm can be used to break current public key cryptography schemes such as the RSA algorithm [22, 23], the digital signature algorithm (DSA) [24] and the elliptic curve digital signature algorithm (ECDSA) [25] encryption protocols. Therefore, with the development of a quantum computer, the public key cryptography schemes need to be updated to more secure ones [26]. Significant efforts are underway to develop large scale quantum cryptography schemes. Moreover, quantum simulation is another promising aspect of quantum computers [27]. With a quantum simulator, it is possible to study the performance of various quantum systems that are difficult or even impossible to be analysed with classical computers [28]. Various types of quantum simulators include nuclear magnetic resonance (NMR) [29], research for new drugs and new deoxyribonucleic acid (DNA) sequencing data [30].

2.1.2 Physical implementation of quantum information processing

Although, there has been great scientific movement to depict the blueprint of quantum computers hardware, there is still not a complete prototype besides some small-scale QC available to the public by IBM [31] and Google [32]. For the realisation of a practical scalable QC, only candidate systems that satisfy the 5 minimal requirements established by David DiVincenzo in 1996 are viable choices. For quantum communication, two additional requirements must be satisfied. The above-mentioned criteria are named as the 'DiVincenzo criteria' [33]. They can be summarised as:

DiVincenzo criteria

- Qubits must be well characterised and scalable.
- Qubits have long coherence times. Longer than the time required to execute a QLG operation.
- Qubits' state must be recognizable.
- Feasible to experimentally operate a universal set of gates.
- Capability for specific qubit measurements.

Quantum communication criteria

- Ability to convert flying to stationary qubits and vice versa.

- Transmit flying qubits in a thorough and responsible way from one predefined location to another.

Several candidate systems exist for encoding qubits; these include among others ion traps, nuclear spin addressed through NMR, cavity quantum electrodynamics (cQED), superconducting qubits and photons [34].

These candidate systems are defined by their qubit coherence timespan and a way to measure the state of the qubit, two physical parameters that are interlinked. Furthermore, the read-out parameter is determined by the time required to retrieve information about its state. Quantum coherence defines how long a quantum state can survive against unwanted interactions with the outside world. A qubit with a very high coherence time is nearly impossible to read-out. Equally if the read-out time is very fast, a qubit is likely to interact with its surrounding environment and lose coherence before a predetermined computation takes place. Consequently, a careful consideration needs to take place before a specific type of qubit is used.

Nuclear magnetic resonance (NMR)

Qubits in the form of nuclear spins in a single molecule, were the first successful experimental demonstration of quantum processors [35]. In this scheme of qubits, the information is stored in the nuclear spin of a single molecule and that information is manipulated with the use of electromagnetic radiation [36]. NMR was already a mature platform for magnetic resonance imaging (MRI) for chemistry and medicine applications, thus it was easily modified for performing operations with spins. They had very rapid progression and moved from two-qubit algorithms to a seven-qubit quantum computer that can factor the number 15 and that was the first experimental demonstration of Shor's algorithm [37]. NMR qubits can operate at room temperature and have long coherence times. However, as the complexity of experimental controls with each qubit increases, scalability is very challenging, and their gate operation is slow. The largest demonstration of NMR QC was formed by 12 qubits [38].

Ion trap

Another approach to a large-scale quantum computer involves qubits in the form of trapped atomic ions. This was originally proposed by Ignacio Cirac and Peter Zoller in 1995. In this scheme, quantum information is stored inside trapped atomic ions that are isolated, electrically-charged atoms, which can be confined and suspended in free space using electromagnetic fields [39]. The representative ion trap geometry for QC purposes is called the linear Paul trap or linear radio-frequency quadruple (RFQ) trap. Quantum information is processed and transferred from one ion to another through a linear "ion string" and the

interaction between adjacent ions along the string is dictated by the Coulomb force [40]. Ion-trap qubits have extremely long coherence times exceeding 10 minutes [41] and are one of the most scalable architectures for QC. Nevertheless, RFQ ions are sensitive to stray electric fields in their surrounding area, which results in disruption of the motion of these ions.

Cavity quantum electrodynamics (cQED)

This scheme is based on the interaction between single atoms with a single mode of the electromagnetic field (single photon). In a cQED system quantum information is represented by photon states and entanglement is preserved with the use of atoms trapped in high quality optical cavities that provide the non-linear interaction between photons [42]. Since photons can carry their state over a long distance for a long time are considered perfect candidates for this scheme. Additionally, the basic principle of a cQED is the simultaneous control of the single atom interactions with the photon while it transfers back and forth the state of a photon to a trapped atom. By using photons as 'flying qubits' an elementary quantum logic circuit (QLC) can be formed using optical cQED presented in Figure 2.2 [43].

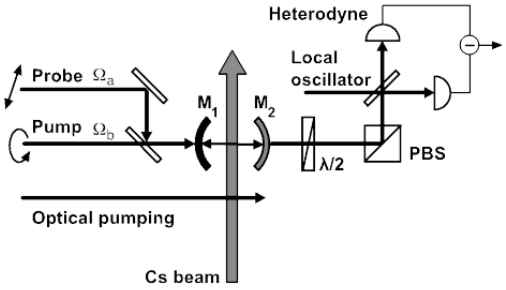

Figure 2.2: Schematic of an elementary quantum logic circuit using optical cavity quantum electrodynamics (cQED) [43].

Superconducting qubits

Another attractive system for the construction of qubits for large-scale quantum information processing units are the superconducting qubits. This is mainly due to their long coherence times typically in the $\approx 100\,\mu s$, compatibility with microwave control and scalable to large-scale networks using modern nanofabrication techniques [44]. This scheme is based on the Josephson tunnel junction and it consists of two superconductors separated by a thin insulating layer in a sandwich form (superconductor-insulator-superconductor). The second superconducting electrode allows for Cooper pairs to tunnel across the insulating barrier hence, it has a non-linear inductor behaviour. They can be referred as multi-level artificial atoms and they can store information in either charge, flux or phase

regime. However, nowadays all superconducting qubits are phase regime based and as a result they are less sensitive to charge noise and have better coherence times in contrast to charge regime based superconducting qubits. Superconducting qubits require dilution refrigerators to maintain low enough temperature, typically in the range of 10 mK in order to remove thermal decoherence effect [45].

Photons

A type of qubit that is capable of long coherence time and can route information at extremely fast speed (speed of light) is the photon. Photons can be used as flying qubits and the information can be encoded or encrypted on the polarisation state of the photon or through time-bin encoding or path encoding on the optical photonics network [46]. Since photon transmission requires less energy compared to electrons, they were considered as a replacement technology for classical computing. It has been experimentally illustrated that photons are one of the promising candidates for scalable QC [47]. Fundamentally single photons are defined as the single quanta of electromagnetic radiation and can be generated by strongly attenuating a coherent laser source at the specific wavelength required. However, this process does not guarantee true single photon emission since the laser follows Poissonian statistics and as a result at many times the source will randomly generate 0 or 1, 2 etc. photons simultaneously [48].

2.2 Linear optical quantum computing

So far in classical computers, logic gate operation and memory devices were linked together with electrical wires. One of the primary advantages for the realisation of an optical QC, is the easy integration between quantum memory devices and QLG through optical waveguides or optical fibres. In other systems such as NMR and ion-traps, the transfer of qubits from one location to another is a very complex process. A well distinguished candidate for practical quantum computing is photon detection with linear optics. Knill, Laflamme and Millburn in 2001 proposed that an efficient quantum computer can be realised with linear optical elements combined with single photons and projective measurements [5]. Some of the basic elements required for a linear optical quantum computing (LOQC) include beam splitters, phase shifters, single photon sources and single photon detectors [8]. Additionally, a feedback loop is required so parts of the circuit can be reconfigured based on the outcome of photon detection [49]. To establish a scalable optical LOQC, high density of these fundamental blocks must be integrated together on a single platform. Nevertheless, considerable engineering challenges still remain to realise such a scheme. For example, a SPS requires the introduction of pump light onto the optical waveguide that has to be filtered out via on-chip optical filtering. Moreover, low power dissipation

optical switches compatible with low temperature detectors must be developed [50, 51].

2.3 Material platforms for linear optical quantum computing

Photonic quantum technologies are a promising approach that could ultimately lead to the realisation of a full-scale quantum computer. Such a system requires integration of all the components in a single monolithic chip including single photon sources, passive circuits, fast phase-modulators, single photon detectors and electronics. Integrated quantum photonic circuits can be realised in different material platforms such as silicon, III-V semiconductors and diamond. In the following section these competing platforms are examined and compared.

2.3.1 Diamond

Diamond is a new platform that is highly attractive for photonic integrated circuits (PICs) with a wide electronic bandgap of 5.47 eV. Also, it is transparent in a broad band from the ultraviolet (UV) 225 nm [52] to 500 µm in the far infrared (IR) [53] with only two absorption bands at about 2.6 µm and 6.2 µm [54]. Additionally, it benefits from a relatively high refractive index $n = 2.4$ that allows for tight confinement of light into sub-wavelength sized waveguides. Diamond fabrication techniques are constantly progressing and that allowed the fabrication of single-photon detectors based on NbN hairpin nanowires integrated with diamond waveguides [55]. One-dimensional (1-D) and 2-D photonic crystal cavities have been fabricated in diamond membranes [56]. Moreover, diamond is a rapidly evolving platform for integrated quantum photonics due to the optically active defects available in diamond referred as colour centres, such as the silicon vacancy centre [57] and the nitrogen vacancy centre [58] that are both suitable for the realisation of efficient single-photon emitters in diamond [59]. However, these colour centres emit at wavelengths below 1 µm which will pose a challenge for long distance communication experiments.

2.3.2 III-V materials

Gallium arsenide (GaAs) and indium arsenide (InAs) are both types of III-V semiconductors. Especially GaAs is a well-characterised material platform for classical integrated photonics due to its high refractive index of 3.7 thus allowing for tight light confinement in GaAs/AlGaAs waveguides and high-density integration [60]. Additionally, quantum dots (QD) can be grown on either GaAs or InAs and can be potentially integrated with waveguide circuits [61]. QDs can offer on-demand emission of single-photons ergo photon indistinguishability. This property among emission efficiency and purity can be enhanced

via photonic crystals that have already been demonstrated in GaAs platforms. Also, on-chip NbN superconducting single-photon detectors have been realised [62] therefore making generation, manipulation and detection of single-photons on a GaAs platform feasible [63]. However, GaAs is incompatible with complementary metal-oxide-semiconductor (CMOS) foundries and suffers from high optical losses that makes scaling to large systems currently unfeasible [64].

2.3.3 Silicon

Nanophotonic fabrication based on silicon substrates has been made possible by taking advantage of currently used integrated circuit (IC) technology fabrication techniques. Specifically two major aspects of IC fabrication that have made nanophotonic circuits possible are the ability to accurately etch anisotropically (Dry Etch) structures with nanometre dimensions, as well as, the development of silicon-on-insulator (SOI) substrate [65, 66]. Being able to accurately define the etching rate, single mode slab waveguide and ridge waveguide structures can be fabricated. Furthermore, alignment of waveguides with other optical devices on the substrate is possible by defining the location of these features through lithography [67].

SOI substrates provide several advantages in nano-optical systems due to their high refractive index between Si ($n = 3.45$) and silicon dioxide SiO_2 ($n = 1.46$) [68]. SOI substrates are made up of a thick silicon layer ($\approx 726\,\mu m$), an insulator (oxide) layer ($\approx 3\,\mu m$) and a top thin silicon layer ($\approx 220\,nm$). As silicon is optically transparent across the fibre-optic telecommunications bands; specifically from 1260 nm to 1625 nm allows easy integration of waveguides and other nanophotonic devices into existing silica based fibre optic networks. By using these substrates, the lower cladding of the waveguide is formed in the underlying insulator layer (air forms the upper cladding), while the core is fabricated out of the thin silicon top layer. Since photons tend to propagate in regions with high refractive index, by utilizing this configuration, light is highly confined along all directions [69]. Furthermore, single mode waveguides core cross-section dimensions can be in the range of nanometres with minimum losses. Despite silicon technology's impressive demonstrations and potential, they have drawbacks as well. Silicon suffers from nonlinear losses at telecom wavelengths. Its energy bandgap (1.1 eV) is higher than the energy of a single photon (0.8 eV) at $\lambda = 1550\,nm$. Therefore, if the silicon device is illuminated with a high intensity light source it can absorb two photons and as a result introduce two-photon absorption (TPA) losses that limits single-photon generation rate on silicon chips [70]. Nevertheless, SOI is an important platform for photonic integrated circuits (PIC) with great potential for miniaturization of photonic structures, leading to integration of many optical components on the same substrate [71].

2.4 Elements of a linear optical quantum computer

Lightwave circuits are composed of single photon sources [72], quantum logic gates [73], single photon detectors [74] and other entangling circuits [75]. Quantum dot (QD) [76], spontaneous parametric down conversion (SPDC), spontaneous four wave mixing (SFWM) [77], nitrogen vacancy (N-V) centres in diamond [78], defects in silicon carbide (SiC) [79] and semiconducting single-wall carbon nanotubes (SWCNTs) [80] are some of the sources capable of operating in the single photon regime. These photonic states are guided through low-loss quantum waveguide circuitry. Additionally, optical components for coupling, splitting or interfering multiple photon states can be integrated on these waveguide circuits [11].

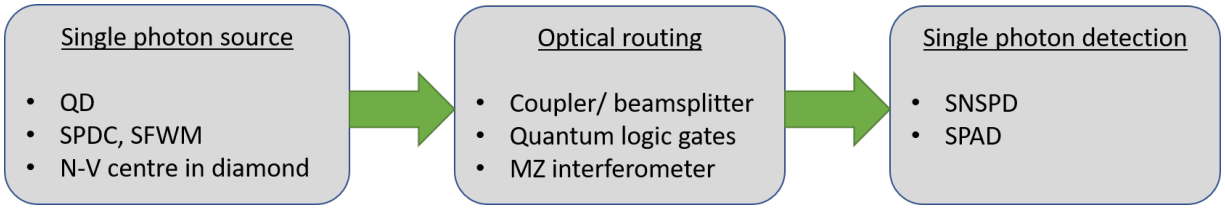

Figure 2.3: Generic schematic for optical quantum information processing.

2.5 Single-photon sources

One of the key components for the implementation of quantum optics experiments are single photon sources (SPS). Single-photon source performance is defined by three characteristic properties: firstly, ability to deliver indistinguishable photons, secondly their purity and thirdly their efficiency [81]. A few approaches to generate single photons will be discussed in this section. Without the ability to efficiently generate single photons, it would be challenging to perform experimental quantum optic studies.

2.5.1 Ideal single-photon sources

In an ideal single-photon source, the emission time of single photons is defined by the user at any arbitrary time. As a result, the source is considered deterministic as it can guarantee the production of single-photons on demand. These generated photons are indistinguishable and the probability of emitting a single-photon is 100%; hence the probability of multiple-photon emission is 0% [82]. For telecom optical wavelength bands and especially at 1550 nm there is not an ideal scheme to generate single photons. Nevertheless, there are several techniques that are close enough and are presented as follows.

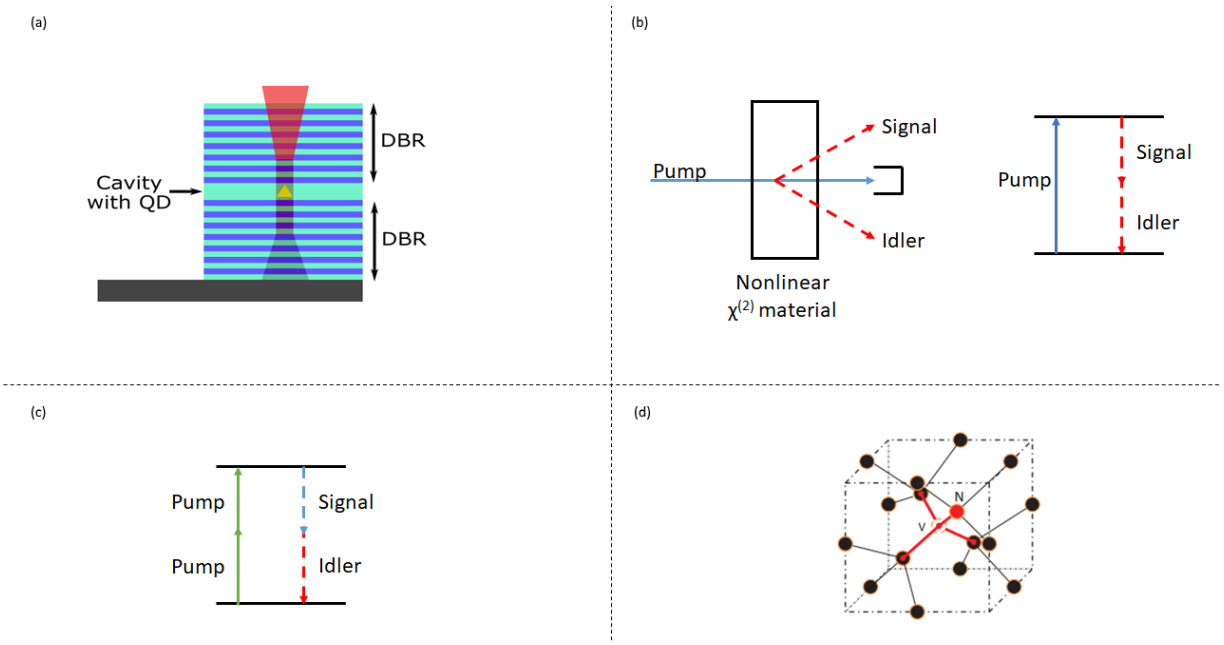

Figure 2.4: Examples of single photon sources. (a) schematic of a Quantum Dot source. A quantum dot is sandwiched between two asymmetric distributed Bragg reflector (DBR) mirrors (not to scale), (b) schematic of a spontaneous parametric down-conversion source of one input photon (Pump) converted to two output photons (Signal and Idler). Image adapted from [83], (c) schematic of a four-wave mixing source, in which two input photons (Pump) are converted to two output photons (Signal and Idler) and (d) schematic of a nitrogen-vacancy centre in diamond. Images adapted from [84–86].

2.5.2 Quantum dots

Quantum dots (QDs) are nanometre-size structures, typically made up of III-V semiconductor heterostructures such as indium phosphide (InP) and gallium arsenide (GaAs). In epitaxially grown QDs, the electrons initially are present in the valence band; whereas, holes are present in the conduction band. By applying an electric field on the QD, an electron is forced in a higher populated band (conduction), thus a hole is left in the valence band. As a result, exciton states will be formed out of these electron-hole pair interactions, which radiatively decay and generate a single photon [87]. The wavelength of the emitted photon is directly related to the energy gap, material of the structure and the dimensions of the QD. The most promising candidates for single-photon generation are InAs/GaAs quantum dot (QD) single-photon sources. They can achieve extremely high purity ($> 99.99\%$) [88] and a photon indistinguishability of up to (97%) [89]. These QD single-photon sources most commonly have an emission wavelength of 940 nm and state-of-the-art QD single photon sources at this wavelength are on the point of becoming commercially available [90, 91]. They offer several advantages as a SPS such as reliable generation of 1 photon state without producing multiple-photon states at high repetition rates. Moreover, because they are grown monolithically they are compatible with on-chip

integration on GaAs platforms [92]. However, hybrid integration with SOI is much more difficult.

2.5.3 Spontaneous parametric down-conversion

Spontaneous parametric down-conversion (SPDC) is by far the most common SPS generator technique, which can be used for the generation of heralded single photons. They were first demonstrated by Hong and Mandel in 1986 [93]. SPDC or spontaneous four-wave mixing (SFWM) are two techniques utilizing a nonlinear optical medium for the generation of heralded single-photons. Followed by the detection of one photon from the photon pair, it "heralds" information about the arrival of the other. In the case of SPDC, single-photons generation requires materials with second order $(\chi^{(2)})$ optical nonlinearities. For example, lithium niobate ($LiNbO_3$) that is among the most common nonlinear crystals, is not compatible with standard nano-fabrication processes and is centimetre-sized. By using SFWM and exploiting the $(\chi^{(3)})$ optical nonlinearity property of silicon, correlated photon pairs can be generated. Nevertheless, by integrating an optically-pumped SPS on the same chip with optical waveguides and single-photon detectors, it requires efficient separation of the generated photon pair (signal and idler) from the pump-field [94]. They also benefit from room temperature operation, in comparison to QD SPS that require cryogenic temperatures.

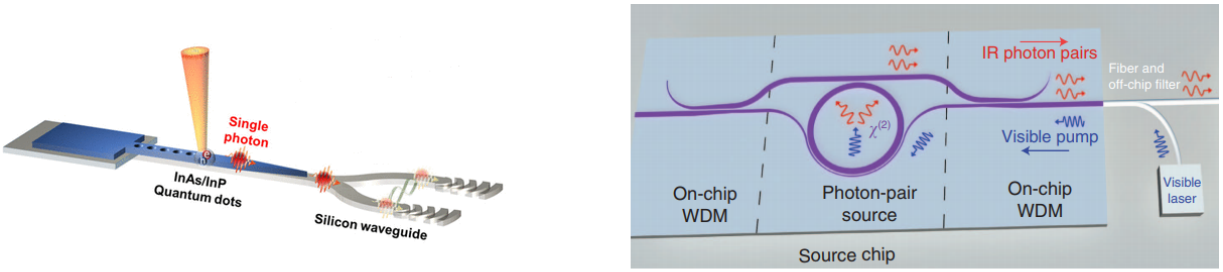

Figure 2.5: (a)Schematic of a hybrid integration of QD on silicon photonic chip. Image adapted from [83], (b) Schematic of a SFWM SPS on a silicon photonic chip. Image adapted from [94]

2.6 Single-photon detectors

Single-photon detectors current research is mainly driven by the vigorous growth of the field of quantum information science over the last few decades. An ideal SPD can be considered as a black box, which generates an electrical signal (voltage/current pulse) when illuminated by a single-photon. In reality, SPDs have many imperfections and when comparing various photon-detection technologies their performance characteristics must

be carefully defined [95]. Based on the materials ability to conduct electricity they are separated into two main groups that include, semiconducting SPDs and superconducting SPDs. This section of the thesis will present the performance metrics of single-photon detection technologies. This is followed by an in-depth look of available SPD technologies with a review of their strengths and weaknesses.

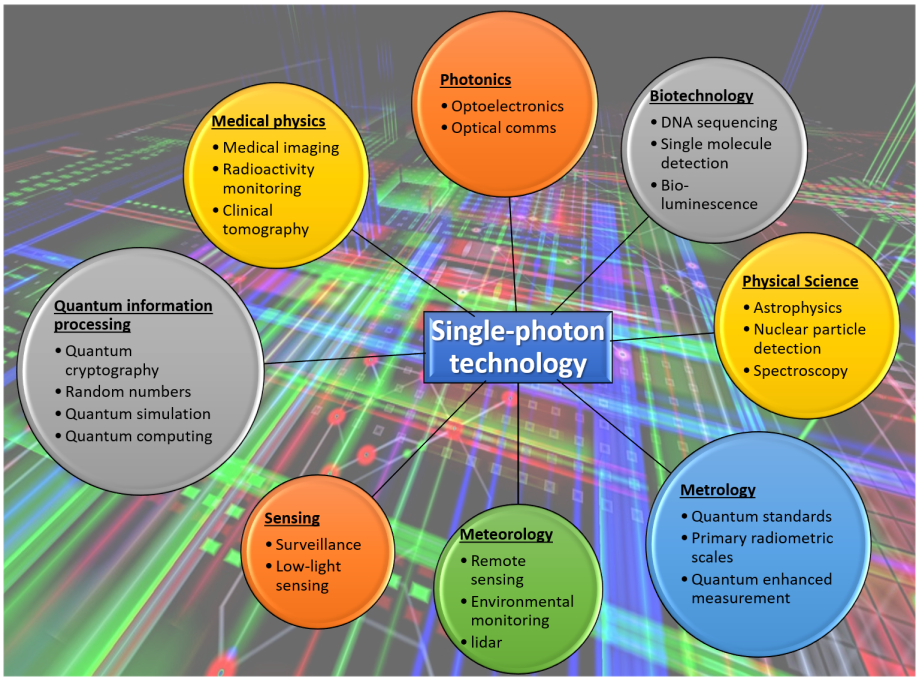

Figure 2.6: Main application areas for single-photon generation/detection technologies, adapted from reference [96].

2.7 Singe-photon detector performance metrics

When comparing single-photon detector technologies for a specific application, there are several important metrics to evaluate such as: detection efficiency, spectral range, dark count rate, timing jitter and photon number resolution. In this section, these parameters are analysed and explained.

2.7.1 Detection efficiency

System detection efficiency (η_{SDE}) is undoubtedly the most crucial parameter of SPDs. It is a dimensionless number stating the probability that a photon will be detected once it is incident on the detector system [97]. By directly comparing the incident number of photons with the recorded device counts per second the efficiency of an SPD can be measured. This (η_{SDE}) is the product of three independent probabilities [51]:

- Photon absorption efficiency (η_{absorb}): determined by the absorbing properties of a given detector. i.e. material and geometry. It represents the probability of a photon absorbed by the detector. It should be noted that η_{absorb} is wavelength dependent.
- Registering efficiency ($\eta_{registering}$): defined as the probability of an output electrical signal after the detector absorbs a photon.
- Coupling efficiency ($\eta_{coupling}$): represents the coupling losses that occur when the incident photons are coupled to the detector. It should be noted that $\eta_{coupling}$ and η_{absorb} [98] can be altered after the fabrication of the detector where $\eta_{registering}$ cannot be changed.

$$\eta_{SDE} = \eta_{coupling} \cdot \eta_{absorb} \cdot \eta_{registering} \tag{2.1}$$

2.7.2 Spectral range

Spectral range is defined as the specific range in the electromagnetic spectrum where the single photon counter is sensitive. This parameter is determined by the material composition and optical design (cavity design) used during the fabrication process, thus its wavelength dependence. To satisfy the requirements of a specific photon-counting experiment and to maintain the signal-to-noise ratio (SNR) as high as possible, the η_{SDE} of the SPD needs to be maximised at the specific wavelength (λ) of the specific experiment. This can be attained by increasing η_{absorb} with the help of techniques such as fabrication of detectors within an optical cavity or with an anti-reflection coating (ARC) [74] and or by modifying the material composition properties, this will result in engineering the energy bandgap of the absorbing material [99].

2.7.3 Dark count rate

Dark count rate (DCR) is defined as the electrical noise or stray light that can produce false signal pulses in addition to photon detection. These false detection events are called dark counts. They are frequently characterized for a 1 second time period. Therefore, they are measured in counts per second (cps) or in Hertz (Hz). The detector in the experimental setup can be triggered because of electrical noise or stray light. By filtering the noise out of the bias circuit and eliminating as much stray light as possible, the DCR is minimized [95].

2.7.4 Timing jitter

Timing jitter (Δ_t) defines the upper limit of the clock speed that a SPD can be used or the maximum count rate of the SPD. It is used for calculating the timing resolution of the SPD based on the variation in the amount of time it takes to convert an instantaneous optical absorption event to an measurable electrical output [95, 99]. Δ_t is quantified by measuring the Full Width at Half Maximum (FWHM) from the histogram of statistical distribution of time delay between the detection of an output pulse from the SPD and when it encounters an incident photon [95].

2.7.5 Dead time

Dead time (τ_d) is defined as the specific recovery time or dead time (τ_d) before SPDs are ready to register subsequent photons. This parameter sets a limit on the maximum count rate of SPDs [95].

2.7.6 Photon number resolution

Photon number resolution (PNR) is defined as the SPDs ability to distinguish multiple photons that are incident on the detector simultaneously. Their output signal is then proportional to the number of photons that impinge on the detectors active area. This thesis focuses on binary detectors that respond in the same manner for single or multiple photons incident on the detector outside its dead time window. PNR is an important performance parameter in quantum photonic applications that take advantage of multi-photon states [100].

2.8 Photon counting technologies

For the realisation of an efficient quantum computer or a quantum communication system, it is important to have a sensitive enough single photon detector. In this section, single photon detectors (SPDs) for integrated quantum photonics will be discussed. SPDs most commonly when they absorb a photon, they produce a voltage pulse (electrical signal). Based on the material's ability to conduct electricity they are separated into two main groups: semiconducting SPDs and superconducting SPDs. In the first group belong the photomultiplier tube (PMT) and the single-photon avalanche diode (SPAD) detectors. The second group includes the transition edge sensor (TES), the superconducting tunnel junction (STJ) and the superconducting nanowire singe-photon detector (SNSPD).

2.8.1 Photomultiplier tubes

Photomultiplier tubes (PMTs) were the first devices that were designed for single photon detection, and they were first demonstrated in 1935 [101]. PMT detectors operate under vacuum conditions. They are made up of a vacuum tube that contains a photocathode that is used for light absorption, several dynodes and an anode. Based on the photoelectric effect, in which the absorption of a single-photon by the photocathode results in the emission of a single electron. Then by multiplication of this single electron photocurrent with a cascaded secondary emission from dynodes, pulses of charge are produced at the anode. This process is repeated until $= 10^6$ electrons are obtained, by increasing the bias voltage at successive dynodes. As a result, a large enough signal is generated that can be detected by room temperature electronics [99, 102]. PMTs with gallium arsenide phosphide (GaAsP) photocathodes are $\approx$ 40% efficient at 500 nm, with low DCR of 100 Hz [102]. Nevertheless, in the main telecom optical wavelength bands their performance is very poor with only $\approx$ 2% detection efficiency at 1550 nm, with DCR of 200 kHz and a timing jitter of $\approx$ 300 ps [102]. In general, PMTs are fragile, require very high voltages to run, and because of their physical dimensions, they cannot be used for integration with waveguide circuits. The schematic of a typical PMT is presented in Figure 2.7.

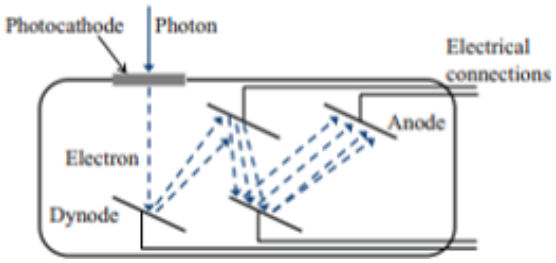

Figure 2.7: Schematic of a typical photomultiplier tube [84].

2.8.2 Single-photon avalanche detectors

The most common commercially available SPD is the single-photon avalanche diode (SPAD). It was originally developed in 1980's as a method to detect individual photons via the use of avalanche photo-diodes using silicon as the substrate [103]. Their mode of operation is called 'Geiger mode' that is the region when a higher voltage than the breakdown voltage is applied to the diode. When a photon hits the active region of the device, there is a generation of an electron-hole pair and charge multiplication takes place. As soon as one detection event takes place, the device resets by lowering the bias voltage below the breakdown voltage, thus the device is ready for subsequent photon detection events [84]. Silicon SPADs (Si-SPADs) single photon operating regime is from 400 nm to 1000 nm with detection efficiency of $\approx$ 5% at 400 nm and a peak efficiency of $\approx$ 77% at 830 nm [104].

At the main telecom optical wavelength bands the Si band-gap of 1.1 ev prevents Si-APD from functioning, thus indium gallium arsenide (InGaAs) detectors were developed that have a bandgap of 0.7 eV. These detectors are ≈ 20% efficient at 1550 nm. They are best suited for applications where the detector is used in a gated setup and triggered for short periods and subsequently suffer from high DCRs [99]. In this mode SPADs are also suffering from an effect called afterpulsing, through which trapped carriers can trigger a subsequent avalanche event that will further deteriorate their performance [105]. The schematic of a typical SPAD is portrayed in Figure 2.8.

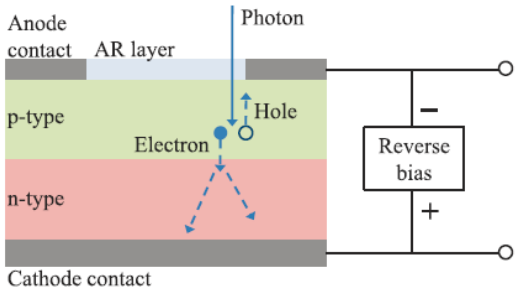

Figure 2.8: Schematic of a single-photon avalanche photodiode (SPAD) [84].

2.8.3 Superconducting single photon detectors

Several types of SPDs use superconductivity as the basis of their detection mechanism. Transition edge sensor (TES), superconducting tunnel junction (STJ), and superconducting nanowire single photon detector (SNSPD) are the three most prominent examples. In order to understand how these detectors operate, a brief overview of superconductivity will be presented first.

Superconductivity: A brief introduction

In July of 1908, the great Dutch physicist Heike Kamerling Onnes in his laboratory at Leiden University achieve a significant breakthrough in the history of science. He was the first who managed to liquefy helium and thus opened an entirely new chapter in low-temperature physics and cryogenics. Following up on his breakthrough, he used liquid helium as a coolant to study the temperature electrical resistance of various metals. That led to the first observation of superconductivity in 1911 [106]. The metal that was under test was mercury since it was easy to prepare pure samples by distillation. Figure 2.9 presents the measured resistance of mercury under liquefied helium that was the first proof of superconductivity [107].

It was observed that the measured resistance of mercury was gradually decreasing upon reaching the boiling temperature of helium 4.2 K and then suddenly dropped to

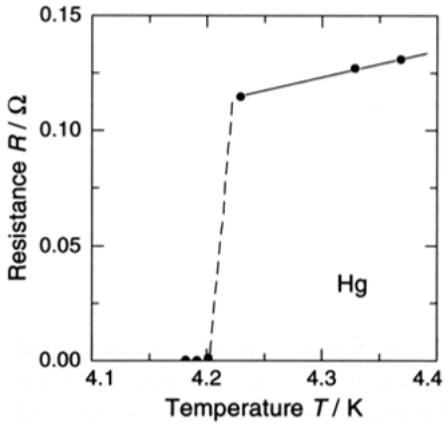

Figure 2.9: Mercury resistance measurement under cooling [107].

zero. Dr. Onnes noted "Kwik nagenoeg nul" which translates as "resistance of mercury is almost zero". He called this mysterious phenomenon "superconductivity" and the same name is still used today [108]. Immediately after this discovery, various other materials were tested under liquefied helium. It was observed a variety of metals can exhibit this phenomenon, when are cooled down below a characteristic temperature of each material that was known as superconducting transition temperature, or specific critical temperature (T_c). In Figure 2.10 are illustrated some of the elements that can exhibit this phenomenon.

Li	Be 0.026 ...	Superconductivity parameters for elements Transition temperature in Kelvin Critical magnetic field in gauss (10^{-4} tesla)									B	C	N	O	F	Ne ... ...
Na	Mg	...									Al 1.140 105	Si* 7 ...	P* 5 ...	S*	Cl	Ar ... ...
K	Ca	Sc	Ti 0.39 100	V 5.38 1420	Cr*	Mn	Fe	Co	Ni	Cu	Zn 0.875 53	Ga 1.091 51	Ge* 5 ...	As* 0.5 ...	Se* 7 ...	Br	Kr ... ...
Rb	Sr	Y*	Zr 0.546 47	Nb 9.50 1980	Mo 0.90 95	Tc 7.77 1410	Ru 0.51 70	Rh 0.0003 0.049	Pd	Ag	Cd 0.56 30	In 3.4035 293	Sn(w) 3.722 309	Sb* 3.5 ...	Te* 4 ...	I	Xe ... ...
Cs* 1.5 ...	Ba* 5 ...	La(fcc) 6.00 1100	Hf 0.12 ...	Ta 4.483 830	W 0.012 1.07	Re 1.4 198	Os 0.655 65	Ir 0.14 19	Pt	Au	Hg 4.153 412	Tl 2.39 171	Pb 7.193 803	Bi* 8 ...	Po	At	Rn ... ...
Fr	Ra	Ac	...														
...			Ce* 2 ...	Pr	Nd	Pm	Sm	Eu	Gd	Tb	Dy	Ho	Er	Tm	Yb	Lu 0.1 ...	...
...			Th 1.368 1.62	Pa 1.4 ...	U* 2 ...	Np	Pu	Am	Cm	Bk	Cf	Es	Fm	Md	No	Lr	...

Figure 2.10: Critical temperature values for a range of superconductors [109].

Two years after the discovery of superconductivity, Dr. Onnes observed the presence of a maximum value of the current density in mercury, above which the "superconductivity" state disappeared. This maximum value was increasing as the temperature was kept well below the T_c, thus concluded that this parameter is temperature dependent [110]. If the

applied current in the material is beyond this maximum value, then it would return at its normal resistive state and it wouldn't be superconducting anymore. This maximum value was termed as critical current (I_c). Additionally, it was observed that superconductivity was highly dependent on the applied magnetic field. Like I_c, superconductivity properties would disappear if the applied magnetic field exceeds a maximum value. That was called critical field (B_c) and it was a function of temperature [111].

2.8.4 Transition edge sensor

Transition edge sensor (TES) belong to the category of thermal equilibrium detectors. They are employed in applications where high sensitivity is required, that includes heat measurements or infrared radiation where they operate as bolometers. Biasing the detector close to its transition temperature, a steep increase in the resistance of the superconductor occurs due to a photon or a charged particle causing very small variations in its temperature. Their main advantages include very high sensitivity to single photons with near unity detection efficiency at telecommunication wavelengths [112]. Additionally, their output pulse height is proportional to the energy produced based on the number of single photons absorbed, thus TES are capable of photon number resolution (PNR) [113]. Nevertheless, TES operating temperature is $\approx 50\,\mathrm{mK}$ and limited by their slow thermal recovery time. The schematic representation of a typical TES is portrayed in Figure 2.11.

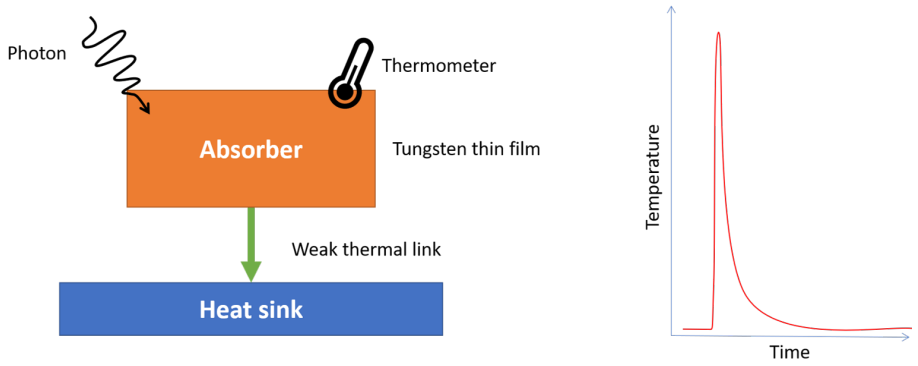

Figure 2.11: Schematic representation of a transition edge sensor (TES). A photo absorption event increases the temperature of the absorber and subsequently dissipated to a heatsink by means of a weak thermal link [114].

2.8.5 Superconducting tunnel junction

Superconducting tunnel junction (STJ) consists of two-superconductors separated by a thin insulating layer in a sandwich form (superconductor-insulator-superconductor). They operate by breaking Cooper pairs in a superconducting material with the use of its absorbed energy and as a result the generation of free energy carriers. The number of these

free carriers is proportional to the energy of the absorbed photon [115]. These devices have been successfully used in astrophysics applications. They have a maximum detection efficiency of ≈ 20% at visible wavelengths [116]. Nevertheless, the maximum count rate in both TES and STJ is in the range of 100 kHz which is considered their main limiting factor. Additionally, STJs operating temperature is ≈ 300 mK [116, 117]. The schematic representation of a superconducting tunnel junction (STJ) is presented in Figure 2.12.

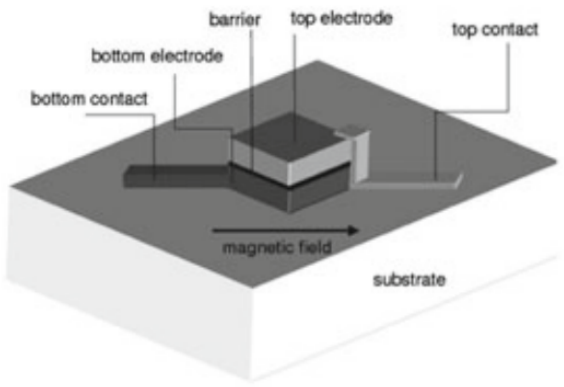

Figure 2.12: Schematic representation of a superconducting tunnel junction (STJ) [115].

2.8.6 Superconducting nanowire single photon detectors

Superconducting single-photon detectors (SNSPDs or SSPDs) are made up by an ultra thin (≈ 5 nm) superconducting layer, deposited onto a substrate and afterwards patterned to nanoscale dimension (≈ 100 nm) nanowires. The nanowires are patterned in meander geometry to create a square (active area) of 15x15 μm^2 that will yield a high detection efficiency. SNSPDs operation is based on the absorption of a single photon which in turn will generate an electrical pulse that is characteristic to each single photon absorbed [118]. They are the most sensitive type of SPDs. They can offer low dark counts, low timing jitter and short reset times. Moreover, they can offer a wide spectral range from visible to mid infrared wavelengths [9, 119, 120].

Gol'tsman *et al.* developed the first SPD based on niobium nitride (NbN) nanowires in 2001 [121], which set the basis of today's progressive SNSPDs. Their detector design was made up of 5 nm thick and 200 nm wide NbN nanowires. Its principle of operation relied on the ability of a single-photon to generate a resistive region in the superconducting nanowire. They observed that when a photon carrying super-current, was absorbed in the nanowire, a resistive hotspot region was formed. When the nanowire cross section was small enough, a voltage pulse was measurable [121]. The detector was cooled down well below its critical temperature (T_c) at 4.2 K and current biased (DC source) with a current close to its critical current (I_c) Figure 2.13[i]. Then a resistive (hotspot) region is formed on

the active area of the detector, when the nanowire absorbs an incident number of photons carrying enough energy. As a result, there is a disruption in the superconductivity in that region as Cooper pairs in the superconductor are split into quasiparticles Figure 2.13[ii]. The supercurrent is forced to flow along the periphery of the hotspot region in order to bypass it. Since the NbN nanowires are very narrow, a slight increase of the local current density around the resistive area is observed that exceeds the superconducting critical current density. As a result, a resistive barrier is generated along the width of the nanowires Figure 2.13[iii]. Employing electron-phonon scattering (Joule heating) via the DC bias link, energy is exchanged between the electrons in the hotspot region and the phonons in the nanowire Figure 2.13[v]. Using phonon-phonon scattering, energy is coupled to the substrate, resulting in absorption of the electron energy by the substrate, which operates as a heatsink. As the hotspot region cools and shrinks, it returns into its superconducting state, where the nanowire starts carrying bias current again Figure 2.13[vi]. The formation of the hotspot generates a measurable output voltage pulse across the nanowire via the use of room temperature electronics and the bias current across the nanowire resets back to its original value Figure 2.13[i] [95, 121, 122].

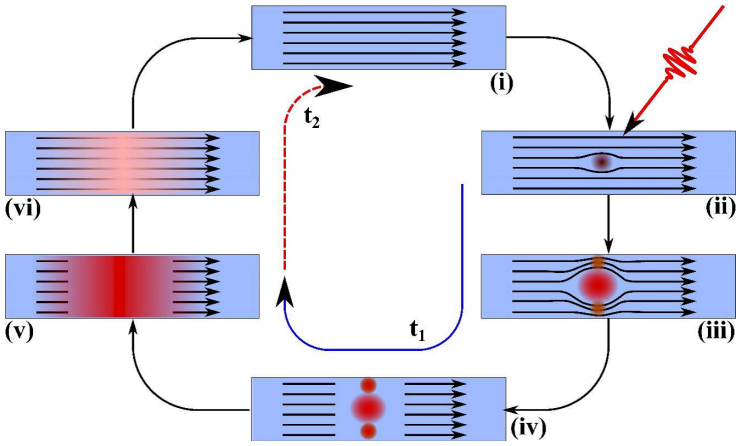

Figure 2.13: Operation principle of a superconducting nanowire single-photon detector (SNSPD) [95].

Recent experimental observations have lead to the refinement of the above model. In contrast to the original hotspot model where the breakage of electron Cooper pairs forms the hotspot region, the second model suggests that vortex-antivortex pairs are responsible for the stability of the superconducting nanowire. This model follows the phase transition mechanism in superconducting thin films suggested by Berezinskii, Kosterlitz and Thouless. According to Ivry *et al.* [123] there are two schemes that govern the vortex-antivortex disruption of superconductivity. a) During the photon absorption event, heat is generated on the wire that consequently reduces the energy barrier and a vortex penetrates the wire. Since the superconducting wire is current biased, the vortex penetrates across its entire width and as a result the superconductivity is disrupted and the wire becomes resistive.

b) During the photon absorption event, a vortex-antivortex pair is generated. Since the superconducting wire is current biased, a Lorentz force is applied on the vortex and the antivortex in opposite directions. This vortex-antivortex pair breaks when the Lorentz force is large enough and hence the wire resets back at its resistive state. Based on these observations, Engel *et al.* [124] came to the conclusion that currently no single model can completely explain the detection mechanism of an SNSPD. The first model is valid at high photon energies, while the second model is valid at low energies. He suggested that the governing mechanism is dictated by the device geometry and material.

2.8.7 Superconducting thin films

For the realisation of highly efficient SNSPD detectors, it is crucial to optimise the structural properties of the superconducting thin films prior to their fabrication. In order to tackle that requirement, the relationship between the normal resistive and low temperature state of the superconducting material is firstly investigated. From this experiment the critical temperature (T_c) of a superconducting thin film is extracted. T_c is defined as the temperature at which the resistance of the thin films drops to zero (i.e. becomes resistive). Thin films with high T_c allow for the realisation of SNSPDs with high sheet current density (J_c) that allows for higher I_c, which subsequently increases the signal-to-noise (SNR) ratio and lowers the timing jitter of the SNSPD. Additionally, the thickness (τ) and the sheet resistance (R_s) are two parameters that can optimize the superconducting property of thin films [125]. ($R_s = \frac{\rho_{20K}}{\tau}$) , where ρ_{20K} denotes the resistivity of the thin film at 20 K. ($\rho_{20K} = \frac{R_{20K} * d * width}{length}$), where R_{20K} is the resistance of the thin film at 20 K [126]. Moreover, the purity of thin films can be estimated through another important parameter called residual resistivity ratio (RRR). This is defined as the resistivity ratio of the films at 300 K to that at 20 K and is extracted from the resistance-temperature (R-T) measurements [127]. RRR is a gauge of material quality and can provide information of crystal defects and impurities in the thin film. It can also provide information with regards the nature of a thin film, which can be either metallic or insulating. For metallic superconducting thin films, high RRR values should be aimed during the thin film optimisation process. This indicates high crystalline structure of the film and higher metallic film purity. One good example is niobium (Nb) based thin films. Nevertheless, for applications where insulating films are required, low RRR values should be aimed during the thin film optimisation process. Especially for NbN and niobium titanium nitride (NbTiN) thin films RRR > 1 indicates metallic resistance-temperature characteristics and excellent crystalline properties [128]. Whereas, RRR < 1 indicates insulating resistance-temperature characteristics. Either during thin film growth process or lithography, defects or constrictions along the nanowire can be introduced. This occurs in regions where the cross-sectional area of the nanowire is reduced. As a consequence at the centre of the constriction J_c is reduced and the detector

cannot be biased at a high current close to its I_c hence the η_{SDE} is reduced [123]. Also, constrictions can occur due to high surface roughness of the substrate material. Especially if the surface roughness is comparable with the thin film thickness their I_c is limited due to potential incisions in the SNSPD active area.

2.8.8 Evolution of SNSPD design

The field of single-photon detection has grown at an exponential rate since the original discovery of the first SNSPD devices from Prof. Gol'tsman's group. As a result, many research programmes have been initiated across the world with the goal of demonstrating and exploiting high performance SPDs. As described in 2.7.1, the η_{SDE} of an SNSPD device is completely dependent on the product of $\eta_{coupling}$, η_{absorb}, $\eta_{registering}$ probabilities.

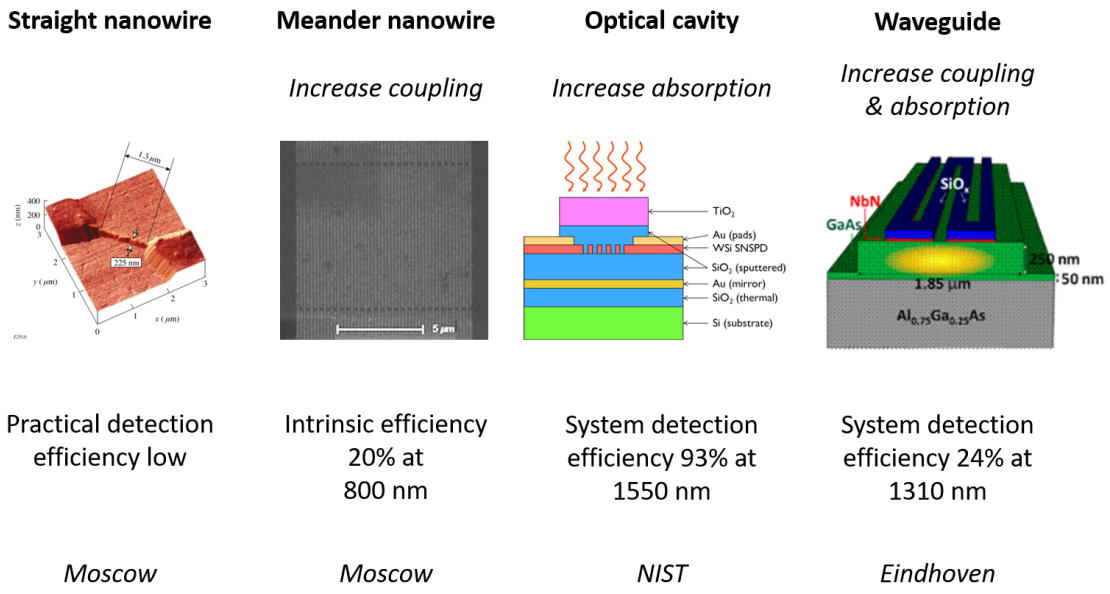

Figure 2.14: Evolution of SNSPD design. Images adapted from [9, 62, 129, 130]

Enhancing $\eta_{coupling}$ - The detectors proposed from Prof. Gol'tsman's group were based on a micro-bridge design that had a very low practical detection efficiency. This was mainly due to the fact that their device was consisted of an extremely narrow NbN stripe (200 nm), thus the probability of an incoming light to impinge upon the active area of the detector was limited. In order to overcome this limitation, it was proposed the realization of an SNSPD device meandering over a square area of 10x10 µm^2 [130]. This approach has yielded a maximum intrinsic efficiency of $\approx 20\%$ at 800 nm. Subsequently, it was suggested a self-aligning method that allowed for precise alignment of the light output from a single-mode fibre to the centre of the SNSPD active area, resulting in $\eta_{coupling}$ close to unity [131].

Enhancing $\eta_{absorption}$ - By improving the coupling probability alone, the likelihood of a single photon impinging on the active area of an SNSPD and subsequently absorbed by the nanowire is less than unity. Typically, light is coupled from an optical fibre or free-space vertically atop the ultra-thin nanowires (4-8 nm), thus only a small portion of it is absorbed; whereas the rest of it is typically lost into the substrate. There have been proposed two techniques in order to enhance $\eta_{absorption}$. (a) Micro-cavity enhanced design in which absorption is boosted by enclosing the SNSPD in an optical cavity, which virtually extends the interaction time between the nanowire-photon [74]. (b) Waveguide-coupled enhanced design in which absorption is boosted by fabricating a nanowire atop a single-mode travelling-waveguide. In this scheme, injected light propagates along the waveguide and single-photons are coupled evanescently to the superconducting nanowire. Finally, leading to unity absorption [132].

Enhancing $\eta_{registering}$- By reducing the width of the nanowires, the $\eta_{registering}$ is improved. Additionally, by using parallel nanowire configurations referred to as superconducting nanowire avalanche photodetector (SNAP) can result in higher output signals. When a photon is absorbed in one of the branches of the device, that element becomes resistive and additional current is redirected into the other elements, subsequently exceeding the critical current of the parallel elements and the entire device becomes resistive [133]. However, if the device is not biased high enough, the avalanche might not be triggered as the diverted current is not enough to trigger the next parallel branch of the device. The device waits for either the occurrence of a dark count or for a second photon to be absorbed in another element to switch the whole device into its resistive state. Nevertheless, if this does not occur the SNAP will recover back into its superconducting state whilst the avalanche process was not completed and it will register a count. Additionally, the registering probability can be improved by switching from crystalline to amorphous thin film superconducting material with a smaller energy gap such as amorphous WSi or MoSi. These devices can exhibit near unity $\eta_{registering}$ due to their amorphous nature, leading to uniform nanowires across a large area. They can be deposited on various substrates as they do not set strict requirements on substrate choice. Also, the lower carrier density and smaller superconducting energy gap are considered to be the reasons behind the generation of a larger hotspot region in contrast to crystalline based materials and hence saturated internal detection efficiency is attained [1, 95].

2.8.9 Material candidates for SNSPDs

The first SNSPD device was demonstrated using a niobium nitride (NbN) nanowire from Goltsman's group from Moscow. NbN is a traditional superconductor with critical temperature (T_c) around 15 K, thus it can operate at liquid helium temperatures 4.2 K [121].

Nevertheless, many other materials were explored in the last decade for potential optimisation of SNSPDs for higher efficiency, another superconducting material NbTiN was explored by Dorenbos from Delft University of Technology (TU Delft) [134] for fabrication of SNSPDs on Si substrates. These materials are based on a crystalline structure, they depend on the crystal phase of the films and as a result they suffer from crystal defects that can limit the fabrication yield [9]. It has been shown that amorphous materials such as tungsten silicide (WSi) [9], molybdenum silicide (MoSi) [135] and molybdenum germanium (MoGe) [136] have robust superconducting properties compared to crystalline based thin films. Moreover, because of their high degree of homogeneity they allow for the robust fabrication of uniform nanowires over larger areas.

Table 2.1 shows the comparison between various SNSPD materials in terms of bulk T_c , thin film T_c, their film type and bulk energy gap [1].

SNSPD material comparison					
Material:	NbN	NbTiN	WSi	MoSi	MoGe
Bulk T_c (K):	16	15	5	7.5	7.36
Thin film T_c (K):	8.6 (3 nm)	9.5 (6 nm)	3.7 (4.5 nm)	4.5 (6 nm)	4.5 (6.2 nm)
Crystal structure :	Polycrystalline	Polycrystalline	Amorphous	Amorphous	Amorphous
Bulk Energy gap ($2\,\Delta_0$ meV):	4.9	4.5	1.52	2.28	2.2

Table 2.1: SNSPD materials comparison [1, 2].

2.9 Photonic integrated circuits

Realisation of a universal programmable quantum computer requires many photonic elements and assembling all these elements with bench-top optics is challenging and unrealistic. Therefore, in order to make a scalable and practical LOQC is required to integrate all the elements of a quantum information processor onto a single chip. This section deals with basic elements required for LOQC in optical waveguide circuits.

2.9.1 Waveguide integrated single-photon sources

In silicon platform thanks to its nonlinear optical properties pairs of photons can be spontaneously generated through SFWM in a spiralled-shaped optical waveguide. In SFWM, two photons from a laser (pump) source are annihilated by a $(\chi^{(3)})$ non-linear medium such as photonic crystal (PhC) to create the photon pair (signal and idler). However, this SPS is probabilistic, not scalable and suffers from two-photon absorption (TPA). A good alternative is the realisation of a SPS in a resonator-shaped waveguide considering,

a) footprint is typically smaller than aforementioned spiral-shaped ones and b) pairs of emitted photons can be uncorrelated (spectrally separable) [137, 138].

2.9.2 Waveguide integrated single-photon detectors

Waveguide integrated SNSPDs on a lithium niobate substrate have been previously used as candidates for planar lightwave circuits [139]. NbN SNSPD on top of silicon (Si) waveguide nanophotonic circuits (Figure 2.15) with 91 % detection efficiency at telecommunication wavelengths as well as the realisation of NbTiN SNSPD on top of silicon nitride (Si_3N_4) waveguide nanophotonic circuits with 52.5 % on-chip detection efficiency at telecommunication wavelengths have been previously demonstrated by Tang group at Yale University. [12, 140] Additionally, a NbN SNSPD on top of Si_3N_4 waveguide nanophotonic circuit has been demonstrated by Karlsruhe Institute of Technology (KIT) research institute in Germany [141].

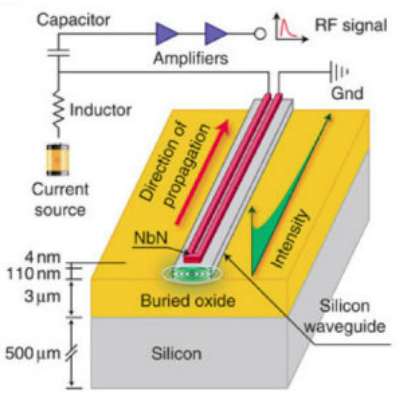

Figure 2.15: Si Nanophotonic waveguide covered with a U-shaped NbN nanowire [12].

In the University of British Columbia (UBC) it was presented a coherent perfect absorber waveguide integrated NbTiN SNSPD on SOI substrate (Figure 2.16). This was done by patterning an asymmetric nanobeam cavity around the superconducting wire. They have presented $\approx$ 96 % on-chip quantum efficiency, dark count rate $<$ 0.1 Hz and timing jitter of $\approx$ 53 ps [142].

Moreover, Massachusetts Institute of Technology (MIT) group have introduced a hairpin-shaped SNSPD fabricated on $\approx$ 200 nm Si_3N_4 membrane and then transferred on a SOI photonic integrated circuit (PIC) (Figure 2.17). By splitting the fabrication process in two individual processes (SNSPD and PIC) they have showed an average system detection efficiency above 10 % and an average timing jitter of $\approx$ 50 ps among ten detectors. This is the first device that has demonstrated on-chip photon correlation measurements of non-classical light [13].

Detectors on GaAs ridge waveguides have been demonstrated by Fiore at TU Eidhoven (Figure 2.18) with $\approx$ 20 % efficiency at telecommunication wavelengths and timing jitter

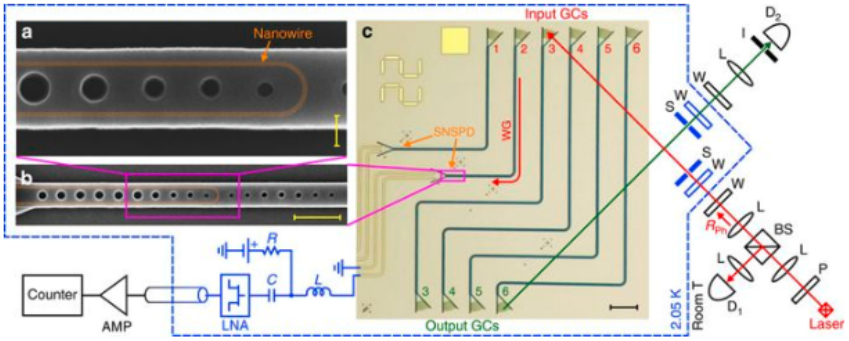

Figure 2.16: Si waveguide integrated NbTiN SNSPD designed as a coherent perfect absorber with an asymmetric nanobeam cavity around a superconducting nanowire [142].

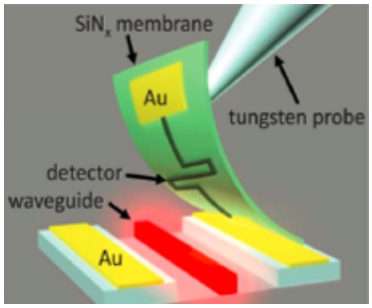

Figure 2.17: Membrane transfer of a NbN SNSPD onto a photonic waveguide [13].

of $\approx 60\,\text{ps}$ [62]. Also, in the Walter Schottky Institute at Technical University of Munich (TUM) it was reported the use of self-assembled InGaAs quantum dots (QD) embedded into the optical mode of a GaAs ridge waveguide detector (Figure 2.19) with a timing jitter of $\approx 72\,\text{ps}$ [143].

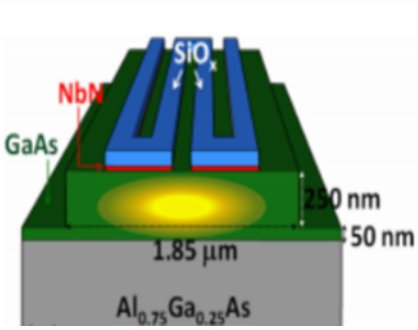

Figure 2.18: GaAs ridge waveguide covered with a U-shaped NbN superconducting nanowire from TU Eindhoven (TU/e) [62].

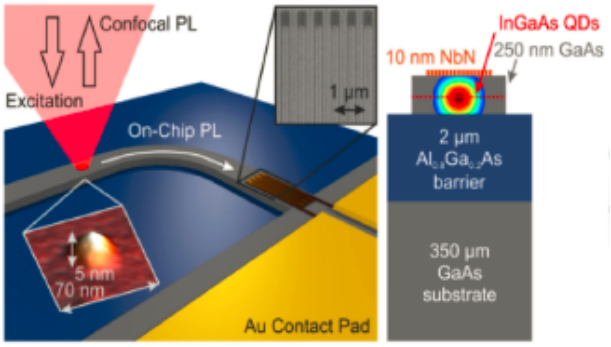

Figure 2.19: InGaAs quantum dots embedded in GaAs ridge waveguide with a U-shaped NbN nanowire [143].

2.9.3 Fundamental building blocks

In addition to highly efficient SPSs and SPDs integrated in optical waveguides, sophistically optical circuits are required for the realisation of a LOQC. For those circuits, fundamental optical components such as beam splitters and Mach-Zehnder interferometers (MZI) are required [144]. In every photonic integrated circuit (PIC) the most basic building block is an optical waveguide. It can be described as the integrated optical equivalent of an optical fibre and is the component that connects various optical devices by guiding light between different optical components across the chip.

Beam-splitters

Beam-splitters are passive optical blocks in waveguide circuits used for splitting light from one input channel into several output channels. They can be implemented by either multi-mode interference (MMI) couplers or directional couplers. The latter consists of two parallel waveguides in a close distance so as the optical mode of the one overlaps with the other. Its coupling coefficient is tuned by both the spacing of the waveguides and the total length of the coupler. Often beams-splitters are designed with a 50:50 split ratio, meaning that light from one input port is split equally between both output ports. MMI couplers operation is based on the self-imaging principle in which, input signal from a single-mode waveguide is launched into a multi-mode waveguide and as a result higher order modes are allowed to be excited on the waveguide [145]. MMI couplers in comparison to directional couplers are more tolerant to fabrication imperfections, which makes them a very attractive building block for PICs [146].

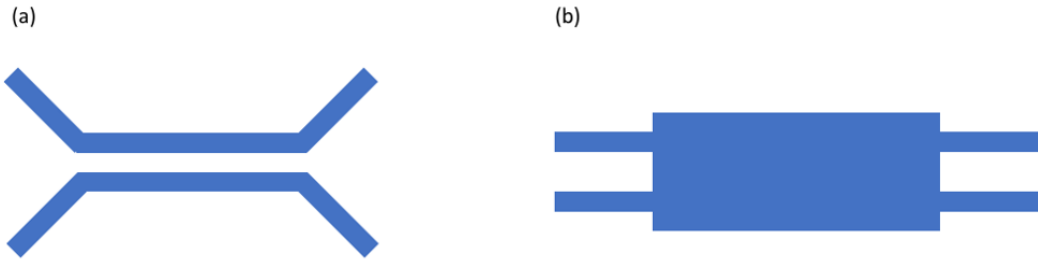

Figure 2.20: Schematic of two beam-splitter examples. a) directional coupler , b) multi-mode interference (MMI) coupler.

Mach-Zehnder interferometer

On-chip interferometers are made up by combining waveguides with two beam-splitter blocks. They are used for switching of photons between optical paths and for measurements concerning variations in the amplitude or phase of light due to photon absorption. Mach-Zehnder interferometer (MZI) can be used for two-photon quantum interference experiments in which two photons are launched in the two input ports of an MMI. With the use of tunable delay line at one of inputs, the relative arrival time is altered. Each output port of the MMI is then monitored with a single photon detector and coincidences which are due to correlated detection events are recorded. This allows for the realisation of a Hong-Ou-Mandel interferometer or two-photon interference which is used by many quantum information processing experiments such as entanglement swapping [147].

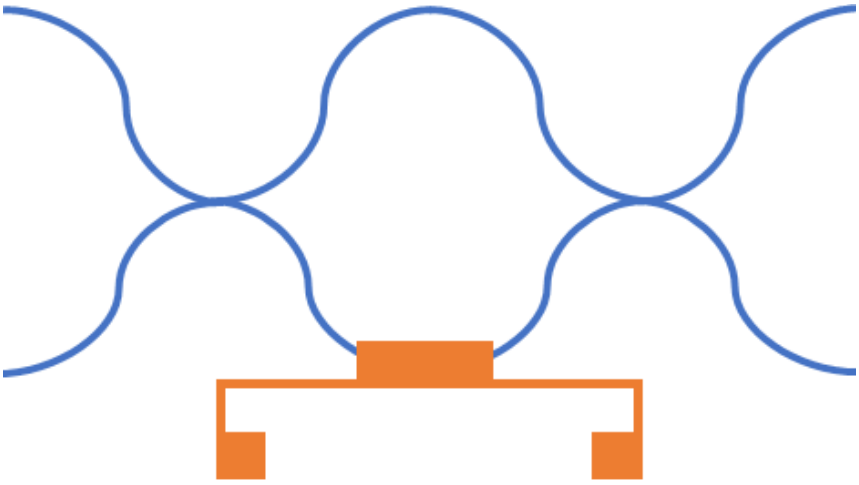

Figure 2.21: Schematic of an Mach-Zehnder interferometer implemented in silicon-on-insulator waveguides [148].

Fibre-to-chip couplers

SOI platform due to its large refractive index allows for large scale integration of nanometre sized optical waveguides with typical dimensions 500 nm x 220 nm. However, that makes

fibre coupling challenging since the cross-sectional area of a typical SMF28 fibre core is $\approx$ 9 µm that is almost 600 times larger that of an optical waveguide, therefore an intermediate block is required to adjust the mode-field diameter.

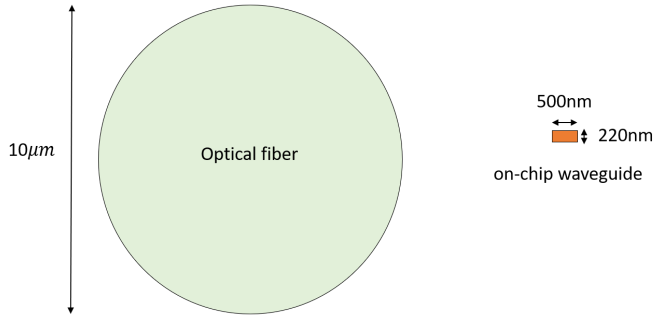

Figure 2.22: Illustration of mode mismatch between an optical fibre and a silicon waveguide.

Several approaches to tackle this mode mismatch problem were suggested. One of them is end-fire coupling, however this scheme requires high alignment accuracy and limits the positioning of waveguide launch at the edge of the chip. Whereas, the second one is based on grating couplers, which are advantageous to end-fire coupling since they can be realised with much smaller footprint that is ideal when high density of devices needs to be fabricated on the chip. A grating coupler (GC) is described as an optical block that can be used as an input/output (I/O) component that enables coupling of light between the single mode optical fibres and on-chip waveguides. Within this thesis only focusing grating couplers are used as the means for fibre to chip coupling (in-coupling). It is common to see in literature GC designs that employ a fully etched grating that takes place in the same etch step as the waveguides themselves. However, these designs typically suffer from large back reflection to the optical waveguide [149]. As a result, only shallow etched GC were used for the requirements of this work since they create fewer back reflections and their design is simpler.

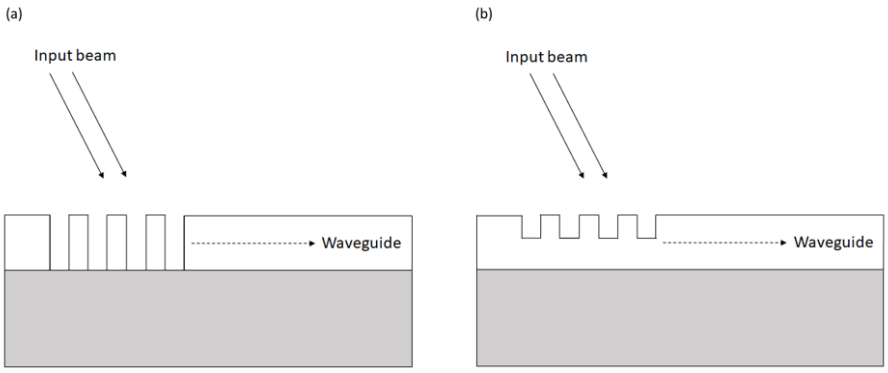

Figure 2.23: Fibre-to-chip grating couplers. (a)Schematic of a single-etch grating coupler design , (b) Schematic of a shallow-etch grating coupler design.

2.9.4 Applications of waveguide circuits with SNSPDs

Many quantum information processing experiments such as entanglement swapping [150] and measurement device independent quantum key distribution (QKD) [151] operate based on Hong-Ou-Mandel (HOM) interference.

Hong-Ou-Mandel interference

Hong-Ou-Mandel (HOM) interference is a two-photon interference measurement firstly demonstrated by Hong, Ou and Mandel [152]. In the original Hong-Ou-Mandel experiment in 1987, two identical (indistinguishable) single-photons are sent through the two separate input ports of a 50:50 beam splitter and each output port is connected to a single-photon detector. If these two photons reach the beam splitter at the exact same time interval, they will interfere and always come out as pairs from either output port 1 or 2 Figure 2.24(a)) of the beam splitter (no coincidence). However, by introducing path delays between the relative arrival time of either of these photons at the beam splitter (coincidence) can tune the distinguishability between them. In this experiment by varying the path delay, a dip in the coincidence at zero delay (t = 0) will be revealed (HOM dip) as demonstrated in Figure 2.24(b).

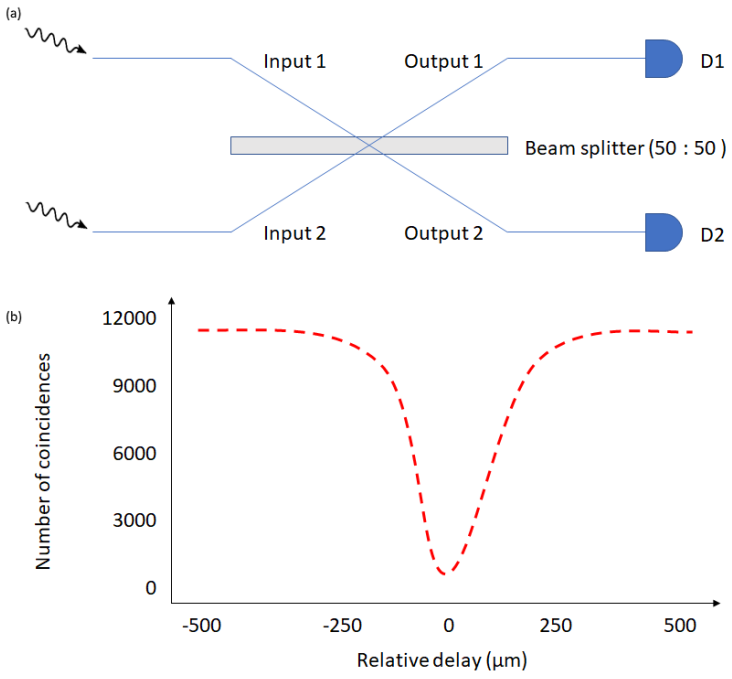

Figure 2.24: Two-photon interference (HOM dip). (a) Experimental setup for two-photon experiment. D1 and D2 denote single-photon detectors, (b) Coincidence dip demonstration, acquired at output ports of the beam-splitter (Output 1 and Output 2) by tuning their distinguishability.

Quantum key distribution

Quantum key distribution (QKD), which is the most mature form of quantum information processing, uses single-photons for the secure exchange of cryptographic keys between two spatially separated parties (Alice and Bob) based on the laws of quantum mechanics [153]. However, the equipment used in the practical QKD systems have imperfections (loopholes), which can be exploited by an eavesdropper (Eve) to gain full information about the key. An example of such a loophole is a blinding attack on the SPD [154], which opens a side channel and allows Eve to gain full information about the key without causing any additional quantum bit error rate. To remove all detector side-channel attacks Lo, Curty and Qi proposed a new scheme called as measurement device-independent QKD [155].

Measurement device independent quantum key distribution

In measurement device independent quantum key distribution (MDI-QKD), a third untrusted central node (Charlie) links Alice and Bob via a quantum channel (optical fibre). Alice and Bob each send a polarization (horizontal, vertical, diagonal or anti-diagonal) encoded photon to Charlie. Then based on HOM effect, Charlie subjects Alice and Bob into a two-photon interference via a 50:50 beam splitter and announces coincidences measured. Based on this, Alice and Bob construct a shared key [156]. However, even in the case of an Eve taking complete control of the measurement devices, Alice and Bob will notice and reset the transmission process [157]. MDI-QKD can also allow for many users to connect on the same Charlie [158]. The basic setup of an MDI-QKD system is portrayed in Figure 2.25.

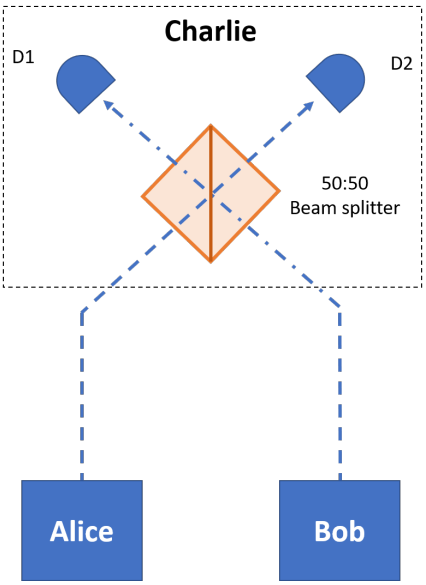

Figure 2.25: Basic setup of MDI-QKD protocol. Alice and Bob each transmit a single-photon that is routed to a 50:50 beam splitter. Then based on two-photon interference operation performed by Charlie, Alice and Bob generate a shared key. [156]

Chapter 3

Fabrication and experimental methods

The fabrication of SNSPD devices is a long process, thus it requires care at each individual fabrication step to minimise fabrication errors and in worst case contamination of the whole substrate. This chapter is divided into two parts; the first part describes the techniques used and procedures followed for optimising the fabrication process for the realisation of a superconducting nanowire single-photon detector (SNSPD) integrated in optical cavities and optical waveguide circuits. The second part describes low temperature electrical and nano-optical characterisation of these devices with emphasis on the experimental apparatus.

3.1 Fabrication methods

SNSPD device fabrication was carried out in the James Watt Nanofabrication Centre (JWNC) at the University of Glasgow. The centre houses over £32 M state-of-the-art micro and nanofabrication facilities within a 1350 m^2 clean room. This chapter begins with an introduction of the tools and processes used to fabricate single pixel SNSPD devices integrated with optical cavities, waveguides and circuits. The process begins by sputtering or deposition of a thin film of superconducting material onto a Si substrate. This was done both at the University of Glasgow and at the National Institute of Information and Communications Technology (NICT) Advanced ICT Research Institute, Kobe, Japan.

3.1.1 Superconducting thin film growth

For the thin film growth requirements of this thesis, two DC magnetron tools were used: one for MoSi thin films that were grown in the James Watt Nanofabrication Centre (JWNC) at the University of Glasgow and a second for NbTiN thin films that were grown

in the National Institute of Information and Communication Technology (NICT) in Japan. For all the thin film growth, Si substrates were used.

Sputtering of superconducting thin films

For the deposition of superconducting thin films, the most common technique is DC magnetron sputtering. Quantum Sensors Group (QSG) of Glasgow University oversaw the purchase of a new sputtering system (Plassys MP 600 S confocal UHV sputter system) that has been installed in the James Watt Nanofabrication Centre (JWNC) for the thin-film deposition stage of SNSPD's fabrication process. Thanks to its ultra-high vacuum (UHV) chamber (< 5 x 10^{-9} Torr), it is possible to achieve smooth and uniform deposition across up to 6-inch (150 mm diameter) wafer thin films. It is equipped with a load lock for speedy sample exchange. Additionally, the system has five confocal sputtering targets mounted on separate guns (MeiVac MAK guns with 3" diameter targets [159]). The following targets are in use: Nb, Mo, Ge, Si and Ti as illustrated in Figure 3.1(a). It is fitted with a liquid nitrogen trap that allows cooling down of the samples close to 77 K prior to deposition. Likewise, an internal heater that gives the capability of reaching up to 800 °C for heating samples during deposition. The distance between the target and substrate is set to 10 cm. The Plassys VI sputtering system is illustrated in Figure 3.1(b).

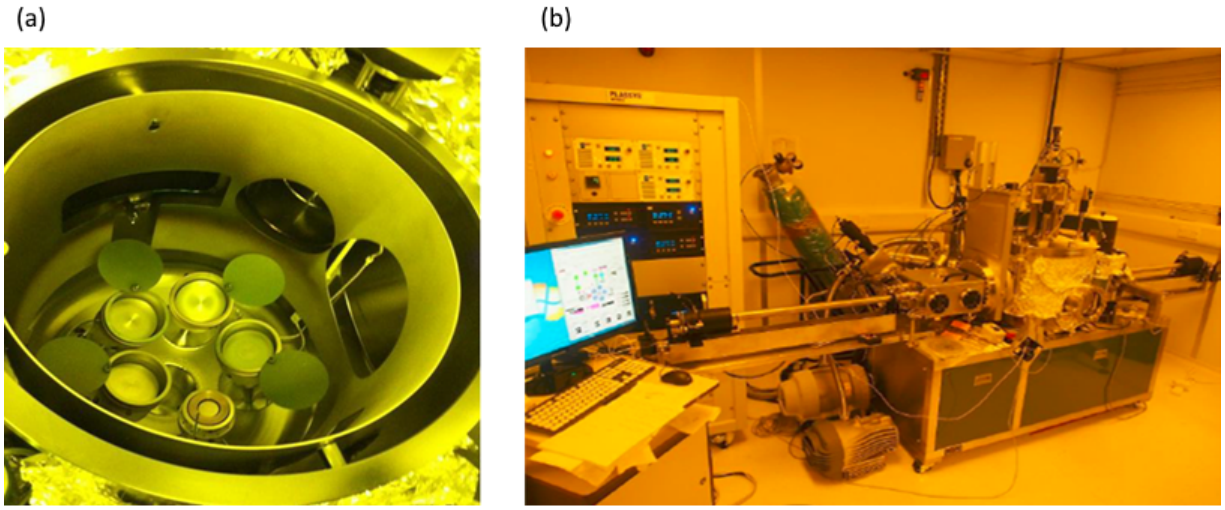

Figure 3.1: Plassys VI sputtering system. (a) view inside the main chamber of the Plassys VI sputter system showing 5 confocal sputter guns. (b) Plassys VI sputtering system in the James Watt Nanofabrication Centre at the University of Glasgow.

At National Institute of Information and Communication Technology (NICT), Kobe Japan NbTiN thin films were grown on Si substrates via a reactive DC magnetron sputtering system made by TOKKI corporation. It can achieve a vacuum pressure of (8 x 10^{-8} Torr) and is also equipped with a load lock for speedy sample exchange. Additionally, the system has three 6" diameter confocal sputtering targets mounted on separate guns. The following targets are in use: Nb, NbTi (80:20) alloy and Al. The distance between the target and substrate is set to 50 mm. Since this distance is quite small there is less chance for contaminants to reach the substrate and contaminate the thin film quality. The NICT sputtering system is illustrated in Figure 3.2.

Figure 3.2: DC magnetron sputtering system in the NICT research centre in Kobe, Japan.

DC magnetron sputtering is among the most favourable methods for high quality deposition of thin films of one target material onto a substrate. In a DC magnetron sputtering system both the target and the substrate are placed in a vacuum chamber, where an ion plasma is generated by applying a fixed, high frequency electric field (e-field) [160]. Additionally, it uses a closed magnetic field that traps the electrons and subsequently lowers the ionization pressure that yields in high quality thin-films. The formation of a low pressure nitrogen / argon gas flow in the main chamber, will bombard

the surface of the metal or alloy based target. As a result, some atomic sized particles will be ejected from the target and deposited onto the substrate [160, 161]. Film thickness (τ) is calibrated by a systematic growth of various deposition rates and times. To optimize the electrical properties of the thin films grown on a substrate, they were electrically tested over a range of discharge currents and power values. Additional information of the thin film sputtering optimisation is found in the work performed by Banerjee [162].

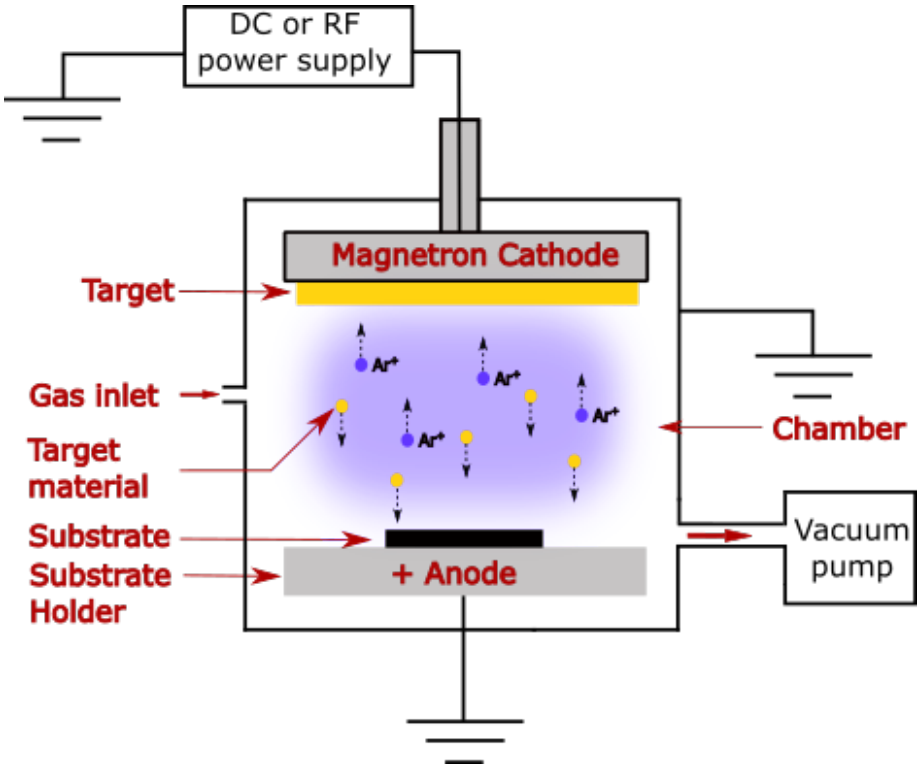

Figure 3.3: Schematic representation of the sputtering process. The vacuum chamber is pumped to base pressure and a high purity Ar (inert) gas is introduced (blue dots/cloud). Ar subsequently bombards the target and with the electric field generated by the current applied between the anode and the cathode, the vaporized target coating atoms (yellow dots) are driven towards the substrate and condense. As a result, a thin film coating is formed on the substrate.

3.1.2 T_c measurement setup

In 2014 for the requirements of my MSc in Nanoscience and Nanotechnology, a multichannel (eight channel) thin film low temperature characterisation setup based on a Gifford-McMahon closed-cycle refrigerator [163] has been developed. In this setup, one sample is characterised via the use of a four-point resistance measurement; each sample resistance is estimated as well as their respective temperature values were recorded. Then the system automatically switches to the next one and repeats the same process. This setup will underpin optimisation of better quality thin film deposition. The goal is to achieve higher

transition temperatures that will lead to future higher efficient SNSPD devices [164]. This low temperature characterisation setup is illustrated in Figure 3.4.

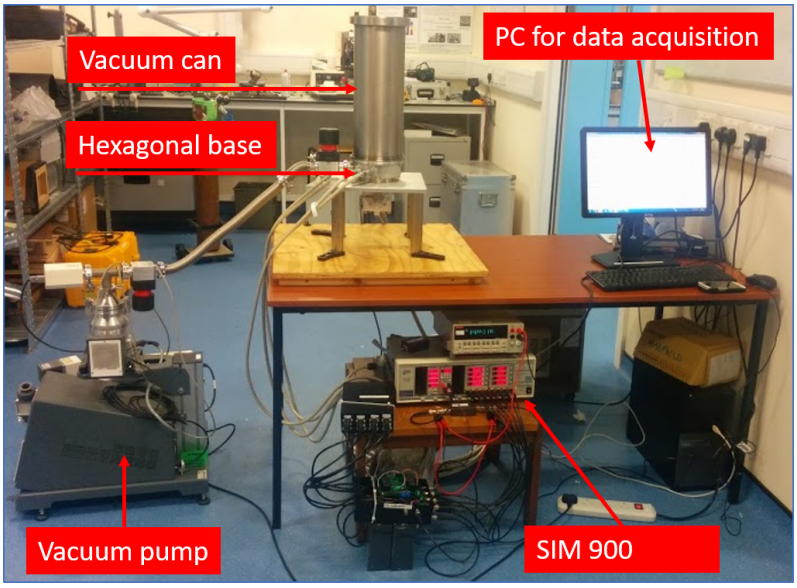

Figure 3.4: Low temperature characterisation setup after its construction.

3.1.3 Electron beam lithography (e-beam)

In any micro or nano-fabrication process, lithography is used to define a pattern onto a material (substrate). There are three competing technologies currently used for patterning a sample: (a) photolithography, (b) nanoimprinting and (c) electron-beam lithography.

Photolithography - Photolithography is the most popular technique among the three [165]. It operates based on a light source (lamp) radiating through a photomask to a photosensitive resist on the substrate. The photomask contains the pattern to be transferred [165]. The photoresist can be either cured or dissolve in the presence of light that subsequently will leave behind a pattern on the substrate. It is a cost-effective solution for high-volume production, typically wafer-scale level. Nevertheless, it is diffraction limited meaning that the minimum pattern feature size is limited by the wavelength of the lamp. In the JWNC fabrication facility, the lowest feature size achievable with an optical photolithography tool is 365 nm. Additionally, depending on the complexity of the photolithography mask, it can take a lot of time to fabricate one and it can be expensive. In order to prototype and develop a chip-level based technology, photolithography has limited flexibility. Likewise, its limited minimum pattern feature size made this technology not suitable for the fabrication requirements of this work.

Nanoimprinting - Nanoimprint lithography (NIL) unlike photolithography, in which a pattern is created through the use of light, NIL is an alternative wafer-scale capable lithography process, which relies on the direct mechanical deformation (heat/pressure) of the resist and as a result nanometre minimum pattern feature size resolution is achievable [165]. However, it requires a stamp/mold (negative mask) that contains the pattern to be transferred on the substrate, which can be costly. Moreover, since high temperature and pressure are required, the mold can shrink/deform which will alter the desired dimensions of the pattern on the substrate. Also, the substrate can be contaminated from this technique.

Electron-beam lithography(EBL) - EBL is the most favourable technique for rapid prototyping and patterning nanometre-sized features. Electron-beam (e-beam) lithography is a tedious and costly patterning process. However, it offers higher-level of resolution and it provides the required flexibility for chip-level prototype and development. In an e-beam lithography system, the user is required to design a pattern file with the aid of a computer-aided design (CAD)-based software (LayoutEditor [166] and L-Edit [167] software packages have been used in this work). Afterwards, a pattern generator software called Beamer is used to split the pattern design (fracture) into trapezoid blocks (or 'fields'). This is done because the mechanical stage of the e-beam tool has a limited movement. The minimum and maximum separation distance as well as the design of these trapezoids needs to be carefully defined as it will affect the final pattern quality. Subsequently, Beamer will automatically position those trapezoids on a predefined square lattice grid. Then the user will define the dot size, which the machine will expose. The size of those dots is called beam size (BS) and the separation distance between subsequent dots is called beam step size (BSS) that is in fact an integer multiple of the resolution. The pattern is now fractured into multiple smaller blocks ready to be exposed.

In the JWNC, electron-beam lithography (EBL) is performed using a Vistec VB6 UHR EWF unit, which is a large area high resolution EBL tool. A schematic of the tool can be seen in Figure 3.5. A filament source generates a beam of electrons at 100 keV, which are then accelerated away from the source and diverted into a column where a series of apertures and magnetic fields are located and they are used to focus the beam. As a result, non-uniform substrate height or tilt errors are corrected. There are a range of variable apertures that are used to select the beam size by adjusting their diameter. Also, by taking into consideration the BSS and the exposing dose of the resist, the writing spot is determined. Emission of secondary electrons is caused as a result of these accelerated electrons that penetrate through the resist material and into the substrate until they collide with atomic electrons or nuclei. These secondary electrons depending on the tone of resist i.e. negative or positive, can either help to form cross-linking bonds or to break

them. Depending on the type of substrate, resist and beam spot size, the (area/volume) spread of secondary electrons will change. After, the e-beam exposure the sample needs to be developed. This is done by immersing the sample in a solvent that will dissolve any non-crosslinked molecules (negative tone) or the fragments (positive tone).

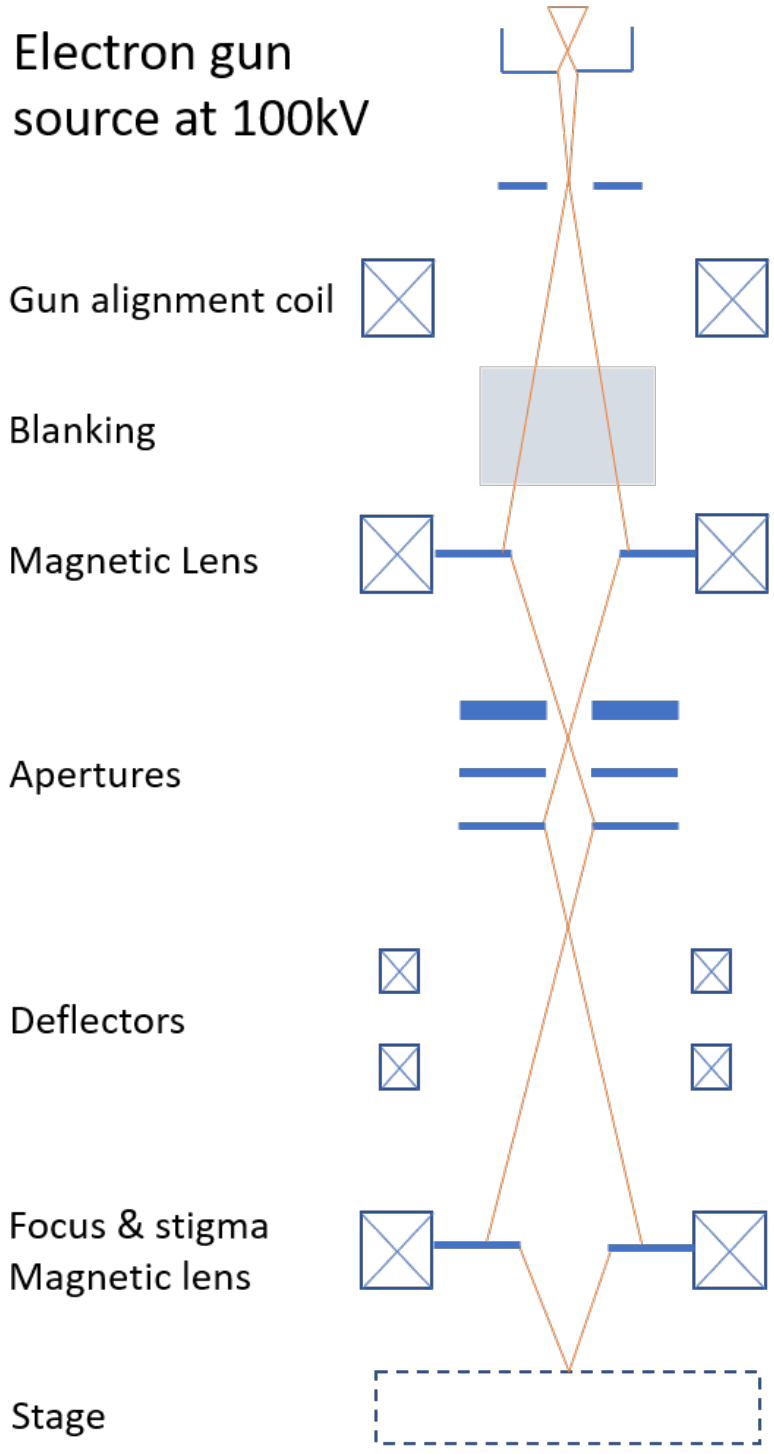

Figure 3.5: Simplified schematic of the VB6 electron beam machine

Therefore, is required to execute a dose test in order to determine the dose of electrons

to be used ($\mu C\,cm^{-2}$). Both the dose used, and the BSS selected are the main factors that define the edge roughness on optical waveguides. By choosing a wrong value of dose or BSS, light scattering is affected, and propagation losses are introduced.

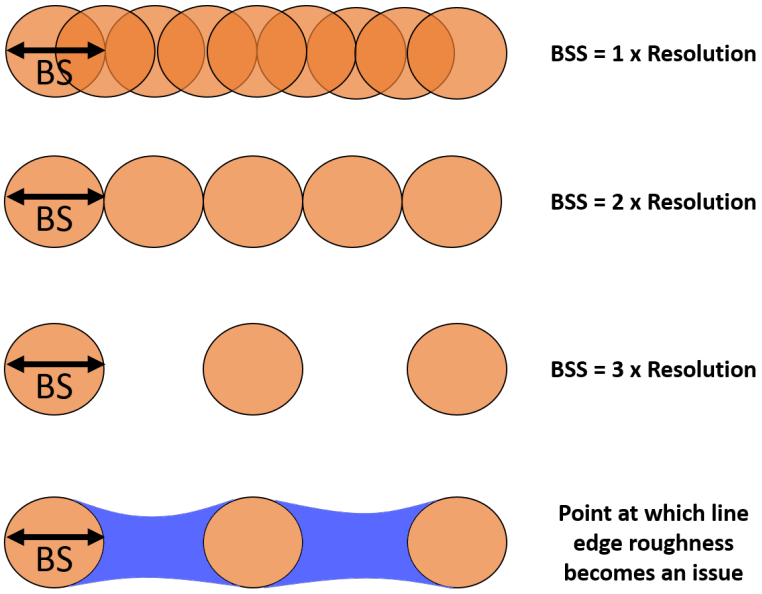

Figure 3.6: Graphical representation of how the SS and BSS choice affects the lithography patterning. Note the BSS is linearly increasing from top to bottom. The bottom of the figure illustrates a value of BSS at which the line edge roughness becomes an issue. Adapted from [168]

By choosing an extremely small BSS, it leads in longer writing times as the same area is exposed repeatedly and that can be very expensive. Whereas, by choosing a large BSS some areas might be left unexposed. As a result, bigger features that do not require high resolution were written with a much bigger BSS. Table 3.1 summarises the different e-beam parameters used for pattern definition.

Parameter	Low resolution	High resolution
Resolution (nm)	1	1
Beam size (BS) (nm)	33/65	4/6
Beam spot size (BSS) (nm)	16/32	2/3
Electron acceleration (keV)	100	100

Table 3.1: Electron beam parameters for pattern definition.

The exposure resolution in an EBL tool is limited by the electron scattering effects, often referred to as the proximity effect as illustrated in Figure 3.7. This effect is critical in designs with condensed patterns over a small area since these scattering electrons will cause exposure of regions adjacent to those addressed by the e-beam that results in undesired exposure of the resist. Consequently, this can lead into deviations from the original designed feature size of the pattern written. This issue can be resolved by running

proximity correction software based on Monte Carlo simulations that eliminates the extra exposure created from the finite size of the electron beam by adjusting the exposure dose relative to the resist thickness, type of substrate and the pattern density.

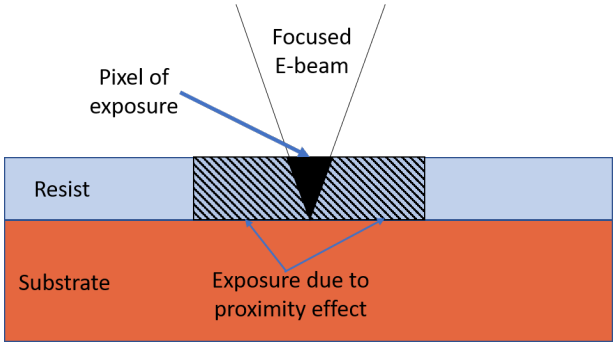

Figure 3.7: Schematic representation of the proximity effect. The area surrounding the exposure pixel also gets exposed.

The area that can be written without the need to translate the sample stage mechanically is called the field size, which is another important parameter to be considered during the lithographic process. At the boundaries between subsequent fields, discontinuities might appear on the patterns. At the resolution used in this work (1nm) it translates to a field size of 1048.576 x 1048.576 μm^2. Moreover, the EBL presents a mechanical drifting because of long exposure times. For half an hour exposure a 50 nm drift was measured whereas over 2 hours exposure a 150 nm drift was measured in both x and y coordinates. Consequently, nanowires present in subsequent fields might display stitching errors as present in Figure 3.8. In order to extenuate the stitching perpendicular to the meandered nanowire, alignment correction is performed every 15 minutes. Additionally, the stitching along the nanowire direction is minimized by incrementing the exposure dose at the boundaries between adjacent fields.

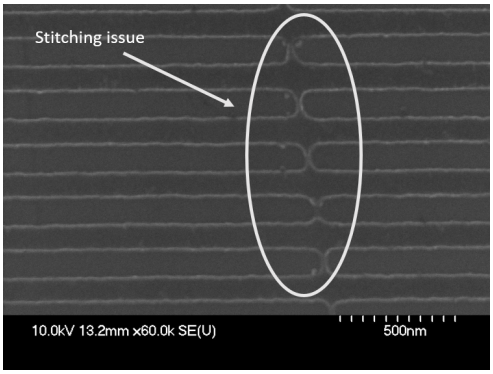

Figure 3.8: Scanning electron microscope image of stitching error on a meandered nanowire on the axis parallel to the nanowires. Visible after e-beam resist development.

3.1.4 Resists

Before submitting a sample for EBL a layer of resist needs to be placed on top of the substrate. The type of resist used in EBL is a solution of a polymer and solvent. By placing the sample on a spinner and with the use of a disposable pipette, the resist is coated on the sample. The final thickness of the resist is highly dependent on the spinning speed, dilution and the spinning duration (time). After spinning the resist an edge beading effect is present on the substrate. This is mainly due to the fact that resist builds up at the corners of the sample as a result of surface tension, thus an uneven profile is observed at the corners of the sample. For achieving consistency of our pattern writing is very important to make sure the resist has uniform thickness throughout the area to be exposed. After spinning, with the use of an oven or a metal hotplate, the resist is baked to evaporate the resist solvent (soft bake).

Resists are separated into two main categories: positive tone and negative tone. When writing a pattern with a positive tone resist, the resist is exposed with the EBL and the exposed areas are cleared out. Whereas in the case of negative tone resist only the patterned areas remain and everything else is removed during development process. Those two types of resists are portrayed in Figure 3.9.

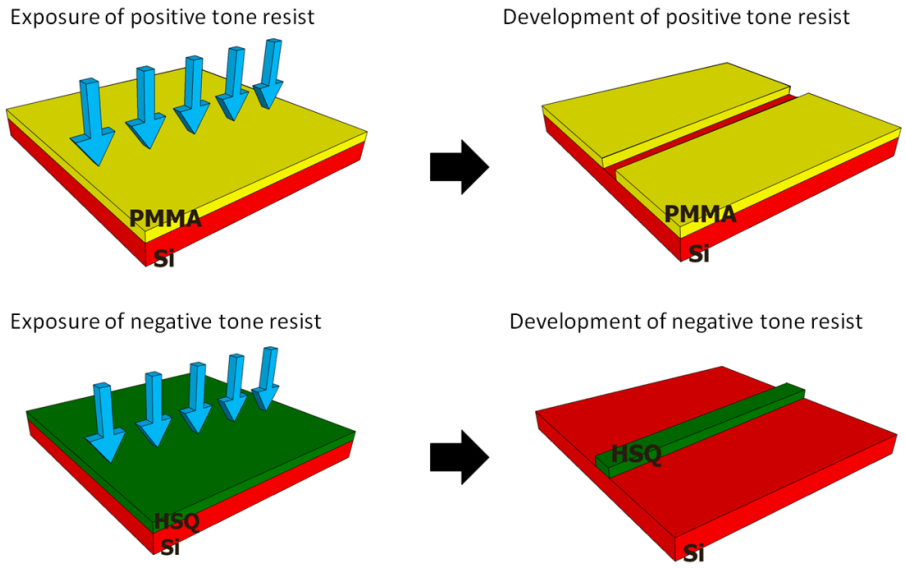

Figure 3.9: Illustration of the exposure and development of a positive tone resist (top) and a negative tone resist (bottom).

Some widely used positive tone resists are poly methyl methacrylate (PMMA) and ZEP [169, 170]. While, a commonly used negative resist is hydrogen silsequioxane (HSQ) [171]. E-beam resists are categorized based on their contrast and sensitivity as defined below:

- **Contrast**: defined as the ability of a resist material to differentiate between unex-

posed and exposed areas.

- **Sensitivity**: defined as the amount of electron energy (keV) required to irradiate a negative tone resist in order to maintain its original thickness after development or, a positive resist to clear out. Higher energy requires higher exposure dose; therefore, lower sensitivity. Resists that are capable of high sensitivities, require lower dose to fully expose the resist. Additionally, the higher the sensitivity of a resist the lower electron energy required for exposure.

Depending on the requirements of each fabrication step, the most suitable resist has been used. In total, for the requirements of this work three different resists (two positive and one negative) have been used, notably their main features will be introduced, in the rest of this section.

PMMA

Poly methyl methacrylate (PMMA) is the most popular positive e-beam resist that can offer low contrast, medium sensitivity and poor etch resistance [172]. Therefore, for the requirements of this work, PMMA was used for the low-resolution features, which had minimum feature size of 640 nm and between adjacent features had a spacing of 1 µm. Consequently, PMMA was used for the deposition of the metallic layers for the contact pads that offered the electrical connection of the SNSPD devices and the alignment markers for the subsequent e-beam fabrication runs.

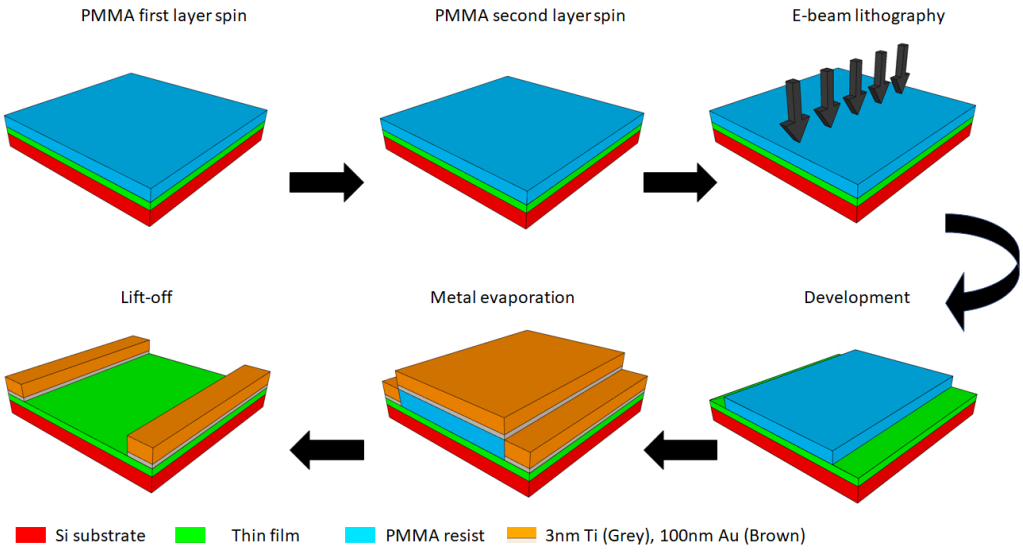

Figure 3.10: Alignment markers and contact pad fabrication steps. Starting from a substrate with a superconducting thin film, through an EBL step, followed by metal evaporation and lift-off, alignment markers and contact pads are defined on the chip.

ZEP520-A

ZEP is another positive e-beam resist that can offer high contrast, high sensitivity and good etch resistance [173]. ZEP is ideal for applications where the pattern can be left without a cladding or for shallow etching fabrication as it can be easily stripped away from the substrate with an organic solvent (Microposit remover 1165). For the requirements of this work, ZEP was used for the high-resolution features, which had minimum feature size of 90 nm and between adjacent features had a spacing of less than 100 nm. Consequently, ZEP was mainly used for the definition of the nanowire structures, coplanar waveguide transmission lines and as an etching mask for etching through the uncovered thin film to form the nanowires.

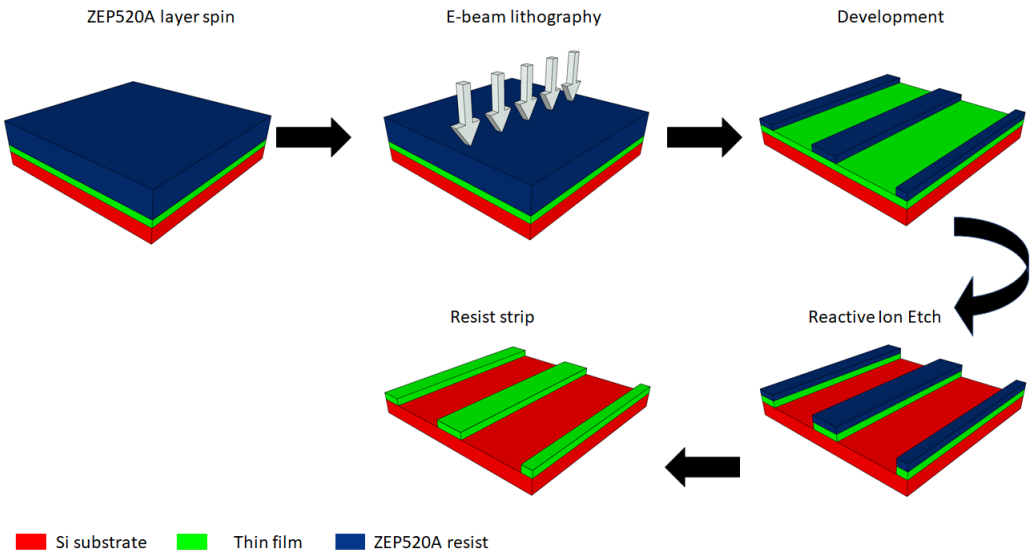

Figure 3.11: Illustration of the main fabrication steps required for the definition of nanowires with ZEP resist.

HSQ

Hydrogen silsesquioxane (HSQ), is the most common negative tone e-beam resist, which offers high contrast, low sensitivity and good etch resistance. It is the resist typically chosen for high resolution silicon photonic patterns that require low writing times. In this work, HSQ was used for the definition of the silicon waveguides and photonic circuits on the waveguide integrated SNSPD devices that where fabricated atop a silicon-on-insulator (SOI) substrate.

The fabrication procedure for Si waveguides, which is presented in Figure 3.12, is the following :

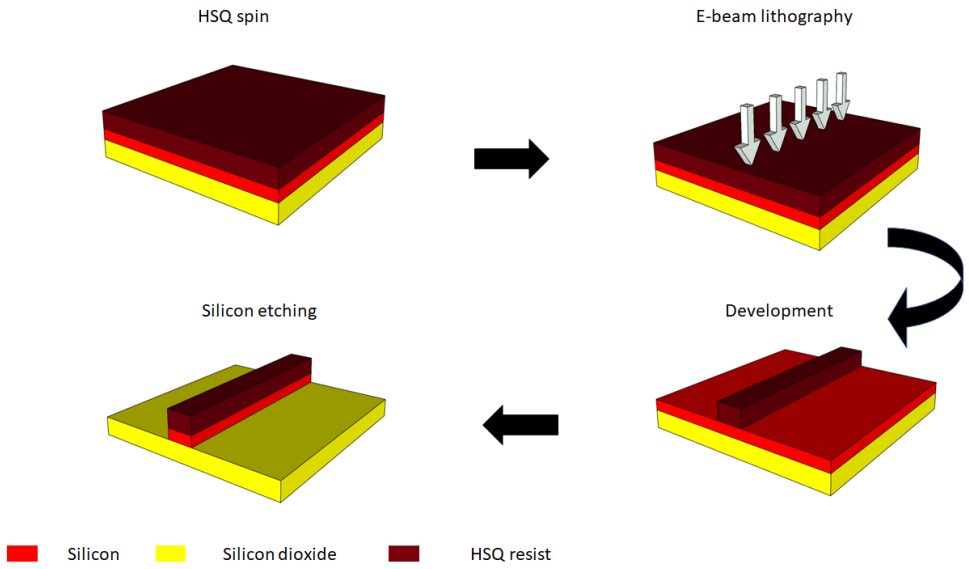

Figure 3.12: Illustration of the main fabrication steps required for the definition of Si waveguides with HSQ resist. Only the first two layers of the SOI (Si and SiO_2) are shown. The last Si layer is omitted.

3.1.5 Metal contacts

The first and most vital step in the fabrication of high quality SNSPD devices, is the metallic layer deposition for layer-to-layer alignment in subsequent e-beam runs. When the e-beam exposes the metallic square/cross marker more electrons are backscattered compared with the substrate; therefore, is accurately located. The ability to locate markers is crucial for maintaining layer-to-layer overlay accuracy in subsequent fabrication steps and for machine calibration. For the metallic layer evaporation and their subsequent lift-off, PMMA resist was used. The fabrication procedure for the metallic layers, which is presented in Figure 3.10, is the following :

1. PMMA 2010 series single layer with 15% concentration is spun on the sample and then baked at 150 °C on a hotplate for 5 minutes.

2. PMMA 2041 series single layer with 4% concentration is spun on the sample and then baked at 150 °C on a hotplate for 5 minutes.

3. The sample is loaded on the e-beam tool and exposed with the parameters shown in Table 3.1 and with a dose of 750 $\mu C\,cm^{-2}$.

4. The resist is developed with an MIBK:IPA dilution of 1:1 for 30 seconds at 23 °C, then followed by 1 minute rinse in IPA. It is recommended to optically inspect the

sample prior to metallisation. This step will verify how the pattern was written and the development outcome.

5. 3 nm titanium (Ti) and 100 nm gold (Au) are deposited by an e-beam metal evaporator. Subsequently, lift-off takes place in a beaker with acetone at 50 °C for at least two hours.

During optimization of the lift-off process, some errors were identified and mitigated as presented in Figure 3.13(a) thicker metallic layers were deposited in contrast to resist thickness, metal is found over unintended areas that may not be removed during lift-off process, (b) proper undercut profile after development and lift-off takes place only on intended areas, (c) Resist is not developed properly, as a result adhesion is reduced and important features may be lost during lift-off.

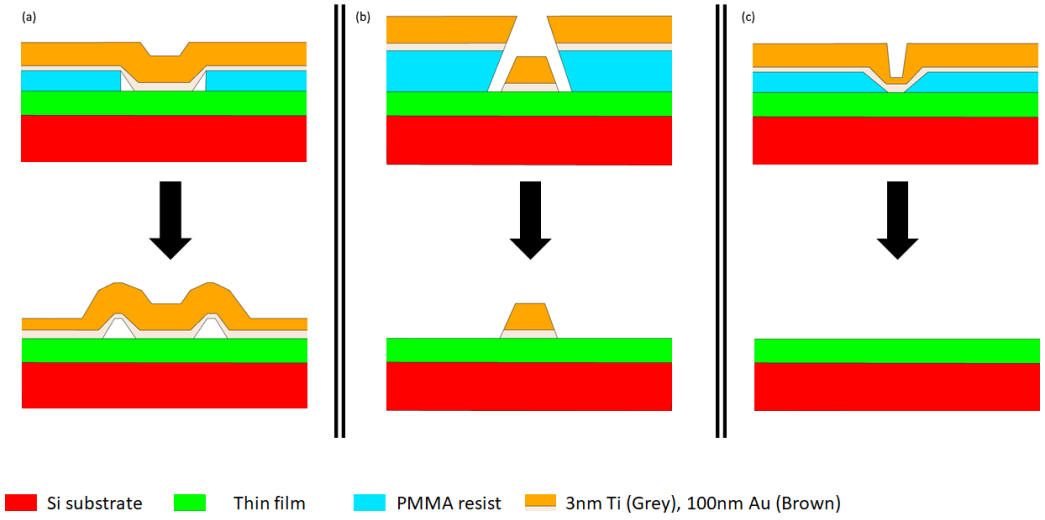

Figure 3.13: Unsuccessful lift-off errors and successful process. (a) evaporated film is thicker than resist, may stay over unintended areas after lift-off, (b) proper development and lift-off process and (c) resist is not developed properly, metallic film may come off from intended features.

Layer to layer alignment

Prior to EBL exposure, the machine is switched to SEM mode that allows to scan the surface of the sample and locate regions of the surface containing alignment marks. With the use of four alignment markers positioned at the corners of a square, the alignment will compensate for scale, rotation, offset and keystone misalignment errors as illustrated in Figure 3.14(a). Additionally, through analysis of backscattered electron signal the marker edges are identified as portrayed in Figure 3.14(b). If the measured position deviates from the design, the EBL tool will automatically adjust the positions at which the beam will strike during pattering.

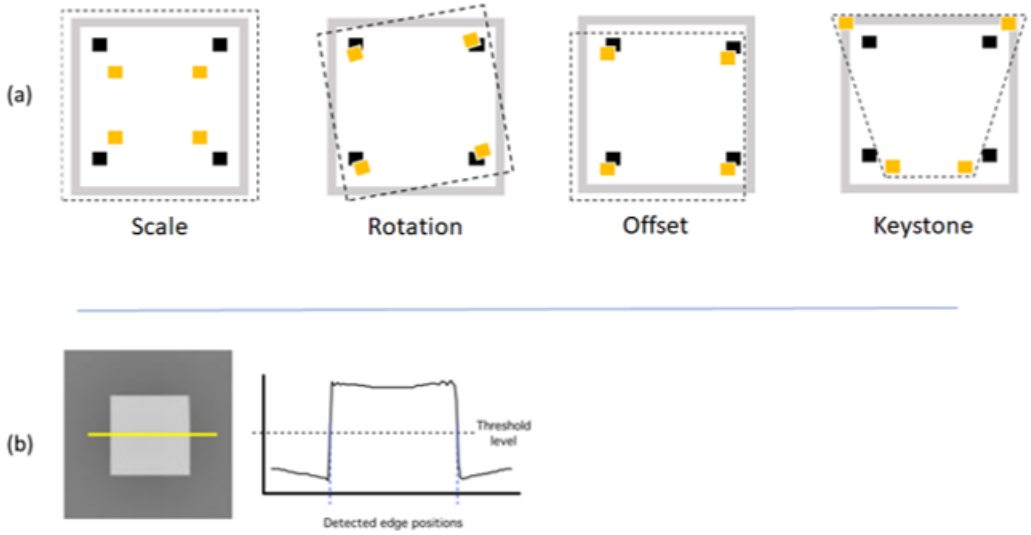

Figure 3.14: Registration and alignment of e-beam pattern. (a) alignment markers are used to adjust the orientation of the e-beam pattern. Four alignment errors must be accounted namely scale, rotation, offset and keystone errors. The markers must be positioned in the corners of a square area in order to remove keystone error. (b) Metallic marker precise position is detected by a line scan across its edges.

3.1.6 Etching techniques

The last but most fundamental step for the fabrication of SNSPD devices, is the transfer of the nanowire pattern onto the superconducting thin film. This is done through selectively removing the unmasked material via etching. There are two methods of etching that involve wet and dry etching. In the wet etching method, liquid chemicals are used as etchants to remove unwanted materials from a substrate. Whereas, in the case of dry etching, reactive ions are used. For the etching requirements of this thesis, dry etch was used as it can provide uniformity, accurate control over etching depth and anisotropy (i.e vertical side walls on Si waveguides).

The main steps involved in a dry etching process are:

1. The reactive species are produced in a plasma due to RF discharge.
2. The reactive species are transferred onto the materials surface via diffusion.
3. Reactive species are absorbed onto the materials surface.
4. Volatile by-products that have been generated due to the chemical reaction between material and reactive species are pumped out of the main chamber. A very important step since these volatile by-products can be deposited on the materials surface and it will result in a reduction of the etching rate.

In the JWNC at Glasgow University, both Inductive Coupled Plasma (ICP) and Reactive Ion Etching (RIE) tools are available. These tools are the most popular types of dry etchers.

Reactive ion etching (RIE) - RIE is a tool that can achieve high etching resolution due to the fact that it takes advantage of both chemical and physical interaction between accelerated ions and the sample. A typical RIE system consists of a vacuum chamber with two parallel electric plates and a wafer plate that is located in the bottom of the chamber. Gas enters the chamber through tiny inlets that are located on the top of the chamber and it exits with the use of a vacuum pump system through the bottom of the chamber. The plasma generation and ion acceleration is controlled by the RF electric field (frequency of 13.56 MHz is often used) power applied on both the parallel electrodes. That will lead to physical and chemical attack of the unmasked material due to ion acceleration. That power also regulates the plasma generation. Depending on how dense the plasma is, the etching rate will vary. However, an increase of the RF power results in an increase of the etching rate, a decrease of the etching selectivity and it increases the damage to the sample. RIE can produce an anisotropic profile and good selectivity between the mask and the material to be etched if the recipe is tuned properly. A typical RIE system is illustrated in Figure 3.15. For all nanowire etching presented in this thesis, an Oxford Plasmalab 80 plus RIE tool is used with a ZEP520A resist as the etching mask.

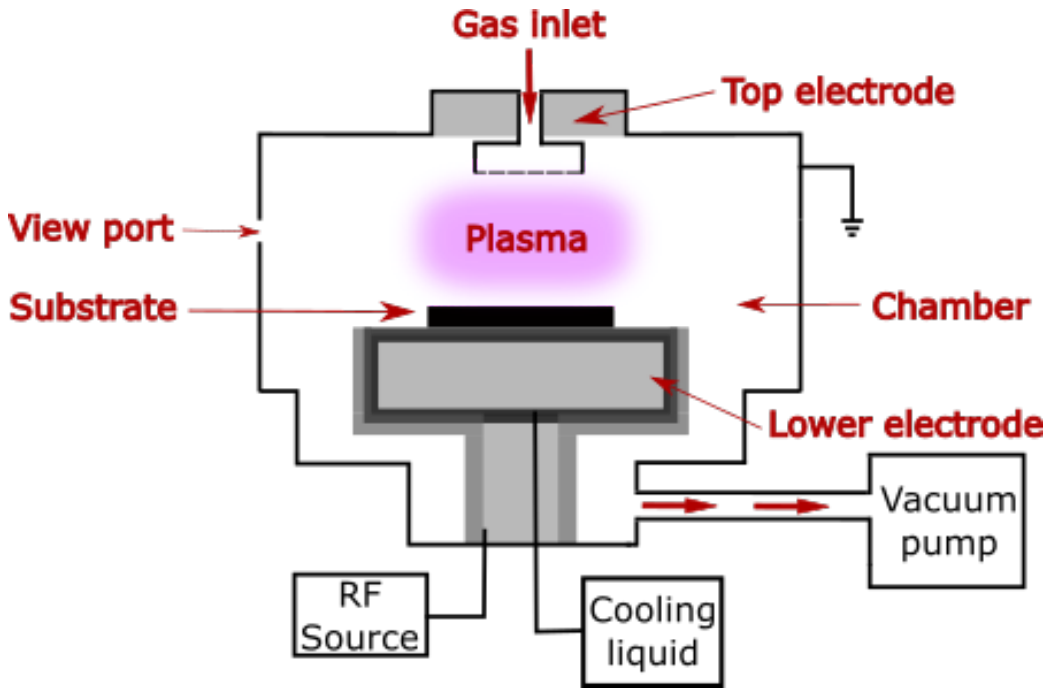

Figure 3.15: Schematic of the main chamber of the RIE tool. For all the nanowire etching, CF_4 gas was used.

The RIE recipe for nanowire etching is summarised in Table 3.2. This recipe was adjusted to accommodate different materials and film thickness.

Nanowire etching parameters for RIE 80+	
Gas	CF_4
Gas flow (sccm)	50
Pressure (mTorr)	50
RF power (W)	80
Temperature (°C)	21

Table 3.2: Nanowire etching parameters on the RIE 80 plus.

3.1.7 Superconducting nanowire meanders

After the metallic alignment markers and contact pads, the meandering nanowires are defined through Reactive ion etching (RIE) using ZEP520-A resist as an etching mask. This procedure, which is schematically presented in Figure 3.11, is the following :

1. A solution of ZEP520-A and Anisole with a ratio of 2:1, is spun on the sample at 4000 rpm for 60 seconds and then baked at 180 °C on a hotplate for 4 minutes.

2. The sample is loaded on the e-beam tool and exposed with BS 4nm , BSS 2 nm and a clearing dose of 250 µC cm^{-2}.

3. The sample is developed with O-xylene for 60 seconds at 23 °C, then followed by 30 seconds rinse in IPA.

4. The meander features are now defined on the resist and ready to be transferred to the superconducting film. This is done with a Reactive ion etching (RIE) tool and the use of tetrafluorometene (CF_4) gas, which is used to etch through the unprotected NbTiN layer to form the superconducting nanowires. The ZEP520-A resist serves as the etching mask. To ensure full clearance of the film even from the narrowest features of the pattern, the full etch time was monitored by an interferometer.

5. ZEP resist is stripped of the sample, by O_2 ashing the sample at 150 W for 2 minutes using an oxygen plasma Fab 505 asher. In order to ensure there is no residue of ZEP left, the sample is chemically stripped with nMP solvent (Microposit remover 1165) overnight at 80 °C. It is necessary to ensure there is no resist residue left as that might deteriorate the electrical connection between the contact pads and the SNSPD device. It was observed that only a chemical strip with an nMP solvent was not sufficient and a lot of resist residue was left on the sample. However, O_2 ashing of ZEP resist must be applied sparingly to avoid the degradation of SNSPD superconducting properties. Complete removal of the resist from the nanowire results in its oxidation, which in turn could reduce its T_c and I_c.

Inductive coupled plasma reactive ion etching (ICP-RIE) - In contrast to conventional RIE, the ion energy and ion density are controlled by two independent RF power generators, thus material surface damage is avoided. Additionally, plasma generation and etching take place into two separated chambers. The plasma generation is achieved by RF biasing a copper coil that is wrapped around the chamber. Ions are accelerated towards the material surface by a secondary RF power supply that is located at the back of the mounted sample. Therefore, by independently varying the RF power of the two power supplies, accurate control over the etching rate, good selectivity and high anisotropy are achieved. All the silicon etching runs presented in this thesis were performed on the ICP tool from Surface Technology Systems (recently renamed to SPTS technologies).

Etching time depends on both the thickness and the material that needs to be etched away. If the etching time is not properly calculated, it can result in either over-etching or under-etching issues. However, the latter is rarer, since the etching process can be inspected by an interferometer.

Additionally, for the waveguide integrated SNSPD devices an extra etching step is required, in order to transfer the pattern into Si core.

3.1.8 Silicon etching

In silicon photonics, among the most effective chemistries for Si etching with low propagation losses anisotropically are SF_6/C_4F_8 [174] and SF_6/O_2 [175]. However, if C_4F_8 or O_2 gas are not used, the etching becomes completely isotropic. The differences between an isotropic and an anisotropic etching profile are present in Figure 3.16.

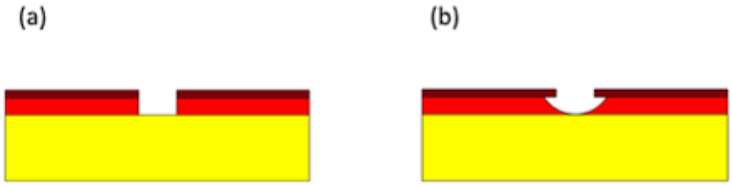

Figure 3.16: Difference between isotropic and anisotropic dry etching. (a) Anisotropic, (b) Isotropic.

In the first etching gas combination (SF_6/C_4F_8), the etching gas is SF_6 and the introduction of C_4F_8 acts as the passivation gas. It produces a sidewall protecting layer on the sidewalls of the waveguide due to the combined action of fluoride and carbon radicals. Moreover, the sidewall damage is minimised, since no physical etching is applied on the sidewalls and the chemical etching is reduced. In the second etching gas combination (SF_6/O_2), the introduction of O_2 improves the verticality of the etching profile, as it reduces the plasma density and consequently it forms a passivation layer from the combination of fluorite, oxygen and silicon radicals. However, the etching mask might

deteriorate faster, and the etching rate is significantly slower.

For the Si etching presented in this thesis, all the experimental samples were etched using an STS-ICP tool, with SF_6/C_4F_8 as the preferred etching chemistry, which is also known as the modified Bosch process [165]. It can offer high (3:1) selectivity between Si and the HSQ etching mask, low etching rates in the range of 150 nm/min and also vertical profile. The etching recipe was developed by previous users in the JWNC and the etching parameters can be found in Table 3.3.

Si etching parameters for STS ICP	
Gas	SF_6 / C_4F_8
Gas flow rate (sccm)	30 / 90
Plate power (W)	12
Coil power (W)	600
Pressure (mTorr)	9.8
Etching rate (nm /min)	150

Table 3.3: Si etching parameters on the STS-ICP tool.

3.1.9 Fabrication process for cavity integrated SNSPD devices

Two different designs of cavity SNSPD devices were fabricated including, front-side and back-side cavity single pixel SNSPD devices.

Front-side - SNSPD devices where integrated with tantalum pentoxide/silica dielectric Bragg reflector optical cavities that where grown atop a silicon substrate. For the fabrication of front-side cavity SNSPD devices, two subsequent EBL runs were performed; one for the metallic layer definition and another one for the nanowires and completion of the coplanar waveguide transmission lines. The fabrication procedure followed for the complete fabrication of a front-side cavity SNSPD device is as follows. Firstly, the substrate was cleaned with acetone and IPA. Each of the cleaning steps, took place in an ultrasonic bath for 5 minutes. Afterwards, the sample was dried out with a nitrogen (N_2) gun. The sample is then dehydration baked at 180 °C on a hotplate for 5 minutes. Then the substrate is RF cleaned and thin films of superconducting NbTiN (7.5 nm) are grown on top of the substrates, Figure 3.17(1). After this, the T_c was measured with a resistive measurement (wirebonding the film on a sample mount).

For the alignment markers and contact pads, PMMA 2010 series single layer with 15% concentration was spun at 5000 rpm for 60 seconds onto the sample, followed by being baked at 150 °C on a hotplate for 5 minutes, Figure 3.17(2). After this, PMMA 2041 series single layer with 4% concentration was spun at 5000 rpm for 60 seconds onto the sample, followed by being baked at 150 °C on a hotplate for 5 minutes, Figure 3.17(3). The alignment markers and contact pads design were then written by EBL onto the PMMA with a dose of 750 µC cm^{-2}, Figure 3.17(4). This was followed by developing the PMMA with an MIBK:IPA dilution of 1:1 for 30 seconds at 23 °C, and then by 1 minute rinse in

IPA, Figure 3.17(5). Titanium (to promote adhesion) and gold were then deposited by an e-beam evaporator, Figure 3.17(6). Excess metal and resist are removed in a beaker with acetone at 50 °C for at least two hours to complete lift-off, Figure 3.17(7).

To pattern the film, a solution of ZEP520-A and anisole with a ratio of 2:1, was spun on the sample at 4000 rpm for 60 seconds, followed by being heated at 180 °C on a hotplate for 4 minutes, Figure 3.17(8). The nanowires and coplanar waveguide transmission lines were then written by EBL onto the ZEP as in Figure 3.17(9) with a dose of 220 µC cm^{-2}. This was followed by developing the ZEP with Oxylene for 60 seconds at 23 °C, and then by 30 seconds rinse in IPA, Figure 3.17(10). Thereafter, an RIE tool with the use of CF_4 gas, was used to etch through the unprotected superconducting thin layer to form the superconducting nanowires, Figure 3.17(11). Next, the ZEP resist was stripped from the sample, an oxygen plasma Fab 505 asher was used to O_2 ash the sample at 150 W for 2 minutes. In order to reassure there was no residue of ZEP left, the sample was chemically stripped with nMP solvent (Microposit remover 1165) overnight at 80 °C, Figure 3.17(12).

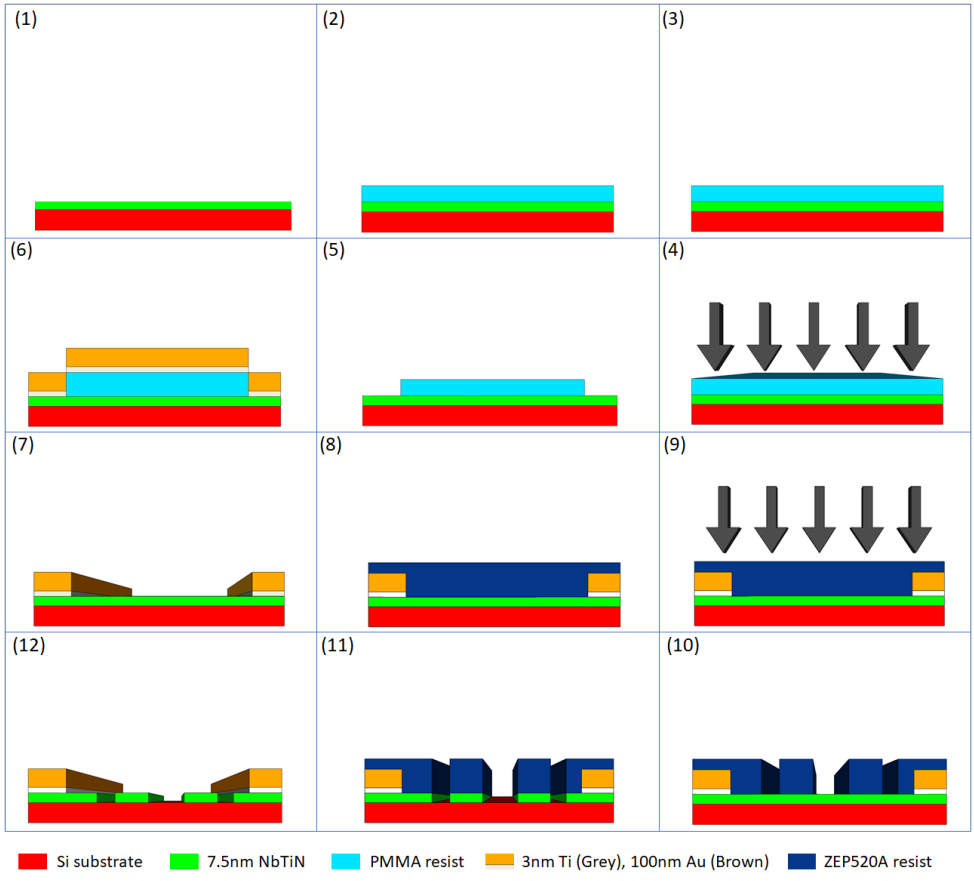

Figure 3.17: Process used to fabricate a front-side cavity SNSPD device. (Thickness not to scale) Si substrate cleaned and NbTiN thin film is sputtered (1). Spin bilayer of **PMMA** resist, EBL, develop, metallise (thin Ti adhesion layer, Au) and lift off in acetone, completing the **gold contact pads** and **alignment markers** (2-7). Spin **ZEP** resist, EBL, develop, etch (CF_4 RIE), then strip ZEP, to pattern the **nanowire and coplanar waveguides** (8-12).

In Figure 3.18 , optical and scanning electron microscope (SEM) pictures from one of the fully fabricated sample are illustrated.

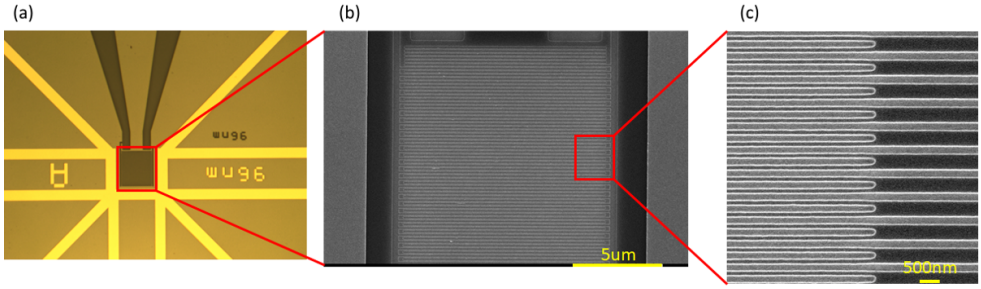

Figure 3.18: Fully fabricated SNSPD integrated on a front-side cavity. (a) Optical microscopy image of a single detector with the metallic contact pads, (b) Scanning electron image of a NbTiN SNSPD with an active area of 15x15µm^2, (c) Magnified image of an area of the nanowire showing a well-defined linewidth.

Back-side - the SNSPD devices where fabricated on top of thermally oxidized silicon substrates then a cavity was formed on top of the nanowire with the use of silicon monoxide (SiO) and a silver (Ag) mirror. For all the back-side cavity SNSPD devices both the thin film deposition and the fabrication took place in National Institute of Information and Communications Technology (NICT) in Japan. The fabrication process for back-side cavity SNSPD devices, it requires three runs with an i-line stepper, one for the metallic layer deposition, a second one for the coplanar waveguide transmission lines and a third for the optical cavity patterning. Additionally, one EBL run is required for the nanowire patterning. The fabrication procedure followed for the complete fabrication of a front-side cavity SNSPD device is as follows. Firstly, the substrate was cleaned with acetone and IPA. Each of the cleaning steps, took place in an ultrasonic bath for 5 minutes. Afterwards, the sample was dried out with a nitrogen (N_2) gun. The sample is then dehydration baked at 180 °C on a hotplate for 5 minutes. Then the substrate is RF cleaned and thin films of superconducting NbTiN (7.5 nm) are grown on top of the substrates, Figure 3.19(1). After this, the T_c was measured with a resistive measurement (wirebonding the film on a sample mount).

For the alignment markers and contact pads, primer HMDS was spun on the substrate at 4000 rpm for 5 seconds. Followed by a photoresist MIR703 spun at 4000 rpm for 60 seconds and then baked at 105 °C on a hotplate for 1 minute, Figure 3.19(2). The alignment markers and contact pads design were then written by photolithography onto the MIR703, Figure 3.19(3). This was followed by developing the AZ-300MIF for 1 minute at room temperature (RT), and then by 1 minute rinse in water and dried with a nitrogen (N_2) gun. Prior to metallic layer evaporation, the substrate was RF cleaned with Argon (Ar) gas at 5 sccm flow rate for 5 minutes. Then 4 nm Titanium (Ti) and 100 nm Gold

(Au) were deposited by a metal evaporator as in Figure 3.19(4-5). Excess metal and resist were removed in a beaker with acetone at 50 °C for 1 hour. Then rinsed with ethanol and dried with a nitrogen (N_2) gun to complete lift-off, Figure 3.17(67).

To pattern the film, a solution of ZEP520-A and anisole with a ratio of 2:1 (120 nm), was spun on the sample at 5000 rpm for 60 seconds, followed by being heated at 180 °C on a hotplate for 3 minutes, Figure 3.19(7). The nanowires were then written by EBL onto the ZEP as in Figure 3.17(8) with a dose of 384 µC cm^{-2} and a SS of 50 pA. This was followed by developing the ZEP with Oxylene for 60 seconds at 22 °C, and then by 60 seconds rinse in IPA and dried with a nitrogen (N_2) gun. Thereafter, an RIE tool with the use of CF_4 gas, was used to etch through the unprotected NbTiN layer to form the superconducting nanowires, Figure 3.19(9-10). Next, the ZEP resist was stripped from the sample, by immersing the sample in nMP solvent for 3 hours at 50 °C then ultrasound was applied for 1 minute. This was followed by an additional ultrasonic dose in ethanol for 30 seconds and dried with (N_2) gun, Figure 3.19(11).

For the coplanar waveguide (CPW) transmission lines, primer HMDS is spun on the substrate at 4000 rpm for 5 seconds. Followed by a photoresist MIR703 spun at 4000 rpm for 60 seconds and then baked at 105 °C on a hotplate for 1 minute. The CPW transmission lines were then written by photolithography onto the MIR703 as seen in Figure 3.19(14). The sample was developed with AZ-300MIF for 1 minute at RT, followed by 1 minute rinse in water and dried with a nitrogen (N_2) gun. Next 100 nm niobium nitride (NbN) was sputtered on the sample that would serve as the electrical contact between the sample and room temperature electronics, Figure 3.19(15-16). Excess metal and resist were removed in a beaker with acetone at 50 °C overnight. Then rinsed with Ethanol and dried with a nitrogen (N_2) gun to complete lift-off, Figure 3.19(17).

Lastly, for the optical cavity pattern, primer HMDS was spun on the substrate at 4000 rpm for 5 seconds. Followed by a photoresist MIR703 spun at 4000 rpm for 60 seconds and then baked at 105 °C on a hotplate for 1 minute, Figure 3.19(18). The optical cavity pattern was then written by photolithography onto the MIR703 as seen in Figure 3.19(19). The sample was developed with AZ-300MIF for 1 minute at RT, followed by 1 minute rinse in water and dried with a nitrogen (N_2) gun. Then SiO evaporation took place (thickness of SiO was designed as $\lambda/4$ of the experiment wavelength), Figure 3.19(20-21). Prior to metallic layer evaporation, the substrate was RF cleaned with Argon (Ar) gas with 5 sccm gas flow for 5 minutes. Then 3 nm titanium (Ti) and 150 nm silver (Ag) were deposited by a metal evaporator,Figure 3.19(22). Excess metal and resist were removed in a beaker with acetone at 50 °C for 1 hour. Then rinsed with ethanol and dried with a nitrogen (N_2) gun to complete lift-off, Figure 3.19(23). Finally, primer HMDS was spun on the substrate at 4000 rpm for 5 seconds. Followed by a photoresist MIR703 spun at 4000 rpm for 60 seconds and then baked at 105 °C on a hotplate for 1 minute. Then a dicing saw was used

to dice the samples into 3x3 mm^2 dies.

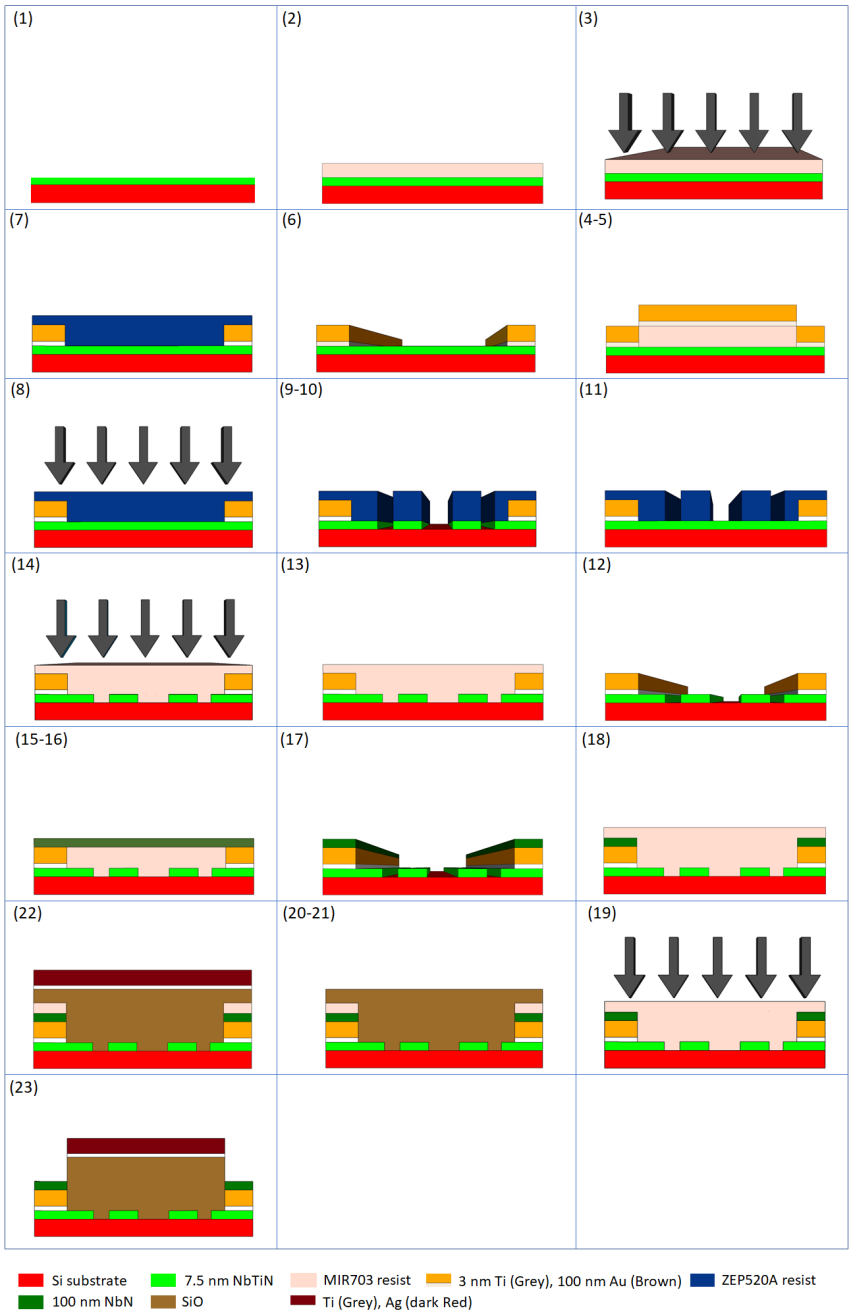

Figure 3.19: Process used to fabricate a back-side cavity SNSPD device. (Thickness not to scale) Si substrate cleaned and NbTiN thin film is sputtered (1). Spin HMDS/MIR703, photolithography, develop, metallise (thin Ti adhesion layer, Au) and lift off in acetone, completing the **alignment markers** (2-6). Spin **ZEP** resist, EBL, develop, etch (CF_4 RIE), then strip ZEP, to pattern the **nanowires** (7-12). Spin HMDS/MIR703, photolithography, develop, sputter NbN and lift off in acetone, completing the **coplanar waveguide transmission lines** (13-17). Spin HMDS/MIR703, photolithography, develop, sputter SiO, metallise (thin Ti adhesion layer, Au) and lift off in acetone, completing the **optical cavity** (18-23).

3.1.10 Fabrication process for waveguide integrated devices

Waveguide integrated SNSPDs fabrication process is similar with the cavity integrated SNSPDs with the addition of three extra EBL steps for the definition of the grating coupler, Au pad protection and waveguide circuits. The process followed for the complete fabrication of a waveguide integrated SNSPD device is as follows. Firstly, the substrate was cleaned with acetone and IPA. Each of the cleaning steps, took place in an ultrasonic bath for 5 minutes. Afterwards, the sample was dried out with a nitrogen (N_2) gun. The sample is then dehydration baked at 180 °C on a hotplate for 5 minutes. Then the substrate is RF cleaned and thin films are grown on top of the substrates, Figure 3.20(1). After this, the T_c was measured with a resistive measurement (wirebonding the film on a sample mount).

For the alignment markers and contact pads, PMMA 2010 series single layer with 15% concentration was spun at 5000 rpm for 60 seconds onto the sample, followed by being baked at 150 °C on a hotplate for 5 minutes, Figure 3.20(2). After this, PMMA 2041 series single layer with 4% concentration was spun at 5000 rpm for 60 seconds onto the sample, followed by being baked at 150 °C on a hotplate for 5 minutes, Figure 3.20(3). The alignment markers and contact pads design was then written by EBL onto the PMMA with a dose of 750 µC cm^{-2}, Figure 3.20(4). This was followed by developing the PMMA with an MIBK:IPA dilution of 1:1 for 30 seconds at 23 °C, and then by 1 minute rinse in IPA. Titanium (to promote adhesion) and gold were then deposited by an e-beam evaporator, Figure 3.20(5-6). Excess metal and resist are removed in a beaker with acetone at 50 °C for at least two hours to complete lift-off, Figure 3.20(7).

To pattern the film, a solution of ZEP520-A and anisole with a ratio of 2:1, was spun on the sample at 4000 rpm for 60 seconds, followed by being heated at 180 °C on a hotplate for 4 minutes, Figure 3.20(8). The hairpin-shaped nanowire, series inductors and coplanar waveguide transmission lines were then written by EBL onto the ZEP as in Figure 3.20(9) with a dose of 220 µC cm^{-2}. This was followed by developing the ZEP with Oxylene for 60 seconds at 23 °C, and then by 30 seconds rinse in IPA. Thereafter, an RIE tool with the use of CF_4 gas, was used to etch through the unprotected superconducting thin layer to form the superconducting nanowires, Figure 3.20(10-11). Next, the ZEP resist was stripped from the sample, an oxygen plasma Fab 505 asher was used to O_2 ash the sample at 150 W for 2 minutes. In order to reassure there was no residue of ZEP left, the sample was chemically stripped with nMP solvent (Microposit remover 1165) overnight at 80 °C, Figure 3.20(12).

A solution of ZEP520-A and anisole with a ratio of 2:1, was spun on the sample at 4000 rpm for 60 seconds, followed by being heated at 180 °C on a hotplate for 4 minutes, Figure 3.20(13). The shallow (70 nm) grating coupler part was then written by EBL onto the ZEP as in Figure 3.20(14) with a dose of 220 µC cm^{-2}. This was followed by

developing the ZEP with Oxylene for 60 seconds at 23 °C, and then by 30 seconds rinse in IPA. Thereafter, an ICP-RIE tool with the use of C_4F_8/SF_6 gases, is used to transfer the written pattern into Si, Figure 3.20(15-16) . Next, the ZEP resist was stripped from the sample, an oxygen plasma Fab 505 asher was used to O_2 ash the sample at 150 W for 2 minutes. In order to reassure there was no residue of ZEP left, the sample was chemically stripped with nMP solvent (Microposit remover 1165) overnight at 80 °C, Figure 3.20(17).

To mask Au contact pads, PMMA 2010 series single layer with 15% concentration was spun on the sample at 5000 rpm for 60 seconds and then baked at 150 °C on a hotplate for 5 minutes, Figure 3.20(18). Subsequently, the pattern was written by EBL onto the PMMA as in Figure 3.20(19) with a dose of 750 µC cm^{-2}. This was followed by developing the PMMA with an MIBK:IPA dilution of 1:1 for 30 seconds at 23 °C, and then by 1 minute rinse in IPA, Figure 3.20(20). A fresh solution of hydrogen silsesquioxane (HSQ) and methyl isobutyl ketone (MIBK) with a ratio of 1:1, thereafter was spun on the sample at 2000 rpm for 60 seconds and then baked at 95 °C on a hotplate for 15 minutes, Figure 3.20(21). HSQ is extremely sensitive resist, thus before each exposure a dose test was run in order to find the correct exposure dose. The deep (220nm) grating coupler and waveguide structures were then written by EBL onto the ZEP as in Figure 3.20(22) with a dose of 1400 µC cm^{-2}. To improve the edge roughness of the mask [176] and the etching selectivity of HSQ to Si [177], the sample was post-baked after exposure at 180 °C for at least one hour. This was followed by developing the HSQ with TMAH at 21 °C for 30 seconds, and then by 1 minute rinse in RO water and 30 seconds in IPA. Thereafter, an ICP-RIE tool with the use of C_4F_8/SF_6 gases was used to transfer the written pattern into Si. Finally, the PMMA resist used for the protection of the Au contact pads was stripped from the sample with SVC-14 solvent at 80 °C for 2 hours and then rinsed for 30 seconds in IPA.

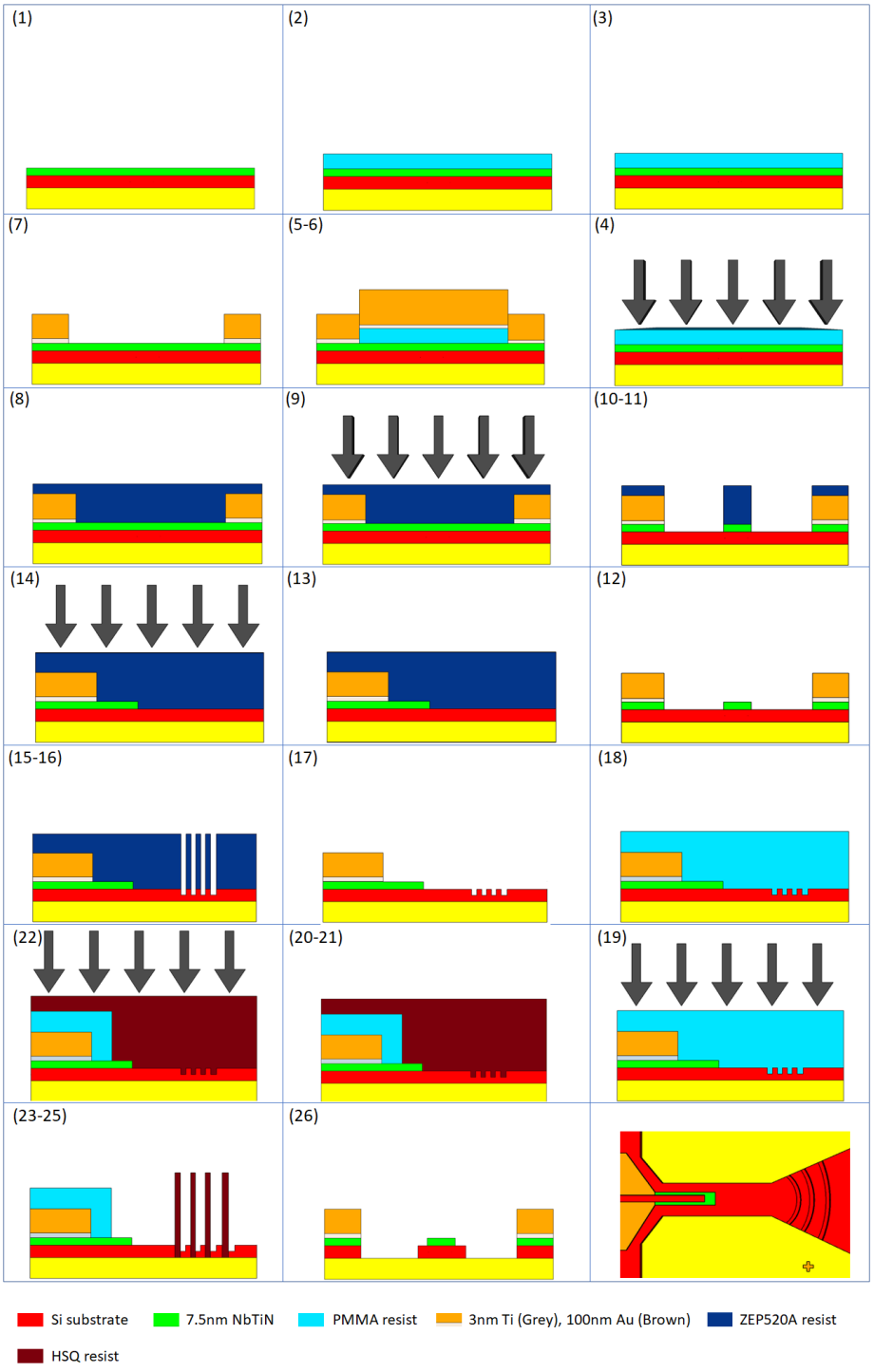

Figure 3.20: Process used to fabricate a waveguide integrated SNSPD. (Thickness not to scale) SOI substrate cleaned and thin film is sputtered (1). Spin bilayer of **PMMA** resist, EBL, develop, metallise (thin Ti adhesion layer, Au) and lift off in acetone, completing the **gold contact pads** and **alignment markers** (2-7). Spin **ZEP** resist, EBL, develop, etch (CF_4 RIE), then strip ZEP, to pattern the **nanowire and coplanar waveguide**(8-12). View is now cross-section along waveguide (13). Spin **ZEP** again, EBL, develop, etch (C_4F_8 + SF_6 ICP-RIE) and strip ZEP to pattern **shallow (70 nm) grating coupler components**(13-17). Spin **PMMA**, EBL, develop to **mask Au contact pads** (18-20). Spin **HSQ**, EBL, develop, and deep etch (C_4F_8 + SF_6 ICP-RIE) to pattern **deep (220nm) grating coupler and waveguide structures**(21-25). View in (26) is across the hairpin-shaped nanowires.

3.2 Experimental methods

This section presents the methods used to characterise the SNSPD devices and explains how the measurements present in later Chapters were performed.

3.2.1 Device screening and preparation

Subsequent to device fabrication, completed devices are screened through a two-point room temperature (R_{300K}) resistance measurement with a probe station. Section 4.2 includes a table with R_{300K} values for NbTiN thin films grown on a DBR substrate. Based on the measured square resistance ($R_{\square}$) of the superconducting film and the nanowire geometry, the device resistance is estimated. By comparing the estimated value with the measured resistance of the SNSPD device, the devices are either rejected or accepted for use in an experiment. Excessively low R_{300K} indicates a short in the circuit, whereas overly high R_{300K} implies a heavily constricted nanowire. Therefore, devices that are found with either too high R_{300K} or too low R_{300K} are rejected.

Accepted samples are cleaved into 3x3 mm^2 dies and mounted on a gold-plated (1 µm) oxygen-free high thermal conductivity (OFHC) copper sample mount. A photograph of the sample mount used is presented in Figure 3.21. The SNSPD chip is then wire bonded on the sample mount with a Kulicke & Soffa 4123 wedge wire bonder with the use of aluminium (Al) wire, which provides the electrical connection between the SNSPD chip and the sample mount. Subsequently, the devices are mounted on a cryostat and cooled down for low temperature electrical characterisation.

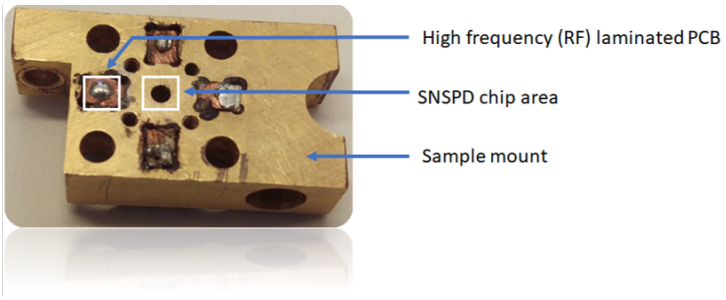

Figure 3.21: Photograph of the sample mount for the SNSPD chip.

3.2.2 Closed-cycle refrigeration

SNSPDs are highly sensitive devices, hence their performance is highly affected by temperature oscillations. The absence of a stable temperature will cause instability of dark count rate at a fixed bias current and detection efficiency. There are various techniques that can be utilized for cooling down an SNSPD device, among the most common are immersion

of the sample in liquid helium or the use of a closed-cycle cryocooler. By immersing a sample in a liquid helium (He), it is possible to cool it down and reach a temperature of 4.2 K. However, the use of liquid He is expensive and potentially hazardous [178]. This issue is eliminated by the use of cryogen-free and closed-cycle cryocoolers capable of reaching lower temperatures allowing new material candidates for SNSPDs to be studied. The Quantum Sensors Group (QSG) at University of Glasgow is in possession of various cryocooler systems, designed to operate at different base temperatures and for various applications. For the experiments performed in this thesis, two types of cryocoolers have been used for low temperature electrical and optical characterisation of SNSPD devices both integrated with optical cavities and waveguide optical circuits. These two types of refrigerators are built around a pulse tube (PT) and a Gifford-McMahon (GM) cryocooler. The operating principle through compression and expansion of a fluid to achieve cooling is like that of a domestic refrigerator. In this case, high purity ^{4}He gas is used to achieve very low temperatures.

PT coolers contain no moving parts within the coldhead, hence lower mechanical vibration is achieved during operation in contrast to GM coolers. Additionally, they have a remote rotary motor, which can be mounted away from the cryostat in order to avoid transferring vibrations to the sample. Nevertheless, few microns of movement are created due to the expansion of the He gas inside the coldhead. In QSG this type of cryostat was given the name "Kelvinator" and it is composed of a two-stage cryostat with a Cryomech PT403-RM coldhead with a remote motor connected to a water-cooled CP839 compressor that can reach a base temperature of 3.5 K. In addition, another PT cryostat is available in the lab, similar to Kelvinator with an additional ^{3}He stage that reaches a base temperature of 350 mK. Since this cryostat was installed in the Rankine building at the University of Glasgow, it was named "Rankinator".

GM coolers suffer from vibrational noise since their rotary valve motor is attached at the base of the cold-head. They are also susceptible to fail faster than PT coolers as they contain moving parts within the coldhead. However, they are more compact and easier to troubleshoot in case of a fault as opposed to PT coolers. In QSG there are several types of GM coolers, but the one used for the experiments in this thesis is based on a Sumitomo RDK101D cold head and an air-cooled HC-4A Zephyr, consequently it was named "Zephynator".

Black-body radiation

In above-mentioned cryostats light is delivered to SNSPD devices with optical fibres entering the cryostat via a hermetically-sealed feed-through. As a result, black-body radiation (BBR) is coupled from room temperature (300 K) to the cryostat and can potentially increase the dark count rate of the SNSPD (discussed in Section 2.7.3) if not effectively

filtered out [179]. Based on Planck's law the peak black-body radiation at $T = 300$ K is $\lambda = 9.66\,\mu$m and it increases to $\lambda = 8280\,\mu$m at $T = 350$ mK. BBR diminishes with lower temperature and from 3.5 K to 0.35 K, BBR is reduced by four orders of magnitude (Figure 3.22).

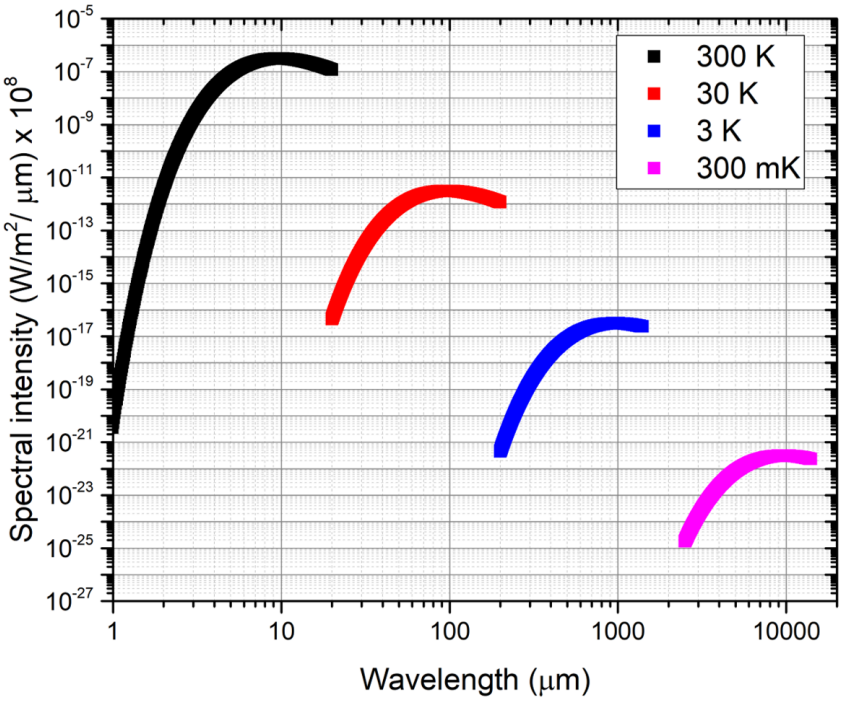

Figure 3.22: Black-body radiation (BBR) curves at 300 K, 30 K, 3 K and 350 mK. As the temperature drops the BBR is decreased and its peak shifts to larger wavelengths.

All three cryostats are described in detail in the following sections with emphasis in the electronics and optical components installed within the cryostat, as well as the measurements carried out by the author to benchmark the performance of the fabricated devices.

3.2.3 Low temperature electrical and optical characterization

For the requirements of fast screening of the SNSPD devices, a Sumitomo RDK101D Gifford-McMahon (GM) coldhead with an HC-4A Zephyr air-cooled compressor cryostat was used. It consists of two cooling stages (Figure 3.23), the first stage operates at ≈ 40 K while the second stage operates at ≈ 4 K. On the second stage, a stand-off-stage (sample stage) is installed that is spaced with the 4 K stage through a lead (Pb) block that reduces temperature oscillations. The stand-off stage is thermally linked with the 4 K stage with brass screws and it can reach a base temperature of ≈ 2.2 K. Lakeshore DT-670 calibrated Si-diode thermometers are mounted on the sample, 4 K and 40 K stages to accurately monitor their respective temperatures. From room temperature the cryostat can reach a base temperature of ≈ 2.2 K in 9 hours. Custom designed gold-plated aluminium radiation

shields, flanges for optical/electrical feed-throughs and blank plates have been machined at the University of Glasgow. Then are attached on the body of the cryostat with the use of commercially available O-ring seals and the whole fridge is thermally shielded from the environment with the use of a vacuum can. Readout and biasing of SNSPDs is done with 50 Ω impedance matched hermetic SMA connectors fitted on the flange plate and soldered on the one side of a brass coaxial cable. Whereas, on the other side an SMP connector is crimped and connected on the sample mount. Additionally, the thermometer cables are soldered to 12-pin Fischer connectors. The optical link between the detectors and room temperature equipment (i.e. laser) occurs through a hermetically sealed fibre feed-through with 16 optical fibres that are spliced on the fibre-coupled SNSPD devices (Figure 3.24). Before turning on the compressor unit, the cryostat is pumped down to a pressure of $< 10^{-5}$ mbar.

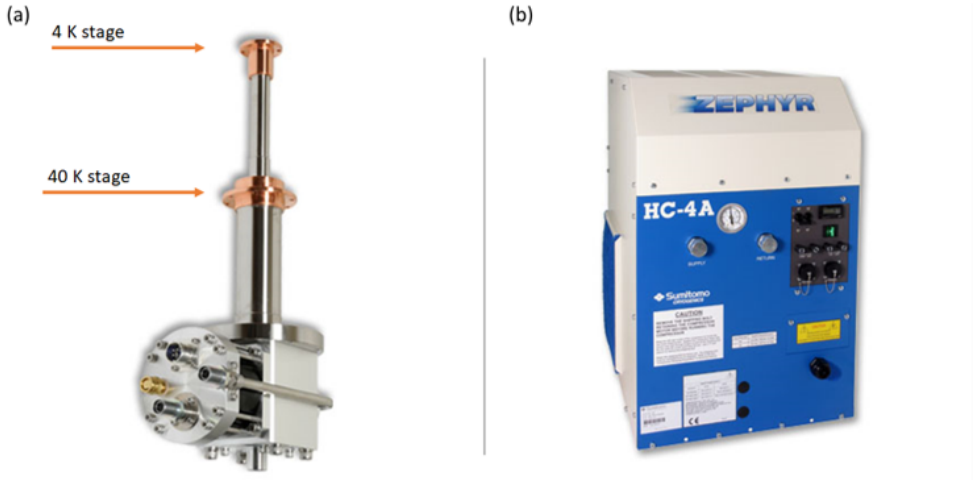

Figure 3.23: Photograph of the (a) Sumitomo RDK-101D Gifford-McMahon (GM) two stage coldhead, (b) HC-4A Zephyr air-cooled compressor. Reproduced from reference[180].

The cold head cyclic operation it can be divided into four main steps including [178]:

i. Displacer is positioned at the bottom of the coldhead and a high pressure inlet valve opens. Then the displacer is moved to the top of the coldhead. Consequently, gas flows from the regenerator to the bottom of the coldhead. The heat from the gas is absorbed by the regenerator, hence its temperature is reduced. As a result, the cold head temperature is reduced.

ii. High pressure inlet valve closes and a low pressure outlet valve opens while the displacer position is fixed at the top. Part of the gas flows to the low pressure side of the compressor via the regenerator, hence the gas in the coldhead expands. This expansion results in a further reduction of the gas temperature.

iii. With the use of a motor, the displacer is forcefully moved to the bottom of the coldhead, which causes the gas to flow through the heat exchange region and heat is removed from the target region.

iv. Gas is heated back to room temperature as it flows through regenerator to the exhaust valve. After this step, pressure oscillation is restarted by the warm end of the compressor.

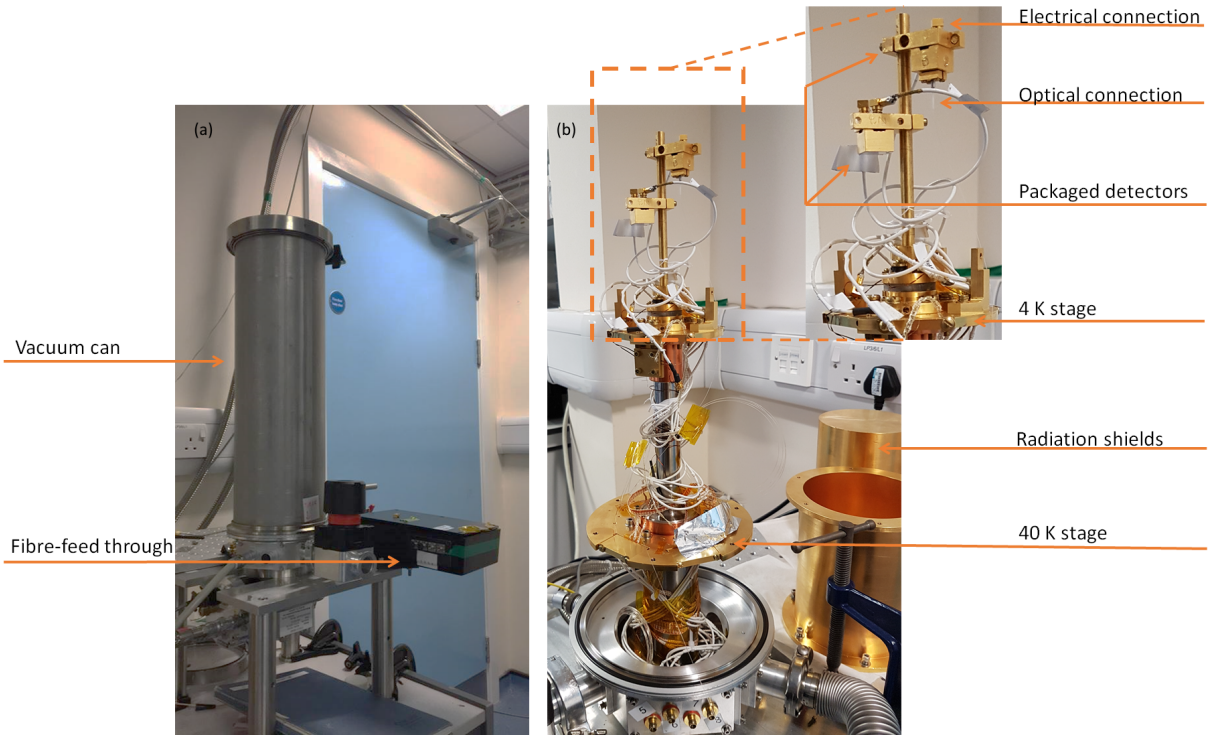

Figure 3.24: Photograph of the GM based cryostat used for basic SNSPD characterisation with a base temperature of 2.2 K . (a) The cooler is housed within a vacuum can, (b) The fibre-coupled SNSPD devices are mounted on the 4 K stage of the coldhead and are electrically connected with the use of SMP connectors.

3.2.4 T_c characteristics

The very first parameter that needs to be verified is the T_c of an SNSPD that will give us the maximum temperature, where the film superconducts. For best operation, the detector needs to be kept cold well below its T_c [181]. This property can be measured either during cooling down or warming up of the cryostat. After the initial screening of the SNSPD devices through the measurement of R_{300K}, they are wirebonded on a sample mount and bolted on the custom stand-off stage in the cryostat. In order to extract the T_c of the SNSPD, a resistance measurement is performed across the device and the change in temperature is recorded from the Lakeshore DT-670 calibrated Si-diode thermometer. For

this measurement, an isolated DC voltage source (SRS SIM928) in series with a 100 Ω load resistor, were used to provide the bias current source as shown in Figure 3.25, with the 50 Ω shunt resistor disconnected from the circuit. The isolated voltage source and the temperature monitoring modules were installed within a Small Instrumentation Module (SIM-900) from Stanford Research Systems (SRS). The SRS SIM-928 was chosen as the isolated DC voltage source, which delivers ± 20 V with millivolt resolution and is capable of a load upto ± 10 µA. A 4-channel digital voltmeter (SIM-970) is used to record both bias voltage (V_1) and voltage drop (V_2) across the device. The three thermometers situated at the stand-off, 4 K and 40 K stages were chosen with a 4-wire configuration (better accuracy), soldered with constantan wires and terminated with a vacuum-sealed hermetic connector on a vacuum flange. Their resistance values are recorded by a diode temperature monitor module (SIM-922) also housed in the SIM-900 rack. It comes with a calibration curve that is used to compare the actual measured resistance value with the preconfigured calibration curve. That allows for continuous temperature control from 300 K down to 1.4 K.

T_c measurement during cool-down:

1. SNSPD devices under test are biased and the bias voltage, voltage drop across the SNSPDs and the three stage temperatures are simultaneously recorded.
2. Cryostat is turned on and reaches its base temperature of ≈ 2.2 K. At base temperature the data acquisition stops, and the compressor is switched off.
3. Cryostat slowly warms up. At ≈ 15 K the compressor is turned back on and the process is repeated for other SNSPD devices.

T_c measurement during warm-up:

1. Cryostat is turned on and reaches its base temperature of ≈ 2.2 K.
2. SNSPD devices under test are biased and the bias voltage, voltage drop across the SNSPDs and the three stage temperatures are simultaneously recorded.
3. Compressor is turned off and the cryostat slowly warms up. At ≈ 15 K the data acquisition stops, and the compressor is turned back on.
4. Process is repeated for other SNSPD devices.

The T_c is defined as the resistance-temperature point in which the resistance sharply transitions to the zero-resistance region.

If the SNSPD superconducts and its T_c is reasonable then its I_c can be determined by examining the I-V characteristics of the nanowires.

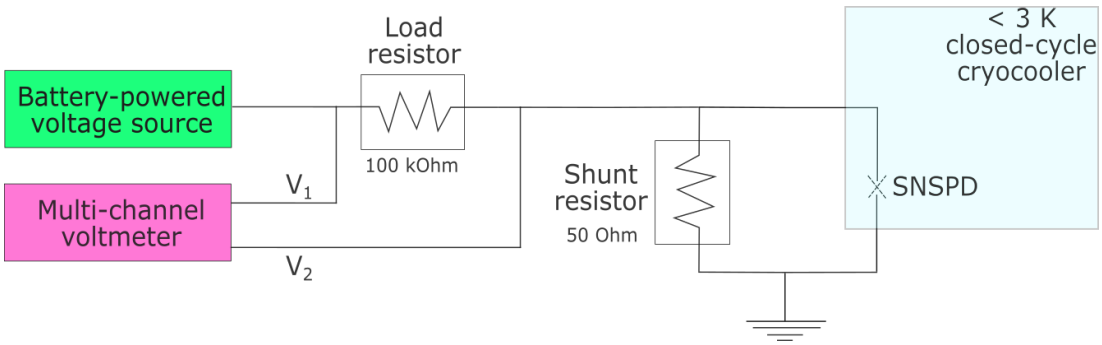

Figure 3.25: Schematic of DC measurements setup for basic superconducting properties: I_c and critical temperature T_c (50 Ω shunt resistor disconnected.)

3.2.5 I-V characteristics

Another important parameter that can define the performance of an SNSPD device is the I_c, which is defined as the maximum current a detector can support before its superconducting state breaks down and becomes resistive. For an SNSPD to operate in the single-photon regime it is crucial that it is operated with a stable current bias value just below its I_c [95]. For this measurement the experimental setup (Figure 3.25), ensures a steady and noise-free output voltage signal. The R_{load} is used to define the current supplied to the SNSPD based on $I = (V_1 \ / \ R_{load})$. Current is passing through the SNSPD device, and its resistance is monitored. Via the use of an automated computer program, the voltage value (V_1) varies to a range of bias voltages ($V_1 \ / \ R_{load} > I_c$) until it reaches the point where the supplied current is bigger than the critical current. Based on that, the critical current I_c is determined by measuring the potential difference [(V_1-V_2 / R_{load}) - (V_2 / R_{shunt})] across the SNSPD. For this measurement, a 50 Ω shunt resistor is used that is significantly lower than the SNSPD resistance during its resistive state. This shunt resistor is added in parallel with the SNSPD and prevents the SNSPD from remaining into a resistive state without recovery (latching). This is done by diverting the applied current away from the SNSPD when the detector is resistive therefore allowing it to recover back to its superconducting state.

For the SNSPD presented in Figure 3.26 its superconducting properties are lost for a current higher than ≈ 21 µA.

3.2.6 Dark count rate (DCR) characterisation

DCR is the noise that can produce false signal pulses in addition to photon detection (see further discussion in Section 2.7.3). This can be easily determined by varying the current bias of the device from a small value up to its critical current and measure its dark counts with the use of a universal counter (Agilent 53131A). By executing this experiment is possible to check if the device has any dark counts, also to monitor how the device

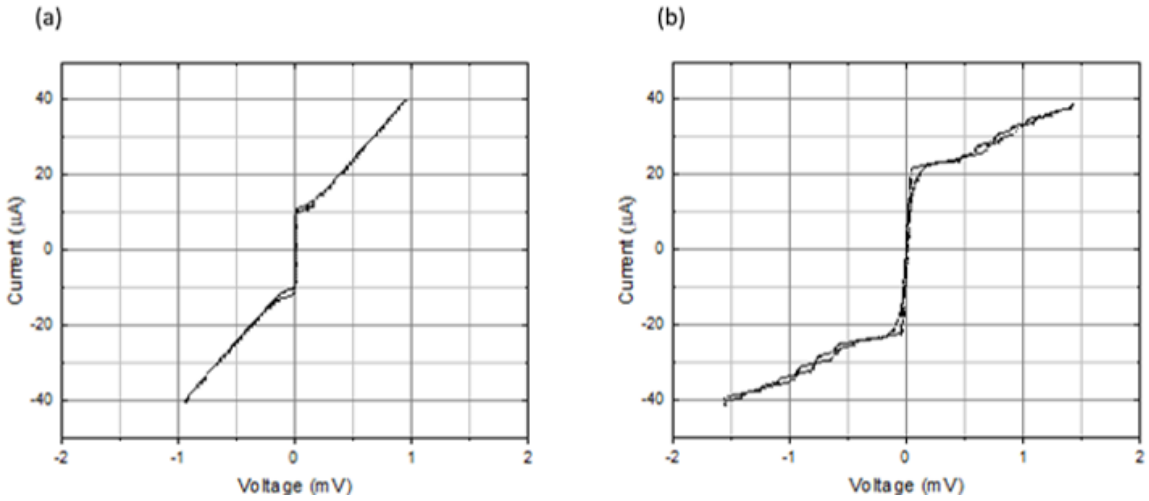

Figure 3.26: SNSPD I-V characteristic graph with and without a shunting resistor at 2.2 K using a two-wire measurement. (a) shows the current-voltage characteristic without a shunt resistor, (b) shows same detector current-voltage characteristic with a 50 Ω shunt. Data measured at 2.2 K

performs when the bias current is approaching the I_c value. The experimental setup used for this measurement is shown in Figure 3.27.

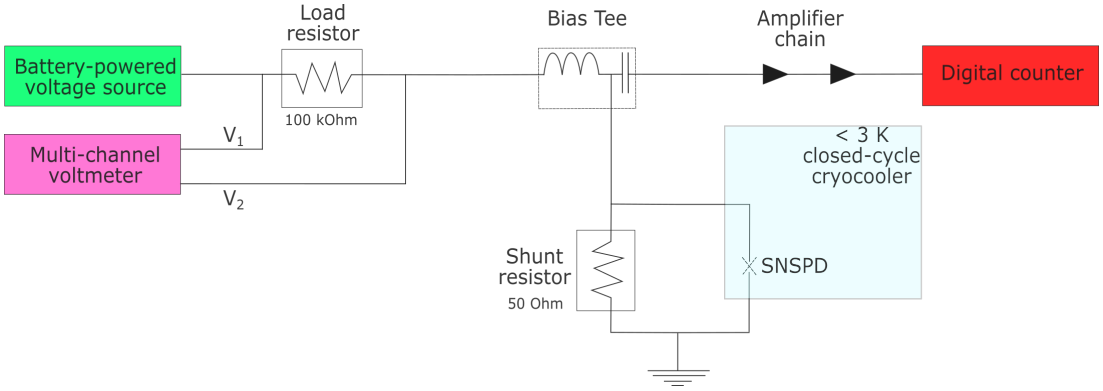

Figure 3.27: Schematic of DCR measurements setup.

3.2.7 Kinetic inductance characterisation

The counting rate of SNSPDs is limited by their kinetic inductance (L_k) hence lower L_k SNSPDs have faster recovery times. Kinetic inductance (L_k) characterisation gives information about the relaxation time of Cooper pairs in a superconductor. In addition, it can be used to give information about the uniformity of an SNSPD device [182]. Since the L_k is the result of Cooper pair ballistic motion, when the current density is increased towards the I_c value, the Cooper pairs density is reduced and the forces the remaining pairs to speed up in order to maintain the current. Moreover, the kinetic inductance increases as the current density approaches the critical current density. Consequently, this

measurement gives an indication if the current density is indeed close at its critical value only at a localised point (constriction) or across the whole nanowire cross-sectional area (no-constriction). The inductance (L) is measured with a computer controlled Via Bravo vector network analyzer (VNA) with a frequency response from 0.1-50 MHz that simultaneously measures the phase and amplitude of the reflected signal. The experimental setup is illustrated in 3.28. In order to verify the uniformity of the nanowires, the dependence of the inductance with respect the bias current (I_b) is analysed. This is achieved with the use of an automated computer program that varies the bias current (I_b) of the SNSPD in a range of bias currents from zero up to I_c (confirmed by I-V characteristics 3.2.5), and records the total inductance as a function of (I_b).

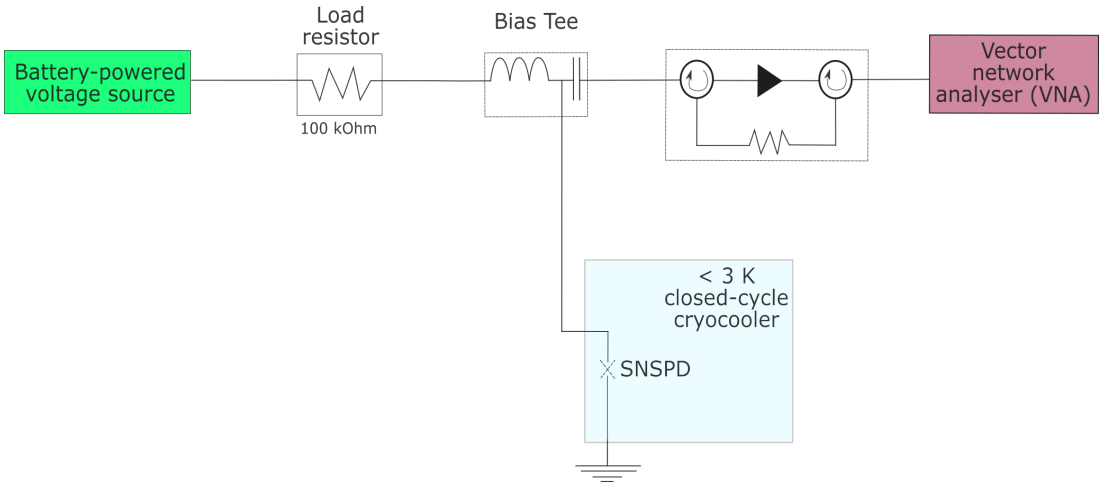

Figure 3.28: Schematic of the setup used to measure the kinetic inductance of an SNSPD. The circuit inbetween the VNA and the SNSPD is used to attenuate VNA output to a safe region for the SNSPD and re-amplifies the returning signal.

Afterwards, L_k is normalized at the value of $L_{k,0}$, which is the inductance when $I_b = 0$ and I_b is normalized at the value of I_c. Then are fitted with equation 3.1 derived from Ginzburg-Landau theoretical model of a completely uniform device with the introduction of a constriction (C) factor. This parameter was firstly used by Kerman *et al.* and is defined as the nanowire uniformity across the nanowire cross-sectional area [182].

$$\frac{L_k}{L_{k,0}} = 1 + \frac{4}{9}C^2\left(\frac{I_b}{I_c}\right)^2. \tag{3.1}$$

Where L_k is the kinetic inductance, $L_{k,0}$ is the kinetic inductance at zero bias current, I_c is the critical current and I_b is the bias current. From this equation, the constriction factor C or the measure of uniformity can range from 0 to 1 and is used to adjust the fit. For a completely uniform device $C = 1$ as illustrated in Figure 3.29.

Afterwards, SNSPDs are fibre coupled with the use of an OFHC copper square cap to assure perpendicular position of the fibre-ferrule with respect the SNSPDs chip surface. If the device is designed for front-side coupling, the cap is screwed onto the front side,

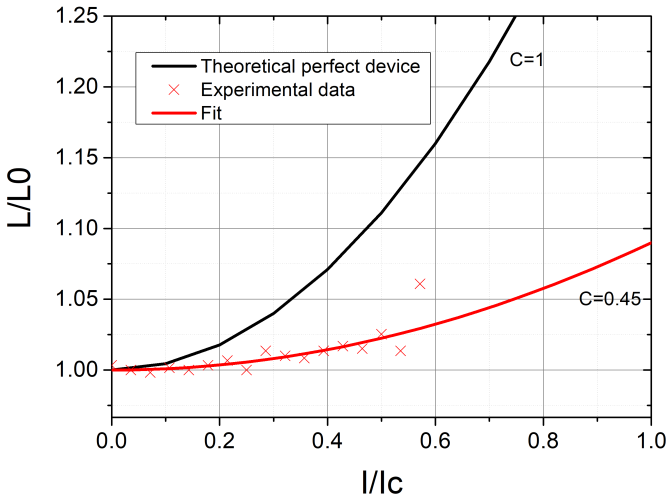

Figure 3.29: Normalised kinetic inductance ($L_k/Lk, 0$) with normalised bias current (I_b/I_c) for theoretically uniform SNSPD (C=1) shown alongside an experimental result (C=0.45).

otherwise if it is designed for back-side coupling, the cap is screwed onto the back side. Two separate sample mount designs are used for these two coupling regimes. The schematic of a front-side coupled SNSPD device with an image of the aligned device as seen through the optical microscope are portrayed in Figure 3.30.

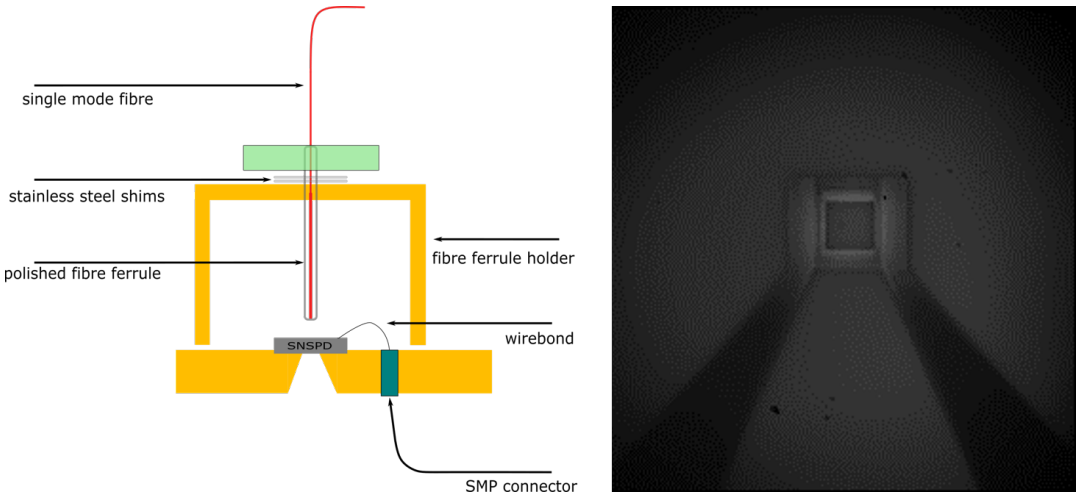

Figure 3.30: Schematic of a front-side coupled SNSPD device (left) and an optical image of the aligned device imaged through microscope (right).

3.2.8 Fibre alignment of SNSPDs

Precision alignment between the core of a single mode fibre and the SNSPDs active area is achieved by the use of a confocal microscope integrated with an infrared InGaAs camera as seen in Figure 3.33 that allows viewing the SNSPDs active area through the substrate. This setup can be used for both front and back-side coupled detectors. Also, the optical system allows coupling of SNSPDs from 630 - 2000 nm. The procedure to accurate align a fibre ferrule over the SNSPDs active area, involves two steps: a) Z-axis positioning and b) X-Y axis positioning.

Z-axis positioning: The separation between the chip surface and the end of the zirconia ferrule is controlled by thin (10-200µm) steel shims (Figure 3.30). The separation distance is verified through an optical coherence tomography (OCT) [181]. This technique can achieve micrometre resolution by simply using a white light source. It is a form of interferometry in which low-coherence white light is guided through an optical fibre to a fibre beam splitter. The light is split across two paths, one path leads to a reference mirror and one to the sample surface. The two light beams will reflect and will interfere. As a result, the path length difference information is contained in the interference pattern. The profile of the reflected signal intensity over the broad spectrum is recorded by the spectrometer at the receiver end. The separation distance is obtained by analysing the frequency spectrum of the interfered signal. The experimental OCT setup is portrayed in Figure 3.32.

The separation distance between the end of the zirconia ferrule and the chip surface should be in the range of 30-50 µm. However, during cooldown this separation distance will be altered due to partial shrinkage of the sample mount and as a result, the fibre ferrule will come closer to the sample surface and might crash the chip. Therefore, at room temperature the separation distance between the fibre ferrule and the chip surface must be more than 40 µm to prevent damage.

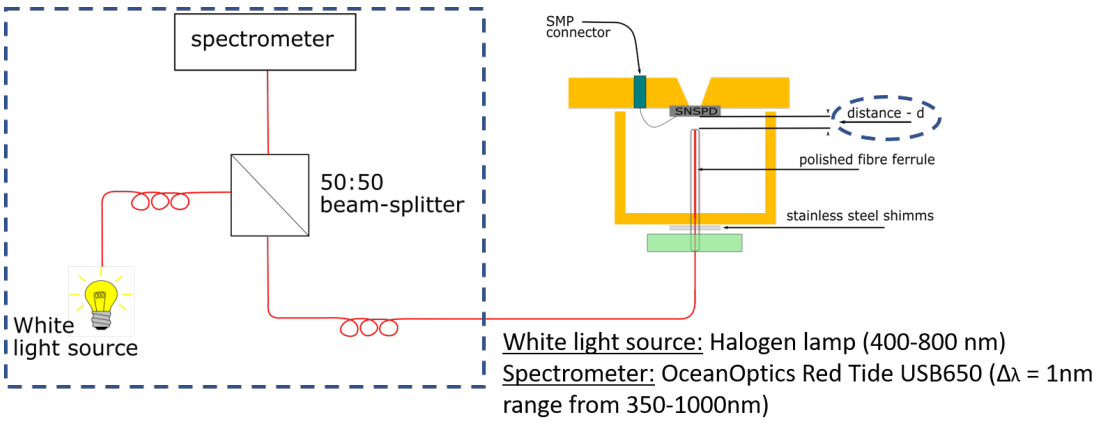

Figure 3.31: Schematic of the optical coherence tomography setup and packaged SNSPD.

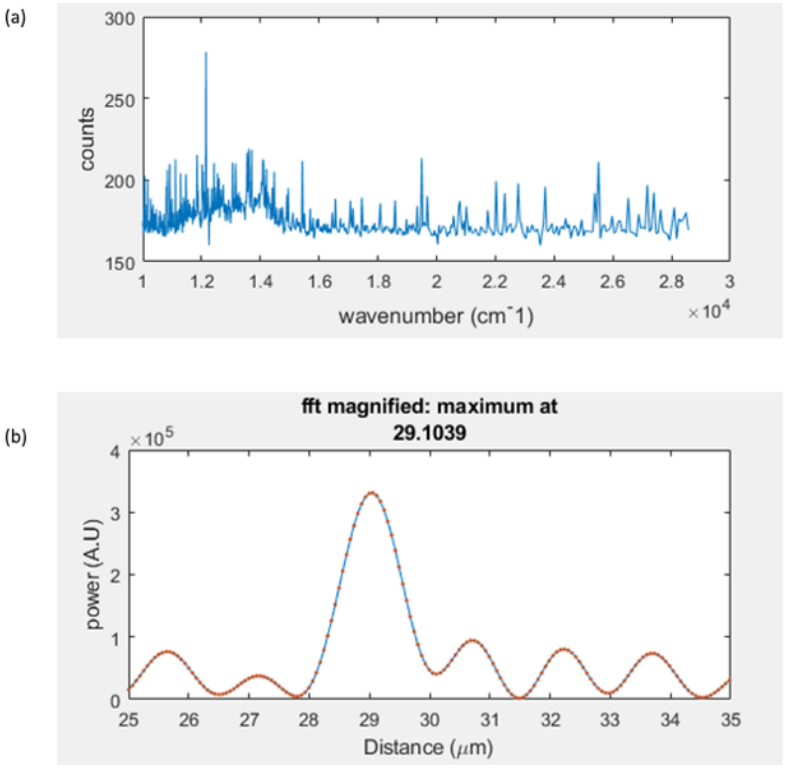

Figure 3.32: (a) Example of an OCT trace, (b) A fast Fourier transform (FFT) processed result. The separation distance between the chip surface and the fibre ferrule is approximately 29 µm.

X-Y axis positioning: After the fibre alignment in the Z-axis, the sample mount is attached on the X-Y translation stage of the fibre-alignment rig as present in Figure 3.33. Subsequently, the fibre ferrule holder cup is loosened and is moved independent from the sample mount, whereas the crucible on top of the shims guarantees to sustain the fibre ferrule position. The setup in Figure 3.33 has an integrated camera, which is used to align single mode optical fibre with SNSPDs. By shining a laser light through the fibre core, the detector is viewed through the back side of the substrate. By adjusting the X-Y translation stages, the laser spot is shifted until it reaches the SNSPD active area as presented in Figure 3.30(right).

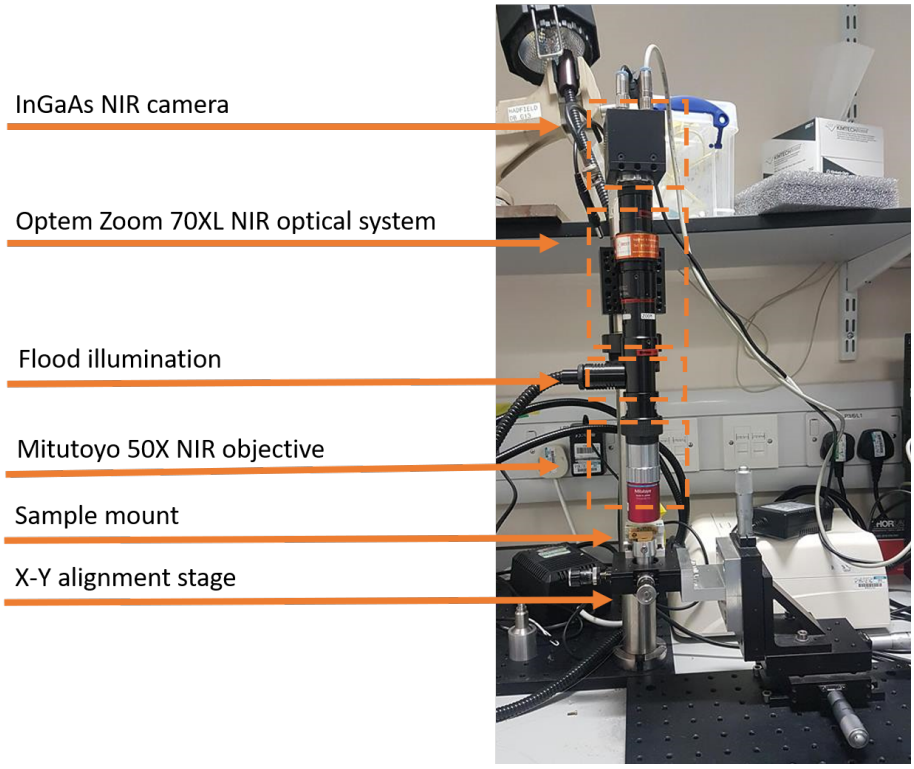

Figure 3.33: Schematic of the fibre-alignment rig.

The packaged SNSPD device is mounted at the cold head, fibre spliced into the fridge, electrically connected and the cryostat is cooled-down.

3.2.9 Detection efficiency measurement

The system detection efficiency (η_{SDE}) in an SNSPD is calculated using the calibrated light source method [99] in which, a calibrated pulsed or continuous wave laser source is fed through an optical attenuator chain that heavily attenuates the output, and is possible to determine the incident power (P). Based on that is possible to calculate the number of photons entering the cryostat per second (R_{input}) with the relationship $R_{input} = (\mathrm{P}\lambda/\hbar\mathrm{c})$, where $\hbar\mathrm{c}/\lambda$ is the energy of a single photon per second entering the cryostat for a given wavelength λ. η_{SDE} is calculated by the ratio of the number of detected photons (R_{output}) to the number of photons entering the cryostat (R_{input}). However, for each bias current there is a known number of DCR, subsequently the η_{SDE} is formed as the ratio of the number of detected photons minus the DCR divided by the number of incident photons.

$$\eta_{SDE} = \frac{R_{output} - DCR}{R_{input}}. \tag{3.2}$$

The η_{SDE} is measured with the setup present in Figure 3.34. A diode laser driven by a pulse pattern generator (PPG), generates optical pulses with a repetition rate of 1 µs or 1 MHz. The laser pulses are routed to a single-mode fibre programmable optical

attenuator chain (2 x JDS Uniphase HA9). Each of the optical attenuators is calibrated over a range of at least 60 dB with a Thorlabs PM-300 optical power meter. In total this optical attenuator chain can provide from 0 upto 120 dB of attenuation and because of that, photon flux onto the active region of the SNSPD can be altered.

In order to perform a η_{SDE} measurement, the SNSPD is current biased at a fixed bias current (I_b) with an isolated DC voltage source (SRS SIM-928) connected in series with a 100 kΩ resistor. The output signal-pulse from the detector is amplified with a room-temperature amplifier-chain (RF Bay Inc. 1x LNA-580 and 1x LNA-1000) with a total of 56dB amplification and can be monitored with an oscilloscope. This will allow to check the pulse shape and its amplitude. By varying the level of attenuation, the average number of photons per pulse (μ) is controlled and simultaneously the device count rate (CR) response is registered with an Agilent 53132A frequency counter. The counter is configured to record every 1 second the detector counts so as to synchronize with the GM cryocooler (1Hz) cycle and to register the pulses that are within a specific threshold voltage. The count rate, at extremely low photon flux (blocked beam or high level of attenuation) corresponds to the DCR of the device. However, at high photon flux the CR will saturate at the repetition rate of the laser (1 MHz) due to the inability of the SNSPD for multi-photon resolution. For this measurement, the period of each pulse must be notably longer than the reset time of the detector. This will prevent the arrival of photons during the detectors dead time and the detector will be able to recover back to its superconducting state rapidly during subsequent detection events. The η_{SDE} can be extracted by fitting the collected data with the use of 3.2[99].

$$CR = DCR + f(1 - e^{-\eta\mu}) \tag{3.3}$$

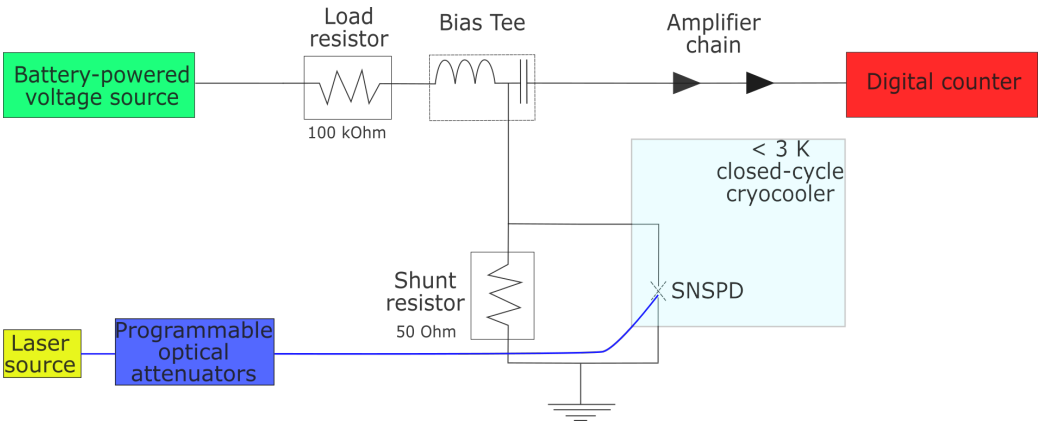

Figure 3.34: Schematic of the setup used for the system detection efficiency measurements. The laser source can be either a pulsed laser or a continuous wave (CW) laser that routed through a programmable attenuators chain, with a total of 120 dB attenuation. Then light is entering the cryostat through the fibre feed-through and directed to the SNSPD under test.

3.2.10 Timing jitter measurement

In an ideal detector, the absorption of a single photon, will lead in the generation of an output electric pulse. However, in a practical system this is not true. The timing uncertainty between the absorption of a single-photon from an SNSPD and the generation of an output electrical pulse is defined as the timing jitter (Δt). This measurement gives information regarding timing resolution limit *i.e.* the maximum count rate of the detector. For accurate timing measurements, is essential to use either a time correlated single-photon counting (TCSPC) card or a fast oscilloscope. The apparatus used for this experiment utilizing the TCSPC method is shown in Figure 3.35. A femtosecond mode-locked fibre Kphotonics CNT-1550-TK laser (central wavelength $\lambda = 1560$ nm) with 50 MHz repetition rate that generates narrow optical pulses which are routed to a 90:10 beamsplitter. The 90% output is connected to a chain of programmable optical attenuators used to attenuate the pulses down to single-photon regime and then coupled to the SNSPD. The output electrical pulses from the device, are amplified through a room temperature amplifier chain (56dB amplification) and connected to the **Input** port of the time correlated single-photon counting (TCSPC) card. Whereas, the 10% is used as input for an InGaAs fast photodiode (Thorlabs DET08CFC InGaAs, λ= 800-1700 nm, <70ps rise time) and is electrically connected into the **Sync** port of the time correlated single-photon counting (TCSPC) card. A PicoQuant PicoHarp 300 is used for TCSPC that is capable of recording the arrival of SNSPD pulses within a 4 ps time-bin. The time interval between a start (InGaAs fast photodiode) and a stop (SNSPD) signal are recorded and a histogram is formed. For a conventional SNSPD (single-wire meander), the response shape is Gaussian. Therefore, the full-width at half-maximum (FWHM) timing jitter is extracted from the Gaussian fit on the histogram.

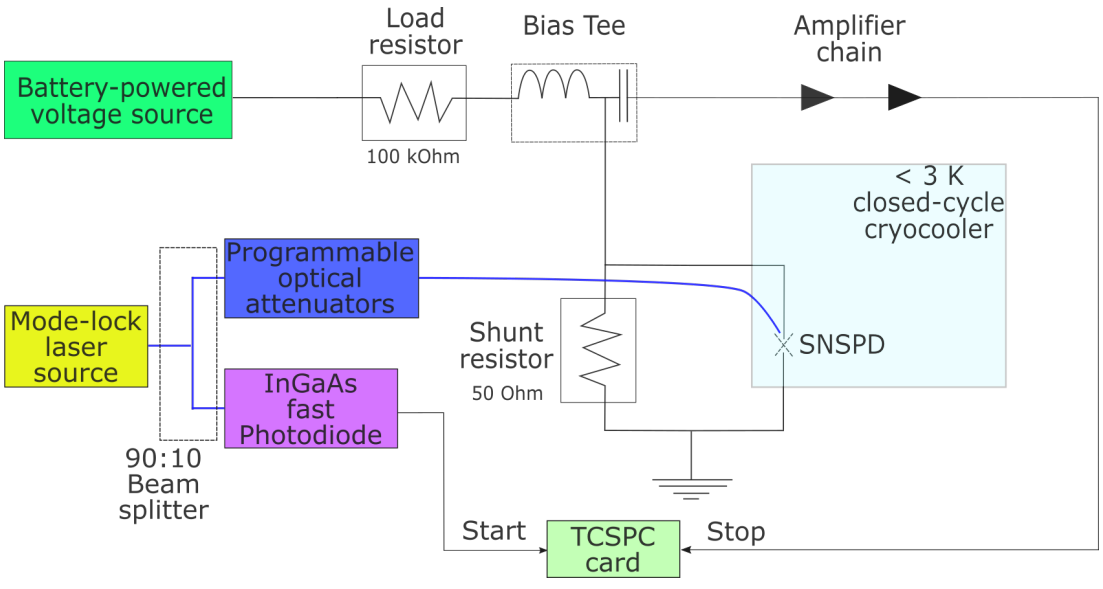

Figure 3.35: Schematic of the setup used for the TCSPC measurements.

3.2.11 Nano-optical measurements

Kelvinator - Nano-optical characterisation of the cavity SNSPD devices reported in this thesis was performed in Kelvinator cryostat, which is based on a Cryomech PT403-RM two-stage pulse tube coldhead with an CP830 water-cooled compressor that can achieve a base temperature of 3.5 K. The thermometers, electrical wiring and optical fibres are connected similarly to the GM cryostat (used for basic superconducting characterisation) described previously in Section 3.2.3. Au plated copper radiation shield is wrapped with mylar foil in order to enhance black-body radiation shielding. Nano-optical measurements are achieved with the use of a bespoke machined confocal microscope configuration setup composed of a single-mode fibre and a microscope lens tube setup [183]. This confocal microscope configuration setup is mounted on a stack of three piezoelectric stepper motors (Attocube systems) that allows the confocal microscope system to move in x and y-axes over a large area (5x5 mm^2). The third piezoelectric motor is used for the focus of the confocal microscope. Additionally, a stack of two independent scanning motors (Attocube systems) gives the ability for small area 30x30 μm^2 scanning across the device with sub-nanometre resolution. The three stepper motors were controlled by an Attocube ANC300 piezo motion controller whereas, the two scanner motors were controlled by an Attocube ANC200 motion controller. The microscope housing is attached via a flexible thermal link to the 2nd stage of a pulse-tube cooler (Cryomech PT-403) as illustrated in Figure 3.36. Light delivered from the single-mode fibre to the microscope lens tube setup is firstly collimated by a Geltech 352280-C lens with numerical aperture (NA) = 0.15 and then focused by a Geltech 352330-C lens with NA = 0.68. Both these lenses come with an anti-reflection coating (ARC) designed for 1050 nm to 1620 nm. The Kelvinator miniature microscope has two sets of microscope lenses, one for 1550 nm and another one with a suitable ARC designed for 940 nm. Therefore, we have the capability to nano-optical measurements at either 1550 nm or 940 nm by simply interchanging the microscope lenses and splicing the appropriate fibre.

Reflection mapping

To create a reflection map of the device under test, a bright light source is connected through a fibre circulator (at room temperature) and then via a break out box and hermetic feedthrough into the cryostat is connected to the miniature confocal microscope setup as pictured in Figure 3.36. Light is reflected from the electrically connected chip and guided through the focusing lens to the optical fibre and into the circulator located outside the cryostat. That is collected by an InGaAs fast photodiode. Based on the measured reflectance of the substrate, is possible to work out regions with different reflection. For the reflection map a a superluminescent diode (S5FC1550P-A2) with $\lambda = 1550$ nm is used. Then the reflection map for the device of interest is generated as portrayed in Figure 3.37

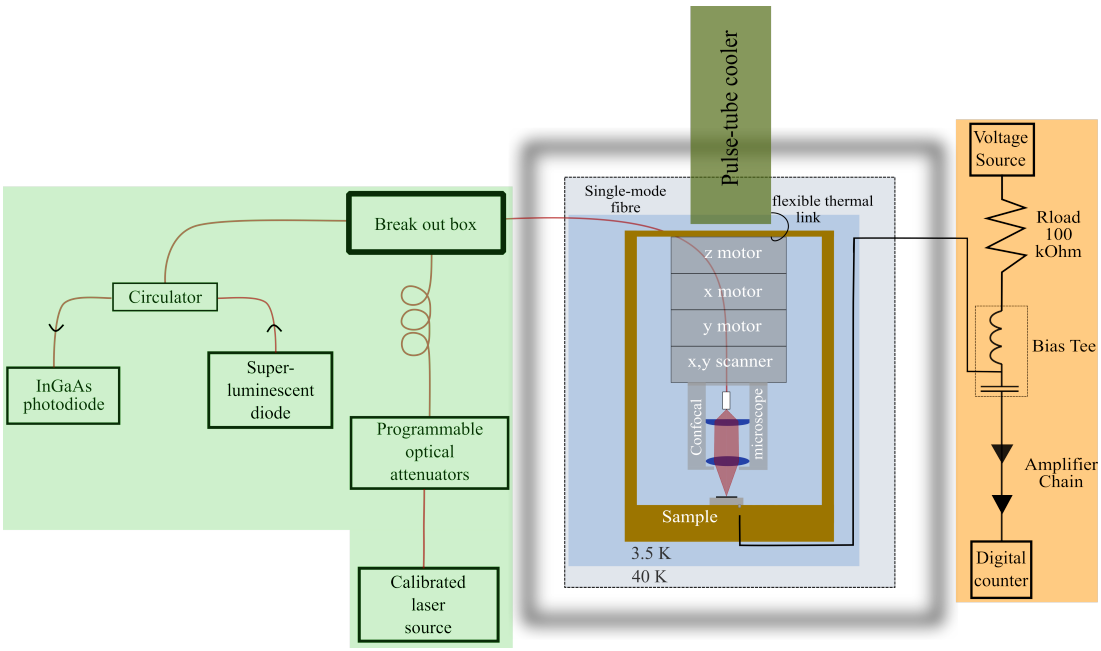

Figure 3.36: Nano-optical configuration for single photon measurements, as well as room temperature optics and electronics for counts map and local detection efficiency measurements. Piezoelectric positioners and confocal microscope are mounted in a gold-plated oxygen-free copper housing, which is attached to a pulse tube cooler. Green coloured area indicates optical components. Orange coloured area indicates the electronics components. Blue coloured box indicates the low temperature environment.

and it can be verified that we are on top of the correct device by looking at the appropriate device design. The resolution of the reflection mapping can reach up to $\approx 2\,\mu m$ at $\lambda = 1550\,nm$.

Single-photon detector photoresponse mapping

A single-photon detector photoresponse mapping uses the same setup (Figure 3.36), as soon as the surface of the chip is mapped and the active area of the device is located, the superluminescent diode, circulator and the InGaAs photodiode are disconnected and the calibrated laser source and a programmable attenuator chain are connected. Light from the calibrated laser source is routed through a chain of programmable optical attenuators and light is attenuated down to single-photon level with a photon flux of 0.1 photons/pulse and via the optical fibre feed-through on the cryostat through a single-mode fibre that is attached on the fibre-based confocal microscope light reaches the SNSPD device. Similarly, with the system detection efficiency measurement for a fibre coupled device, it is possible to characterise the local detection efficiency of an SNSPD. The device is current-biased with the use of a bias tee and through room temperature amplification (56 dB) the dark count rate (DCR) is recorded with an Agilent 53131 universal counter. While the microscope scans across the device active area and the count rate (CR) recorded at each

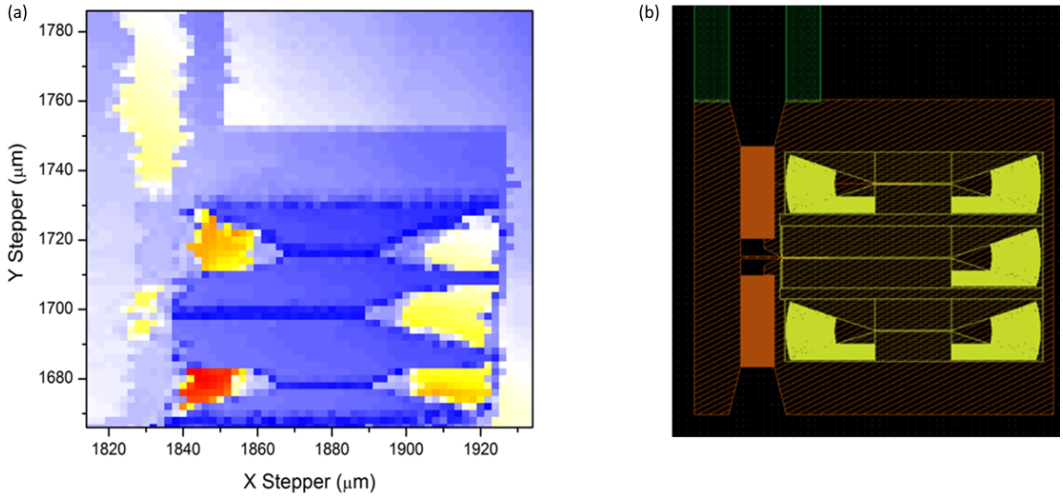

Figure 3.37: Reflection map for the device of interest and device design for verification. (a) low temperature reflection mapping of a sample containing waveguides (blue coloured), grating couplers (yellow coloured) and an SNSPD detector cooled at 3.5 K, (b) gds design of the same device. Kinetic inductors (orange coloured), coplanar waveguide lines (green coloured), waveguides and grating couplers (yellow coloured). The SNSPD detector is located on the centre waveguide.

position a photoresponse map of the device is developed. To prevent the SNSPD from latching, during the extended scan time a 50 Ω shunt resistor is used.

Rankinator - The nano-optical testing of waveguide integrated SNSPD devices reported in this thesis was performed in the Rankinator cryostat, which is based on a Cryomech PT405-RM two-stage pulse tube coldhead with an additional ^4He /^3He sorption pump connected to a CP2870 water-cooled compressor that allows characterization of SNSPD devices at 350 mK. Similar with Kelvinator cryostat, a 1550 nm confocal microscope is attached to a stack of stepper and scanner motors (Attocube systems) that allows scanning across the device with sub-nanometre resolution. This cryostat can achieve low black body radiation noise thanks to three shields: i) 300 K outer shield, ii) 50 K shield and iii) 3 K shield. In order to achieve a base temperature of 350 mK for device characterisation, four coax cables are connected from the 300 K stage to the 4 K stage and beryllium copper (BeCu) wiring is used from the 4 K to 350 mK stage due to its low specific heat capacity. Through a hermetically sealed fibre feed-through, 16 optical fibres enter the fridge.

3.2.12 Mid-infrared characterisation

Characterisation of 2.3 µm backside metallic mirror cavity SNSPD devices took place in a cryostat identical to Zephynator (described in section 3.2.3), except with different fibres installed inside. For mid-infrared characterisation, and specifically for 2.3 µm a lot

of components are still not commercially available off-the-shelf. For example, optical-fibres can be supplied only from a handful of companies and particularly for mid-infrared there is a fibre available from Thorlabs (SM-2000) that is single-mode from 1.7 to 2.3 µm and has a mode field diameter (MFD) of 13 ±1 µm at 2 µm [184] that makes it suitable for fibre-coupling of the 15 x 15 µm^2 SNSPD devices. Additionally, filters, attenuators and beam splitters are not available as a commercial unit integrated with single-mode fibre while in telecommunication wavelengths of 1.3 and 1.5 µm most of the equipment is available off-the-shelf. Therefore, due to the shortage of commercially available fibre optical-attenuators, free-space infrared neutral density (ND) filters from Spectrogon with optical density (OD) values of 0.3 (50% transmission), 0.6 (25% transmission), 1.0 (10% transmission), 1.45 (3.6% transmission), 2.0 (1% transmission) and 3.0 (0.1% transmission) were installed in an optical bench to attenuate the light down to single photon regime. For this experiment as a single-photon source, an optical parametric oscillator (OPO) was used that can generate pico-second pulse-widths of light from 1.4 - 4.2 µm [185]. The OPO gives a signal and an idler output and through a grating that can adjust the wavelength. For this experiment the grating was adjusted until a peak was achieved at approximately 2.33 µm as verified by an optical spectrum analyser (OSA) illustrated in Figure 3.38. Then a narrow band-pass filter (BPF) with a centre wavelength of 2328 nm ± 43 nm is added to the circuit to filter the rest of the spectrum. The experimental apparatus for mid-infrared characterisation of SNSPDs is illustrated in Figure 3.39. Each neutral density (ND) filter was carefully calibrated with a Thorlabs PM100D optical power meter.

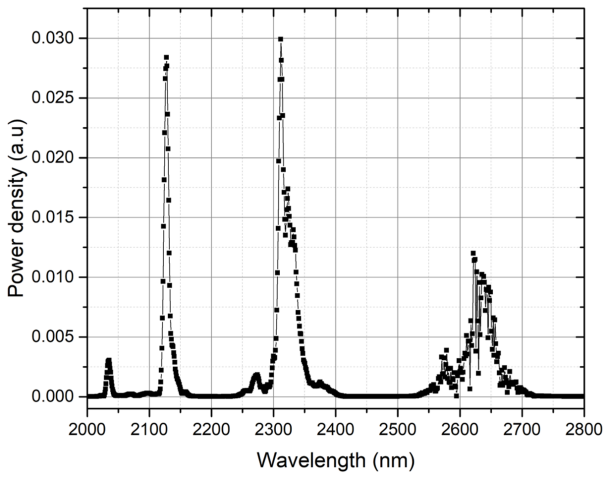

Figure 3.38: Optical parametric oscillator spectrum from idler output with the grating adjusted for a peak at 2.33 µm measured with an optical spectrum analyser.

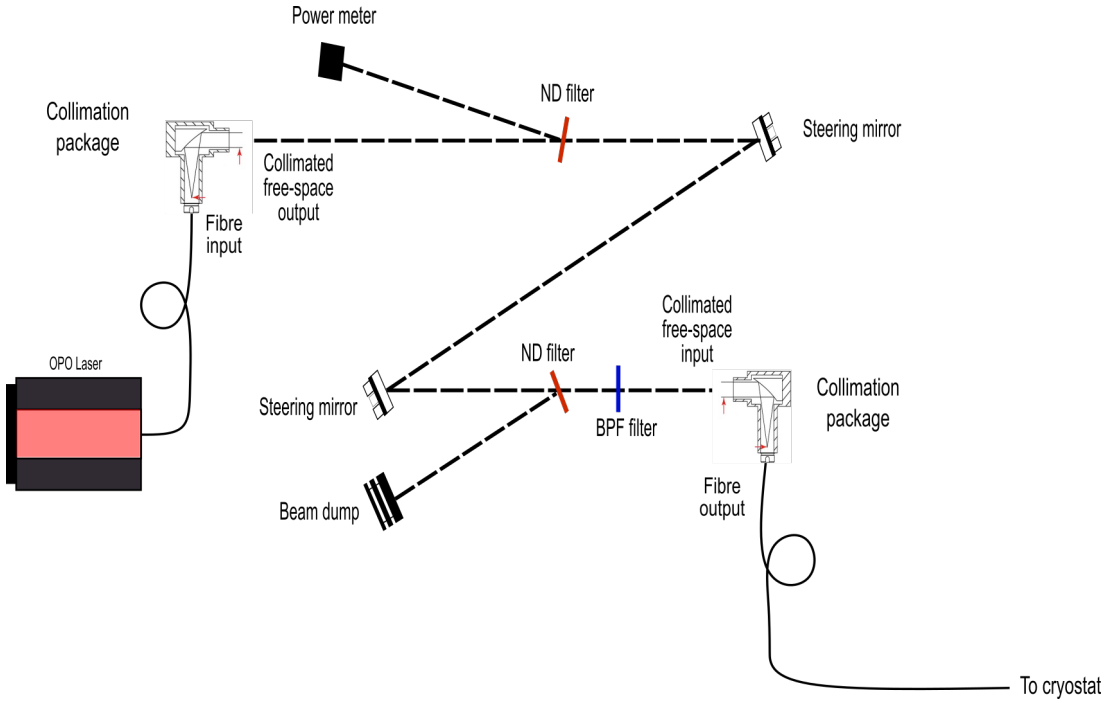

Figure 3.39: Schematic of mid-IR test apparatus including optical parametric oscillator (OPO).

Chapter 4

Cavity enhanced detectors

This chapter focuses on SNSPDs embedded in NbTiN cavities, two different types of cavity integerated SNSPDs are explored. First is the front side cavity integrated SNSPD devices for near-infrared (λ = 940 nm) applications that take advantage of distributed Bragg reflectors (DBR) as their cavity reflectors. While the second is back side cavity integrated SNSPD devices designed for infrared (λ = 1550 nm) and mid-infrared (λ = 2333 nm) applications that take advantage of metallic mirrors as their cavity reflector.

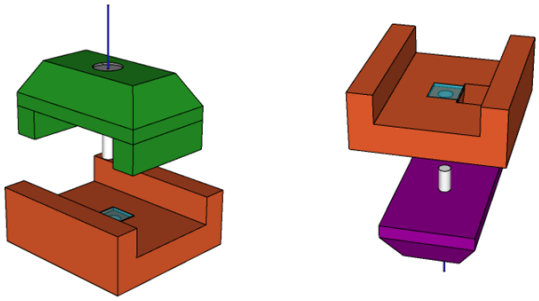

Figure 4.1: Schematic representation of front and back side coupled SNSPD designs. Left shows a front side coupled SNSPD device, the fibre cap (green coloured) is attached on top of the SNSPD device. Right shows a back side coupled SNSPD device, the fibre cap (dark magenta coloured) is attached on the back side of the SNSPD device through a hole in the centre of the sample mount.

This chapter describes in detail the fabrication process for both these designs, followed by a discussion on their electrical and optical characterisation techniques and their properties.

4.1 Frontside coupled - Detectors fabricated on DBR substrates for $\lambda = 940$ nm

In the near infrared (NIR) wavelength range, the energy of a single photon is of order 1eV making detection an extremely challenging task. Off-the-shelf semiconductor photon-counters including single-photon avalanche photodiodes (SPADs) and photomultiplier tubes (PMTs) perform very well in the visible range. However, moving into NIR wavelengths, their performance declines [186, 187]. Particularly close to 940 nm wavelength, there is a gap in performance: the detection efficiency of Si SPADs drops steeply beyond 900 nm, whereas InGaAs SPADs typically operate between 1.1-1.6 µm. Therefore, the development of highly efficient detectors with low dark count rates and high timing resolution at 940 nm is essential for exploitation of QD sources (described in Section 2.5.2) in quantum key distribution (QKD) [188] and QIP systems. Most applications with SNSPDs have been focused on telecommunication bands (1310-1550 nm). Nonetheless, to characterise the performance of a QD single-photon source and exploit these sources in QIP applications, highly efficient SNSPDs operating at 940 nm are required. Initial efforts at QD single-photon source characterisation used early generation SNSPDs without an optical cavity and thus with limited efficiency [189, 190]. Very recently, a SNSPD based on NbN superconducting film in an optical cavity with a system detection efficiency (SDE) $> 80\%$ at 940 nm [191] has been reported and a broadband design (500-1100 nm) with a peak efficiency of 30% at 800 nm [192] has also been reported. Moreover, a design on non-periodic DBR optimized for (650-900nm) with a peak efficiency of 82.3% at 808 nm [193] has been demonstrated.

In the case of a perpendicularly illuminated SNSPDs grown atop bare Si substrates, photons have only one attempt to impinge upon the device active area, thus the absorption probability η_{abs} is limited. To overcome this limitation, the use of a reflector underneath the SNSPD device was proposed to enhance the absorption[194]. In this configuration, if a photon passes through the detector, it can reflect back to the SNSPDs active area and lead to the generation of an electrical pulse. This mirror gives a second chance for a photon to impinge with the SNSPD. However, it generates reflection-losses on the illumination side. Consequently, this concept was taken a step forward, with the introduction of an anti-reflection coating (ARC) to minimize those reflection-losses [74]. Based on the cavity design, the detector absorption is boosted at the desired experimental wavelength. SNSPD devices integrated with optical cavities for front side-illumination are highly desirable since they allow for easier and more efficient fibre-coupling. However, the fabrication of uniform and constriction-free nanowires on top of an optical cavity is difficult mainly due to the fact that low surface roughness is required to ensure uniform film growth. In this section, the possibility to fabricate SNSPD devices that are designed for front-side illumination on

top of a distributed Bragg reflector (DBR) cavity to enhance the η_{abs} is investigated. A DBR is defined as either a structure formed from multiple layers of alternating materials with different refractive indices or as an one-dimension photonic crystal with a periodic distribution in the effective refractive index. It is made up from a stack of alternating low and high refractive index layers. Each layer in the DBR stack is designed to have a quarter-wavelength ($\lambda/4$) optical thickness with λ = experimental wavelength. The reflections from adjacent layers builds up leading to constructive interference, hence the designed DBR acts as a narrowband high reflection filter centred nearby the experimental wavelength. The number of bilayer repeats needed in order to obtain a specific reflectivity value will depend on the refractive index contrast between the two materials chosen for the cavity.

4.1.1 Distributed Bragg reflector cavity design

The DBR bilayers are typically grown on top of a Si substrate using an ion-beam sputtering method [195]. For this experiment a tantalum pentoxide (Ta_2O_5)/ silicon dioxide (SiO_2) distributed Bragg reflector (DBR) cavity structure was designed with centre λ = 940 nm. The number of bilayer repeats required in order to achieve maximum light reflection from the top surface of the substrate are calculated with the use of Essential Macleod software from Thin film centre inc. Essential Macleod calculates the electric field distribution at the nanowire detector under perpendicular illumination. Prior to DBR cavity growth, the absorption probability of 7.5 NbTiN thin film was simulated for various number of DBR bilayer repeats. The results are present in Figure 4.2.

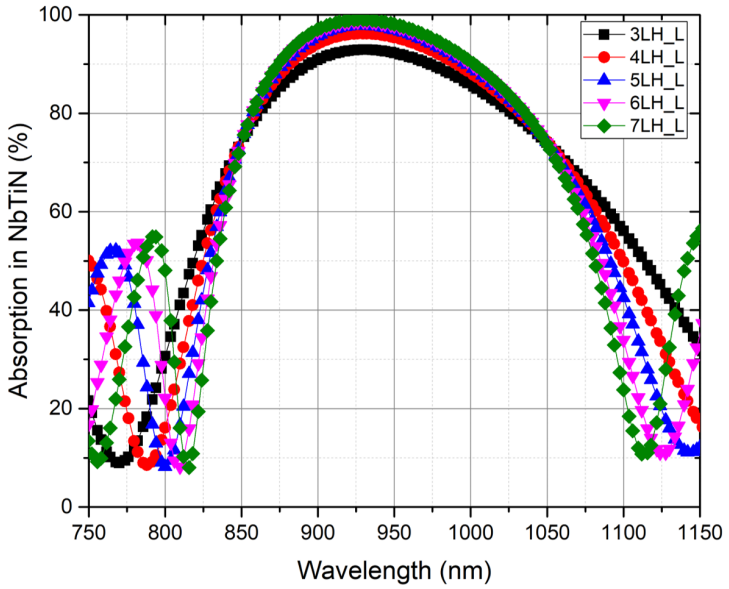

Figure 4.2: Simulated absorption in NbTiN thin film while the DBR bilayer repeats are varied. L denotes low refractive index material (SiO_2), while H denotes high refractive index material (Ta_2O_5).

The best fit is reached with the use of 7 bilayer repeats of SiO_2 / Ta_2O_5 with designed thickness of 161 nm and 111 nm respectively. Additionally, a final SiO_2 161 nm thick layer is added, which acts as a quarter-wavelength ($\lambda/4$) anti-reflection coating (ARC) optimized for incident wavelengths in the range of 850 - 1050 nm. After the DBR cavity is grown on top of a Si substrate (Helia Photonics Ltd grew the DBR bilayers), its reflectance is experimentally characterised and the fitted data are plotted (red) with the simulated results (black) as illustrated in Figure 4.3. For this DBR cavity, the measured reflectance of the bilayers is $> 98\%$ at 940 nm.

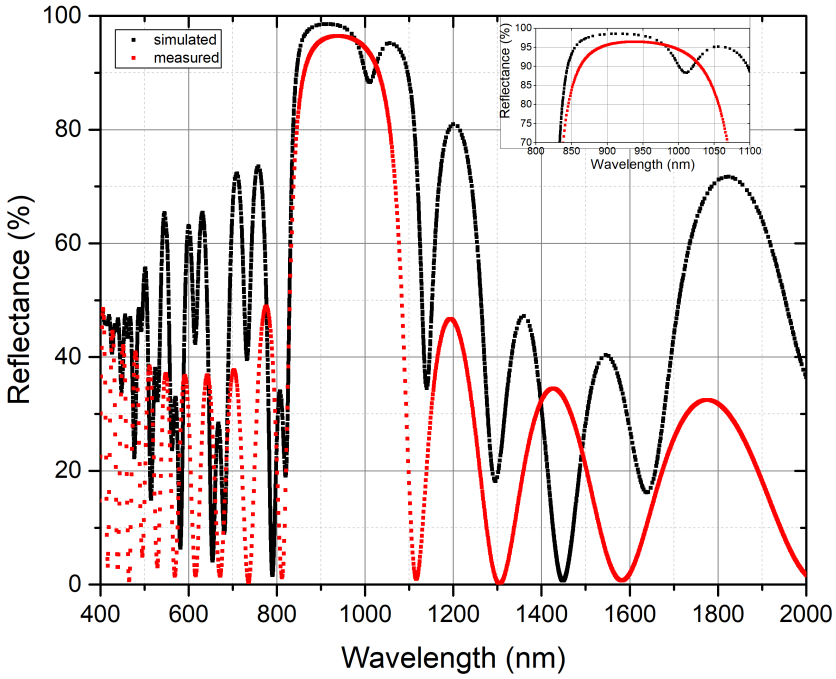

Figure 4.3: Comparison between simulated and experimental reflectance characterisation of DBR cavity Ta_2O_5 / SiO_2 on Si substrate.

During the reflectance characterisation, only the DBR cavity and the silicon substrate total reflectance was calculated (superconducting thin-film not present).

4.1.2 Coplanar waveguide transmission line design

The coplanar waveguide (CPW) transmission line, which serves as the electrical link between the chip and room temperature electronics needs careful design to match the $50\,\Omega$ impedance of the room temperature electronics. The CPW signal-plane (S) width is set $\approx 5\,\mu m$ close to the SNSPD active area. Then based on the substrate thickness, relative permittivity (ϵ_r) of the substrate and the centre frequency required for the electrical signal transmission ($\approx 2\,GHz$) (Figure 4.4). Based on the assumption the DBR layers ($\approx 1\,\mu m$)

do not play any role in the RF response of the electrical signal. The ground-plane spacing (G) is calculated as ≈ 2.9 µm with the use of TX-line transmission line calculator tool from National Instruments (NI) AWR design environment [196].

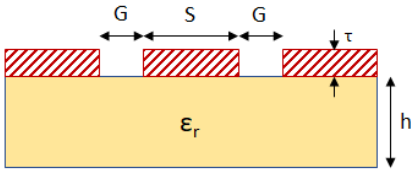

Figure 4.4: Graphical representation of the parameters used for the CPW calculation of the ground-plane (G) width, which is related to the signal-plane (S) width, the relative permittivity (ϵ_r) and the thickness of the substrate, the thin film thickness (τ), the centre frequency for the electrical signal (≈ 2 GHz) and impedance matched at 50 Ω.

This calculation assumes that below the Si substrate is air and there is no ground-plane underneath it. The same calculation process is repeated at 1 mm away from the SNSPD device, where the Au contact pads will be defined for the wire-bonding connections. Therefore, the signal-plane width (S) is set in the range of ≈ 300 µm to allow for comfortable wire-bonding between the sample mount and the Au contact pads. The ground-plane spacing (G) is calculated as ≈ 160 µm. Subsequently, the beginning and the end points of the CPW are mismatched in size, thus the CPW is tapered to compensate for that, as shown in Figure 4.5(a).

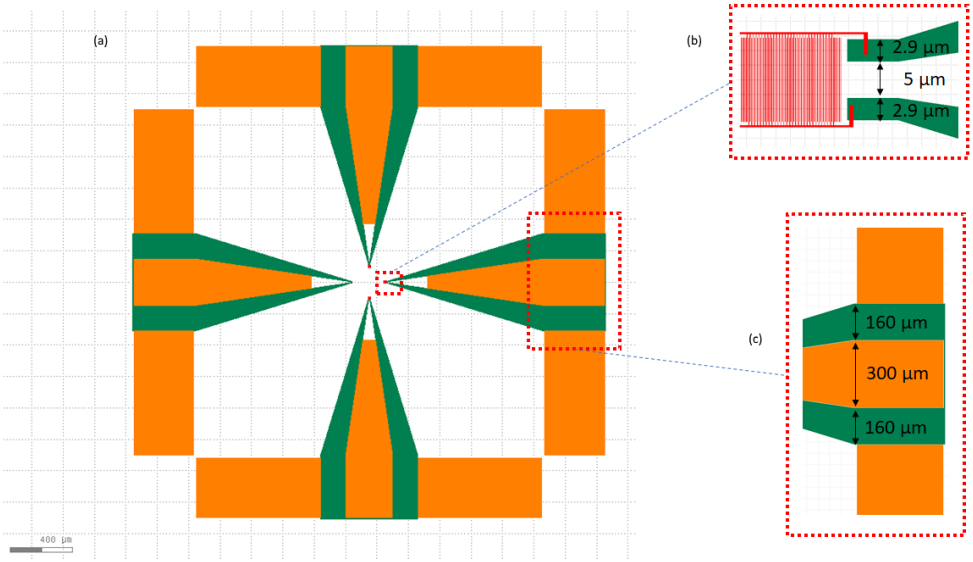

Figure 4.5: SNSPD GDS design. (a) the whole length of the CPW is illustrated (green-coloured) (b) zoomed-in area close to the SNSPD active area and (c) zoomed-in area close to the Au contact pads for the wire-bonding connections.

4.1.3 Device fabrication

The NbTiN thin films that were used for this work were deposited by DC reactive sputtering at room temperature (described in section 3.1.1) in the National Institute of Information and Communication Technology (NICT) in Japan. The film thickness (τ) was controlled by the deposition rate and deposition time [120]. A 7.5 nm NbTiN thin film was grown on top of a DBR optimized for maximum absorption at 940 nm (Figure 4.6).

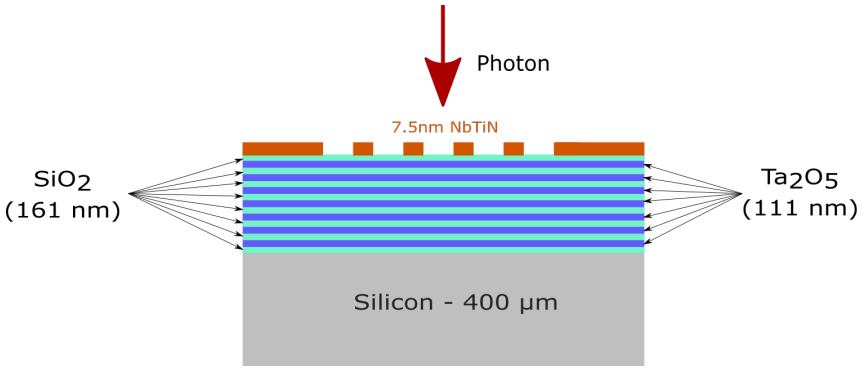

Figure 4.6: Schematic of SNSPD on DBR/Si substrate (not to scale).

Surface roughness after NbTiN thin film deposition was measured using atomic force microscopy (AFM) at the University of Glasgow. Various areas of the sample were scanned and a root mean square roughness (Rq) of 1.247 nm was recorded as shown in Figure 4.7. This value is relatively high compared to the surface roughness of 0.18 nm reported by Zhang *et al.* on a similar DBR substrate [191].

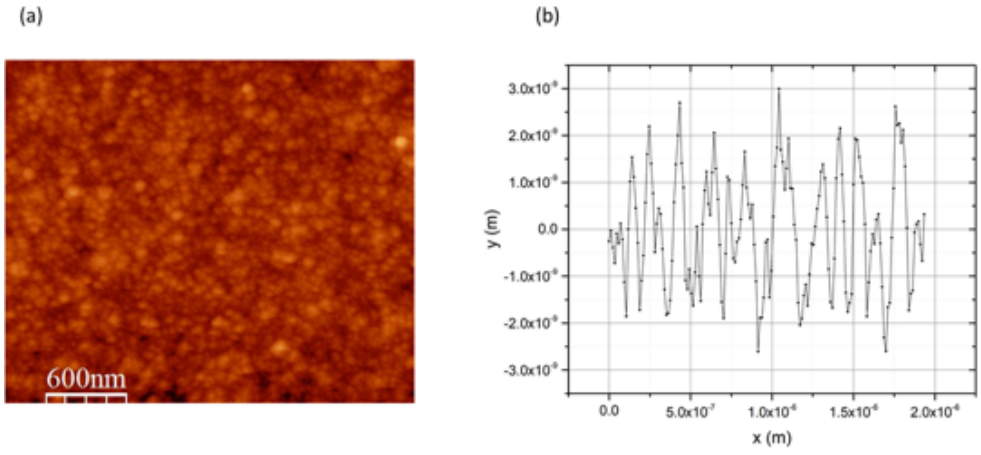

Figure 4.7: Surface roughness measurements. (a) AFM micrograph of a region of the sample (scanning area 3x3 µm). (b) roughness variation over the 3x3 µm area. A root mean square roughness of 1.247 nm was recorded.

The devices were then patterned and fabricated in the James Watt Nanofabrication Centre (JWNC) at University of Glasgow. The SNSPD nanowire width was 95 nm and the spacing was 105 nm meandering over a square area of 15x15 µm^2.

Two electron-beam lithography (EBL) steps were used during the fabrication process. EBL was carried out by a Vistec VB6 UHR EHF EBL tool at 100 keV (described in Section 3.1.3). The first EBL step used a PMMA bilayer positive tone e-beam resist to pattern alignment markers and bonding contact pads. After development in MIBK:IPA, 100 nm Au (with 3 nm Ti adhesion layer) were deposited by ultra-high vacuum electron-gun evaporation and lift-off. The nanowire and 50 Ω impedance matched coplanar waveguide (CPW) electrodes were patterned in the second EBL step with the use of 165 nm ZEP-520A positive tone e-beam resist. Then the pattern was transferred into the NbTiN film by reactive-ion etching (RIE) with the use of CF_4 gas.

4.1.4 Transmission electron microscopy analysis

The structural properties of the SNSPD DBR device has been characterised via high resolution transmission electron microscopy (TEM). The transmission electron microscope facilities available in the School of Physics and Astronomy, University of Glasgow (FEI Tecnai T20 microscope) have been used for this purpose. Before the TEM analysis, electron transparent cross sections have been prepared using a dual beam focused ion beam (FIB) system. Figure 4.8(a) shows a TEM image of the SNSPD cross-section with the DBR substrate. Additionally, in Figure 4.8(b) a zoomed in TEM image of the SNSPD cross-section active area is shown. During our TEM analysis, we have also examined the thickness variation of each subsequent bilayer at 8 different points across the imaged area shown in Figure 4.8 (corresponding to a span of 5 micrometres) and their mean value was calculated. Additionally, the average intensity variation of each subsequent layer was extracted, and it was observed that the average intensity profile is increasing from the Si substrate interface up to the top SiO_2 where the NbTiN thin film was grown on as displayed in Table 4.1. The SiO_2 layers show higher intensity variation in comparison to the Ta_2O_5 layers (increasing from 1.2 nm for SiO_2 and 0.6 nm for Ta_2O_5 for the first bilayer repeat, to 6.02 nm for SiO_2 and 4.50 nm for Ta_2O_5 in the seventh bilayer repeat). The uppermost SiO_2 layer has an average intensity variation of 6.4 nm over the length scale of 5 micrometres sampled, which approaches the thickness of the superconducting NbTiN film (7.5 nm) making up the SNSPD device, indicating that the roughness of the DBR may begin to affect the uniformity of the patterned SNSPD device. Consequently, if the superconducting thin film is not uniform, the maximum bias current (I_c) of the SNSPD will be limited and the detector will not perform at its peak performance.

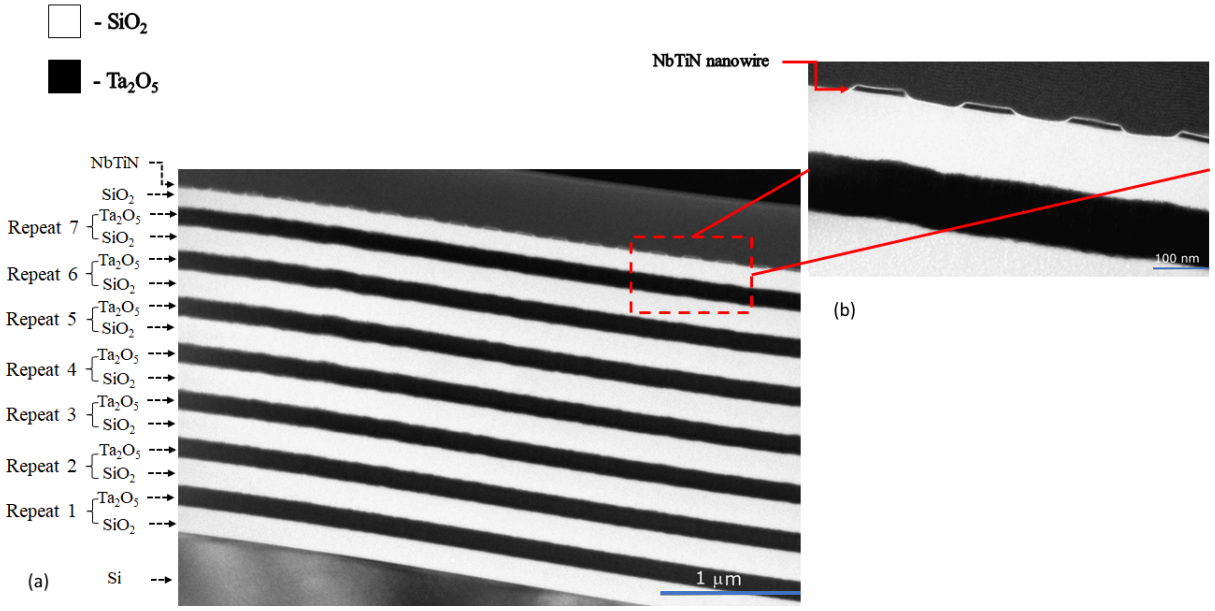

Figure 4.8: (a) TEM image of the SNSPD cross-section showing the DBR layers atop Si. There are in total 7 repeats of SiO_2/Ta_2O_5 with a final SiO_2 layer acting as a $\lambda/4$ cavity before the NbTiN nanowires. (b) zoomed-in TEM image of the SNSPD cross-section area illustrating the last (Repeat 7) of the DBR layers, the $\lambda/4$ cavity SiO_2 layer and the NbTiN nanowires. Note the device is capped with Pt prior to FIB sectioning.

Bilayer repeat:	**SiO_2 bilayer thickness (nm)**	**average intensity profile for SiO_2 layer (nm)**	**Ta_2O_5 bilayer thickness (nm)**	**average intensity profile for Ta_2O_5 layer (nm)**
1	138	1.2	141	0.60
2	185	2.55	150	1.48
3	196	3.21	152	1.93
4	198	4.45	152	1.93
5	202	5.07	152	2.38
6	199	5.89	154	3.44
7	201	6.02	153	4.5
8	191	6.4	-	-

Table 4.1: Measured thickness of each subsequent bilayer at 8 different points across the 5 micrometres lateral width of the structure of Device 1 imaged in Figure 4.8 and their mean values are tabulated. Additionally, the surface roughness for each of the SiO_2 and Ta_2O_5 bilayers is presented. SiO_2/Ta_2O_5 bilayer was repeated 7 times with a final SiO_2 layer acting as a $\lambda/4$ cavity before the NbTiN SNSPD device. The DBR was grown on top of a Si substrate.

4.1.5 Electrical characterisation

The devices were mounted and cooled in the setup illustrated in Figure 3.36 where low temperature electrical and optical characterisations were performed as described in section 3.2.11. The NbTiN SNSPD devices were characterized in terms of basic superconducting properties that include: critical temperature T_c, current voltage characteristics (I-V curve) and normalized inductance versus normalized bias current (L-I curve).

Basic electrical properties			
Device ID:	$\mathbf{R}_{300K}$	$\mathbf{T}_c$	$\mathbf{I}_c$
940nm batch	2.5-3 MΩ	7-8 K	15-18 µA

Table 4.2: Electrical properties of SNSPDs fabricated on 940 nm Ta_2O_5/SiO_2 DBR substrates.

Prior to NbTiN SNSPD fabrication, the transition temperature (Tc) was firstly optimized for bulk NbTiN films. 100 nm thick NbTiN films have been grown at various nitrogen flow rates while other parameters kept unchanged. Samples where then patterned with a simple photolithography pattern that allowed for the low temperature characterisation (four-point wire measurement). The samples where then immersed into a liquid helium with base temperature of 4.2 K and their Tc was recorded. As soon as the best conditions were reached for the highest Tc for a bulk NbTiN, the thickness was decreased down to sub 10 nm by decreasing the deposition time.

To confirm the uniformity of the nanowires, we analysed the change in the inductance while varying the bias current (I_b) [197] as described in Section 3.2.7. Figure 4.9 portrays measured data for two SNSPD devices fabricated on top of Ta_2O_5/SiO_2 DBR cavities. Acquired data are fitted with equation 3.1. In this, the parameter C is used to adjust the level of fitness. Completely uniform nanowire device (black line) has a $C = 1$. The device with the highest obtained nanowire uniformity value has $C = 0.65$.

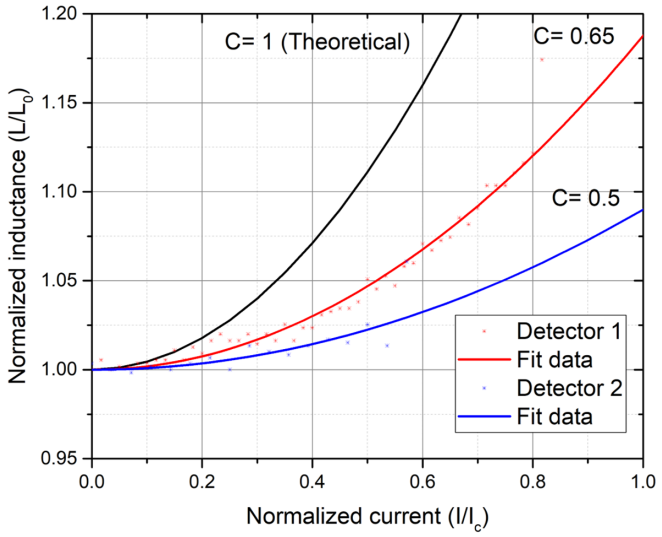

Figure 4.9: Normalized inductance of two detectors versus their variation of the normalized bias current at $T = 3.5$ K; the inductance was normalized at the value of L_o representing the inductance of the SNSPD at bias current ($I_b = 0$) and the bias current was normalized at the value of I_c of the SNSPD. The black (solid line) represents the theoretical curve for $C = 1$, based on Ginzburg-Landau theory for nanowires with no cross-sectional constrictions. The fitted C values for the detectors are $C = 0.65$ (red line) and $C = 0.5$ (blue line).

4.1.6 Optical characterization at 940 nm wavelength

The ultimate test for SNSPDs uniformity is the single-photon mapping of their photoresponse at target wavelength. To characterise the local system detection efficiency of the SNSPD, a low temperature confocal miniature microscope setup was used (see Section 3.2.11) to locate the active area and to map the surface of the chip. Figure 4.10(b) illustrates the output voltage signal of the InGaAs photodiode versus the relative x-y positions indicating the device active area. The device was then current-biased using a bias tee and through room temperature amplification (56 dB), the dark count rate (DCR) of the NbTiN SNSPD was measured using an Agilent 53131 universal counter. The photoresponse uniformity of the SNSPD was confirmed by mapping the device area with a 940 nm calibrated pulsed laser at a repetition rate of 1 MHz. The input photon flux illuminating the device was maintained below 1 photon per pulse. To prevent the SNSPD from latching, during the extended scan time a 50 Ω shunt resistor was used. The optical spot was scanned across the same area as the photo reflection map Figure 4.10(c).

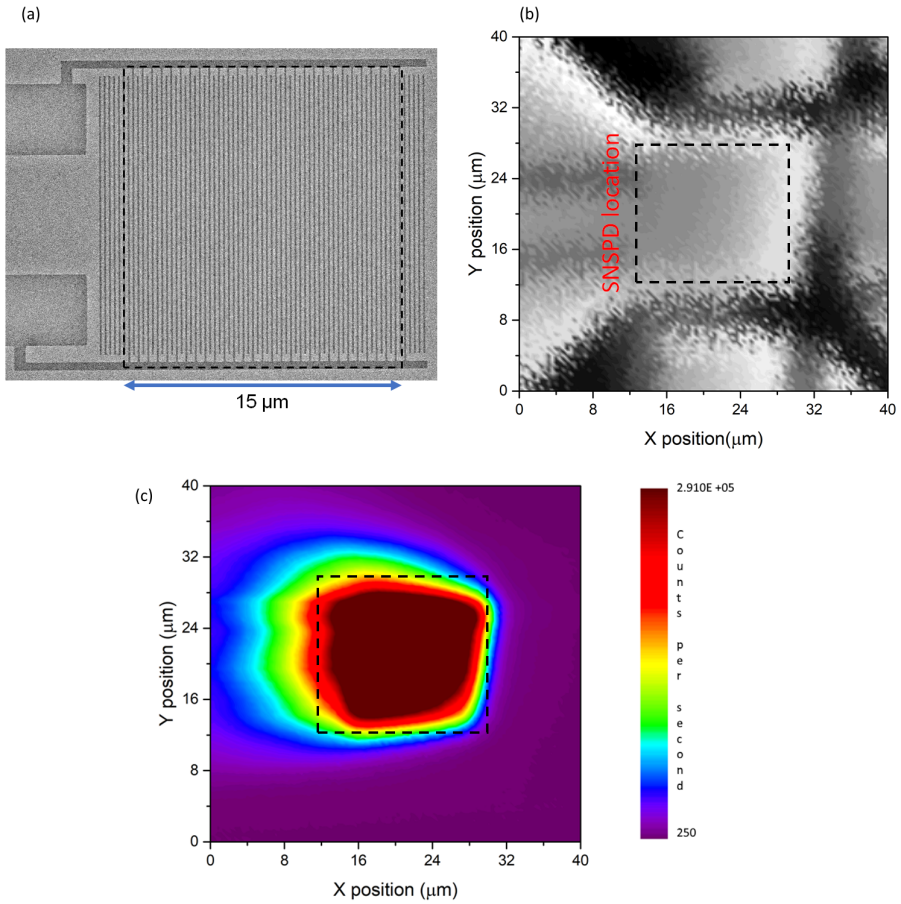

Figure 4.10: (a) A NbTiN SNSPD with an active area of 15x15 µm^2 as seen under a scanning electron microscope (SEM), (b) the same device is cooled at 3.5 K. The laser beam is raster scanned across the device area, simultaneously the reflected light is recorded, and an image is built. For this measurement a continuous wave (CW) broadband laser λ = 1550 nm is used, (c) laser diode is switched to a λ = 940 nm and attenuated down to few photon regime. The miniature microscope scans across the same area as (b) and the number of output pulses observed at each position is recorded as the photoresponse map of the device. The black box represents the active area of the device.

The counts map is capable of resolving variations in the single photon sensitivity across the 15x15 µm^2 active area of the device due to its sub-nanometre step size resolution. Non-uniform nanowires could be introduced when the thin film is grown on the substrate as a result of the deposition process or because of inhomogeneity in the DBR substrate. Moreover, constricted nanowires could be introduced during the EBL and dry etching processes. At the highest responding point, the local η_{SDE} of the SNSPD is calculated and shown in Figure 4.11 indicating a peak SDE of 55% at 100 dark count rate, while the device was biased at 17 µA (95% of I_c). During this experiment it was observed a change in the slope of efficiency just after I_b = 22 µA that might be attributed to an imperfect subtraction of the DCR from the experimental data during computation of the η_{SDE}.

By maintaining the spot of the confocal microscope in the same position used for the

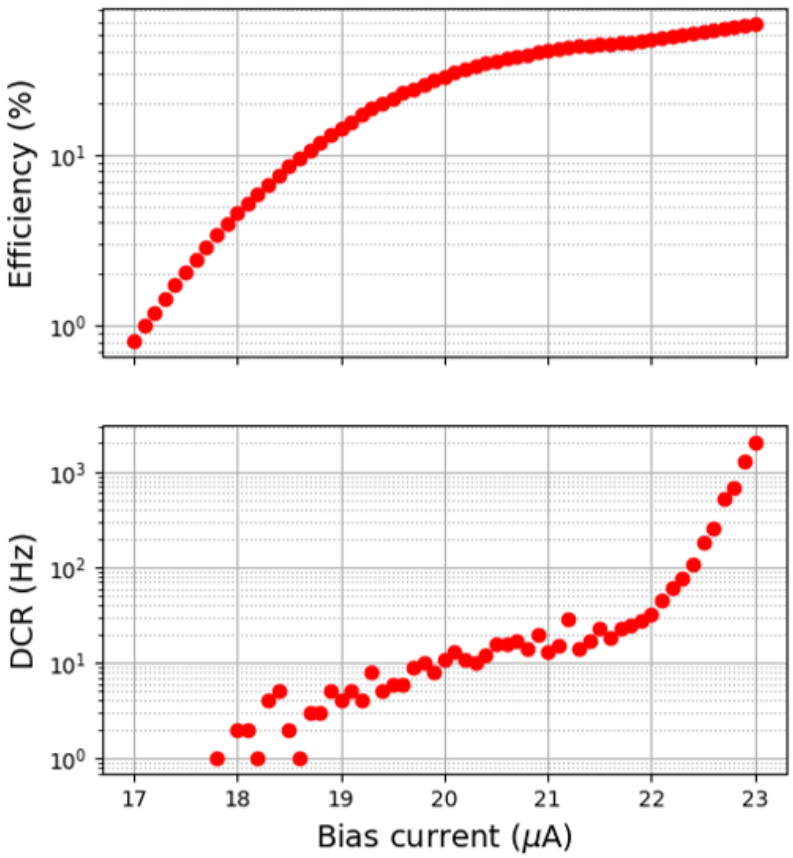

Figure 4.11: Measured system detection efficiency (η_{SDE}) of a 15 x 15 µm^2 meander NbTiN SNSPD on a Ta_2O_5/SiO_2 DBR substrate. The SNSPD is current biased at a fixed point and its count rate as a function of input photon flux is recorded. Subsequently, this data is fitted to a sigmoid curve and the efficiency is calculated. The experiment was performed in a 3.5 K pulse tube cryostat illuminated with a λ = 940 nm laser diode. Top - System detection efficiency with bias current, bottom - DCR with bias current.

SDE measurements, the timing jitter was acquired for that device. For the experimental apparatus see section 3.2.10. A λ = 1550 nm femtosecond mode-locked fibre laser and an Agilent Infinium DSO80804A 8 GHz oscilloscope were used for the timing jitter measurements illustrated in Figure 4.12. The FWHM timing jitter was extracted from the Gaussian fit to the histogram. The (FWHM) jitter of this device is 60 ps at $I/I_c = 0.85$.

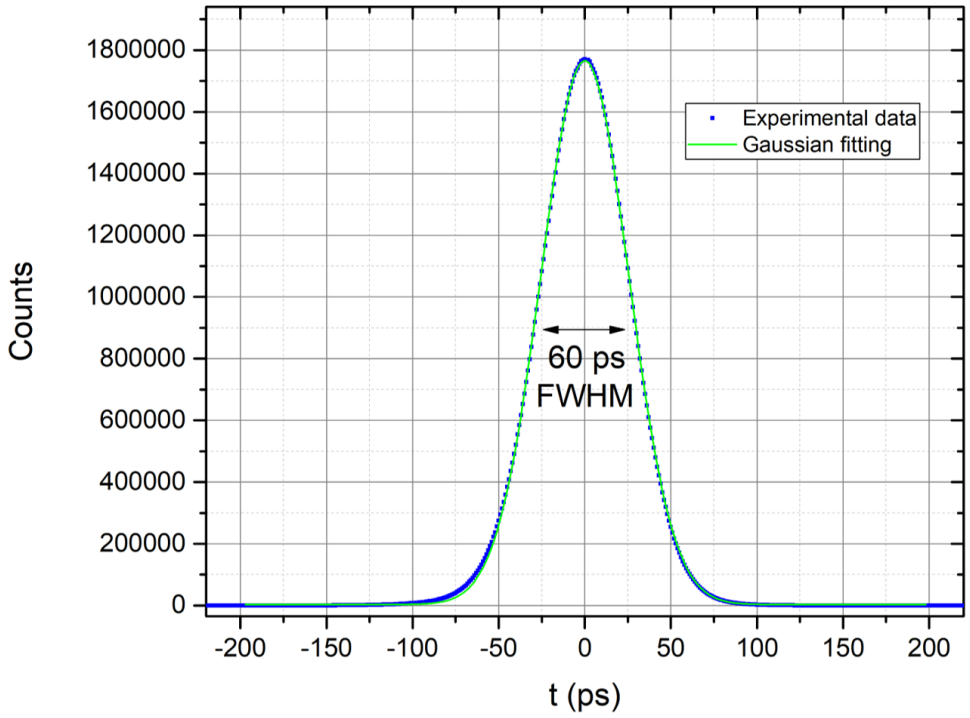

Figure 4.12: Timing jitter of a 15 x 15 µm^2 meander NbTiN SNSPD on a Ta_2O_5/SiO_2 DBR substrate measured using a $\lambda = 1550$ nm mode-locked laser diode and an Agilent Infinium DSO80804A 8 GHz oscilloscope. Measured response histogram (blue data-points) is fitted to a Gaussian distribution (green solid-line) at $I_b = 15\,\mu A$. Device measured at $T = 3.5\,K$.

Additionally, SNSPD devices from the same fabrication run were manually fibre-coupled with a 4.4 µm core diameter 780HP single-mode fibre and cooled to $T = 2.2$ K with the help of a two-stage type Gifford-McMahon (GM) cryocooler (see Section 3.2.3). In Figure 4.13(b) the SDE is illustrated as a function of I_b for the best device measured with 940 nm. Due to the meandering geometry of the nanowire devices, their efficiency depends on the polarisation of the photons that impinge upon the active area of the device [198]. The polarization of the incident light was controlled with a 2-paddle manual fibre-coupled polarizer, that was inserted between the programmable attenuators and the SNSPD, which allowed regulation of the photon-counts from the SNSPD. Figure 4.13(a) shows the maximum count-rate (CR_{max}), minimum count-rate (CR_{min}) and DCR of the SNSPD with respect to I_b. Also, we have extracted a maximum system detection efficiency (η_{SDEmax}) and a minimum system detection efficiency (η_{SDEmin}) with respect to I_b as presented in Figure 4.13(b). A low polarization dependence of 1.20 ± 0.03 was recorded while varying the I_b. This is quite low compared to literature maybe due to the optical cavity design that is pushing the light absorption efficiency to very high levels hence the optical cavity design needs to be tuned in order to eliminate the polarization dependence of SNSPDs.

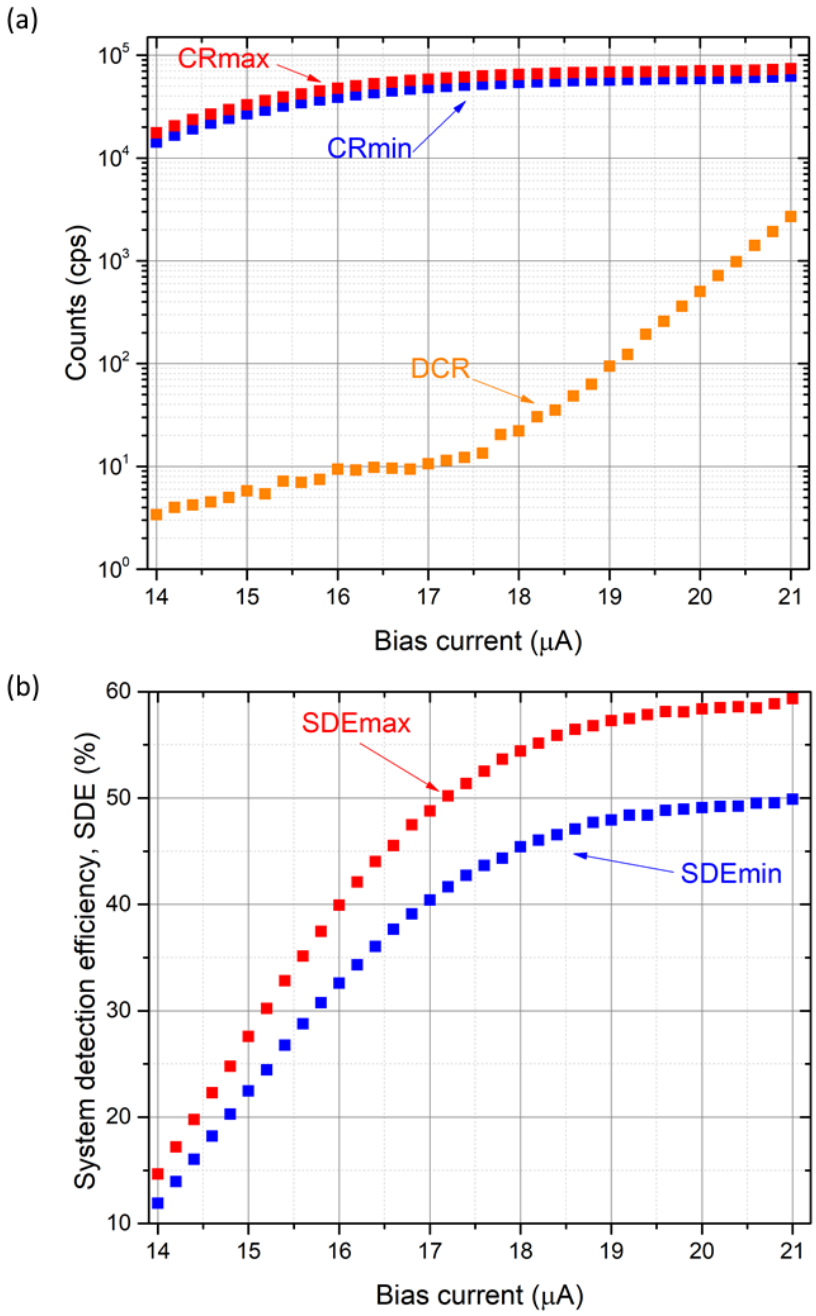

Figure 4.13: Fibre-coupled device measurements at 2.2 K for a 15 x 15 μm^2 meander NbTiN SNSPD on a Ta_2O_5/SiO_2 DBR substrate. (a) DCR and device count-rate versus I_b. (b) system detection efficiency, η_{SDE} versus bias current, I_b for maximum and minimum polarization of the light at $\lambda = 940$ nm. The SDE$_{max}$ (red data-points) and SDE$_{min}$ (blue data-points) curves were obtained by adjusting the polarization to reach the maximum and minimum count-rate of the SNSPD.

Furthermore, another SNSPD device from the same batch was manually fibre-coupled with a 9 μm core diameter SMF28 fibre and tested at 2.2 K. Figure 4.14 shows η_{SDE} and DCR versus I_b. From the experimental data is observed that multimode fibre coupling further enhances the η_{SDE}, reaching 90% for 200 Hz without polarization control.

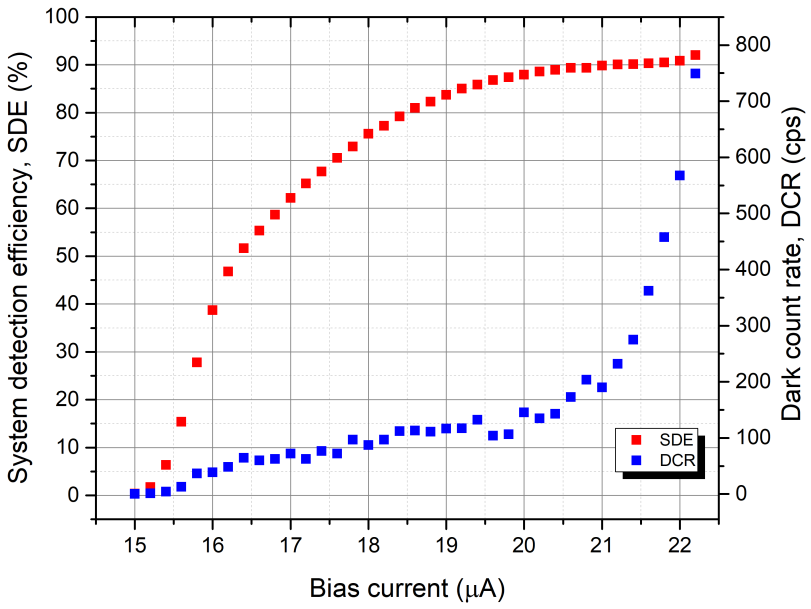

Figure 4.14: Multi-mode fibre-coupled device measurements at 2.2 K for a 15 x 15 μm^2 meander NbTiN SNSPD on a Ta_2O_5/SiO_2 DBR substrate. System detection efficiency, η_{SDE} at 940 nm wavelength (unpolarized illumination) and dark count rate (DCR) as a function of bias current I_b.

4.2 Backside coupled - Detectors fabricated on metallic-based cavity substrates

At telecommunication wavelengths and especially at 1550 nm, the state of the art SNSPD device is made of tungsten silicide (WSi) with a system detection efficiency (η_{SDE}) of 93% [199]. However, these devices are exhibiting relatively high timing jitter response in comparison to niobium based SNSPD devices. Moreover, the integration of these devices in a practical system is difficult as sub-Kelvin temperatures are required and are only attainable with expensive refrigeration equipment. At National Instruments of Information and Communications Technology (NICT) in Japan, NbTiN films were grown at high sputtering pressure (10 mTorr), in order to realise NbTiN films with smaller grain size approaching that of an amorphous material. This could improve the device yield due to the larger hotspot size generation in amorphous materials (i.e WSi and MoSi) and hence the fabrication of wider nanowires that could allow for lower probability of constrictions. Moreover, due to the higher current density present in NbTiN, their timing response (timing jitter) properties are much faster in contrast to amorphous materials. Therefore, it should be possible to realise an SNSPD device based on a NbTiN thin film with an amorphous nature [123]. In order to optimize the thin film growth, NbTiN bulk films were grown on Si substrates for 100 seconds at 10 mTorr with an argon (Ar) flow of 100 sccm

and the only variable was nitrogen flow that was varied from 20 to 35 sccm in steps of 2.5 sccm. After the film growth, photoresist AZ5206 was spun on the sample at 4000 rpm for 1 minute and then baked on a hotplate at 105 °C for 1 minute. Subsequently, the test pattern illustrated on Figure 4.15 was exposed on the sample via an MJB4 photolithography tool from Suss Microtech [200]. The pattern was then developed with AZ-300MIF developer at RT for 1 minute followed by 1 minute rinse in water and dried with a nitrogen (N_2) gun. A Reactive Ion Etching (RIE) tool with the use of CF_4 gas, is used to etch through the unprotected NbTiN layer to form the superconducting nanowires. The wire thickness was confirmed by measurements with Dektak profilometer.

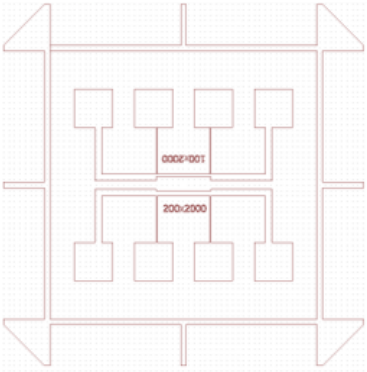

Figure 4.15: Test pattern for four-point wire measurements.

The samples were then immersed into liquid helium with base temperature of 4.2 K and their residual resistivity ratio RRR, resistivity ρ_{20K} measured at 20 K and superconducting transition temperature (T_c), were measured using a four-point wire resistance measurement (Table 4.3). The ρ_{20K} and RRR are varied with the mole fraction of N_2 at a total pressure of 10 mTorr as illustrated in Figure 4.16(a). The ρ_{20K} and RRR vary in the range of 676.8 to 780 µΩ cm and from 0.83 to 0.81 respectively. Also, in Figure 4.16(b) the T_c is varied with the mole fraction of N_2. The T_c varies in the range of 12.8 to 14.4 K. When the mole fraction of N_2 was 25%, as presented in Figure 4.16(b), the sputtered NbTiN films had their optimum T_c of 14.4 K. Moreover, at the same mole fraction the ρ_{20K} is 737.5 µΩ cm and RRR is 0.787 as illustrated in Figure 4.16(a).

10 mTorr NbTiN bulk film optimisation							
Deposition time (s)	**N_2 in Ar+N_2(%)**	**Thickness (nm)**	**R_{300K} (Ω)**	**R_{20K} (Ω)**	**T_c (K)**	**RRR**	**ρ (μΩ cm)**
100	20	141	794	960	13.5	0.83	676.8
100	22.5	121	913	1120	13.5	0.81	677.6
100	25	125	929	1180	14.4	0.79	737.5
100	27.5	118	1017	1280	14.2	0.79	755.2
100	30	122	1002	1280	13	0.78	780.8
100	32.5	115	948	1205	12.8	0.79	692.8
100	35	120	1053	1300	13	0.81	780

Table 4.3: NbTiN bulk film optimisation grown at 10 mTorr for potential use in SNSPD fabrication.

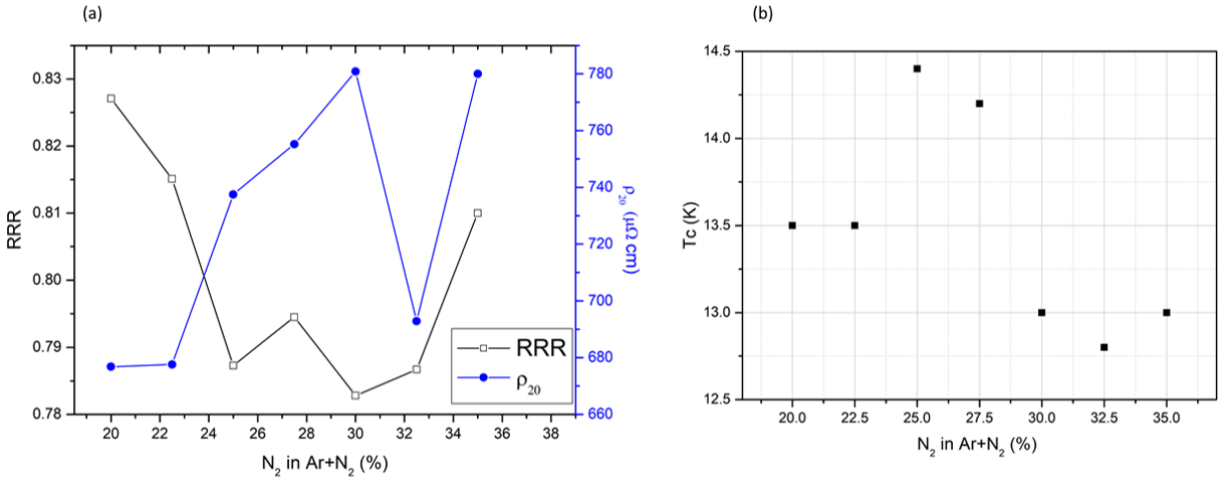

Figure 4.16: (a) Resistivity ρ_{20K} and residual resistivity ratio (RRR) as a function of the mole fraction of N_2 at a total pressure of 10 mTorr. (b) Critical temperature (T_c) as a function of the mole fraction of N_2 at a total pressure of 10 mTorr. The maximum T_c is reached for the N_2 mole fraction of 25 %.

After the optimal point of the mole fraction of N_2 was found, the film thickness was varied from ≈ 140 nm (bulk) to ≈ 5.6 nm (thin) by adjusting the deposition time from 100 seconds to 2 seconds and RRR, ρ_{20K} and T_c were recorded (Table 4.4). Figure 4.17 presents the critical temperature (T_c) and ρ_{20K} as a function of the film thickness at a constant concentration of N_2 + A_r for a total pressure of 10 mTorr. The thickness of deposited films thicker than 10 nm was directly measured by Dektak. However, the thickness of films less than 10 nm thick was estimated based on the deposition time and rate. From the recorded data is observed that T_c dramatically decreases and the ρ_{20K} suddenly increases when the thickness is altered from bulk to thin films [127]].

10 mTorr NbTiN thin film optimisation									
Deposition time (s)	**N_2 in A_r+N_2(%)**	**Thickness (nm)**	**Width (µm)**	**Length (µm)**	**R_{300K} (Ω)**	**R_{20K} (Ω)**	**T_c (K)**	**RRR**	**ρ (µΩ cm)**
100	25	125	100	2000	929	1180	14.4	0.787	737.5
50	25	72.8	100	2000	1540	1910	13.6	0.806	695.24
20	25	30.8	100	2000	2715	3300	11.2	0.822	508.2
10	25	16.8	100	2000	4098	4900	11	0.836	411.6
5	25	9.8	100	2000	6340	7450	9	0.851	365.5
4	25	8.4	100	2000	7300	8500	8.8	0.858	357
3	25	7	100	2000	8711	10290	7.8	0.846	360.15
2	25	5.6	100	2000	11015	13450	6.7	0.818	376.6

Table 4.4: NbTiN bulk film optimisation grown at 10 mTorr for potential use in SNSPD fabrication.

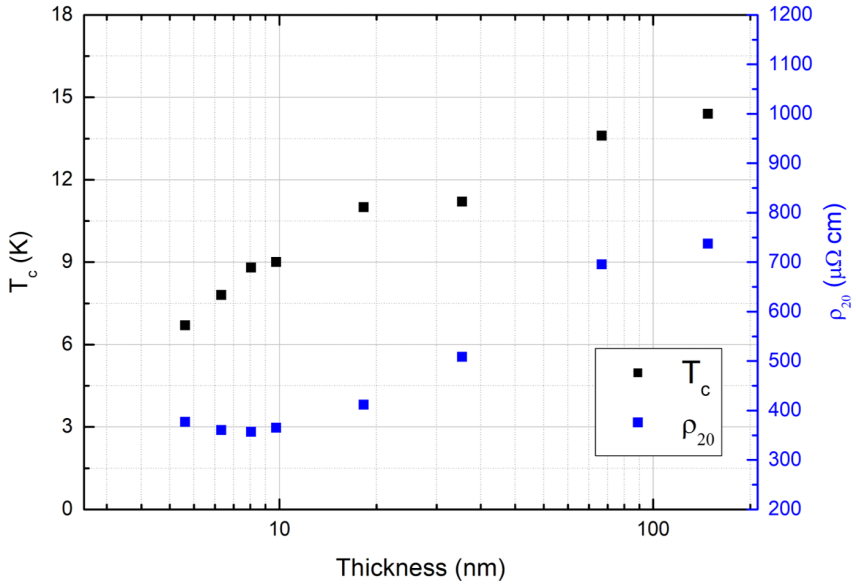

Figure 4.17: Sputtered NbTiN films on Si substrates at NICT Japan. Critical temperature (T_c) and resistivity ρ_{20K} as a function of the film thickness at a constant concentration of N_2 + A_r for a total pressure of 10 mTorr.

For the devices described in this section, the optical cavity structure was integrated on top of the nanowires for rear illumination through the substrate. Two metallic mirror cavities were designed with peak absorption at 1550 nm and 2330 nm respectively. For the 1550 nm devices, NbTiN thin films sputtered at both 10 mTorr and 2 mTorr total pressure were used.

4.2.1 Metallic mirror cavity design for 1550 nm

The metallic mirrors are typically grown through a high vacuum metal evaporation method [201]. For this experiment, the cavity design was identical to the one used by National Instruments of Information and Communications Technology (NICT), in which NbTiN thin films are housed in an optical cavity atop a Si substrate for backside coupling operation [202].

The optimized design for 1550 nm operation is illustrated in Figure 4.18(a). Also, the simulated absorption probability of the cavity for wavelengths ranging from 1200 nm - 2200 nm is shown in Figure 4.18(b). The obtained simulation results indicate an enhancement on the absorption probability of the nanowires by 94% at its centre wavelength of 1550 nm with the inclusion of the metallic mirror cavity design. The simulation model looks at the absorption spectrum of a 7.5 nm NbTiN thin film and does not take into account any reflections at bottom of the interface.

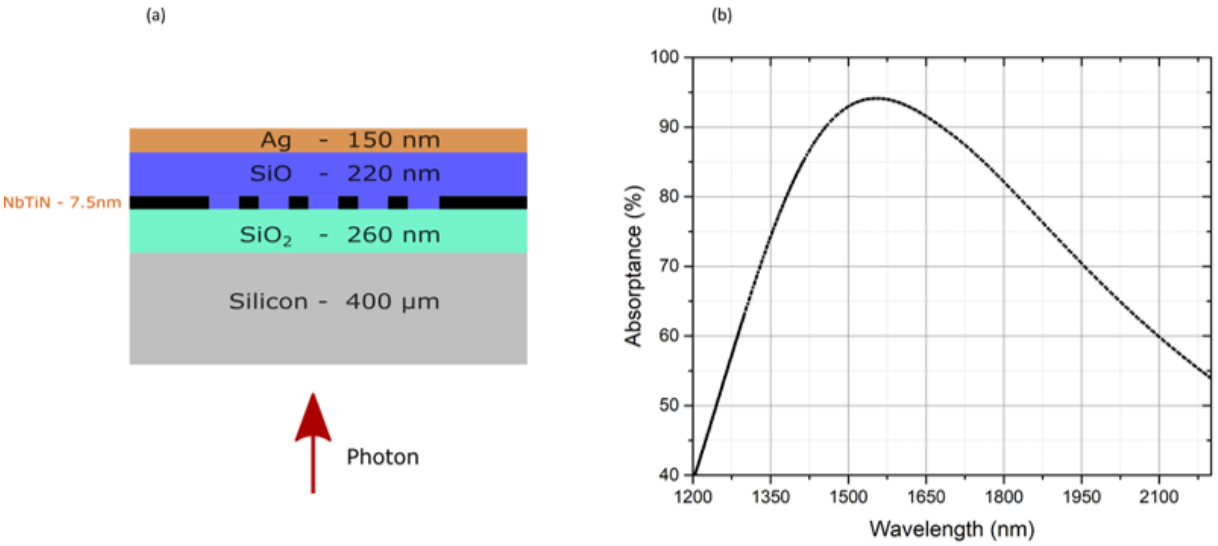

Figure 4.18: 1550 nm metallic mirror cavity design. (a) schematic of SNSPD on metallic mirror cavity (not to scale), (b) simulated absorption spectrum of cavity with a 7.5 nm NbTiN thin film for a wavelength range from 1200 nm - 2200 nm. The refractive index (n) and extinction coefficient (k) data used for NbTiN are listed in Appendix C .

4.2.2 Device fabrication

The NbTiN thin films that were used for this work were deposited by DC reactive sputtering at room temperature (described in Section 3.1.1) in the National Institute of Information and Communication Technology (NICT) in Japan. The film thickness was controlled by the deposition rate and deposition time [120]. As mentioned in Section 4.2, NbTiN thin films where deposited at two different sputtering conditions (Table 4.5).

NbTiN sputtering conditions					
Wafer ID:	**Deposition time (s)**	**RF clean time (s)**	**Pressure (mTorr)**	**Ar : N_2 ratio**	**Thickness (nm)**
1	2	60	2	100:33	7.5
2	3	60	10	100:25	7

Table 4.5: NbTiN sputtering conditions for a total pressure of both 2 mTorr and 10 mTorr.

The low and high pressure NbTiN thin films were grown on top of 2" thermally oxidised

Si wafers. On top of the NbTiN thin films a metallic mirror cavity was grown that was optimized for maximum absorption at 1550 nm (Figure 4.18). The devices were then patterned and fabricated in NICT (described in Section 3.1.9). Seven different nanowire designs were used for the fabrication of the 1550 nm metallic mirror cavity SNSPD devices, as summarised in Table 4.6. Device ID one to four (1-4) out of total seven devices employ a parallel configuration between subsequent nanowires (described in Section 2.8.8. These devices are called superconducting nanowire avalanche photodetectors and due to the reduction in their nanowire length, the kinetic inductance is minimised. This results in an enhancement of the detector's maximum count rate.

1550 nm design layout			
Device ID:	**Width (nm)**	**Gap (nm)**	**Device structure**
1	100	100	2SNAP (15 x 15 μm^2)
2	80	80	2SNAP (15 x 15 μm^2)
3	60	80	2SNAP (15 x 15 μm^2)
4	40	60	2SNAP (15 x 15 μm^2)
5	100	100	Single wire (15 x 15 μm^2)
6	80	80	Single wire (15 x 15 μm^2)
7	60	80	Single wire (15 x 15 μm^2)

Table 4.6: SNSPD design layout fabricated on 1550 nm metallic mirror cavity. 2SNAP denotes a configuration of two nanowires connected in parallel.

4.2.3 Device characterisation

The devices were mounted, wire-bonded and fibre-coupled. Then low temperature electrical and optical characterisation of the devices took place in a cryostat similar to Zephynator (described in Section 3.2.3) with a base temperature of 2.2 K. The NbTiN SNSPD devices were characterized in terms of their basic superconducting properties that include: critical temperature T_c and current voltage characteristics (I-V curve) as summarized in the following Table 4.7.

Device ID:	Wafer ID:	Nanowire dimensions			Device structure	T_c (K)	I_c(μA)
		Depth (nm)	Width (nm)	Gap (nm)			
F06	1	7.5	100	100	Single wire	7.71	20.12
G06	1	7.5	80	80	Single wire	7.85	16.69
H06	1	7.6	60	80	Single wire	7.86	12.52
D10	2	7	100	100	Single wire	7.15	13.59
E10	2	7	80	80	Single wire	7.03	9.91
C09	2	7	60	80	Single wire	6.93	7.43
C06	1	7.5	80	80	2SNAP	7.69	40.78
D06	1	7.5	60	80	2SNAP	7.79	28.7
E06	1	7.5	40	60	2SNAP	7.74	20.5
B01	2	7	80	80	2SNAP	7.03	19.58
C01	2	7	60	80	2SNAP	6.67	5.63
D08	2	7	40	60	2SNAP	6.89	11.53

Table 4.7: 1550 nm SNSPD characterisation for the SNSPDs fabricated with low and high pressure NbTiN thin films.

Subsequently, for the same devices listed in Table 4.7 the bias current dependencies of the SDE has been examined as illustrated in Figure 4.19 .

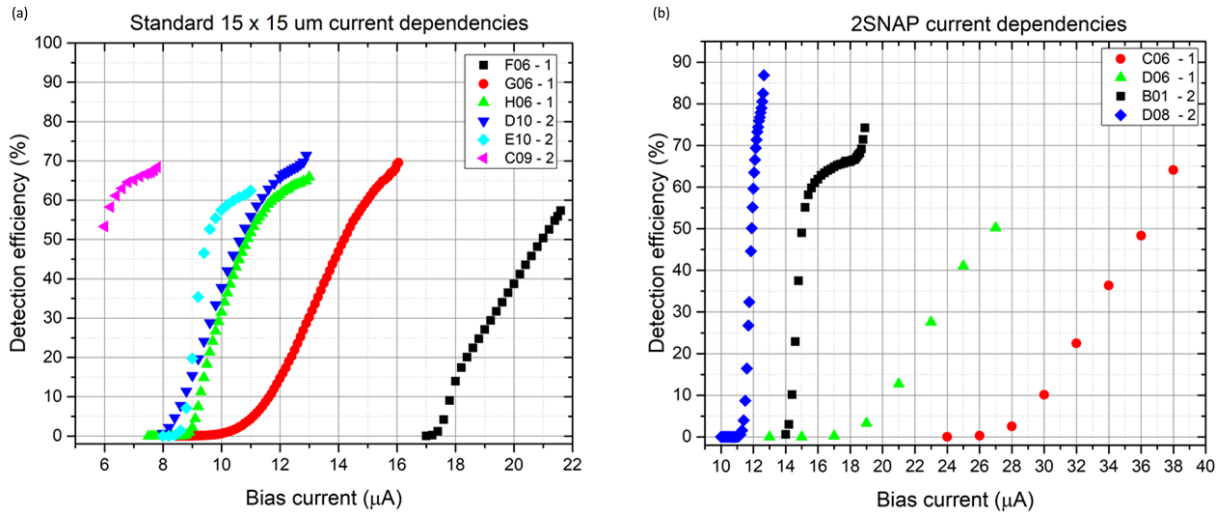

Figure 4.19: Bias current dependencies of SDE. (a) single nanowire configuration, (b) 2 parallel nanowire (2SNAP) configuration

4.2.4 Metallic mirror cavity design for 2.33 μm

SNSPDs offer excellent single photon detection over a wide spectrum of photon energies from visible to mid-infrared. Since 2013 [9] SNSPDs have been clearly demonstrated to combine record speed and single photon detection efficiency; consequently, are promising candidates for applications that include remote sensing and greenhouse gas monitoring [95]. Potential applications of photon counting in the mid-infrared region such as remote sensing

of greenhouse gases in the atmosphere [203] is an area of high interest. Especially, the spectrum around 2 µm can be used for detection of water (H_2O) and carbon monoxide (CO) absorption lines in an exoplanet atmosphere [204]. Moreover, the region around 2.3 µm can be used to probe water (H_2O), carbon monoxide (CO) and methane (CH_4) gases [205].

Similar to Section 4.2.1, NbTiN thin films are housed in a double cavity on top of a Si substrate for backside coupling operation as presented in Figure 4.20(a). The metallic cavity was designed for peak absorption at 2.33 µm using Essential Macleod software from Thin film centre inc. for determining the design parameters for the optical cavity while the NbTiN thin film was fixed at 6 nm as shown in Figure 4.20(b). Then using Comsol multiphysics software, the absorption of a single nanowire (40 nm width, 60 nm gap and 6 nm thick) was simulated over 1.4 - 3.4 µm wavelength range as illustrated in Figure 4.20(c). The obtained simulated results indicate an enhancement on the absorption probability of the thin film by 99.85% and on a single nanowire by 80% with the inclusion of the metallic mirror cavity design.

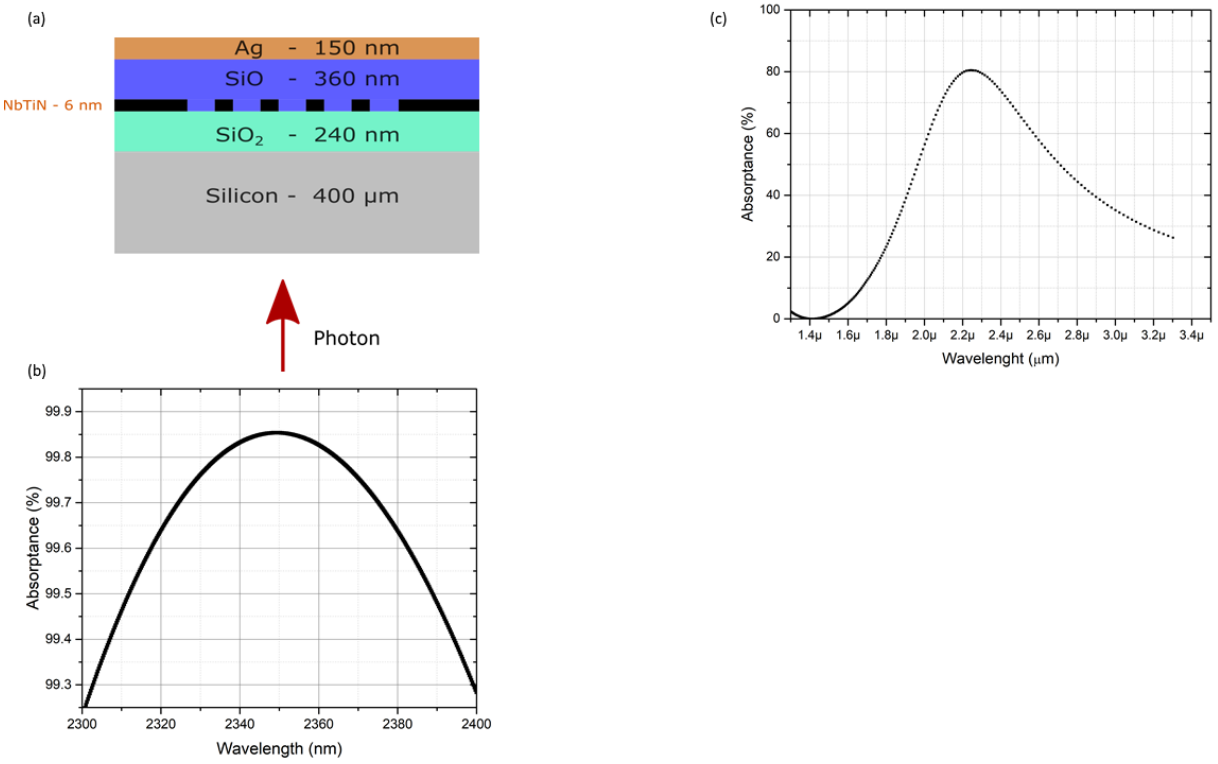

Figure 4.20: 2333 nm metallic mirror cavity design. (a) schematic of SNSPD on metallic mirror cavity (not to scale), (b) simulated absorption spectrum of optical cavity with a 6 nm NbTiN thin film for a wavelength range from 2300 nm to 2400 nm and (c) simulated absorption spectrum of a 6 nm thick, 40 nm wide nanowire for a wavelength range from 1400 nm to 3400 nm. For both simulations TE polarisation was used.

From these simulation models it was observed that when only a single nanowire was used the absorptance rate dropped from 99.87 % to approximately 80 % that is attributed

to the much smaller active area of the nanowire.

4.2.5 Device fabrication

The NbTiN thin films that were used for this work were deposited by DC reactive sputtering at room temperature (described in Section 3.1.1) in the National Institute of Information and Communication Technology (NICT) in Japan. To extend the sensitivity of the detectors in the mid-infrared regime, their nanowire width must be drastically reduced [199]. Therefore, 6 nm NbTiN thin films were grown on top of a 2" diameter thermally oxidised Si wafer. The devices were then patterned and fabricated in NICT (described in Section 3.1.9). On top of the NbTiN nanowires a metallic mirror cavity was grown that was optimized for maximum absorption at 2333 nm (Figure 4.20). Eight different nanowire designs were used for the fabrication of the 2333 nm metallic mirror cavity SNSPD devices, as summarised in Table 4.8. The four out of the eight design configurations employ superconducting nanowire avalanche photodetectors (SNAP). This configuration should compensate for the signal to noise ratio (SNR) of the ultra narrow nanowires.

2333 nm design layout			
Device ID:	**Width (nm)**	**Gap (nm)**	**Device structure**
1	40	60	2SNAP (15 x 15 μm^2)
2	40	60	2SNAP (35 x 35 μm^2)
3	60	80	2SNAP (15 x 15 μm^2)
4	60	80	2SNAP (35 x 35 μm^2)
5	40	60	Single wire (15 x 15 μm^2)
6	40	60	Single wire (35 x 35 μm^2)
7	60	80	Single wire (15 x 15 μm^2)
8	60	80	Single wire (35 x 35 μm^2)

Table 4.8: SNSPD design layout fabricated on 2333 nm metallic mirror cavity. 2SNAP denotes a configuration of two nanowires connected in parallel.

4.2.6 Device characterisation

The devices were mounted, wire-bonded and fibre-coupled. Then low temperature electrical and optical characterisation of the devices took place in a cryostat similar to Zephynator (described in Section 3.2.3) with a base temperature of 2.2 K. The NbTiN SNSPD devices were characterized in terms of their basic superconducting properties that include: critical temperature T_c and current voltage characteristics (I-V curve) as summarized in the following Table 4.9.

After initial screening in the 2.2 K GM cryocooler, the device with best electrical performance was benchmarked in terms of dark count (DC) variation with respect to bias current (I_b) in three different configurations: a) no fibre connection , b) device fibre-coupled with an SM-2000 fibre and fibre blocked at room temperature (fibre feed-through)

Basic electrical properties		
Device ID:	**T_c** (K)	**I_c** (µA)
2333 nm batch	4 - 6.6	2.5 - 7

Table 4.9: Electrical properties of SNSPDs fabricated on 2333 nm metallic cavity substrates.

and c) device fibre-coupled with an SM-2000 fibre and fibre taped on the 4 K stage of the cryostat as illustrated in Figure 4.21.

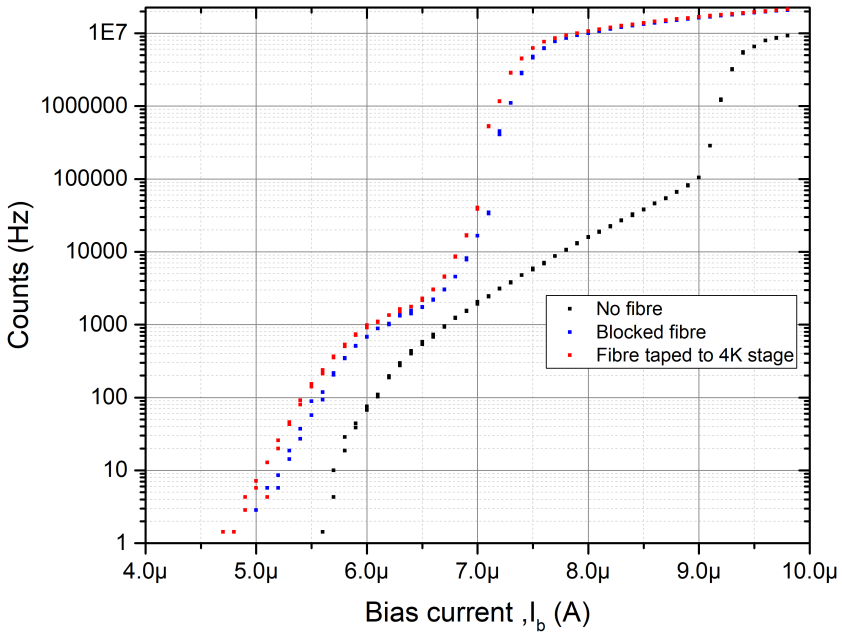

Figure 4.21: Dark count (DC) dependance with bias current (I_b) for three configurations a) no fibre connection, b) device fibre-coupled with SM-2000 fibre but fibre-blocked at room temperature and c) device fibre-coupled with SM-2000 but fibre was taped on the 4 K stage of the cryostat. The experiments were performed with a 15 x 15 µm^2 SNAP NbTiN SNSPD in a 2.2 K Gifford-McMahon (GM) cryoocoler.

From this experiment it was observed that the device DCR jumps to $\approx 10^7$ dark counts when the device I_c is approached and the counter used for this measurement is saturating. The excessively high DCR might be attributed to the noise photons from both stray light penetrated into the fibre and from the blackbody radiation of the fibre itself. In order to suppress this effect, the SNSPD device was cooled down in the ^{3}He cryocooler with a base temperature of 350 mK and the dependence of both the I_c and dark counts (DC) with temperature were recorded and compared to data acquired at 2.2 K. The I_c improves from 8 µA (measured at 2.2 K) to 12 µA (measured at 350 mk) as shown in Figure 4.22(a). The dark counts are more dominant at 2.2 K while at 350 mK they are suppressed, allowing

the device to operate closer to its I_c as shown in Figure 4.22(b).

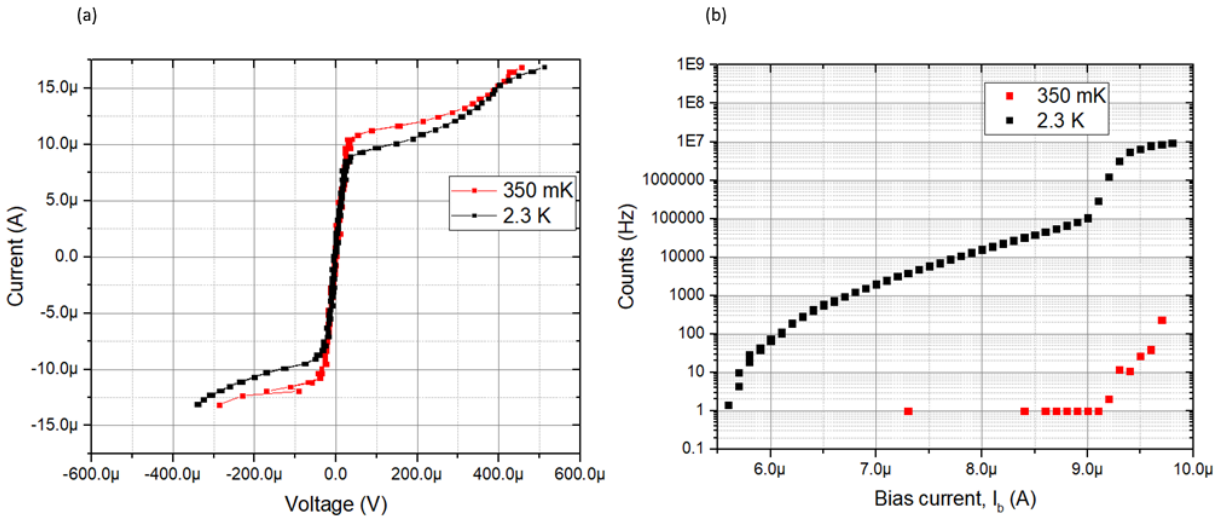

Figure 4.22: (a)Critical current (I_c) dependance with temperature with a 50 Ω shunt resistor, (b) dark count (DC) dependance with temperature. The experiments were performed with a 15 x 15 µm^2 SNAP NbTiN SNSPD in a 2.2 K Gifford-McMahon (GM) cryoocoler and in a 350 mK pulse tube (PT) cryocooler.

Furthermore, the timing jitter of this device was recorded at an applied bias of 9.6 µA (0.80 I/I_c) as presented in Figure 4.23. This device at $\lambda = 2333$ nm had a (FWHM) jitter of 84 ps .

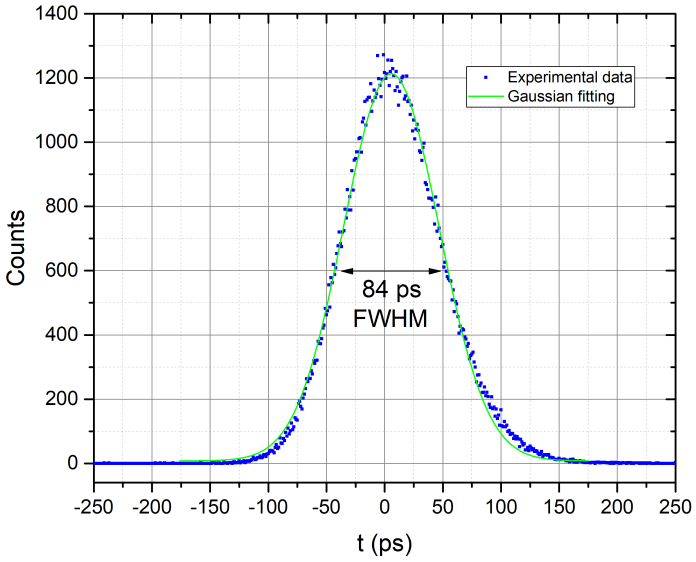

Figure 4.23: Timing jitter of a 15 x 15 µm^2 NbTiN SNAP SNSPD device measured using a $\lambda = 2333$ nm mode-locked laser and a Picoquant time-correlated single photon counting (TSCPC) card. Measured response histogram (blue data-points) is fitted to a Gaussian distribution (green solid-line) at $I_b = 9.6$ µA. Device measured at $T = 350$ mK.

Subsequently, the device was fibre-coupled and mounted on the 2.2 K cryostat. With the use of the experimental apparatus described in Section 3.2.12, the light was attenuated down to single photon regime (0.05 photons per second) with the use of a stack of ND filters with a total of 7.3 OD (equivalent to 73dB) attenuation (Figure 4.24(a)) and by monitoring the counts and the dark counts of the device (Figure 4.24(b)), its system detection efficiency(η_{SDE}) was calculated as 0.05 %.

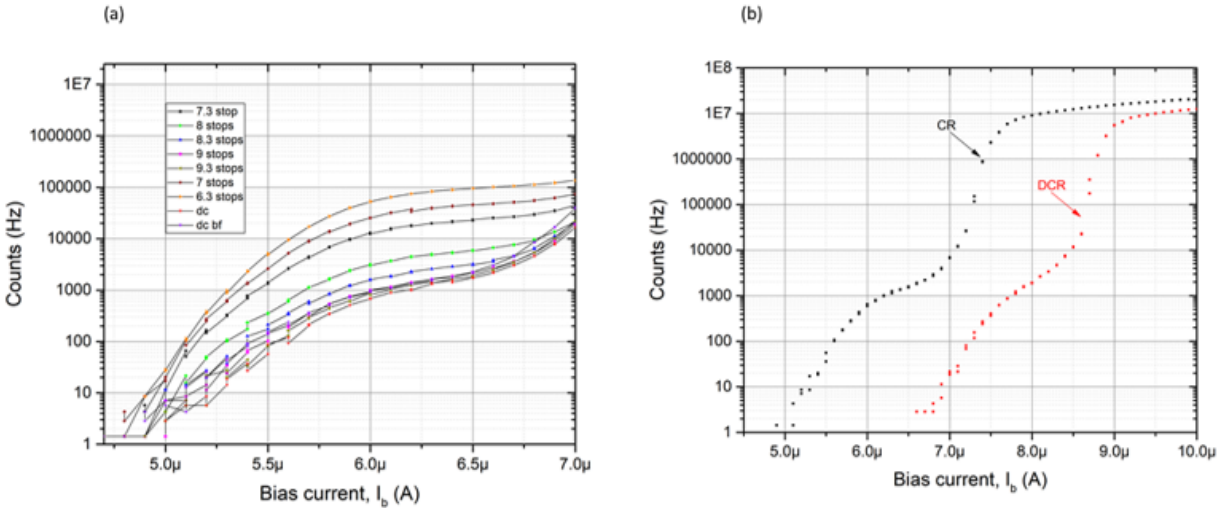

Figure 4.24: (a) the variation of the counts is observed with respect to the I_b of the SNSPD while the level of attenuation is increased at $\lambda = 2333\,\text{nm}$ and (b) after the attenuation is set in single photon regime (0.05 photons per second), the counts and dark counts of the device are monitored and its η_{SDE} is extracted. Device measured at $T = 2.2\,\text{K}$.

4.3 Conclusions

Two different types of cavity integrated NbTIN SNSPDs were fabricated, fibre-coupled and low-temperature characterised. The first is front side cavity integrated SNSPD devices for near-infrared applications that take advantage of distributed Bragg reflectors (DBR) as their cavity material. Electrical and optical characterisation in our advanced nano-optical photoresponse mapping setup at $T = 3.5$ K showed an overall $\eta_{SDE} = 55\%$ at $\lambda = 940$ nm, dark count rate (DCR) = 100 Hz timing jitter of 60 ps at $\text{I/I}_c = 0.85$. Additionally, devices from the same fabrication run were manually fibre-coupled and optically characterized at $T = 2.2$ K. One device was coupled with single mode fibre (4.4 µm core diameter), showed an overall $\eta_{SDE} = 57.5\%$ at $\lambda = 940$ nm, dark count rate (DCR) = 100 Hz and a low polarization dependence of 1.20 ± 0.03. A second device was coupled with multimode fibre (9 µm core diameter) showed a maximum $\eta_{SDE} = 90\%$ at $\lambda = 940$ nm, dark count rate (DCR) = 200 Hz. Our TEM analysis shows that the DBR roughness increases with the number of bilayer repeats, and the rms roughness of the top layer of our DBR stack (6.4 nm)

approaches the thickness of the NbTiN superconducting thin film (7.5 nm). Therefore, reducing the number of DBR repeats may achieve the optimal trade-off between optical absorption and SNSPD uniformity.

While the second is back side cavity integrated SNSPD devices designed for infrared and mid-infrared applications that take advantage of metallic mirrors as their cavity material. Two metallic mirror cavities were designed with peak absorption at 1550 nm and 2330 nm respectively. For the 1550 nm devices, a peak η_{SDE} value of $\approx 84.5\%$ at $\lambda = 1550$ nm, (DCR) = 23.5 Hz at $T = 2.2$ K on a two-parallel nanowire (2SNAP) configuration was achieved. Additionally, for the 2330 nm devices a peak η_{SDE} value of $\approx 0.05\%$ was recorded at $\lambda = 2330$ nm for $T = 2.2$ K. These SNSPD devices were cooled down in a ^{3}He cryocooler with $T = 350$ mK and the dependence of both the I_c and dark counts (DC) with temperature recorded and compared to data acquired at 2.2 K. From this experiment it was observed that at high count rates ($\approx 10^7$) the counter is saturating and the SNSPD device is suffering from a huge amount of DC mainly due to blackbody radiation at 2.2 K. Furthermore, the timing jitter of this device was measured at 350 mK indicating a full width half maximum (FWHM) of 84 ps, which at the time of writing this report is the first jitter measurement at 2330 nm recorded. In order to suppress the huge amount of dark counts created by blackbody radiation at 2.2 K, these devices should be operated at lower temperatures ($T = 350$ mK) as described in Section 3.2.2 and coupled with a cold optical filter that should completely block the blackbody radiation except the signal passband [206].

Characterised devices are summarised in Tables 4.10,4.11 and 4.12.

940 nm SNSPD devices								
A/A	Device No	Line width (nm)	Gap width (nm)	Device Structure	R (Ohm)	Tc (K)	Ic (uA)	DE (%)
1	S29789-1a	95	95	Standard 15 x 15 um	3 M	-	-	-
2	S29789-1b	95	95	Standard 15 x 15 um	2.96 M	-	-	-
3	S29789-1c	95	95	Standard 15 x 15 um	2.97 M	-	-	-
4	S29789-1d	95	95	Standard 15 x 15 um	4.3 K	-	-	-
5	S29789-2a	95	95	Standard 15 x 15 um	3 M	8	22	38
6	S29789-2b	95	95	Standard 15 x 15 um	2.97 M	7.95	18	55
7	S29789-2c	95	95	Standard 15 x 15 um	3 M	7.91	17.5	-
8	S29789-2d	95	95	Standard 15 x 15 um	4.3 K	7.9	-	-
9	S29789-3a	95	95	Standard 15 x 15 um	2.87 M	-	-	-
10	S29789-3b	95	95	Standard 15 x 15 um	2.99 M	-	-	-
11	S29789-3c	95	95	Standard 15 x 15 um	Open	-	-	-
12	S29789-3d	95	95	Standard 15 x 15 um	4.37K	-	-	-
13	S29789-4a	95	95	Standard 15 x 15 um	2.95 M	-	-	-
14	S29789-4b	95	95	Standard 15 x 15 um	2.89 M	-	-	-
15	S29789-4c	95	95	Standard 15 x 15 um	2.73 M	-	-	-
16	S29789-4d	95	95	Standard 15 x 15 um	4.3 K	-	-	-

Table 4.10: 940 nm SNSPDs performance statistics.

1550 nm SNSPD devices								
A/A	Wafer ID	Device No	Line width (nm)	Gap width (nm)	Device Structure	Tc (K)	Ic (uA)	DE (%)
1	1	F06	100	100	Standard 15 x 15 um	7.71	20.12	54.8(53dc)
2	1	G06	80	80	Standard 15 x 15 um	7.85	16.69	65.99(51dc)
3	1	H06	60	60	Standard 15 x 15 um	7.86	12.52	76.6 (50dc)
4	2	D10	100	100	Standard 15 x 15 um	7.15	13.59	67.34(50dc)
5	2	E10	80	80	Standard 15 x 15 um	7.03	9.91	61.33(39dc)
6	2	C09	60	80	Standard 15 x 15 um	6.93	7.43	67.6(46dc)
7	2	E09	80	80	SC-2SNAP	-	18.29	74.6(41dc)
8	2	F09	60	80	SC-2SNAP	-	10.85	84.5(23.5dc)
9	2	G09	40	60	SC-2SNAP	-	3.59	Not possible
10	2	B1	80	80	SC-2SNAP	7.03	19.58	66.19(55dc)
11	2	C1	60	80	SC-2SNAP	6.67	5.63	Not possible
12	2	D1	40	60	SC-2SNAP	-	4.5	Not possible
13	2	G5	80	80	SC-2SNAP	6.93	22.46	53.22(50dc)
14	2	D6	60	80	SC-2SNAP	6.84	16.4	69.67(36dc)
15	2	D8	40	60	SC-2SNAP	6.89	11.53	44.6(42dc)
16	1	C6	80	80	SC-2SNAP	7.69	40.78	64(55dc)
17	1	D6	60	80	SC-2SNAP	7.79	28.7	50.25(23dc)
18	1	E6	40	60	SC-2SNAP	7.74	20.5	not possible

Table 4.11: 1550 nm SNSPDs performance statistics.

23300 nm SNSPD devices							
A/A	Device No	Line width (nm)	Gap width (nm)	Device Structure	Tc (K)	Ic (uA)	DE (%)
1	F4	40	60	SC-2SNAP (35 X 35 um)	6.6	6.75	-
1	F5	60	80	SC-2SNAP (15 X 15 um)	5	-	-
1	F6	60	80	SC-2SNAP (15 X 15 um)	5.5	-	-
1	F7	40	60	Standard 15 x 15 um	4	-	-
1	F8	40	60	Standard 35 x 35 um	5.2	-	-
1	F9	60	80	Standard 15 x 15 um	6.1	-	-
1	F10	60	80	Standard 35 x 35 um	6	-	-

Table 4.12: 2330 nm SNSPDs performance statistics.

Chapter 5

Superconducting detectors integrated with Si waveguide circuits

This chapter details progress on combining silicon photonic circuits with superconducting nanowire single-photon detectors (SNSPDs). Each individual component has been simulated and a fabrication process was developed by the author at the University of Glasgow to integrate MoSi and NbTiN SNSPDs with single mode waveguides which is detailed in Section 3.1.10.

5.1 Silicon quantum photonic integrated circuits

Telecommunication industry offers the perfect platform for next generation waveguide quantum optic circuits and as a result, a wide range of complex device components such as transmitters, routers and detectors for high-speed optical signals were developed for data communication systems in materials such as silicon, silica and GaAs [144]. In integrated quantum photonic platforms, quantum logic gates operation is controlled via photonic integrated circuits and that offers a promising approach towards miniaturised linear optical quantum circuits. Silicon has emerged as the ideal platform for integrated quantum photonics because of its material properties that allow for tight confinement of light and as a result higher density of circuits with smaller footprint. In infrared optical communications, at approximately 1.5 µm, the signal loss over long distances in optical fibres is minimum. Similarly, low loss integrated silicon-on-silica photonic circuits make this wavelength band an excellent choice for emerging quantum information processing applications. Thanks to the high refractive index contrast between the silicon waveguide core and the silicon oxide cladding in silicon-on-insulator (SOI) substrates, high-density complex circuits can be fabricated on a small footprint.

5.2 Integration of detectors with waveguides

Since the first SNSPD there have been several different varieties, each with their own improvements in terms of SPD parameters. The most promising of these has been the integration of superconducting nanowires on optical waveguides. Integration of high performance SPDs such as SNSPDs with waveguide circuit platforms is a major goal in the field of integrated quantum photonics [207]. Our group has already investigated the single-photon response of waveguide integrated MoSi superconducting nanowires [208]. However, those devices were made of simple designs just for the benchmarking of detector performance. In order to integrate optical waveguide with SPDs to complex silicon photonic circuits, new complex structures had to be designed that incorporated input/output grating couplers. For the realisation of such a device, commercially available silicon-on-insulator (SOI) substrates with a 220 nm thick Si layer atop a 2 µm thick oxide layer are used. The total substrate thickness is ≈ 730 µm. The silicon waveguides used for this experiment were designed with a cross-section of 600 x 220 nm^2 (width x height). These values are dictated by the requirement to support only transverse electric (TE) mode propagation at 1.55 µm, in which the electric field is parallel to the substrate. In this scheme a hairpin-shaped nanowire is fabricated directly on top of the optical near-field of the guided mode and as a result propagating light along the waveguide is absorbed by the nanowire. The dimensions of the nanowire detector are determined by both the material choice (MoSi and NbTiN) and the requirement of high sensitivity to single photons (with photon $E = \frac{hc}{\lambda} = 0.799$ eV). For this type of detector both amorphous (MoSi) and polycrystalline (NbTiN) thin films were used.

Figure 5.1: Silicon on insulator wafer used to create Si waveguide circuits integrated with single-photon detectors. The thin films were deposited on top by DC magnetron sputtering. MoSi thin films were co-sputtered from separate Mo and Si targets in University of Glasgow [209, 210].

To get a better understanding of how a waveguide field is being absorbed by the SNSPD nanowire, a numerical implementation of Maxwell's equations is required. This can be achieved with a Finite-Difference-Time-Domain (FDTD) software package. FDTD is a numerical analysis software capable enough to provide insight in optoelectronic systems that are very hard to manually analyse. The FDTD method solves Maxwell's equations for the electric and magnetic field in the time domain. More specifically FDTD uses finite

differences as approximations of both the spatial and temporal derivatives of Faraday and Ampère's laws as present in Maxwell's equations [211].

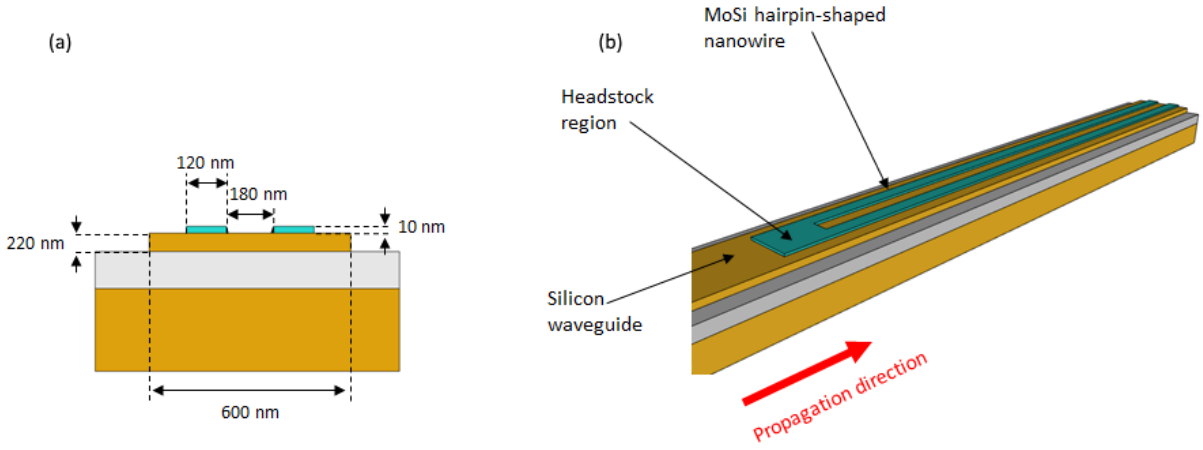

Figure 5.2: (a) cross-section of waveguide-integrated SNSPD device. MoSi thin film is shown in turquoise, Si is shown in gold and SiO_2 in silver with all dimensions labeled. (b) section of the waveguide detector illustrating the hairpin-shaped nanowire aligned parallel to the waveguide propagation axis.

5.3 Modelling of waveguide detectors

With the use of spectroscopic ellipsometry, the index of refraction (n) and extinction coefficient (k) of $Mo_{83}Si_{17}$ were acquired over the wavelength range of 270 - 2400 nm on 10 nm thick MoSi films (with 5 nm Si capping layer). The ellipsometry was performed by LOT-QuantumDesign GmbH [212] and the films were grown by Archan Banerjee at the University of Glasgow by DC magnetron sputtering. Subsequently, numerical simulations were executed for the waveguide integrated SNSPD devices with the use of finite-difference-time-domain (FDTD) commercial package from Lumerical. FDTD operates in the time domain and can simulate multiple range of frequencies at once. Nevertheless, Lumerical FDTD software is CPU intensive and requires large amounts of internal memory. Therefore, is required to balance the accuracy of each simulation with regards the computer hardware available. Before running each simulation, is important for the user to select and optimize the mesh fineness, the simulation accuracy and the symmetrical boundary conditions. With this simulation model, the power absorbed across the nanowire is monitored while its length and width are varied as illustrated in Figure 5.3. Photon absorption probability above 99% is expected for a nanowire length of $\approx 15\,\mu m$. This absorption probability can be enhanced even further by increasing the cross-sectional area of the nanowire. Nevertheless, by using thicker and wider wires the likelihood to register a count immediately upon single-photon absorption is reduced. Therefore, during the fabrication

process is crucial to pattern an SNSPD device with minimum cross-sectional deviation across a large area (10 - 20 µm). In waveguide SNSPD devices, is typical to have two parallel nanowire strips which are connected by a 180° bend.

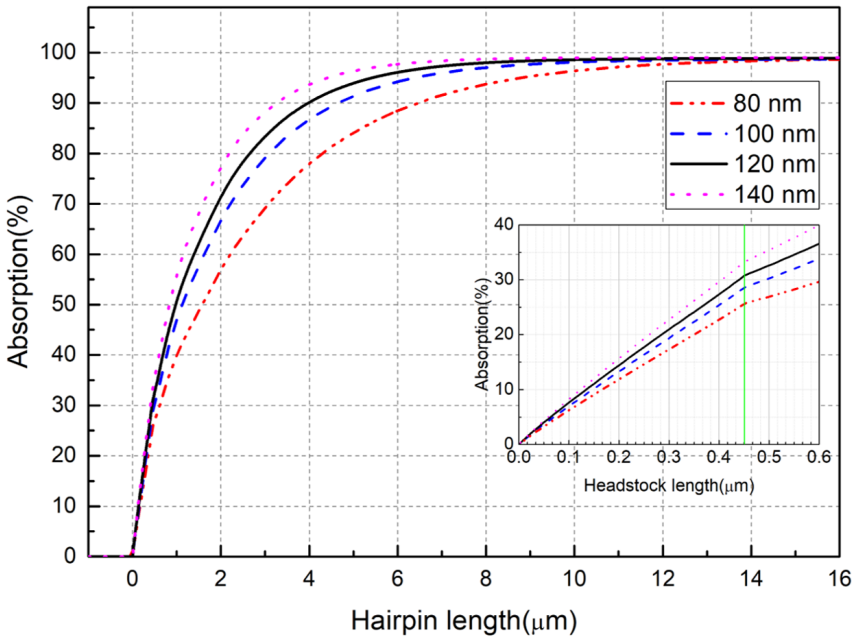

Figure 5.3: FDTD simulation of absorbed optical power as a function of detector length for various wire widths. All simulations involve 600 nm width Si waveguide, 10 nm thick MoSi (with 5 nm Si capping layer) and a TE-polarised laser source with $\lambda = 1550$ nm illumination.

5.4 Modelling grating coupler design

For the design of a grating coupler (GC) some initial conditions must be fulfilled. These include constraints in the design due to the wafer type used i.e the buried oxide thickness and the top silicon layer thickness. Also, the central wavelength and the incidence angle are predetermined by the application requirements. For this project, only shallow grating coupler designs were used (described in Section 2.9.3) and the initial design parameters used are listed in Table 5.1.

Si	SiO_2	Etch depth	λ	$\theta_{incidence}$
220 nm	2 µm	70 nm	1550 nm	9 °

Table 5.1: Initial values for grating coupler design.

With the initial values listed in Table 5.1, it was obtained a coupling loss of ≈ - 10 dB over 1.5 - 1.6 µm wavelength span. Additionally, the refractive effective index of

the grating was calculated and because of the shallow etched GC nature, two different refractive effective indices were calculated as follows: a) shallow etched region, $n_{eff1} = 2.53$ and b) un-etched region, $n_{eff2} = 2.85$. For the initial design a fill factor (FF) of 50 % was used. Then the total refractive effective index, n_{eff} can be calculated as the weighted-average of n_{eff1} and n_{eff2} indices.

With the n_{eff} known the period of the grating (Λ) can be calculated from the Bragg condition:

$$\Lambda = \frac{\lambda}{n_{eff}} - sin\theta_{incidence} \tag{5.1}$$

For an incident angle of 9 °, the grating period is calculated to be approximately $\Lambda = 630\,\text{nm}$. Given the initial conditions and the grating period analytic calculation, the initial GC design was simulated for both TE and TM polarisations of light and its efficiency versus wavelength is illustrated in Figure 5.4.

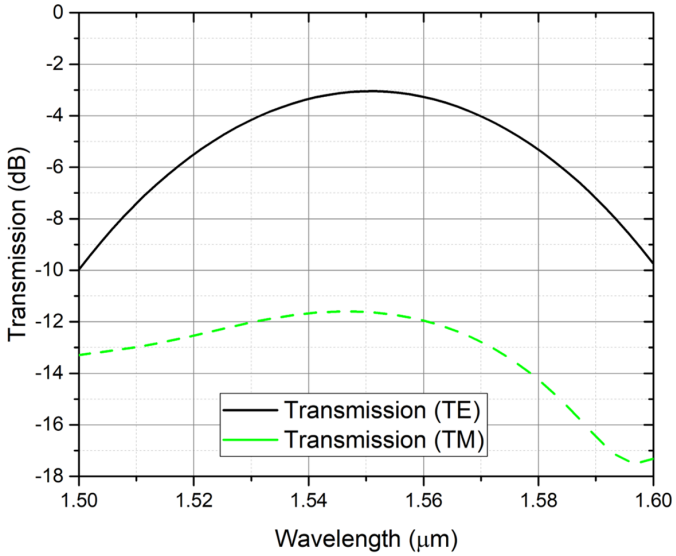

Figure 5.4: Grating coupler insertion loss (efficiency) versus wavelength for TE and TM polarized light.

Since the GC was designed for transverse electric (TE) polarization, it blocks transverse magnetic (TM) polarized light. For this design, an insertion loss of -3 dB and a central wavelength of 1550 nm. As soon as the initial design was ready, the GC design was modified by adjusting various design parameters such as the fill factor, the periodicity and the etch depth in order to reach maximum transmission. The impact of these parameters on the performance of the GC are analysed in the following sections.

Fill factor - also known as duty cycle it is related with the grating period since FF = W/Λ, (where W is the width of the grating teeth for the case of a uniform GC). Therefore, as the FF increases the n_{eff} increases.

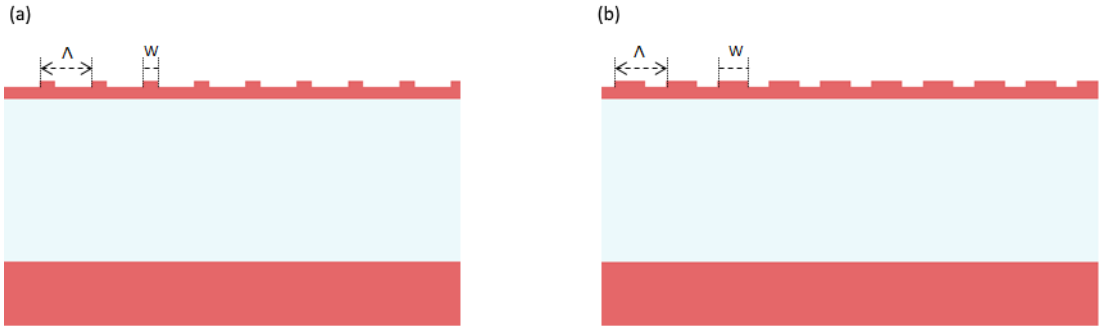

Figure 5.5: Schematic illustration of grating coupler fill factor (FF) for a) fill factor = 0.3 and b) fill factor = 0.6.

The FF was varied from 0.3 - 0.6 and it was observed that while the FF increases, the GC performance shifts towards longer wavelengths especially the central wavelength shifted from 1525 nm to 1575 nm as illustrated in Figure 5.6. For this simulation, all the parameters are constant except of the FF.

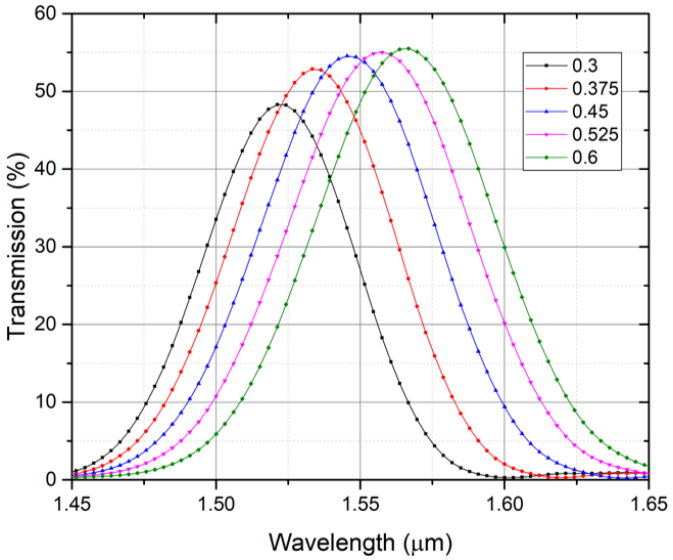

Figure 5.6: Grating coupler transmission versus wavelength for various fill factors.

Grating period - The periodicity of the grating is another parameter that affects the grating wavelength. Similar to the FF simulations, all the parameters where kept constant except the period of the grating. The grating period was varied from 620 nm - 700 nm and it was observed a shift in the central wavelength of the grating from 1525 nm - 1625 nm as illustrated in Figure 5.7. At a $\Lambda = 630$ nm the central wavelength is 1550 nm and matches the grating period value calculated with the Bragg condition.

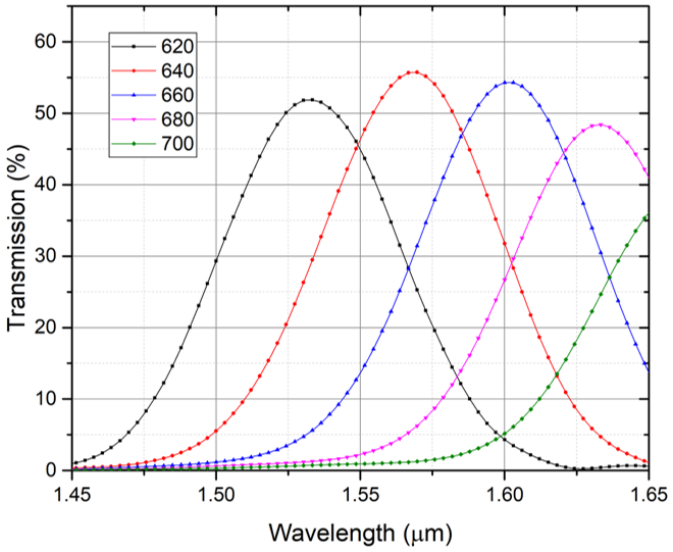

Figure 5.7: Grating coupler transmission versus wavelength for various grating periods.

Etch depth - The etch depth of the shallow etched area of the grating also affects the central wavelength of the grating. As the etch depth decreases, the n_{eff1} increases, hence n_{eff} increases. Based on equation 3.2, the n_{eff} is directly proportional to the central wavelength of the grating; consequently, the etch depth is inversely proportional to the central wavelength of the grating. Figure 5.8 portrays the simulation results for a variation in the etch depth from 60 nm - 80 nm, with all other parameters kept constant.

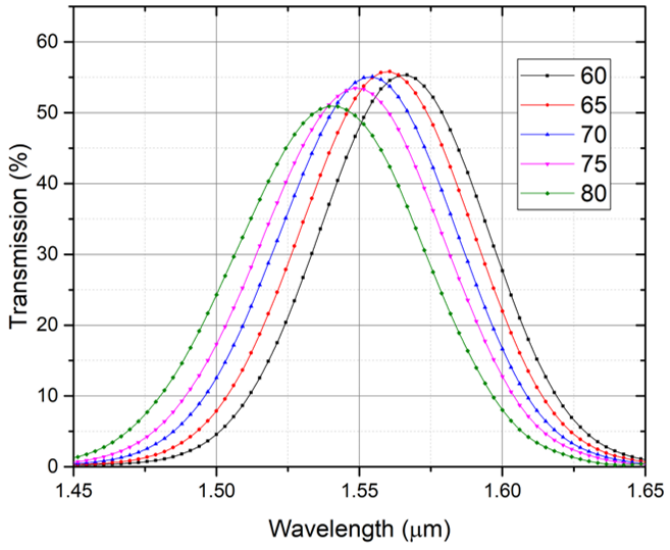

Figure 5.8: Grating coupler transmission versus wavelength for various etch depths.

After the complete optimisation of the GC design, the design parameters are summarised in Table 5.2.

Period (Λ)	Fill factor (FF)	Etch depth	λ	$\theta_{incident}$
630 nm	0.5 (50 %)	70 nm	1550 nm	9 °

Table 5.2: Final values for optimized grating coupler design.

5.5 Device fabrication

The MoSi waveguide integrated SNSPD devices were fabricated as described in Section 3.1.10. In summary, 10 nm MoSi with a 5 nm Si capping layer were sputtered on the SOI substrate. Subsequently, 3 nm Ti / 60 nm Au contact pads and alignment markers were fabricated by EBL followed by a lift-off process. Consecutively, the hairpin-shaped nanowire structure was patterned using e-beam and defined by RIE. Afterwards, the waveguide pattern was fabricated using another e-beam step and the top Si layer was etched using RIE-ICP. A schematic of the waveguide integrated device along with an SEM image of a completely fabricated one are illustrated in Figure 5.9.

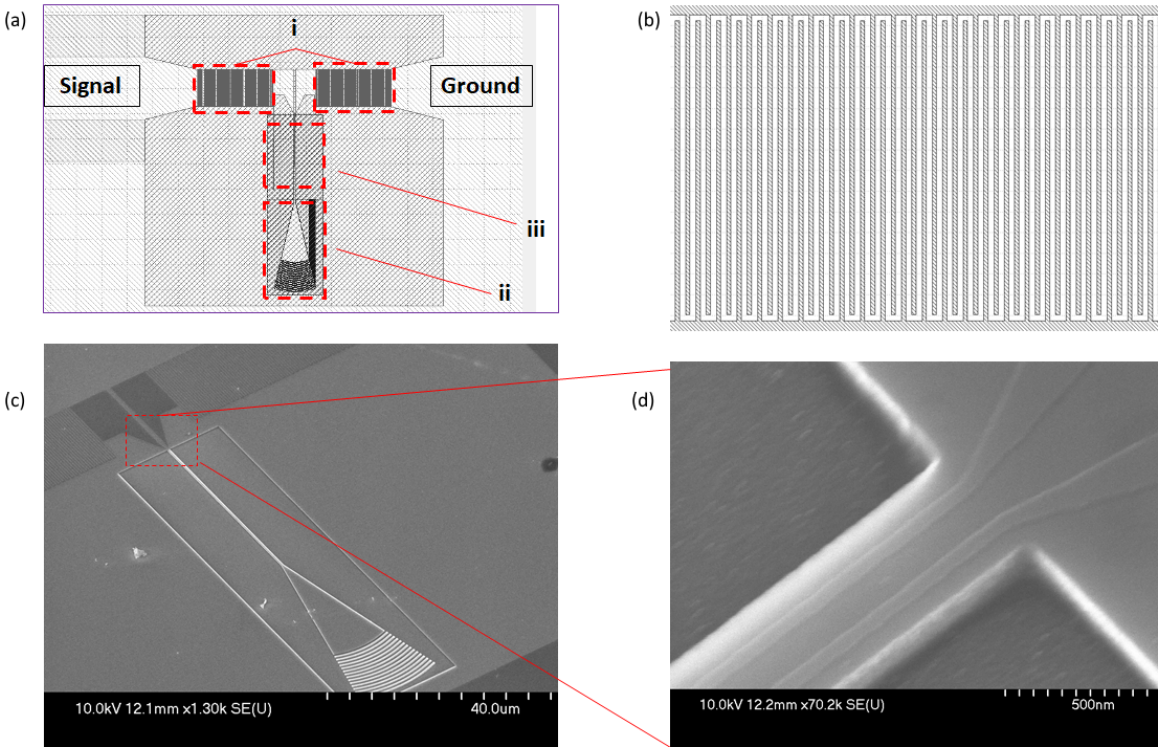

Figure 5.9: (a) schematic of waveguide integrated SNSPD. Series inductors (wider tracks adding additional kinetic inductance) (i) are included in the detector design to prevent latching, (ii) grating coupler area and (iii) hairpin-shaped nanowire area (nanowire width = 120 nm, length = 20 µm). (b) close-up of the series inductor region (inductor width = 200 nm, gap = 200 nm). (c) scanning electron micrograph image of a complete fabricated device and (d) magnified image of an area of the nanowire atop the optical waveguide showing a well-defined linewidth.

5.6 Electrical characterisation

After room temperature screening, the SNSPD devices were mounted in the two-stage Gifford-McMahon (GM) cryocooler with base temperature of 2.2 K described in Section 3.2.3 and characterised in terms of their basic superconducting properties. Additionally, the best device of the batch was furtherly characterised in another cryostat with base temperature of 350 mK described in Section 3.2.11.

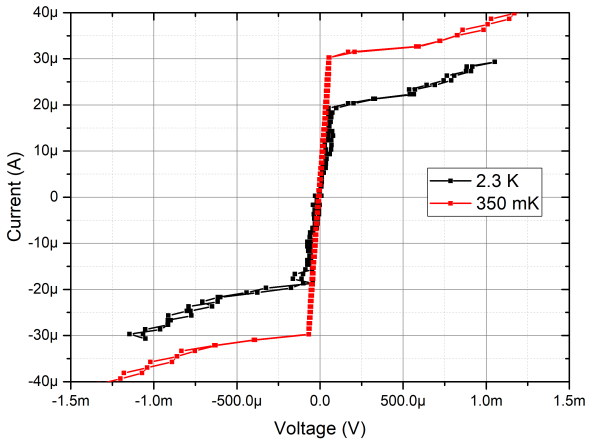

Figure 5.10: Bias current dependence of MoSi device. The device achieved a critical current of 30 µA at 350 mK and 18 µA at 2.2 K.

From this experiment it was observed a critical temperature (T_c) of 6.5 K for this device. Moreover due to the significantly lower base temperature of the 350 mK cryostat compared to the 2.2 K one, the signal to noise ratio of this device had significantly improved and as such the I_c raised from 18 µA measured at 2.2 K to 30 µA. However, the I_c of this device even at 2.2 K is high ($\approx$ 18 µA). Therefore, this device if needed it can be mounted at the sample stage for most PT systems that have a base temperature of up to 4 K and could perform well.

SNSPD's counting rate is limited by their kinetic inductance (L_k). By having shorter nanowires the L_k of the device is minimised. If the L_k is below a certain value, the device will enter into a transition stage between a superconducting and a resistive state, which forbids the further detection of photons typically referred as latching. On the other hand, if the L_k value is too big the hotspot region, generated by the absorption of a photon in the nanowire, is sustained since the Joule heating dominates the natural cooldown (heat dissipation into the substrate) and the device will latch into a resistive state [213]. Since waveguide integrated SNSPDs have lengths in the range of $\approx$ 20 µm compared to $\approx$ 500 µm in the case of meander SNSPDs, their L_k is very small. Since the L_k is proportional to the nanowire length, a shorter nanowire will have lower reset time. Therefore, to avoid latching

of the device, an additional series inductance needs to be simultaneously fabricated with the SNSPD[213, 214].

Furthermore, the investigation of the correct value of L_k that had to be fabricated in series to the SNSPD was carried out. For this experiment the main target was to achieve fast recovery time and no latching of the device. Consequently, four different inductor components that consisted of meander structures with the following lengths 285 µm , 570 µm , 855 µm and 1140 µm were fabricated and tested. The experiment was carried out with the use of Agilent Infiniium DSO80804A digital oscilloscope with 8 GHz bandwidth. The pulse shape for each of the device was recorded, the curves were compared and contrasted as shown in the Figure 5.11.

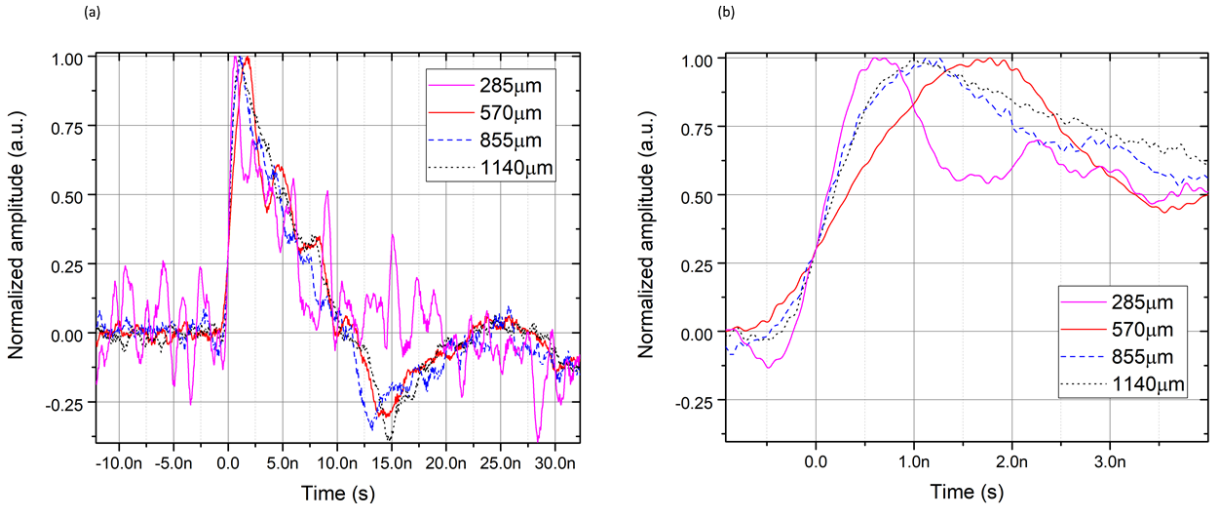

Figure 5.11: (a) Inductance-limited recovery of MoSi nanowires. Normalized amplitude with respect to time (b) zoomed in version of (a). At $t = 0$ illustrating the t_{rise} of the different inductance nanowire lengths.

The rise time of an SNSPD is defined as: $t_{rise} = \frac{L_k}{Z_o + R_{(t)}}$ [181], where Z_o is the load impedance and $R_{(t)}$ is the hotspot resistance. From this experiment it was observed that the device with the smallest L_k wire length (285 µm) had a constriction in the nanowire and as a result the pulse height was very small. Additionally, the one with the 570 µm long series L_k seems to have a much bigger $R_{(t)}$ among the four that explains its slower t_{rise}. From the four different L_K series inductance lengths the 285 µm has just enough L_k for a real experiment and it can be operated without a shunt resistor. Therefore, the SNSPD can give a much cleaner output pulse with lower reflections when it does not use the 50 Ω shunt resistor as illustrated in Figure 5.12.

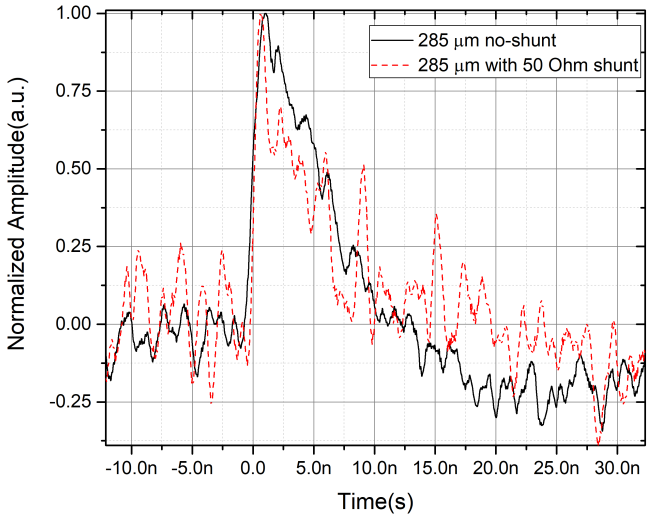

Figure 5.12: Inductance-limited recovery of MoSi nanowires with 285 µm long series L_k bank inductor with and without the use of a 50 Ω shunt resistor.

The falling edge of the output voltage pulses illustrated in Figure 5.11 and Figure 5.12 are distorted due to the low frequency response of the amplifiers used. Therefore, a simulation model for an SNSPD electrical circuit was developed using Cadence PSpice software package similar to [181, 215] in order to extract the L_k from the high frequency leading edge of the output voltage pulses. This model considers all electrical circuitry components including the SNSPD, the bias circuit and the amplifier chain. Moreover, it takes into consideration the two-stage amplification chain bandwidth (580 - 1000 MHz) and gain (56 dB). The SNSPD is represented by a hotspot resistor (*R1*) and an inductor (*L1*). The SNSPD is current biased (*I1*) with the use of a bias tee (*L2* - inductive port) with the generated RF pulse coupled through (*C2* - capacitive port). The transmission line (*T1*) represents the 50 Ω impedance matched coaxial cables used for the generated pulse read-out. With the aid of a current controlled switch (*W1*) that is triggered by a leading edge signal send from the voltage source (*V1*), and subsequently closes by a falling edge from voltage source (*V1*). Furthermore, this output voltage pulse is amplified by a double-stage low noise room temperature amplification chain (*E1* and *E2*). The PSPICE simulation model used for this work is illustrated in Figure 5.13.

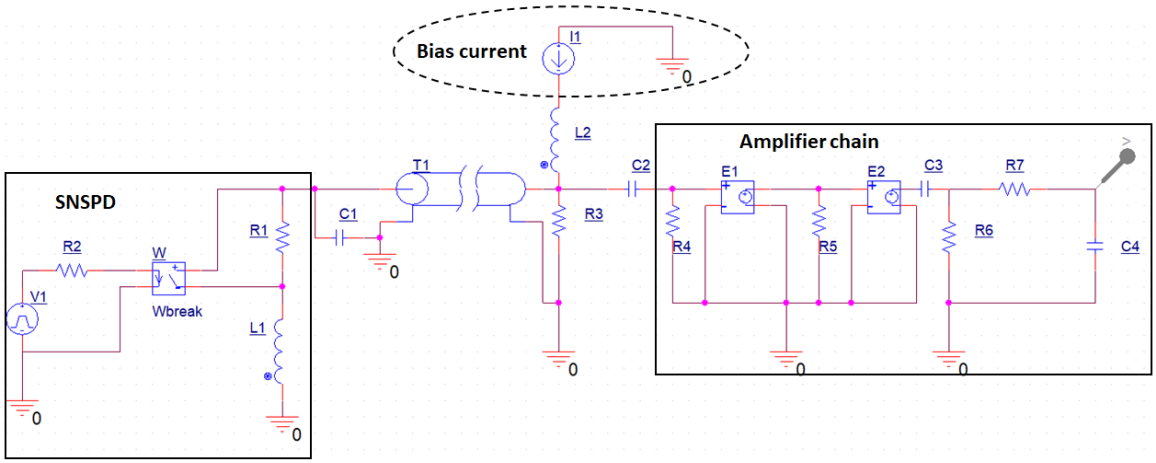

Figure 5.13: Schematic of the PSPICE simulation model of the SNSPD circuitry. The SNSPD device is simulated using an inductor (*L1*) and hotspot resistor (*R1*). It is current biassed using current source (*I1*). The formation and destruction of hotspot region is simulated using current controlled switch *W1*. Bias Tee is represented by capacitor (*C2*) and inductor (*L2*). Transmission line (*T1*) represents the 50 Ω matched coaxial cables. The output voltage pulse is amplified by an amplifier chain (*E1* and *E2*). The SNSPD is shunted with a 50 Ω resistor and the potential difference across the output port of the second amplifier is measured using a voltage measurement probe.

The measured output pulse shape from the SNSPD device with a 285 µm long series L_k (averaged over 256 shots with an 8 GHz bandwidth oscilloscope) along with a simulated pulse generated from the PSPICE model are plotted in Figure 5.14. 200 nH and 280 Ω has been used for *L1* and *R1* respectively in the simulation to match the measured data.

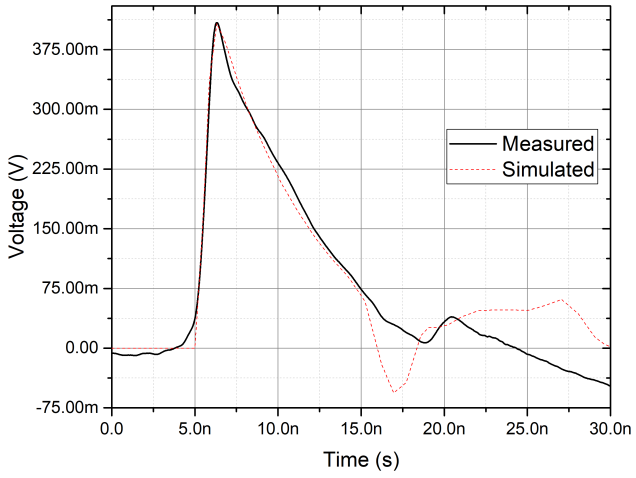

Figure 5.14: Simulation of SNSPD output pulse shape by fitting the recorded output pulse from the SNSPD device with a 285 µm long series L_k (averaged over 256 shots with an 8 GHz bandwidth oscilloscope) with the PSPICE simulation model. 200 nH and 280 Ω has been used for *L1* and *R1* respectively in the simulation (red-dotted line) to match the measured data (black-solid line).

The same procedure was repeated for SNSPD devices with inductor components of 570 µm, 855 µm and 1140 µm and their electrical properties are summarised in Table 5.3.

Device No:	1	2	3	4
Series inductor (µm)	285	570	855	1440
R_{300K} (kΩ)	30	35	30	55
T_c (K)	6.68	6.12	6.31	6.29
I_c (µA)	17.7	26.06	26.4	20.3
J_c (A cm^{-2})	1.77 x 10^6	2.66 x 10^6	2.64 x 10^6	2.02 x 10^6
L_k (H)	200 x 10^{-9}	381 x 10^{-9}	300 x 10^{-9}	410 x 10^{-9}
$L_k/\square$ (H/$\square$)	8.733 x 10^{-11}	1.628 x 10^{-10}	4.862 x 10^{-11}	4.965 x 10^{-11}

Table 5.3: Summary of electrical properties for waveguide integrated SNSPD devices. Experiments were performed in a 2.2 K cryocooler.

5.7 Optical characterisation

Optical mapping of waveguide integrated SNSPDs is performed with the confocal miniature microscope described in section 3.2.11 using a Thorlabs benchtop superluminescent diode S5FC1550P-A2 (λ= 1550nm, 2.5 mW and a FWHM line-width of 90 nm) as the illumination source. In Figure 5.15(a) three optical waveguides with an integrated detector and their respective grating couplers are illustrated. The centre waveguide is the only one integrated with a detector, while the rest are just test structures. This image is the result of a single field of view at 5 K. To ensure the confocal microscope is accurately addressing the correct device, the reflected histogram (power) is compared to an optical micrograph of the same region (Figure 5.15(b)).

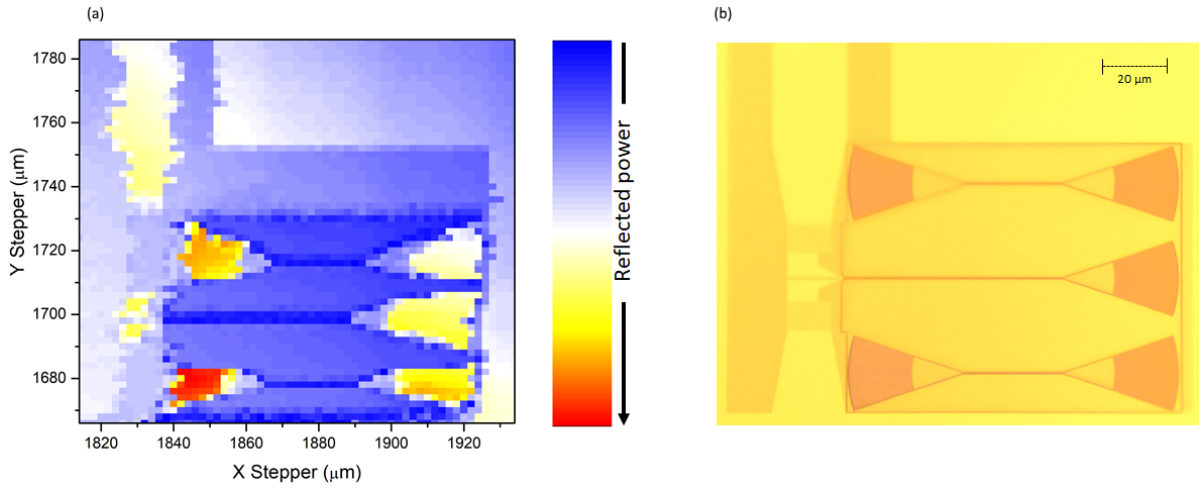

Figure 5.15: (a) Device of interest after reflection mapping of its surface at 5 K using the in-situ microscope and the Attocube motors over a range of 2000 µm , (b) Comparison with an optical micrograph of the same device area. This scheme allows to easily locate and accurately probe the nanoscale features of the integrated detectors.

The FWHM of the beam spot size at $\lambda = 1550$ nm is 2 µm, however it is possible to observe features sub-wavelength sized such as grating couplers and optical waveguides when the confocal microscope is well focused. Taking advantage of this technique, is possible to probe the nanowire with single-photons hence determine the SNSPD local detection efficiency. This is done with experimental apparatus described in Section 3.2.11 by preserving the position of the Attocube motors, the cryostat is cooled down to 350 mK and with the use of the Attocube scanners, the device region is mapped as illustrated in Figure 5.16(a).

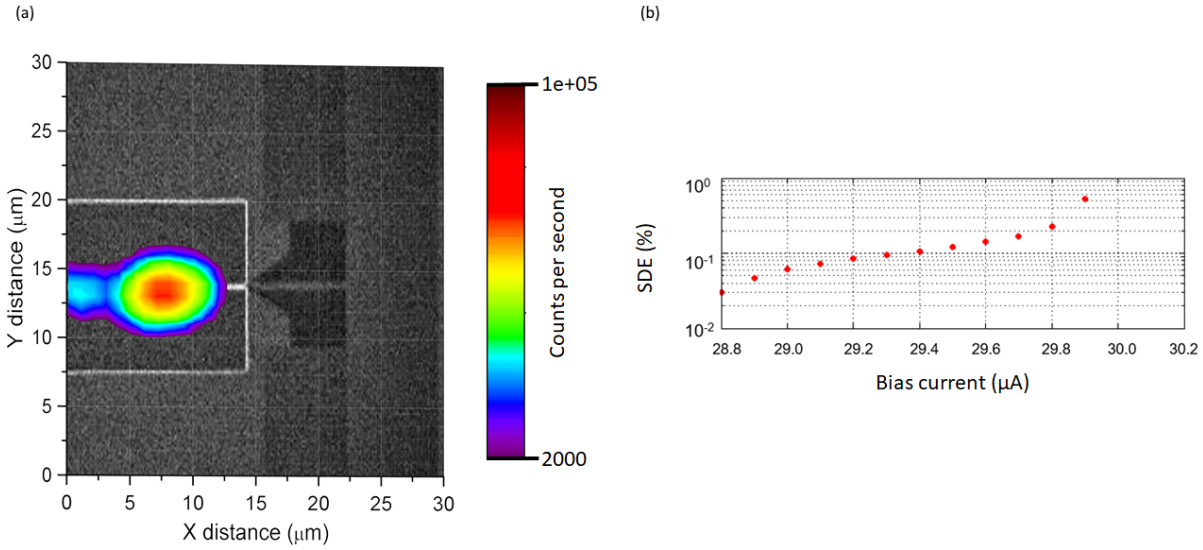

Figure 5.16: (a) counts map of a hairpin nanowire detector measured at $T = 350$ mK. The greyscale image on the base of the figure is an SEM image of the equivalent area. (b) based on the counts map, the optical spot is moved to the position with the maximum photon counting rate and the system detection efficiency (η_{SDE}) is measured.

Without compensation for coupling losses, the system detection efficiency (η_{SDE}) of the device shown is 0.025% at $\lambda = 1550$ nm with 3 dark counts per second.

These waveguide integrated SNSPDs were purposefully designed with the addition of a grating coupler (GC) at the end of the waveguide. This was done for coupling light from the confocal microscope into the chip. Since we didn't have any room temperature setup for confirming the performance of the GC, time correlated measurements were carried out by moving the confocal microscope on top of the hairpin region and then on top of the GC. By maintaining the spot of the confocal microscope in the same position used for the SDE measurements, the detectors response histogram was acquired. That measured 82 ps FWHM jitter at $I_c = 28$ µA is obtained. By carrying out exactly the same experiment, just by moving the microscope on top of the GC, the timing jitter was measured to be 99 ps at $I_c = 28$ µA as shown in Figure 5.17.

Since both the timing jitters are similar, it can be inferred that the GC design is working, and light is passing from the GC coupler through the single mode waveguide and

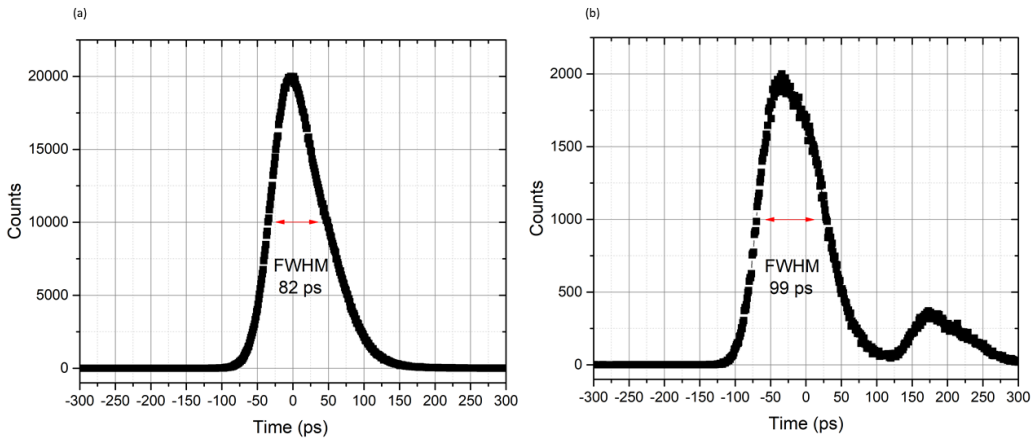

Figure 5.17: Timing jitter (Δ_t) plot with vertical illumination on top of (a) hairpin-shaped nanowire and (b) grating coupler. Both measurements were done at $\lambda = 1550\,\text{nm}$ using the setup described in section 3.2.10. A FWHM timing jitter of 82 ps and 99 ps was obtained respectively.

is absorbed by the SNSPD. From this experiment a second peak was observed; this can be due to the high reflection resulting from the edge of GC and the waveguide or from a high reflection in the microscope-optical system. Also, a slight asymmetry was observed in the jitter histograms that can be attributed to absorption events occurring at different places on the superconducting nanowires.

5.8 Quantum photonic circuits for integration with waveguide SNSPDs

In integrated quantum photonics the generation, routing and control of single-photons is required with high precision and stability. However, so far only a limited amount of components have been integrated on a single chip. Therefore, a crucial step for future scalable quantum information processing units is the increased complexity in the number of the integrated waveguide components. However, before attempting complicated quantum logical operations on-chip, it is essential to firstly demonstrate a quantum optical interference of two photons or HOM demonstration (discussed in Section 2.9.4). A device was designed and fabricated at the University of Glasgow with the intention of performing a Hong-Ou-Mandel dip demonstration with waveguide integrated SNSPDs on the same chip, illustrated in Figure 5.18.

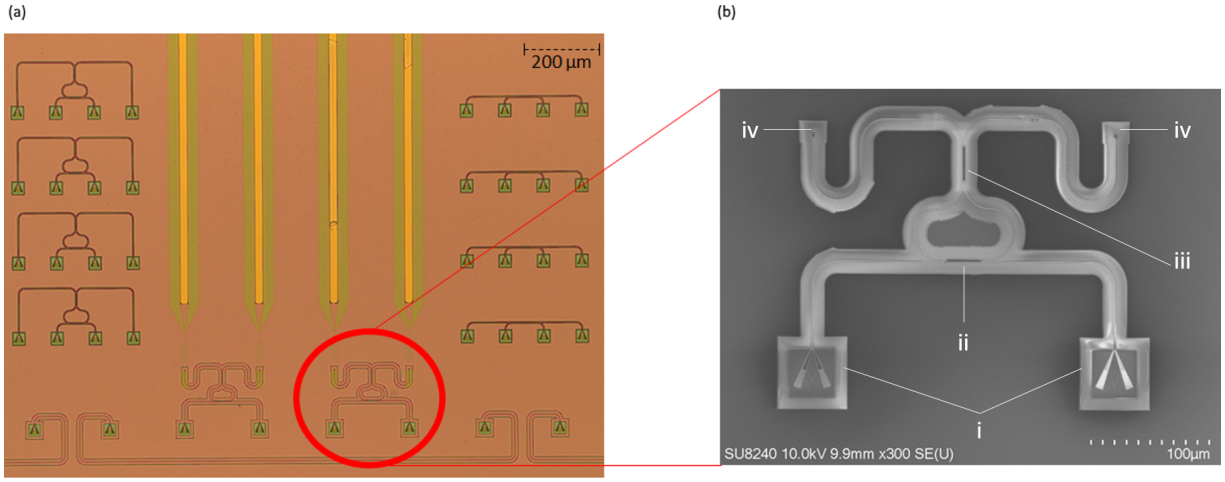

Figure 5.18: Device for on-chip quantum information processing experiment. (a) optical micrograph of a region of the chip illustrating a set of passive test structures and detectors integrated with photonic circuits, (b) zoomed-in SEM image of the red circled area presenting a circuit for Hong-Ou-Mandel dip demonstration including an MMI coupler 50:50 beam splitter (ii), with two detectors (iv) at its two output ports. The device includes grating couplers (i) and an additional MMI coupler in vertical orientation (iii) to ensure maximum alignment is achieved before the experiment takes place.

These devices are designed for the observation of interference effects between indistinguishable photons within single-mode optical waveguides. The circuit is patterned in the top Si layer of an SOI wafer. Two SNSPDs are integrated at the output ports of a multi mode interference (MMI) coupler acting as 50:50 beam splitter housed in Si waveguides with GC for injecting light from an off-chip source for the device characterisation.

5.9 Characterisation of isolated components

This section contains optical characterisation and profile analysis of grating couplers (GC) performed at the University of Glasgow by Dr. Jharna Paul. Additionally, passive circuits including GC and MMI couplers for extraction of GC transmission losses and MMI splitting ratio were fabricated on an SOI substrate in the JWNC by Dr. Jharna Paul and the sample was characterised at room-temperature in the University of Bristol by Dr. Döndü Shahin. and Dr. Archan Banerjee.

Profile analysis of a grating coupler:
Surface grating couplers (GC) profile has been characterised via high resolution transmission electron microscopy (TEM). The sample was prepared for TEM analysis by Dr. Archan Banerjee and Dr. Jharna Paul. The transmission electron microscope facilities available in the School of Physics and Astronomy, University of Glasgow (FEI Tecnai T20 microscope) have been used for this purpose. Before the TEM analysis, electron transpar-

ent cross sections have been prepared using a dual beam focused ion beam (FIB) system. Figure 5.19 illustrates the profile analysis of a grating coupler. Also, the depth profile of the shallow region of the grating coupler was analysed as shown in Figure 5.20.

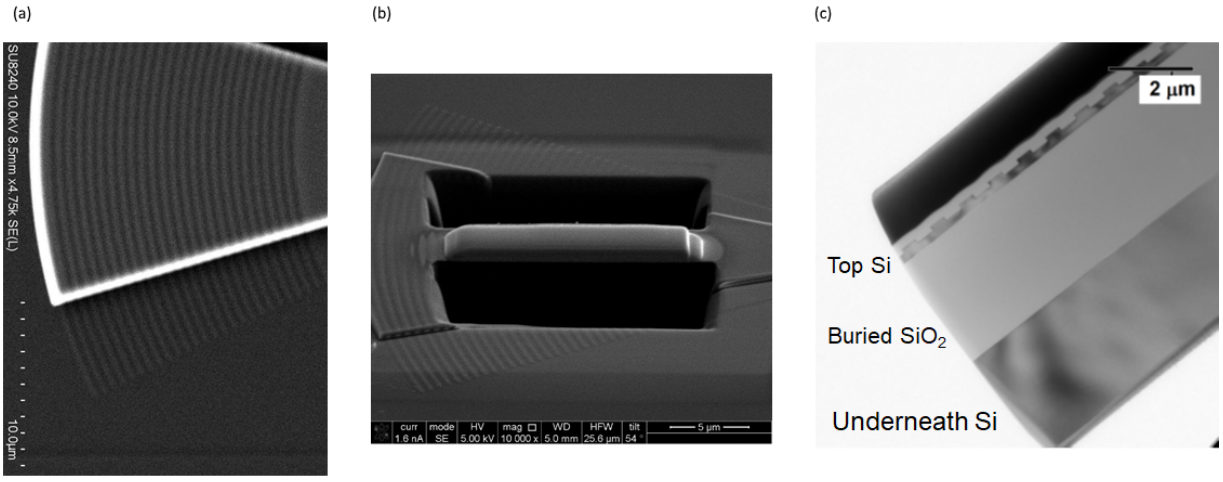

Figure 5.19: Profile analysis of a grating coupler. (a) scanning electron microscopy (SEM) image of a grating coupler, (b) focused ion beam (FIB) cross-section of grating coupler, (c) top view of sectioned grating coupler.

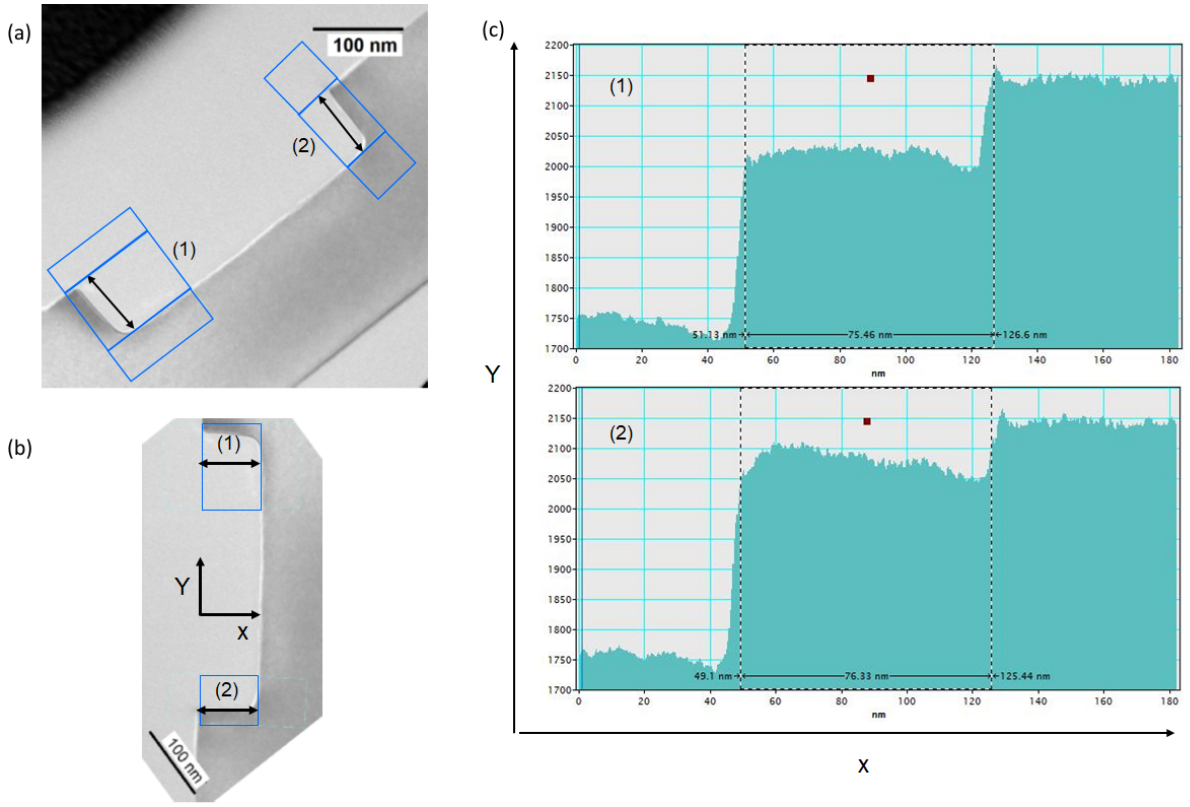

Figure 5.20: Depth profile of shallow-etched grating. (a) side view of shallow-etched grating. Points (1) and (2) indicate the two sides of the shallow-etched region, (b) same region as (a) in vertical orientation, (c) etched depth calculation.

From the TEM analysis it was measured an etched depth of ≈ 76 nm that is closely matched to the expected 70 nm etch depth. Moreover, the width and depth of the ridge and etched sections of the grating coupler, and periodicity of the grating were analysed. From this analysis it is also observed that the design dimensions are closely matched to the ones of the fabricated component as illustrated in Figure 5.21.

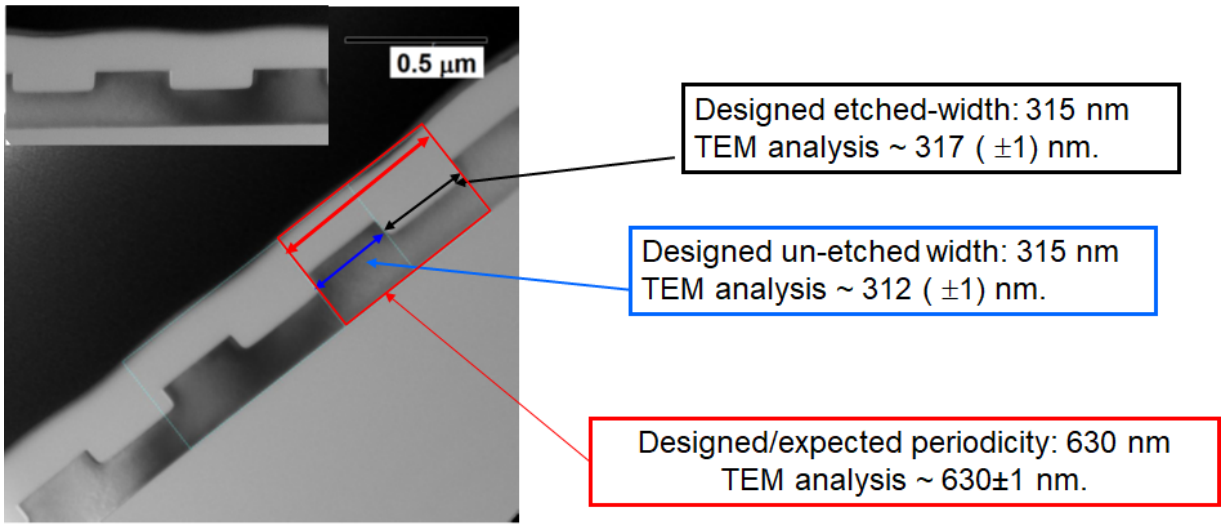

Figure 5.21: Periodicity of grating coupler.

From the TEM analysis it was measured a fill factor of ≈ 0.495 that is closely matched to the expected 0.5 fill factor.

Room-temperature measurement of GC transmission:
The chip illustrated in Figure 5.22 was room-temperature characterised with a 1550 nm laser diode (P = 631 µW (-2 dBm)) and a 4-channel fibre V-groove array.

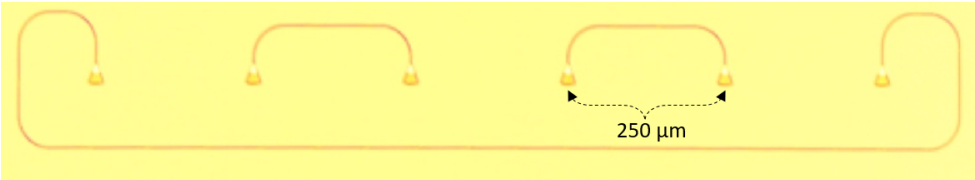

Figure 5.22: Optical micrograph of a set of GC and waveguides. The separation distance between adjacent grating couplers was 250 µm.

A maximum transmission of - 12 dB (100 µW) was measured between two GC as illustrated in Figure 5.23 thus each GC exhibited a 5 dB loss at $\lambda = 1550$ nm. From these data it was extracted an efficiency $\eta = 50\%$ per GC with a 3-dB bandwidth of ≈ 40 nm for $\lambda = 1527$ - 1567 nm.

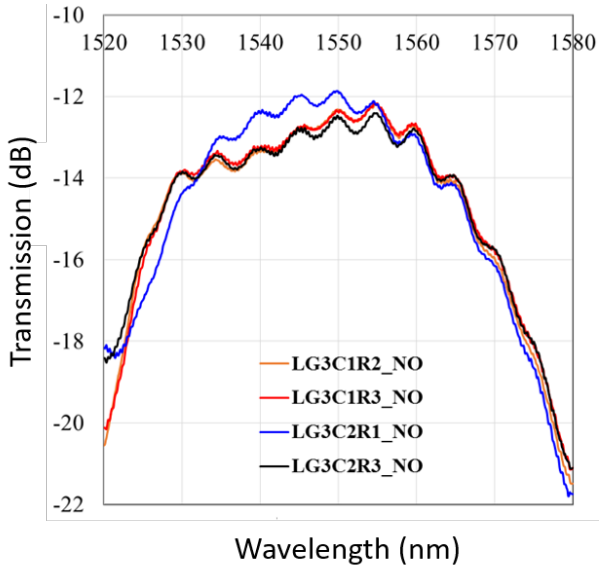

Figure 5.23: Room-temperature characterisation of GC for a wavelength range 1520 - 1580 nm.

Furthermore, an MMI coupler with four GC at both its input and output ports as illustrated in Figure 5.24 was characterised both at room and low temperature (4K) with the use of a Lake shore cryotronics probe station. Port 2 was used as the input and was illuminated via a 1550 nm laser diode (P = 631 µW (-2 dBm)) through a 4-channel fibre V-groove array and outputs at Port 3 and 4 were measured.

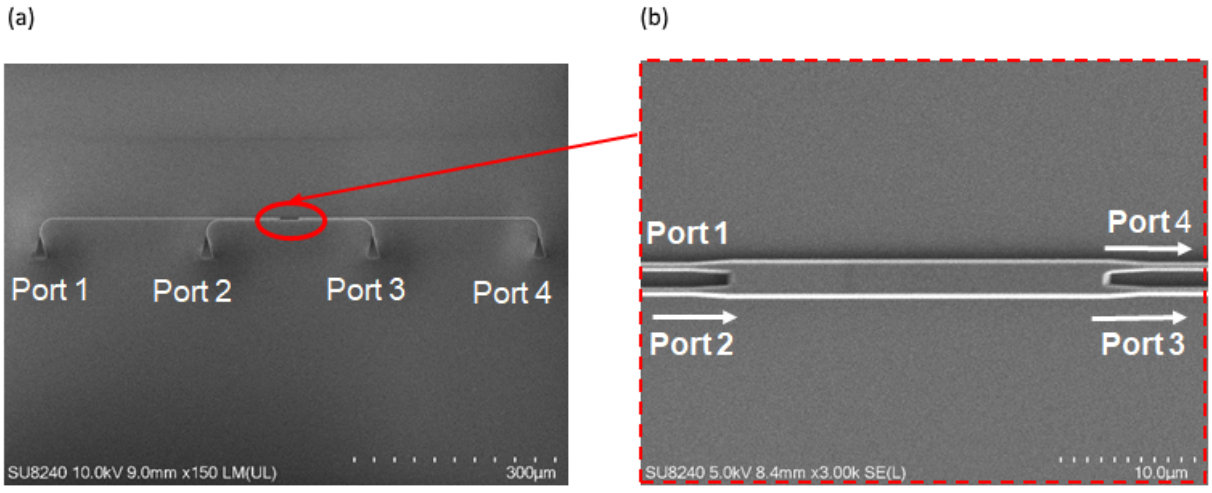

Figure 5.24: SEM of MMI with four GC at both input and output ports. (a) scanning electron micrograph of the complete passive circuit that includes an multi-mode interference (MMI) coupler and four GC both at its input and output ports, (b) zoomed in SEM image of the MMI area.

Figure 5.25 presents transmission characterisation of output Ports 3 and 4 both at room-temperature and low temperature (4K). From these measurements an 8 dB coupling loss per coupler at $\lambda = 1550$ nm was observed.

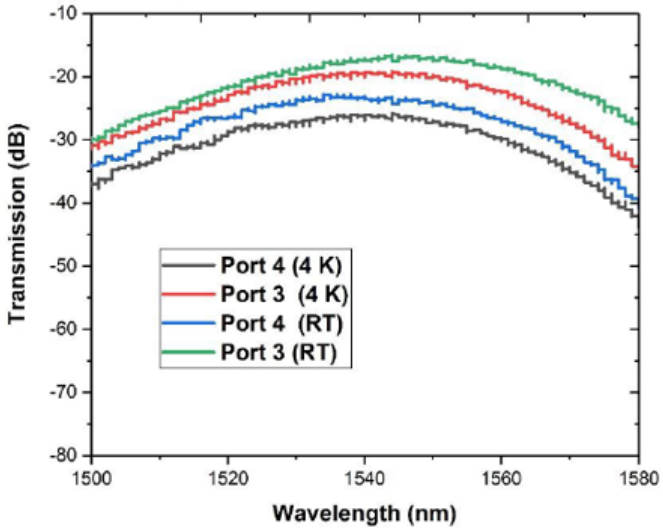

Figure 5.25: Room-temperature and low temperature (4K) multi-mode interference (MMI) coupler characterisation for wavelength range of 1500 - 1580 nm.

To calculate the MMI splitting ratio, the transmission data measured at Port 3 and 4 when the coupler is excited by Port 2 were used. The transmission values at Port 3 and 4 can be expressed by the following equations:

$$T_1 = (\eta_i)^2 * t * (\eta_o)^3 * (\eta_{Loss})^{2b}. \tag{5.2}$$

$$T_2 = (\eta_i)^2 * r * (\eta_o)^4 * (\eta_{Loss})^{a+b}. \tag{5.3}$$

T_1 and T_2 are the transmission measured at Port 3 and 4 respectively. η_i^2 denotes the input coupling efficiency of Port 2. η_o^3 and η_o^4 present the output coupling efficiency of Port 3 and Port 4. η_{Loss}^{2b} and η_{Loss}^{a+b} are the loss factors because of propagation from input to output port (a and b represent the half length of MMI structure up to waveguide.). Any optical loss in the waveguide has been neglected.

By taking the ratio of equations 5.2 and 5.3,

$$\frac{T_1}{T_2} = \frac{t * (\eta_o)^3 * (\eta_{Loss})^{2b}}{r * (\eta_o)^4 * (\eta_{Loss})^{a+b}} = \frac{t * (\eta_{Loss})^{2b}}{r * (\eta_{Loss})^{a+b}} \qquad (assuming(\eta_o^3 \cong \eta_o^4)). \tag{5.4}$$

Converting loss factor from dB to linear scale equation 5.4 becomes:

$$= \frac{t * (10 - \frac{\eta_{Loss}^{2b}}{10})}{r * (10 - \frac{\eta_{Loss}^{a+b}}{10})}. \tag{5.5}$$

Two sets of waveguide structures with two different path lengths were fabricated above the MMI coupler circuits for characterisation of propagation losses. The transmission measurement of both waveguide structures was carried out at room temperature by a Maple Leaf Photonics test bench. Measured transmission data at $\lambda = 1550$ nm as a function of waveguide path length are presented in Table 5.4.

Waveguide length (µm)	Transmission (dB)
750	- 21.36
2750	- 15.5

Table 5.4: Room-temperature waveguide transmission measurement for $\lambda = 1550$ nm as a function of waveguide path length.

Between the two sets of waveguide structures with waveguide path lengths 750 µm and 2750 µm respectively, there is a loss of 5.86 dB that translates to ≈ 29.3 dB per centimetre loss in the coupler.

The values of a and b are extracted from the design file as 338.5 µm and 89 µm respectively. Furthermore, by multiplying the propagation length with the value of loss per unit length extracted above, loss factors η_{Loss}^{2b} and η_{Loss}^{a+b} are calculated.

$$0.7 = \frac{t * 0.88}{r * 0.74} => \frac{t}{r} = 0.63. \tag{5.6}$$

By using equation 5.6 and assuming t + r = 1, the splitting ratio of the MMI is calculated as 61:39 at $\lambda = 1550$ nm (r = 0.61, t = 0.39).

5.10 Conclusions

Through James Watt Nanofabrication Centre (JWNC) in Glasgow and National Institute of Information and Communications Technology (NICT) in Japan, molybdenum silicide (MoSi) and niobium titanium nitride (NbTiN) thin films were grown on silicon-on-insulator (SOI) substrates with a DC magnetron sputtering system. Based on methods developed elsewhere, fabrication processes were developed at the University of Glasgow for the precise alignment of the hairpin nanowires atop single mode silicon waveguides (600 nm). In the first fabrication iteration a 10 nm thick MoSi film was used as the superconducting nanowire material and the waveguides leading to the detector were designed to have an input grating coupler for optical input. These detectors were characterised at 350 mK and an encouraging uniformity and yield was observed for devices with nanowire widths of 120 nm with 180 nm spacing on top of 600 nm wide waveguides as summarised in Table 5.5. However, the η_{SDE} was quite low that is attributed to the constrictions observed in the nanowires and the relatively thick superconducting films used for this work. Moreover,

due the grating coupler coupling efficiency was not characterised, which can be another one explanation for the low efficiency of the SNSPDs.

MoSi waveguide integrated SNSPD devices							
A/A	Device No	Line width (nm)	Length (μm)	Device Structure	R (Ohm)	Tc (K)	Ic (uA)
1	Delta west	120	20	Hairpin-shaped	30 K	6.68	20.7
2	Delta North	120	20	Hairpin-shaped	35 K	6.12	29.8
3	Delta South	120	20	Hairpin-shaped	30 K	6.31	29.95
4	Delta East	120	20	Hairpin-shaped	55 K	6.29	20.2

Table 5.5: MoSi waveguide SNSPDs performance statistics.

In a second fabrication iteration, passive elements were designed and fabricated for extraction of grating coupler (GC) transmission and splitting ratio of multi-mode interference (MMI) couplers. These chips were fabricated at University of Glasgow and characterised at the University of Bristol. The GC achieved an overall transmission of 50% with a 3-dB bandwidth of $\approx$ 40 nm at λ = 1527 - 1567 nm. Moreover, MMI characterisation was carried out both at room and low temperature (4K) and an output splitting ratio of 60:40 was extracted. Following characterisation of isolated components, a 7.5 nm thick NbTiN film was used as the superconducting nanowire material and SNSPD circuits were designed for HOM-dip experiments.

Chapter 6

Conclusions

Quantum photonic circuits integrated on-chip have been a major endeavour over the past decade in the field of optical quantum information science. Silicon photonics is a well-established technology that can be exploited to build a scalable optical quantum computer. The main requirements of scalable optical quantum information processing are to integrate low-loss, scalable optical circuits with highly efficient single photon sources and detectors [99] monolithically on a chip. The silicon platform is suitable for both single photon sources in the form of spontaneous four-wave mixing and waveguide circuits. Since the pioneering work of Gol'tsman et al. on single-photon detectors based on niobium nitride (NbN) superconducting nanowires, superconducting nanowire single-photon detectors (SNSPDs) have undergone rapid development and have emerged with performance metrics superior to other single-photon detectors (SPDs), such as single-photon avalanche photodiodes (SPADs). The need for integrated detectors lead to the concept of a hairpin nanowire integrated with optical waveguide circuits [12]. The main objective of this thesis was the development of next generation superconducting nanowire single-photon detectors for applications in the fields of quantum information processing, quantum cryptography and remote gas sensing. This chapter will summarise the individual conclusions of the two results chapters and suggest promising avenues for future work.

6.1 Detectors enhanced by multilayer cavities

Two different types of cavity integrated NbTiN SNSPDs were fabricated, fibre-coupled and characterised at low temperature. The first is front side cavity integrated SNSPD devices for near-infrared applications that take advantage of distributed Bragg reflectors (DBR) as their cavity material. Electrical and optical characterisation in our advanced nano-optical photoresponse mapping setup at $T = 3.5$ K showed an overall $\eta_{SDE} = 55\%$ at $\lambda = 940$ nm, dark count rate (DCR) = 100 Hz timing jitter of 60 ps at $I/I_c = 0.85$. Additionally, devices from the same fabrication run were manually fibre-coupled and optically

characterized at $T = 2.2$ K. One device was coupled with single mode fibre (4.4 µm core diameter), showed an overall $\eta_{SDE} = 57.5\%$ at $\lambda = 940$ nm, dark count rate (DCR) = 100 Hz and a low polarization dependence of 1.20 ± 0.03. A second device was coupled with multimode fibre (9 µm core diameter) showed a maximum $\eta_{SDE} = 90\%$ at $\lambda = 940$ nm, dark count rate (DCR) = 200 Hz. Our TEM analysis shows that the DBR roughness increases with the number of bilayer repeats, and the rms roughness of the top layer of our DBR stack (6.4 nm) approaches the thickness of the NbTiN superconducting thin film (7.5 nm). Therefore, reducing the number of DBR repeats may achieve the optimal trade-off between optical absorption and SNSPD uniformity. Another alternative solution might be the use of amorphous superconductors. The film uniformity on top of the DBR cavity may be better than polycrystalline superconductors. Also, amorphous superconductors have lower energy gap potentially should give better mid-IR performance. These SNSPD devices are promising candidates for use in quantum dot photoluminescence studies and optical quantum technology applications. For example, single-photon purity of emission can be verified by second order correlation functions $g^2(t)$, which indicate the statistical distribution of photons emitted by the source. High efficiency SNSPDs with low dark counts and low timing jitter, will improve the acquisition of $g^2(t)$, yielding lower uncertainty in the measured data for a fixed acquisition time.

The second design explored was a back side cavity integrated SNSPD device designed for infrared and mid-infrared applications that take advantage of metallic mirrors as their cavity material. Two metallic mirror cavities where designed with peak absorption at 1550 nm and 2330 nm respectively. For the 1550 nm devices, NbTiN thin films sputtered at both 10 mTorr and 2 mTorr total pressure were used. NbTiN films grown at high sputtering pressure (10 mTorr), in order to minimize the film grain and achieve a chemical composition approaching that of amorphous materials. This experiment was carried out with the potential to realise SNSPD devices capable of operating at higher temperature in simpler cryogenic systems and faster timing response for applications in quantum key distribution (QKD) requiring higher timing precision. These devices achieved similar performance characteristics with devices grown at lower sputtering pressure (2 mTorr) NbTiN thin films with a peak η_{SDE} value of $\approx 84.5\%$ at $\lambda = 1550$ nm, (DCR) = 23.5 Hz at $T = 2.2$ K on a two-parallel nanowire (2SNAP) configuration. These SNSPD devices are promising candidates for use in long distance transmission QKD systems. Additionally, for the 2330 nm devices a peak η_{SDE} value of $\approx 0.05\%$ was recorded at $\lambda = 2330$ nm for $T = 2.2$ K. These SNSPD devices were cooled down in a ^{3}He cryocooler with $T = 350$ mK and the dependence of both the I_c and dark counts (DC) with temperature recorded and compared to data acquired at 2.2 K. From this experiment it was observed that the device is suffering from substantial dark counts mainly due to blackbody radiation at 2.2 K. Furthermore, the timing jitter of this device was measured at 350 mK indicating a full

width half maximum (FWHM) of 84 ps, which at the time of writing this report is the first jitter measurement at 2330 nm recorded. In order to suppress the huge amount of dark counts created by blackbody radiation at 2.2 K, these devices should be operated at lower temperatures (T = 350 mK) and coupled with a cold optical filter that should completely block the blackbody radiation except the signal passband [206]. These devices are promising candidates to probe carbon dioxide (CO_2) and methane (CH_4) gases for remote sensing applications. During development of above-mentioned SNSPD devices, it was challenging to minimise coupling losses during the manual fibre coupling and a future direction would be to adopt a self-aligning scheme that will require patterning the devices in a keyhole structure that can fit the ferrule of single-mode fibre and will minimise coupling losses [131]. The parts forming a self-alignment device packaging sample mount were custom designed and machined at the University of Glasgow. A sketch of the proposed sample mount is portrayed in Figure 6.1.

Figure 6.1: Self-alignment device packaging setup. Left key-hole sample mount design including a) SNSPD device shaped in a key-hole b) ferrule c) sample mount d) SMA connector. Right a 10 x 10 mm^2 Si substrate including three detectors after deep Si etching through the DBR substrate.

In our device structure, this requires further technological development as a deep anisotropic etch process has to be developed not just for the Si wafer but also for the DBR heterostructure. With self-alignment, we would expect high η_{SDE} to be consistently achieved. Also, use of anti-reflection coated fibre[191] would allow a modest increase in η_{SDE}.

6.2 Detectors integrated with silicon waveguide circuits

Through James Watt Nanofabrication Centre (JWNC) in Glasgow and National Institute of Information and Communications Technology (NICT) in Japan, molybdenum silicide (MoSi) and niobium titanium nitride (NbTiN) thin films were grown on silicon-on-insulator (SOI) substrates with DC magnetron sputtering. Fabrication processes were developed at the University of Glasgow for the precise alignment of the hairpin nanowires atop single mode silicon waveguides (600 nm). In the first fabrication iteration a 10 nm thick MoSi film was used as the superconducting nanowire material and the waveguides leading to the detector were designed to have an input grating coupler for optical input. These detectors were characterised at 350 mK and an encouraging uniformity and yield was observed. However, the η_{SDE} was quite low that is attributed to the constrictions observed in the nanowires and the relatively thick superconducting films used for this work. Additionally, even though in the fabricated design there were present grating couplers for in/out coupling of light due to the limited movement of the Attocube motors, it was impossible to inject light into the waveguide via a grating coupler and measure the single-photon response through the hairpin-nanowire. Nevertheless, time correlated measurements were done by moving the confocal microscope on top of the hairpin region and then on top of the grating coupler. From this experiment it was inferred that the grating coupler is working, and light is passing from the grating coupler through the single mode waveguide and is absorbed by the SNSPD. To overcome this limitation, a new cryostat with $T = 1$ K continuous operation is currently under construction. This system will allow for rapid waveguide testing by incorporating 10 optical inputs and 8 RF channels. In the second fabrication iteration a 7.5 nm thick NbTiN film was used as the superconducting nanowire material and SNSPD test circuits were designed for HOM-dip experiments. Additionally, passive elements were fabricated for calculating the splitting ratio of multimode interference (MMI) couplers and waveguide losses. During development of above-mentioned SNSPD devices, it was required to strip the positive tone resist for subsequent fabrication steps. By switching to a negative tone resist such as HSQ, there is no need to strip the resist for subsequent fabrication steps and that might allow for a cleaner final device. Additionally, HSQ resist during development will form a silica-like dielectric that will mask over the sensitive nanowires and that potentially will result in a waveguide etching with minimal surface roughness hence lower propagation losses.

6.3 Outlook

The efforts in Glasgow continue towards the on-chip integration of waveguide circuits, single-photon detectors and eventually single-photon emitters. These efforts are boosted by the in-house superconducting thin film deposition capabilities such as the DC magnetron sputtering and a new method utilising atomic layer deposition (ALD) of thin films such as NbN, NbTiN and MoSi on a range of substrates [216]. New low-temperature test system is currently in progress that will improve upon existing low temperature nano-optical test capability. This new setup will have a base $T = 1$ K and will have the capability of parallel testing upto 8 SNSPDs with independent optical inputs, and operation of circuits with up to 8 operational detectors in one cool-down as illustrated in Figure 6.2.

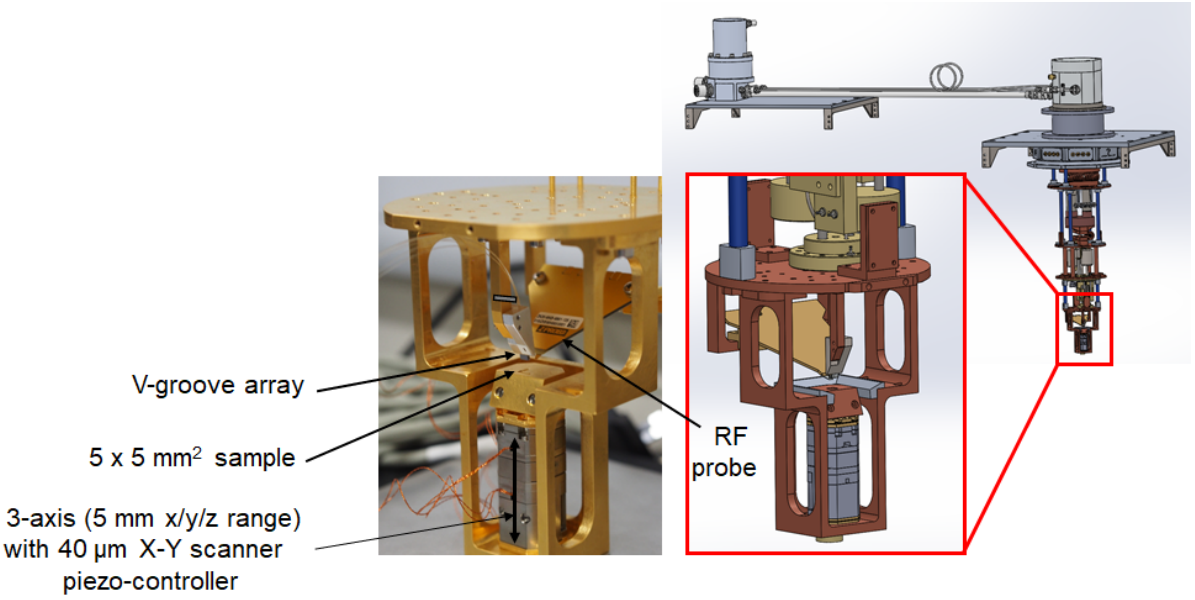

Figure 6.2: New low-temperature test system for waveguide characterisation with a base $T = 1$ K. Illustrating the 4-channel V-groove fiber array, RF probe and the 3-axis piezo-electric motors. Image used with permission from Dr. R.M. Heath .

This will enable speedy testing of quantum logic gates and circuits. Efficient integration of waveguide circuits and single-photon detectors is still a challenging avenue as further optimisation is required in order to achieve low loss transmission in optical waveguide circuits. Another useful technological development would be low loss bonding of a fibre array to a grating coupler array on chip. Moreover, for the realisation of a HOM-dip experiment, the grating coupler transmission, the splitting ratio of the MMI coupler and the waveguide losses need to be thoroughly characterised. For single photon generation, semiconducting quantum dots are the most promising candidate as they can produce photons deterministically and they can be monolithically integrated in GaAs platforms [60]. However, the integration in silicon substrates remains a challenge. Silicon waveguide

spiral photon pair sources [217] and waveguide ring resonators [218] are both promising candidates for silicon quantum photonic integrated circuits. Another future direction would be mid-infrared silicon photonics with on-chip single-photon detection. This is likely to be a promising frontier for on-chip single-photon sensing and integrated quantum photonics.

Bibliography

[1] A.E. Lita, V.B. Verma, R. D. Horansky, J.M. Shainline, R.P. Mirin, and S. Nam. Materials development for high efficiency superconducting nanowire single-photon detectors. In *Symposium VV – Science and Technology of Superconducting Materials*, volume 1807 of *MRS Proceedings*, pages 1–6, 1 2015.

[2] Taeyoon Hong, Kyujin Choi, Kyung Ik Sim, Taewoo Ha, Byung Cheol Park, Hirotake Yamamori, and Jae Hoon Kim. Terahertz electrodynamics and superconducting energy gap of NbTiN. *Journal of Applied Physics*, 114(24), 2013.

[3] Jelena Stajic. The future of quantum information processing. *Science*, 339(6124):1163, 2013.

[4] Andrew A Chien and Vijay Karamcheti. Moore's law: The first ending and a new beginning. *Computer*, 46(12):48–53, 2013.

[5] Emanuel Knill, Raymond Laflamme, and Gerald J Milburn. A scheme for efficient quantum computation with linear optics. *Nature*, 409(6816):46–52, 2001.

[6] Artur Ekert and Richard Jozsa. Quantum computation and Shor's factoring algorithm. *Reviews of Modern Physics*, 68(3):733, 1996.

[7] PG Kwiat, JR Mitchell, PDD Schwindt, and AG White. Grover's search algorithm: an optical approach. *Journal of Modern Optics*, 47(2-3):257–266, 2000.

[8] Pieter Kok, WJ Munro, Kae Nemoto, TC Ralph, Jonathan P Dowling, and GJ Milburn. Linear optical quantum computing. *arXiv preprint quant-ph/0512071*, 2005.

[9] F Marsili, VB Verma, JA Stern, S Harrington, AE Lita, T Gerrits, I Vayshenker, B Baek, MD Shaw, RP Mirin, et al. Detecting single infrared photons with 93% system efficiency. *Nature Photonics*, 7(3):210–214, 2013.

[10] Claus Grupen, Giovanni P Pepe, Roberto Cristiano, Flavio Gatti, Doris Maier, Michael Siegel, Dagmar Henrich, Masayoshi Tonouchi, and Thomas Ortlepp. Superconducting radiation and particle detectors. *Applied Superconductivity: Handbook on Devices and Applications*, pages 843–948, 2015.

[11] Alberto Politi, Martin J Cryan, John G Rarity, Siyuan Yu, and Jeremy L O'Brien. Silica-on-silicon waveguide quantum circuits. *Science*, 320(5876):646–649, 2008.

[12] Wolfram Hans Peter Pernice, C Schuck, O Minaeva, M Li, GN Gol'tsman, AV Sergienko, and HX Tang. High-speed and high-efficiency travelling wave single-photon detectors embedded in nanophotonic circuits. *Nature Communications*, 3:1325, 2012.

[13] Faraz Najafi, Jacob Mower, Nicholas C Harris, Francesco Bellei, Andrew Dane, Catherine Lee, Xiaolong Hu, Prashanta Kharel, Francesco Marsili, Solomon Assefa, et al. On-chip detection of non-classical light by scalable integration of single-photon detectors. *Nature Communications*, 6:5873, 2015.

[14] János A. Bergou and Mark Hillery. *Introduction*, pages 1–8. Springer New York, New York, NY, 2013.

[15] Emanuel Knill, Raymond Laflamme, Howard N Barnum, Diego A Dalvit, Jacek J Dziarmaga, James E Gubernatis, Leonid Gurvits, Gerardo Ortiz, Lorenza Viola, and Wojciech H Zurek. Quantum information processing-a hands-on primer. *Los Alamos Science*, 27:2–32, 2002.

[16] George Boole. *An investigation of the laws of thought: on which are founded the mathematical theories of logic and probabilities*. Dover Publications, 1854.

[17] Alan Mathison Turing. On computable numbers, with an application to the entscheidungsproblem. *Proceedings of the London mathematical society*, 2(1):230–265, 1937.

[18] Benjamin Schumacher. Quantum coding. *Physical Review A*, 51(4):2738, 1995.

[19] Ivan Djordjevic. *Quantum information processing and quantum error correction: an engineering approach*. Academic press, 2012.

[20] David Deutsch and Richard Jozsa. Rapid solution of problems by quantum computation. In *Proceedings of the Royal Society of London A: Mathematical, Physical and Engineering Sciences*, volume 439, pages 553–558. The Royal Society, 1992.

[21] AG Aruna, KH Vani, C Sathya, and R Sowndarya Meena. A study on reversible logic gates of quantum computing.

[22] Ronald L Rivest, Adi Shamir, and Len Adleman. A method for obtaining digital signatures and public-key cryptosystems. *Communications of the ACM*, 21(2):120–126, 1978.

[23] Sara Robinson. Still guarding secrets after years of attacks, rsa earns accolades for its founders. *SIAM News*, 36(5):1–4, 2003.

[24] David Naccache, David M'Raïhi, Serge Vaudenay, and Dan Raphaeli. Can dsa be improved?—complexity trade-offs with the digital signature standard—. In *Advances in Cryptology—EUROCRYPT'94*, pages 77–85. Springer, 1995.

[25] Don Johnson, Alfred Menezes, and Scott Vanstone. The elliptic curve digital signature algorithm (ecdsa). *International Journal of Information Security*, 1(1):36–63, 2001.

[26] Simon Bone and Matias Castro. A brief history of quantum computing. *Imperial College in London, http://www. doc. ic. ac. uk/˜ nd/surprise_97/journa l/vol4/spb3*, 1997.

[27] Seth Lloyd. Universal quantum simulators. *Science*, 273(5278):1073–1078, 1996.

[28] Alán Aspuru-Guzik and Philip Walther. Photonic quantum simulators. *Nature Physics*, 8(4):285–291, 2012.

[29] Katherine L Brown, William J Munro, and Vivien M Kendon. Using quantum computers for quantum simulation. *Entropy*, 12(11):2268–2307, 2010.

[30] Donald Frederick Parsons. Possible medical and biomedical uses of quantum computing. *NeuroQuantology*, 9(3), 2011.

[31] Quantum computing - IBM Q - US. [Online; accessed 03/06/2018].

[32] Google AI blog: A preview of bristlecone, google's new quantum processor. [Online; accessed 03/06/2018].

[33] David P DiVincenzo et al. The physical implementation of quantum computation. *arXiv preprint quant-ph/0002077*, 2000.

[34] Thaddeus D Ladd, Fedor Jelezko, Raymond Laflamme, Yasunobu Nakamura, Christopher Monroe, and Jeremy Lloyd O'Brien. Quantum computers. *Nature*, 464(7285):45–53, 2010.

[35] Isaac L Chuang, Neil Gershenfeld, and Mark Kubinec. Experimental implementation of fast quantum searching. *Physical Review Letters*, 80(15):3408, 1998.

[36] Michael A Nielsen and Isaac L Chuang. Quantum computation and quantum information. *Quantum*, 546:1231, 2000.

[37] Lieven MK Vandersypen, Matthias Steffen, Gregory Breyta, Costantino S Yannoni, Mark H Sherwood, and Isaac L Chuang. Experimental realization of shor's quantum factoring algorithm using nuclear magnetic resonance. *Nature*, 414(6866):883–887, 2001.

[38] C Negrevergne, TS Mahesh, CA Ryan, M Ditty, F Cyr-Racine, W Power, N Boulant, T Havel, DG Cory, and R Laflamme. Benchmarking quantum control methods on a 12-qubit system. *Physical Review Letters*, 96(17):170501, 2006.

[39] Juan I Cirac and Peter Zoller. Quantum computations with cold trapped ions. *Physical Review Letters*, 74(20):4091, 1995.

[40] Philipp Schindler, Daniel Nigg, Thomas Monz, Julio T Barreiro, Esteban Martinez, Shannon X Wang, Stephan Quint, Matthias F Brandl, Volckmar Nebendahl, Christian F Roos, et al. A quantum information processor with trapped ions. *New Journal of Physics*, 15(12):123012, 2013.

[41] Christopher R Monroe and David J Wineland. Quantum computing with ions. *Scientific American*, 299(2):64–71, 2008.

[42] Zachary Burell. An introduction to quantum computing using Cavity QED concepts. *arXiv preprint arXiv:1210.6512*, 2012.

[43] W. Lange H. Mabuchi QA Turchette, CJ Hood and HJ Kimble. Measurement of conditional phase shifts for quantum logic. *Phys. Rev. Lett.*, 75:4710, 1995.

[44] Jay M Gambetta, Jerry M Chow, and Matthias Steffen. Building logical qubits in a superconducting quantum computing system. *npj Quantum Information*, 3(1):2, 2017.

[45] Peter James Joyce O'Malley. *Superconducting Qubits: Dephasing and Quantum Chemistry*. University of California, Santa Barbara, 2016.

[46] Nathan K Langford. Encoding, manipulating and measuring quantum information in optics. 2007.

[47] Nathan K Langford, Sven Ramelow, Robert Prevedel, William J Munro, Gerard J Milburn, and Anton Zeilinger. Efficient quantum computing using coherent photon conversion. *Nature*, 478(7369):360, 2011.

[48] Alan Migdall, Sergey V Polyakov, Jingyun Fan, and Joshua C Bienfang. *Single-Photon Generation and Detection: Physics and Applications*, volume 45. Academic Press, 2013.

[49] Terry Rudolph. Why i am optimistic about the silicon-photonic route to quantum computing. *APL Photonics*, 2(3):030901, 2017.

[50] Menno Poot and Hong X Tang. Broadband nanoelectromechanical phase shifting of light on a chip. *Applied Physics Letters*, 104(6):061101, 2014.

[51] Robert H Hadfield and Göran Johansson. *Superconducting Devices in Quantum Optics*. Springer, 2016.

[52] PJ Dean. Bound excitons and donor-acceptor pairs in natural and synthetic diamond. *Physical Review*, 139(2A):A588, 1965.

[53] Paolo Dore, Alessandro Nucara, Daniele Cannavo, Gianluca De Marzi, Paolo Calvani, Augusto Marcelli, Ricardo S Sussmann, Andrew J Whitehead, Carlton N Dodge, Astrid J Krehan, et al. Infrared properties of chemical-vapor deposition polycrystalline diamond windows. *Applied Optics*, 37(24):5731–5736, 1998.

[54] Rich Mildren and James Rabeau. *Optical engineering of diamond*. John Wiley & Sons, 2013.

[55] Patrik Rath, Oliver Kahl, Simone Ferrari, Fabian Sproll, Georgia Lewes-Malandrakis, Dietmar Brink, Konstantin Ilin, Michael Siegel, Christoph Nebel, and Wolfram Pernice. Superconducting single-photon detectors integrated with diamond nanophotonic circuits. *Light: Science & Applications*, 4(10):e338, 2015.

[56] Janine Riedrich-Möller, Laura Kipfstuhl, Christian Hepp, Elke Neu, Christoph Pauly, Frank Mücklich, Armin Baur, Michael Wandt, Sandra Wolff, Martin Fischer, et al. One-and two-dimensional photonic crystal microcavities in single crystal diamond. *Nature Nanotechnology*, 7(1):69, 2012.

[57] Jonathan C Lee, Igor Aharonovich, Andrew P Magyar, Fabian Rol, and Evelyn L Hu. Coupling of silicon-vacancy centers to a single crystal diamond cavity. *Optics Express*, 20(8):8891–8897, 2012.

[58] Marcus W Doherty, Neil B Manson, Paul Delaney, Fedor Jelezko, Jörg Wrachtrup, and Lloyd CL Hollenberg. The nitrogen-vacancy colour centre in diamond. *Physics Reports*, 528(1):1–45, 2013.

[59] D Yu Fedyanin and Mario Agio. Ultrabright single-photon source on diamond with electrical pumping at room and high temperatures. *New Journal of Physics*, 18(7):073012, 2016.

[60] Simeon Bogdanov, MY Shalaginov, Alexandra Boltasseva, and Vladimir M Shalaev. Material platforms for integrated quantum photonics. *Optical Materials Express*, 7(1):111–132, 2017.

[61] S Fattah Poor, TB Hoang, Leonardo Midolo, CP Dietrich, LH Li, EH Linfield, JFP Schouwenberg, T Xia, FM Pagliano, FWM Van Otten, et al. Efficient coupling of single photons to ridge-waveguide photonic integrated circuits. *Applied Physics Letters*, 102(13):131105, 2013.

[62] JP Sprengers, A Gaggero, D Sahin, S Jahanmirinejad, G Frucci, F Mattioli, R Leoni, Johannes Beetz, M Lermer, M Kamp, et al. Waveguide superconducting single-photon detectors for integrated quantum photonic circuits. *Applied Physics Letters*, 99(18):181110, 2011.

[63] G Reithmaier, M Kaniber, F Flassig, S Lichtmannecker, K Müller, A Andrejew, J Vuckovic, R Gross, and JJ Finley. On-chip generation, routing, and detection of resonance fluorescence. *Nano Letters*, 15(8):5208–5213, 2015.

[64] Christof P Dietrich, Andrea Fiore, Mark G Thompson, Martin Kamp, and Sven Höfling. Gaas integrated quantum photonics: Towards compact and multi-functional quantum photonic integrated circuits. *Laser & Photonics Reviews*, 10(6):870–894, 2016.

[65] Wim Bogaerts, Dirk Taillaert, Bert Luyssaert, Pieter Dumon, Joris Van Campenhout, Peter Bienstman, Dries Van Thourhout, Roel Baets, V Wiaux, and S Beckx. Basic structures for photonic integrated circuits in silicon-on-insulator. *Optics Express*, 12(8):1583–1591, 2004.

[66] Bahram Jalali and Sasan Fathpour. Silicon photonics. *Lightwave Technology, Journal of*, 24(12):4600–4615, 2006.

[67] Wim Bogaerts, Roel Baets, Pieter Dumon, Vincent Wiaux, Stephan Beckx, Dirk Taillaert, Bert Luyssaert, Joris Van Campenhout, Peter Bienstman, and Dries Van Thourhout. Nanophotonic waveguides in silicon-on-insulator fabricated with cmos technology. *Lightwave Technology, Journal of*, 23(1):401–412, 2005.

[68] B Jalali, S Yegnanarayanan, T Yoon, T Yoshimoto, I Rendina, and F Coppinger. Advances in silicon-on-insulator optoelectronics. *Selected Topics in Quantum Electronics, IEEE Journal of*, 4(6):938–947, 1998.

[69] Timo Aalto et al. *Microphotonic silicon waveguide components*. VTT Technical Research Centre of Finland, 2004.

[70] Chunle Xiong, Bryn Bell, and Benjamin J Eggleton. Cmos-compatible photonic devices for single-photon generation. *Nanophotonics*, 5(3):427–439, 2016.

[71] Dirk Taillaert, Roel Baets, Pieter Dumon, Wim Bogaerts, Dries Van Thourhout, Bert Luyssaert, Vincent Wiaux, Stephan Beckx, and Johan Wouters. Silicon-on-insulator platform for integrated wavelength-selective components. In *Proc. of*, pages 115–120, 2005.

[72] Philippe Grangier, Barry Sanders, and Jelena Vuckovic. Focus on single photons on demand. *New Journal of Physics*, 6(1):31, 2004.

[73] Jeremy L O'Brien, Geoffrey J Pryde, Andrew G White, Timothy C Ralph, and David Branning. Demonstration of an all-optical quantum controlled-not gate. *Nature*, 426(6964):264–267, 2003.

[74] Kristine M Rosfjord, Joel KW Yang, Eric A Dauler, Andrew J Kerman, Vikas Anant, Boris M Voronov, Gregory N Gol'Tsman, and Karl K Berggren. Nanowire single-photon detector with an integrated optical cavity and anti-reflection coating. *Optics express*, 14(2):527–534, 2006.

[75] Andrea Del Duce. *Quantum Logic circuits for solid-state quantum information processing*. PhD thesis, UCL (University College London), 2010.

[76] A Kiraz, P Michler, C Becher, B Gayral, Lidong Zhang, E Hu, WV Schoenfeld, PM Petroff, and A Imamoğlu. Quantum dot single photon source. In *Coherence and Quantum Optics VIII*, pages 165–170. Springer, 2003.

[77] Lucia Caspani, Chunle Xiong, Benjamin J Eggleton, Daniele Bajoni, Marco Liscidini, Matteo Galli, Roberto Morandotti, and David J Moss. Integrated sources of photon quantum states based on nonlinear optics. *Light: Science & Applications*, 6(11):e17100, 2017.

[78] Shen Li, Cui-Hong Li, Bo-Wen Zhao, Yang Dong, Cong-Cong Li, Xiang-Dong Chen, Ya-Song Ge, and Fang-Wen Sun. A bright single-photon source from nitrogen-vacancy centers in diamond nanowires. *Chinese Physics Letters*, 34(9):096101, 2017.

[79] A Lohrmann, BC Johnson, JC McCallum, and S Castelletto. A review on single photon sources in silicon carbide. *Reports on Progress in Physics*, 80(3):034502, 2017.

[80] X He, H Htoon, SK Doorn, WHP Pernice, F Pyatkov, R Krupke, A Jeantet, Y Chassagneux, and C Voisin. Carbon nanotubes as emerging quantum-light sources. *Nature Materials*, page 1, 2018.

[81] Andrew J Shields. Semiconductor quantum light sources. In *Nanoscience And Technology: A Collection of Reviews from Nature Journals*, pages 221–229. World Scientific, 2010.

[82] Brahim Lounis and Michel Orrit. Single-photon sources. *Reports on Progress in Physics*, 68(5):1129, 2005.

[83] Je-Hyung Kim, Shahriar Aghaeimeibodi, Christopher JK Richardson, Richard P Leavitt, Dirk Englund, and Edo Waks. Hybrid integration of solid-state quantum emitters on a silicon photonic chip. *Nano letters*, 17(12):7394–7400, 2017.

[84] Matthew D Eisaman, JMAPS Fan, Alan Migdall, and Sergey V Polyakov. Invited review article: Single-photon sources and detectors. *Review of scientific instruments*, 82(7):071101, 2011.

[85] Olivier Gazzano and Glenn S Solomon. Toward optical quantum information processing with quantum dots coupled to microstructures. *JOSA B*, 33(7):C160–C175, 2016.

[86] N Mizuochi, T Makino, H Kato, D Takeuchi, M Ogura, H Okushi, M Nothaft, P Neumann, A Gali, Fedor Jelezko, et al. Electrically driven single-photon source at room temperature in diamond. *Nature Photonics*, 6(5):299, 2012.

[87] Sonia Buckley, Kelley Rivoire, and Jelena Vučković. Engineered quantum dot single-photon sources. *Reports on Progress in Physics*, 75(12):126503, 2012.

[88] Lucas Schweickert, Klaus D Jöns, Katharina D Zeuner, Saimon Filipe Covre da Silva, Huiying Huang, Thomas Lettner, Marcus Reindl, Julien Zichi, Rinaldo Trotta, Armando Rastelli, et al. On-demand solid-state single-photon source with 99.99% purity. *arXiv preprint arXiv:1712.06937*, 2017.

[89] Peter Lodahl, Sahand Mahmoodian, and Søren Stobbe. Interfacing single photons and single quantum dots with photonic nanostructures. *Reviews of Modern Physics*, 87(2):347, 2015.

[90] Sparrow quantum (DK). [Online; accessed 24/06/2018].

[91] Quandela - the light in quantum technologies (FR). [Online; accessed 24/06/2018].

[92] Iman Esmaeil Zadeh, Ali W Elshaari, Klaus D Jöns, Andreas Fognini, Dan Dalacu, Philip J Poole, Michael E Reimer, and Val Zwiller. Deterministic integration of single photon sources in silicon based photonic circuits. *Nano Letters*, 16(4):2289–2294, 2016.

[93] CK Hong and Leonard Mandel. Experimental realization of a localized one-photon state. *Physical Review Letters*, 56(1):58, 1986.

[94] Xiang Guo, Chang-ling Zou, Carsten Schuck, Hojoong Jung, Risheng Cheng, and Hong X Tang. Parametric down-conversion photon-pair source on a nanophotonic chip. *Light: Science & Applications*, 6(5):e16249, 2017.

[95] Chandra M Natarajan, Michael G Tanner, and Robert H Hadfield. Superconducting nanowire single-photon detectors: physics and applications. *Superconductor Science and Technology*, 25(6):063001, 2012.

[96] Christopher J Chunnilall, Ivo Pietro Degiovanni, Stefan Kück, Ingmar Müller, and Alastair G Sinclair. Metrology of single-photon sources and detectors: a review. *Optical Engineering*, 53(8):081910, 2014.

[97] Christine Silberhorn. Detecting quantum light. *Contemporary Physics*, 48(3):143–156, 2007.

[98] Robert M Heath, Michael G Tanner, Robert A Kirkwood, Shigehito Miki, Richard J Warburton, and Robert H Hadfield. A tunable fiber-coupled optical cavity for agile enhancement of detector absorption. *Journal of Applied Physics*, 120(11):113101, 2016.

[99] Robert H Hadfield. Single-photon detectors for optical quantum information applications. *Nature Photonics*, 3(12):696–705, 2009.

[100] Aleksander Divochiy, Francesco Marsili, David Bitauld, Alessandro Gaggero, Roberto Leoni, Francesco Mattioli, Alexander Korneev, Vitaliy Seleznev, Nataliya Kaurova, Olga Minaeva, et al. Superconducting nanowire photon-number-resolving detector at telecommunication wavelengths. *Nature Photonics*, 2(5):302–306, 2008.

[101] Harley Iams and Bernard Salzberg. The secondary emission phototube. *Proceedings of the Institute of Radio Engineers*, 23(1):55–64, 1935.

[102] R Foord, R Jones, CJ Oliver, and ER Pike. The use of photomultiplier tubes for photon counting. *Applied Optics*, 8(10):1975–1989, 1969.

[103] S Cova, A Longoni, and A Andreoni. Towards picosecond resolution with single-photon avalanche diodes. *Review of Scientific Instruments*, 52(3):408–412, 1981.

[104] Silicon avalanche photodiodes , c30902 series. [Online; accessed 04/07/2018].

[105] Rafael Ben-Michael, Mark A Itzler, and Bruce Nyman. Afterpulsing effects in 1.5 μm single photon avalanche photodetectors. In *Lasers and Electro-Optics Society, 2006. LEOS 2006. 19th Annual Meeting of the IEEE*, pages 783–784. IEEE, 2006.

[106] David Goodstein and Judith Goodstein. Richard Feynman and the history of superconductivity. pages 773–791, 1996.

[107] Joe Khachan and Stephen Bosi. The discovery of superconductors. 2008.

[108] H Kamerlingh Onnes. The resistance of pure mercury at helium temperatures. *Commun. Phys. Lab. Univ. Leiden*, 12(120):1, 1911.

[109] Charles Kittel. *Introduction to solid state physics*. Wiley, 2005.

[110] David Dew-Hughes. The critical current of superconductors: an historical review. *Low Temperature Physics*, 27(9):713–722, 2001.

[111] James William Rohlf. Modern physics from aalpha to z0. *Modern Physics from aalpha to Z0, by James William Rohlf, pp. 664. ISBN 0-471-57270-5. Wiley-VCH, March 1994.*, page 664, 1994.

[112] Adriana E Lita, Aaron J Miller, and Sae Woo Nam. Counting near-infrared single-photons with 95% efficiency. *Optics Express*, 16(5):3032–3040, 2008.

[113] Aaron J Miller, Sae Woo Nam, John M Martinis, and Alexander V Sergienko. Demonstration of a low-noise near-infrared photon counter with multiphoton discrimination. *Applied Physics Letters*, 83(4):791–793, 2003.

[114] Yue Zhao. *Characterization of transition edge sensors for the Millimeter Bolometer Array Camera on the Atacama Cosmology Telescope*. Princeton University, 2010.

[115] Didier DE Martin and Peter Verhoeve. Superconducting tunnel junctions. In *Observing Photons in Space*, pages 479–496. Springer, 2013.

[116] A Peacock, P Verhoeve, N Rando, A Van Dordrecht, BG Taylor, C Erd, MAC Perryman, R Venn, J Howlett, DJ Goldie, et al. Single optical photon detection with a superconducting tunnel junction. *Nature*, 381(6578):135–137, 1996.

[117] S Friedrich. Superconducting tunnel junction photon detectors: Theory and applications. *Journal of Low Temperature Physics*, 151(1):277–286, 2008.

[118] Robert J Collins, RH Hadfield, Veronica Fernandez, Sae Woo Nam, and Gerald S Buller. Low timing jitter detector for gigahertz quantum key distribution. *Electronics Letters*, 43(3):180–182, 2007.

[119] Michael G Tanner, CM Natarajan, VK Pottapenjara, JA O'Connor, RJ Warburton, RH Hadfield, B Baek, S Nam, SN Dorenbos, E Bermúdez Ureña, et al. Enhanced telecom wavelength single-photon detection with nbtin superconducting nanowires on oxidized silicon. *Applied Physics Letters*, 96(22):221109, 2010.

[120] Zhen Wang, Shigehito Miki, and Mikio Fujiwara. Superconducting nanowire single-photon detectors for quantum information and communications. *IEEE Journal of selected topics in quantum electronics*, 15(6):1741–1747, 2009.

[121] GN Gol'tsman, O Okunev, G Chulkova, A Lipatov, A Semenov, K Smirnov, B Voronov, A Dzardanov, C Williams, and Roman Sobolewski. Picosecond superconducting single-photon optical detector. *Applied Physics Letters*, 79(6):705–707, 2001.

[122] Anthony Joseph Annunziata. *Single-photon detection, kinetic inductance, and nonequilibrium dynamics in niobium and niobium nitride superconducting nanowires*. PhD thesis, 2010.

[123] Itamar Holzman and Yachin Ivry. Quantum materials for nanoscale quantum sensors: opportunities and challenges in superconducting nanowire single photon detectors. *arXiv preprint arXiv:1807.09060*, 2018.

[124] Andreas Engel, JJ Renema, Konstantin Il'in, and Alexander Semenov. Detection mechanism of superconducting nanowire single-photon detectors. *Superconductor Science and Technology*, 28(11):114003, 2015.

[125] Jonas Zmuidzinas and Paul L Richards. Superconducting detectors and mixers for millimeter and submillimeter astrophysics. *Proceedings of the IEEE*, 92(10):1597–1616, 2004.

[126] Dieter K Schroder. *Semiconductor material and device characterization*. John Wiley & Sons, 2006.

[127] Zhen Wang, Akira Kawakami, Yoshinori Uzawa, and Bokuji Komiyama. Superconducting properties and crystal structures of single-crystal niobium nitride thin films deposited at ambient substrate temperature. *Journal of Applied Physics*, 79(10):7837–7842, 1996.

[128] Zhen Wang, Akira Kawakami, Yoshinori Uzawa, and Bokuji Komiyama. Superconducting properties of single-crystal NbN thin films deposited at ambient substrate temperature. In *Advances in Superconductivity VII*, pages 991–994. Springer, 1995.

[129] G Gol'Tsman, O Okunev, G Chulkova, A Lipatov, A Dzardanov, K Smirnov, A Semenov, B Voronov, C Williams, and Roman Sobolewski. Fabrication and properties of an ultrafast nbn hot-electron single-photon detector. *IEEE Transactions on applied superconductivity*, 11(1):574–577, 2001.

[130] A Verevkin, J Zhang, Roman Sobolewski, A Lipatov, O Okunev, G Chulkova, A Korneev, K Smirnov, GN Gol'tsman, and A Semenov. Detection efficiency of large-active-area NbN single-photon superconducting detectors in the ultraviolet to near-infrared range. *Applied Physics Letters*, 80(25):4687–4689, 2002.

[131] Aaron J Miller, Adriana E Lita, Brice Calkins, Igor Vayshenker, Steven M Gruber, and Sae Woo Nam. Compact cryogenic self-aligning fiber-to-detector coupling with losses below one percent. *Optics Express*, 19(10):9102–9110, 2011.

[132] Luca Redaelli, Gabriele Bulgarini, Sergiy Dobrovolskiy, Sander N Dorenbos, Vall Zwiller, Eva Monroy, and Jean-Michel Gérard. Design of broadband high-efficiency superconducting-nanowire single photon detectors. *Superconductor Science and Technology*, 29(6):065016, 2016.

[133] Francesco Marsili, Faraz Najafi, Charles Herder, and Karl K Berggren. Electrothermal simulation of superconducting nanowire avalanche photodetectors. *Applied Physics Letters*, 98(9):093507, 2011.

[134] S. N. Dorenbos, E. M. Reiger, U. Perinetti, V. Zwiller, T. Zijlstra, and T. M. Klapwijk. Low noise superconducting single photon detectors on silicon. *Applied Physics Letters*, 93(13), 2008.

[135] VB Verma, B Korzh, F Bussières, RD Horansky, SD Dyer, AE Lita, I Vayshenker, F Marsili, MD Shaw, H Zbinden, et al. High-efficiency superconducting nanowire single-photon detectors fabricated from MoSi thin-films. *arXiv preprint arXiv:1504.02793*, 2015.

[136] VB Verma, AE Lita, MR Vissers, F Marsili, DP Pappas, RP Mirin, and Sae Woo Nam. Superconducting nanowire single photon detectors fabricated from an amorphous Mo0. 75Ge0. 25 thin film. *Applied Physics Letters*, 105(2):022602, 2014.

[137] Erman Engin, Damien Bonneau, Chandra M Natarajan, Alex S Clark, MG Tanner, RH Hadfield, Sanders N Dorenbos, Val Zwiller, Kazuya Ohira, Nobuo Suzuki, et al. Photon pair generation in a silicon micro-ring resonator with reverse bias enhancement. *Optics Express*, 21(23):27826–27834, 2013.

[138] Joshua W Silverstone, Raffaele Santagati, Damien Bonneau, Michael J Strain, Marc Sorel, Jeremy L O'Brien, and Mark G Thompson. Qubit entanglement between ring-resonator photon-pair sources on a silicon chip. *Nature Communications*, 6:7948, 2015.

[139] MG Tanner, L San Emeterio Alvarez, W Jiang, RJ Warburton, ZH Barber, and RH Hadfield. A superconducting nanowire single photon detector on lithium niobate. *Nanotechnology*, 23(50):505201, 2012.

[140] C Schuck, WHP Pernice, and HX Tang. NbTiN superconducting nanowire detectors for visible and telecom wavelengths single photon counting on Si3N4 photonic circuits. *Applied Physics Letters*, 102(5):051101, 2013.

[141] V Kovalyuk, W Hartmann, O Kahl, N Kaurova, A Korneev, G Gol'tsman, and WHP Pernice. Absorption engineering of NbN nanowires deposited on silicon nitride nanophotonic circuits. *Optics Express*, 21(19):22683–22692, 2013.

[142] Mohsen K Akhlaghi, Ellen Schelew, and Jeff F Young. Waveguide integrated superconducting single photon detectors implemented as coherent perfect absorbers. *arXiv preprint arXiv:1409.1962*, 2014.

[143] Günther Reithmaier, Stefan Lichtmannecker, Thorsten Reichert, Peter Hasch, Kai Müller, Max Bichler, Rudolf Gross, and Jonathan J Finley. On-chip time resolved detection of quantum dot emission using integrated superconducting single photon detectors. *Scientific Reports*, 3, 2013.

[144] Mark G Thompson, Alberto Politi, Jonathan CF Matthews, and Jeremy Lloyd O'Brien. Integrated waveguide circuits for optical quantum computing. *IET circuits, devices & systems*, 5(2):94–102, 2011.

[145] Amir Hosseini, David N Kwong, Yang Zhang, Harish Subbaraman, Xiaochuan Xu, and Ray T Chen. 1× n multimode interference beam splitter design techniques for on-chip optical interconnections. *IEEE Journal of Selected Topics in Quantum Electronics*, 17(3):510–515, 2011.

[146] Bing Shen, Peng Wang, Randy Polson, and Rajesh Menon. An integrated-nanophotonics polarization beamsplitter with 2.4× 2.4 μm 2 footprint. *Nature Photonics*, 9(6):378, 2015.

[147] Yinghong Xue, Akio Yoshizawa, and Hidemi Tsuchida. Hong- ou- mandel dip measurements of polarization-entangled photon pairs at 1550 nm. *Optics Express*, 18(8):8182–8186, 2010.

[148] Jeremy L O'brien, Akira Furusawa, and Jelena Vučković. Photonic quantum technologies. *Nature Photonics*, 3(12):687, 2009.

[149] Lukas Chrostowski and Michael Hochberg. *Silicon photonics design: from devices to systems*. Cambridge University Press, 2015.

[150] Qi-Chao Sun, Yang-Fan Jiang, Ya-Li Mao, Li-Xing You, Wei Zhang, Wei-Jun Zhang, Xiao Jiang, Teng-Yun Chen, Hao Li, Yi-Dong Huang, et al. Entanglement swapping over 100 km optical fiber with independent entangled photon-pair sources. *Optica*, 4(10):1214–1218, 2017.

[151] Yi-Heng Zhou, Zong-Wen Yu, Ao Li, Xiao-Long Hu, Cong Jiang, and Xiang-Bin Wang. Measurement-device-independent quantum key distribution via quantum blockade. *Scientific Reports*, 8(1):4115, 2018.

[152] Chong-Ki Hong, Zhe-Yu Ou, and Leonard Mandel. Measurement of subpicosecond time intervals between two photons by interference. *Physical Review Letters*, 59(18):2044, 1987.

[153] Dominic Mayers. Unconditional security in quantum cryptography. *Journal of the ACM (JACM)*, 48(3):351–406, 2001.

[154] Lars Lydersen, Carlos Wiechers, Christoffer Wittmann, Dominique Elser, Johannes Skaar, and Vadim Makarov. Hacking commercial quantum cryptography systems by tailored bright illumination. *Nature Photonics*, 4(10):686, 2010.

[155] Hoi-Kwong Lo, Marcos Curty, and Bing Qi. Measurement-device-independent quantum key distribution. *Physical review letters*, 108(13):130503, 2012.

[156] GL Roberts, M Lucamarini, ZL Yuan, JF Dynes, LC Comandar, AW Sharpe, AJ Shields, M Curty, IV Puthoor, and E Andersson. Experimental measurement-device-independent quantum digital signatures. *Nature Communications*, 8(1):1098, 2017.

[157] Eleni Diamanti, Hoi-Kwong Lo, Bing Qi, and Zhiliang Yuan. Practical challenges in quantum key distribution. *npj Quantum Information*, 2:16025, 2016.

[158] Raju Valivarthi, Qiang Zhou, Caleb John, Francesco Marsili, Varun B Verma, Matthew D Shaw, Sae Woo Nam, Daniel Oblak, and Wolfgang Tittel. A cost-effective measurement-device-independent quantum key distribution system for quantum networks. *Quantum Science and Technology*, 2(4):04LT01, 2017.

[159] MAK planar magnetron sputter source. [Online; accessed 12-June-2018].

[160] Milton Ohring. *Materials science of thin films*. Elsevier, 2001.

[161] Shigehito Miki, Yoshinori Uzawa, Akira Kawakami, and Zhen Wang. Fabrication and if bandwidth measurements of nbn hot-electron bolometers. *Electronics and Communications in Japan (Part II: Electronics)*, 85(7):77–83, 2002.

[162] Archan Banerjee. *Optimisation of superconducting thin film growth for next generation superconducting detector applications*. PhD thesis, University of Glasgow, 2017.

[163] R Radenbaugh. Refrigeration for superconductors. *Proceedings of the IEEE*, 92(10):1719–1734, 2004.

[164] Kleanthis Erotokritou. Low temperature characterization of superconducting thin films and devices. Master's thesis, University of Glasgow, 2014.

[165] Zheng Cui. Nanofabrication. *Course notes, ECE*, 730, 2008.

[166] LayoutEditor. [Online; accessed 03-May-2018].

[167] Tanner L-Edit IC Layout - Mentor Graphics. [Online; accessed 03-May-2018].

[168] Charalambos Klitis. *Polarisation selective integrated silicon photonic devices*. PhD thesis, University of Glasgow, 2018.

[169] Mohammad Ali Mohammad, Kirill Koshelev, Taras Fito, David Ai Zhi Zheng, Maria Stepanova, and Steven Dew. Study of development processes for zep-520 as a high-resolution positive and negative tone electron beam lithography resist. *Japanese Journal of Applied Physics*, 51(6S):06FC05, 2012.

[170] H Wang, GM Laws, S Milicic, P Boland, A Handugan, M Pratt, T Eschrich, S Myhajlenko, JA Allgair, and B Bunday. Low temperature zep-520a development process for enhanced critical dimension realization in reactive ion etch etched polysilicon. *Journal of Vacuum Science & Technology B*, 25(1):102–105, 2007.

[171] AE Grigorescu and CW Hagen. Resists for sub-20-nm electron beam lithography with a focus on hsq: state of the art. *Nanotechnology*, 20(29):292001, 2009.

[172] MicroChem NANO PMMA and Copolymer. [Online; accessed 11-May-2018].

[173] ZEP520 ; High Performance Positive EB resist . [Online; accessed 12-May-2018].

[174] Kimmo Solehmainen, Timo Aalto, James Dekker, Markku Kapulainen, Mikko Harjanne, Kaupo Kukli, Päivi Heimala, Kai Kolari, and Markku Leskelä. Dry-etched silicon-on-insulator waveguides with low propagation and fiber-coupling losses. *Journal of lightwave technology*, 23(11):3875, 2005.

[175] Surya Cheemalapati, Mikhail Ladanov, John Winskas, and Anna Pyayt. Optimization of dry etching parameters for fabrication of polysilicon waveguides with smooth sidewall using a capacitively coupled plasma reactor. *Applied Optics*, 53(25):5745–5749, 2014.

[176] Dong-Hyun Kim, Se-Koo Kang, Geun-Young Yeom, and Jae-Hyung Jang. Nanometer-scale fabrication of hydrogen silsesquioxane (HSQ) films with post exposure baking. *Journal of nanoscience and nanotechnology*, 13(3):1918–1922, 2013.

[177] YK Siew, G Sarkar, X Hu, J Hui, A See, and CT Chua. Thermal curing of hydrogen silsesquioxane. *Journal of The Electrochemical Society*, 147(1):335–339, 2000.

[178] TM Flynn. Cryogenic engineering 2nd, 2005.

[179] Konstantin Smirnov, Yury Vachtomin, Alexander Divochiy, Andrey Antipov, and Gregory Goltsman. Dependence of dark count rates in superconducting single photon detectors on the filtering effect of standard single mode optical fibers. *Applied Physics Express*, 8(2):022501, 2015.

[180] Sumitomo 4K cryocoolers. [Online; accessed 04-June-2018].

[181] Chandra Mouli Natarajan. *Superconducting nanowire single-photon detectors for advanced photon-counting applications*. PhD thesis, Citeseer, 2011.

[182] Andrew J Kerman, Eric A Dauler, William E Keicher, Joel KW Yang, Karl K Berggren, G Gol'Tsman, and B Voronov. Kinetic-inductance-limited reset time of superconducting nanowire photon counters. *Applied Physics Letters*, 88(11):111116, 2006.

[183] Robert M Heath, Michael G Tanner, Alessandro Casaburi, Mark G Webster, Lara San Emeterio Alvarez, Weitao Jiang, Zoe H Barber, Richard J Warburton, and Robert H Hadfield. Nano-optical observation of cascade switching in a parallel superconducting nanowire single photon detector. *Applied physics letters*, 104(6):063503, 2014.

[184] SM2000 - single mode optical fibre. [Online; accessed 27/07/2018].

[185] Chromacity spark OPO. [Online; accessed 27/07/2018].

[186] Isamu Takai, Hiroyuki Matsubara, Mineki Soga, Mitsuhiko Ohta, Masaru Ogawa, and Tatsuya Yamashita. Single-photon avalanche diode with enhanced NIR-sensitivity for automotive lidar systems. *Sensors*, 16(4):459, 2016.

[187] Alberto Tosi, Mirko Sanzaro, Niccolò Calandri, Alessandro Ruggeri, and Fabio Acerbi. Low dark count rate and low timing jitter ingaas/inp single-photon avalanche diode. In *Solid State Device Research Conference (ESSDERC), 2014 44th European*, pages 82–85. IEEE, 2014.

[188] Edo Waks, Kyo Inoue, Charles Santori, David Fattal, Jelena Vuckovic, Glenn S Solomon, and Yoshihisa Yamamoto. Secure communication: Quantum cryptography with a photon turnstile. *Nature*, 420(6917):762, 2002.

[189] Robert H Hadfield, Martin J Stevens, Richard P Mirin, and Sae Woo Nam. Single-photon source characterization with twin infrared-sensitive superconducting single-photon detectors. *Journal of Applied Physics*, 101(10):103104, 2007.

[190] A Gaggero, S Jahanmiri Nejad, F Marsili, F Mattioli, R Leoni, D Bitauld, D Sahin, GJ Hamhuis, R Nötzel, R Sanjines, et al. Nanowire superconducting single-photon detectors on GaAs for integrated quantum photonic applications. *Applied Physics Letters*, 97(15):151108, 2010.

[191] WJ Zhang, H Li, LX You, J Huang, YH He, L Zhang, XY Liu, SJ Chen, Z Wang, and XM Xie. Superconducting nanowire single-photon detector with a system detection efficiency over 80% at 940-nm wavelength. *IEEE Photon. J*, 8(2):4500908, 2016.

[192] Vadim V Vorobyov, Alexander Yu Kazakov, Vladimir V Soshenko, Alexander A Korneev, Mikhail Y Shalaginov, Stepan V Bolshedvorskii, Vadim N Sorokin, Alexander V Divochiy, Yury B Vakhtomin, Konstantin V Smirnov, et al. Superconducting detector for visible and near-infrared quantum emitters. *Optical Materials Express*, 7(2):513–526, 2017.

[193] Taro Yamashita, Kentaro Waki, Shigehito Miki, Robert A Kirkwood, Robert H Hadfield, and Hirotaka Terai. Superconducting nanowire single-photon detectors with non-periodic dielectric multilayers. *Scientific reports*, 6:35240, 2016.

[194] I Milostnaya, A Korneev, I Rubtsova, V Seleznev, O Minaeva, G Chulkova, O Okunev, B Voronov, K Smirnov, G Gol'tsman, et al. Superconducting single-photon detectors designed for operation at 1.55-μm telecommunication wavelength. In *Journal of Physics: Conference Series*, volume 43, page 1334. IOP Publishing, 2006.

[195] Gregory M Harry, Andri M Gretarsson, Peter R Saulson, Scott E Kittelberger, Steven D Penn, William J Startin, Sheila Rowan, Martin M Fejer, DRM Crooks, Gianpietro Cagnoli, et al. Thermal noise in interferometric gravitational wave detectors due to dielectric optical coatings. *Classical and Quantum Gravity*, 19(5):897, 2002.

[196] Tx-line: Transmission line calculator. [Online; accessed 22/06/2018].

[197] Andrew J Kerman, Eric A Dauler, Joel KW Yang, Kristine M Rosfjord, Vikas Anant, Karl K Berggren, Gregory N Gol'tsman, and Boris M Voronov. Constriction-limited detection efficiency of superconducting nanowire single-photon detectors. *Applied Physics Letters*, 90(10):101110, 2007.

[198] Vikas Anant, Andrew J Kerman, Eric A Dauler, Joel KW Yang, Kristine M Rosfjord, and Karl K Berggren. Optical properties of superconducting nanowire single-photon detectors. *Optics Express*, 16(14):10750–10761, 2008.

[199] Francesco Marsili, Francesco Bellei, Faraz Najafi, Andrew E Dane, Eric A Dauler, Richard J Molnar, and Karl K Berggren. Efficient single photon detection from 500 nm to 5 μm wavelength. *Nano Letters*, 12(9):4799–4804, 2012.

[200] MJB4 mask aligner. [Online; accessed14/07/2018].

[201] Shigehito Miki, Masanori Takeda, Mikio Fujiwara, Masahide Sasaki, and Zhen Wang. Compactly packaged superconducting nanowire single-photon detector with an optical cavity for multichannel system. *Optics express*, 17(26):23557–23564, 2009.

[202] Shigehito Miki, Taro Yamashita, Hirotaka Terai, and Zhen Wang. High performance fiber-coupled NbTiN superconducting nanowire single photon detectors with Gifford-Mcmahon cryocooler. *Optics Express*, 21(8):10208–10214, 2013.

[203] James B Abshire, Haris Riris, Graham Allan, Xiaoli Sun, S Randy Kawa, Jianping Mao, Mark Stephen, Emily Wilson, and Michael A Krainak. Laser sounder for global measurement of co 2 concentrations in the troposphere from space. In *Laser Applications to Chemical, Security and Environmental Analysis*, page LMA4. Optical Society of America, 2008.

[204] Quinn M Konopacky, Travis S Barman, Bruce A Macintosh, and Christian Marois. Detection of carbon monoxide and water absorption lines in an exoplanet atmosphere. *Science*, 339(6126):1398–1401, 2013.

[205] Remco J de Kok, Matteo Brogi, Ignas AG Snellen, Jayne Birkby, Simon Albrecht, and Ernst JW de Mooij. Detection of carbon monoxide in the high-resolution dayside spectrum of the exoplanet hd 189733b. *Astronomy & Astrophysics*, 554:A82, 2013.

[206] Hiroyuki Shibata, Kaoru Shimizu, Hiroki Takesue, and Yasuhiro Tokura. Ultimate low system dark-count rate for superconducting nanowire single-photon detector. *Optics Letters*, 40(14):3428–3431, 2015.

[207] Damien Bonneau, Erman Engin, Kazuya Ohira, Nob Suzuki, Haruhiko Yoshida, Norio Iizuka, Mizunori Ezaki, Chandra M Natarajan, Michael G Tanner, Robert H Hadfield, et al. Quantum interference and manipulation of entanglement in silicon wire waveguide quantum circuits. *New Journal of Physics*, 14(4):045003, 2012.

[208] Jian Li, Robert A Kirkwood, Luke J Baker, David Bosworth, Kleanthis Erotokritou, Archan Banerjee, Robert M Heath, Chandra M Natarajan, Zoe H Barber, Marc Sorel, et al. Nano-optical single-photon response mapping of waveguide integrated molybdenum silicide (MoSi) superconducting nanowires. *Optics Express*, 24(13):13931–13938, 2016.

[209] D Bosworth, S-L Sahonta, RH Hadfield, and Zoe Helen Barber. Amorphous molybdenum silicon superconducting thin films. *AIP Advances*, 5(8):087106, 2015.

[210] Archan Banerjee, Luke J Baker, Alastair Doye, Magnus Nord, Robert M Heath, Kleanthis Erotokritou, David Bosworth, Zoe H Barber, Ian MacLaren, and Robert H Hadfield. Characterisation of amorphous molybdenum silicide (mosi) superconducting thin films and nanowires. *Superconductor Science and Technology*, 30(8):084010, 2017.

[211] John B Schneider. Understanding the finite-difference time-domain method. *School of electrical engineering and computer science Washington State University.–URL: http://www. Eecs. Wsu. Edu/˜ schneidj/ufdtd/(request data: 29.11. 2012)*, 2010.

[212] LOT quantum design - spectroscopic ellipsometrs. [Online; accessed 07/08/2018].

[213] Andrew J Kerman, Joel KW Yang, Richard J Molnar, Eric A Dauler, and Karl K Berggren. Electrothermal feedback in superconducting nanowire single-photon detectors. *Physical Review B*, 79(10):100509, 2009.

[214] Shigehito Miki, Hirotaka Terai, Taro Yamashita, Kazumasa Makise, Mikio Fujiwara, Masahide Sasaki, and Zhen Wang. Superconducting single photon detectors integrated with single flux quantum readout circuits in a cryocooler. *Applied Physics Letters*, 99(11):111108, 2011.

[215] JA O'Connor. *Nano-Optical Studies of Superconducting Nanowire Single-Photon Detectors*. PhD thesis, Heriot-Watt University, 2011.

[216] Archan Banerjee, Robert M Heath, Dmitry Morozov, Dilini Hemakumara, Umberto Nasti, Iain Thayne, and Robert H Hadfield. Optical properties of refractory metal based thin films. *Optical Materials Express*, 8(8):2072–2088, 2018.

[217] JW Silverstone, D Bonneau, K Ohira, N Suzuki, H Yoshida, N Iizuka, M Ezaki, CM Natarajan, MG Tanner, RH Hadfield, V Zwiller, GD Marshall, JG Rarity, JL O'Brien, and MG Thompson. On-chip quantum interference between silicon photon-pair sources. *Nature Photonics*, 8(2):104–108, 2014.

[218] Stefan F Preble, Michael L Fanto, Jeffrey A Steidle, Christopher C Tison, Gregory A Howland, Zihao Wang, and Paul M Alsing. On-chip quantum interference from a single silicon ring-resonator source. *Physical Review Applied*, 4(2):021001, 2015.

Appendix A List of publications

Journals

- K. Erotokritou, R.M. Heath, G.G. Taylor, C. Tian, A. Banerjee, A. Casaburi, C.M. Natarajan, S. Miki, H. Terai and R.H. Hadfield. Nano-optical photoresponse mapping of superconducting nanowires with enhanced near infrared absorption, Superconductor Science and Technology August 2018 - accepted 27/09/2018

- K. Tsimvrakidis, N.R. Gemmell, K. Erotokritou, S. Miki, M. Yabuno, T. Yamashita, H. Terai and R.H. Hadfield. Enhanced optics for time-resolved singlet oxygen luminescence detection. IEEE Journal of Selected Topics in Quantum Electronics. 2019 Jan;25(1):1-7.

- A. Banerjee, L.J. Baker, A. Doye, M. Nord, R.M. Heath, K. Erotokritou, D. Bosworth, Z.H. Barber, I. MacLaren and R.H. Hadfield. Characterisation of amorphous molybdenum silicide (MoSi) superconducting thin films and nanowires. Superconductor Science and Technology. 2017 Jul 12;30(8):084010.

- J. Li, R.A. Kirkwood, L.J. Baker, D. Bosworth, K. Erotokritou, A. Banerjee, R.M. Heath, C.M. Natarajan, Z.H. Barber, M. Sorel, and R.H. Hadfield, Nano-optical single-photon response mapping of waveguide integrated molybdenum silicide (MoSi) superconducting nanowires. Optics express. 2016 Jun 27;24(13):13931-8.

Appendix B List of Presentations

- K. Erotokritou, R.M. Heath, A. Banerjee, M. Sorel R.H. Hadfield 'Integration of molybdenum silicide superconducting nanowires with quantum photonic circuits for on-chip single photon detection' International Superconductive Electronics Conference ISEC 2017 13-6 2017 Sorrento, Italy (Poster)

- K. Erotokritou, A. Banerjee, R.H. Hadfield, "Waveguide integrated nanowire single photon detectors for quantum information processing," SUSSP71: Frontiers in Quantum Dynamics & Quantum Optics, 21 July – 2 August 2015 University of Strathclyde, UK (Poster)

- K. Erotokritou, J. Li, L. J. Baker, R. A. Kirkwood, A. Banerjee, C. M. Natarajan, R. M. Heath, M. Sorel, R.H. Hadfield, "Integration of MoSi superconducting nanowires with quantum photonic circuits", Photon16 Conference, September 5-8 2016 University of Leeds, UK (Poster)

- K. Erotokritou, J.Li, A. Banerjee, C.M. Natarajan, M. Sorel, R.H. Hadfield, "Waveguide integrated superconducting single-photon detectors", PICQUE Bristol Young Scientists Conference on Quantum Information with Photons, April 4-6 2016 University of Bristol, UK (Talk)

- K. Erotokritou, J.Li, A. Banerjee, C.M. Natarajan, M. Sorel, R.H. Hadfield, "Waveguide integrated superconducting single-photon detectors" , Superconductors-based sensors and quantum technologies, April 18-21 2016 British Council Newton Fund Researcher Links Workshop - Moscow State pedagogical University, Russia (Talk)

Appendix C List of Optical Constants

Variable Angle Spectroscopic Ellipsometry (VASE) measured data of a 5 nm NbTiN thin film and a 5 nm MoSi thin film. [216].

Wavelength (nm)	NbTiN		MoSi	
	Index of refraction (n)	Extinction coefficient (k)	Index of refraction (n)	Extinction coefficient (k)
1200	3.6175	3.6411	5.4155	4.5207
1210	3.6409	3.6478	5.4361	4.5301
1220	3.6637	3.6542	5.4562	4.5394
1230	3.6859	3.6605	5.4759	4.5487
1240	3.7075	3.6666	5.4952	4.5579
1250	3.7285	3.6725	5.514	4.5671
1260	3.749	3.6784	5.5325	4.5763
1270	3.769	3.6842	5.5506	4.5856
1280	3.7885	3.6901	5.5684	4.5949
1290	3.8074	3.6959	5.5858	4.6042
1300	3.826	3.7017	5.6029	4.6136
1310	3.8441	3.7076	5.6198	4.623
1320	3.8619	3.7135	5.6364	4.6326
1330	3.8792	3.7195	5.6527	4.6422
1340	3.8962	3.7256	5.6688	4.652
1350	3.9129	3.7317	5.6847	4.6618
1360	3.9293	3.738	5.7004	4.6717
1370	3.9455	3.7443	5.7159	4.6817
1380	3.9613	3.7508	5.7312	4.6918
1390	3.977	3.7573	5.7464	4.702
1400	3.9924	3.764	5.7614	4.7123
1410	4.0076	3.7707	5.7763	4.7227

1420	4.0226	3.7776	5.7911	4.7331
1430	4.0375	3.7845	5.8058	4.7437
1440	4.0522	3.7916	5.8203	4.7543
1450	4.0668	3.7987	5.8348	4.765
1460	4.0812	3.8059	5.8492	4.7758
1470	4.0956	3.8132	5.8635	4.7866
1480	4.1098	3.8205	5.8778	4.7975
1490	4.1239	3.8279	5.8919	4.8085
1500	4.138	3.8354	5.9061	4.8195
1510	4.1519	3.843	5.9201	4.8306
1520	4.1658	3.8506	5.9341	4.8417
1530	4.1797	3.8582	5.9481	4.8528
1540	4.1934	3.8659	5.962	4.864
1550	4.2071	3.8736	5.9759	4.8752
1560	4.2208	3.8813	5.9898	4.8865
1570	4.2344	3.8891	6.0036	4.8977
1580	4.248	3.8969	6.0174	4.909
1590	4.2616	3.9046	6.0311	4.9203
1600	4.2751	3.9124	6.0449	4.9317
1610	4.2886	3.9202	6.0586	4.943
1620	4.302	3.928	6.0723	4.9543
1630	4.3154	3.9358	6.0859	4.9657
1640	4.3288	3.9436	6.0996	4.977
1650	4.3422	3.9514	6.1132	4.9883
1660	4.3555	3.9591	6.1268	4.9996
1670	4.3689	3.9668	6.1404	5.011
1680	4.3821	3.9745	6.154	5.0223
1690	4.3954	3.9822	6.1675	5.0336
1700	4.4087	3.9898	6.1811	5.0448
1710	4.4219	3.9974	6.1946	5.0561
1720	4.4351	4.005	6.2081	5.0673
1730	4.4482	4.0125	6.2216	5.0785
1740	4.4614	4.02	6.2351	5.0897
1750	4.4745	4.0274	6.2485	5.1009
1760	4.4876	4.0348	6.262	5.112
1770	4.5007	4.0421	6.2754	5.1231

1780	4.5137	4.0494	6.2888	5.1342
1790	4.5267	4.0566	6.3022	5.1452
1800	4.5397	4.0637	6.3156	5.1562
1810	4.5526	4.0708	6.3289	5.1672
1820	4.5656	4.0779	6.3423	5.1781
1830	4.5785	4.0849	6.3556	5.189
1840	4.5913	4.0918	6.3689	5.1998
1850	4.6041	4.0986	6.3822	5.2106
1860	4.6169	4.1054	6.3955	5.2214
1870	4.6297	4.1121	6.4088	5.2321
1880	4.6424	4.1188	6.422	5.2428
1890	4.6551	4.1254	6.4352	5.2534
1900	4.6677	4.1319	6.4484	5.264
1910	4.6803	4.1384	6.4616	5.2745
1920	4.6928	4.1448	6.4748	5.285
1930	4.7053	4.1511	6.4879	5.2954
1940	4.7178	4.1573	6.501	5.3058
1950	4.7302	4.1635	6.5141	5.3161
1960	4.7426	4.1696	6.5272	5.3264
1970	4.7549	4.1757	6.5403	5.3367
1980	4.7672	4.1816	6.5533	5.3468
1990	4.7795	4.1875	6.5663	5.357
2000	4.7916	4.1934	6.5793	5.367
2010	4.8038	4.1991	6.5923	5.3771
2020	4.8159	4.2048	6.6053	5.387
2030	4.8279	4.2104	6.6182	5.397
2040	4.8399	4.216	6.6311	5.4068
2050	4.8518	4.2214	6.644	5.4166
2060	4.8637	4.2269	6.6568	5.4264
2070	4.8755	4.2322	6.6696	5.4361
2080	4.8872	4.2375	6.6824	5.4457
2090	4.8989	4.2427	6.6952	5.4553
2100	4.9106	4.2478	6.708	5.4648
2110	4.9222	4.2529	6.7207	5.4743
2120	4.9337	4.2579	6.7334	5.4837
2130	4.9451	4.2628	6.7461	5.4931

2140	4.9565	4.2676	6.7587	5.5024
2150	4.9679	4.2724	6.7713	5.5116
2160	4.9792	4.2772	6.7839	5.5208
2170	4.9904	4.2818	6.7965	5.5299
2180	5.0015	4.2864	6.809	5.539
2190	5.0126	4.291	6.8216	5.548
2200	5.0236	4.2954	6.834	5.557